

# Analysis of Dual-Frequency Observations of Interplanetary Scintillations Taken by the Pioneer 9 Spacecraft

by

Horen Chang

May 1976

Reproduction in whole or in part  
is permitted for any purpose of  
the United States Government.

Technical Report No. 3552-1

Supported jointly by  
National Science Foundation  
Grant DES 75-00493 and  
National Aeronautics and  
Space Administration  
Grant NGR 05-020-407.

N79-80075

Unclas  
00/93 32508

(NASA-CR-162229) ANALYSIS OF DUAL-FREQUENCY  
OBSERVATIONS OF INTERPLANETARY  
SCINTILLATIONS TAKEN BY THE PIONEER 9  
SPACECRAFT (Stanford Univ.) 211 p

CENTER FOR RADAR ASTRONOMY  
**STANFORD ELECTRONICS LABORATORIES**

STANFORD UNIVERSITY • STANFORD, CALIFORNIA



211 p

32508

ANALYSIS OF DUAL-FREQUENCY OBSERVATIONS OF INTERPLANETARY  
SCINTILLATIONS TAKEN BY THE PIONEER 9 SPACECRAFT

by

Horen Chang

May 1976

Reproduction in whole or in part  
is permitted for any purpose of  
the United States Government.

Technical Report No. 3552-1

Supported jointly by

National Science Foundation Grant DES 75-00493 and  
National Aeronautics and Space Administration  
Grant NGR 05-020-407

Center for Radar Astronomy  
Stanford Electronics Laboratories  
Stanford University                      Stanford, California

© Copyright 1976

by

Horen Chang

## ABSTRACT

Interplanetary scintillation data collected at Stanford during the period 1968-1973 are reported. These data were acquired by sending 50 and 423 MHz signals from Stanford to the sun-orbiting Pioneer 9 spacecraft and then telemetering results back to the earth. For the first time, the integrated electron contents along the propagation path were also simultaneously measured. The closest distance of the propagation path to the sun ranged from 0.1 to 1 A.U. Unlike noisy natural sources such as quasars or pulsars which were used in most previous experiments, our ground transmitter served as a constant-magnitude, monochromatic, point source of observation. As a result, our data are free from some inherent ambiguities contained in the majority of the previous data.

Experimental apparatus and procedures of data reduction are described in considerable detail. The so-called thin-screen diffraction model is reviewed and applied to interpret our observations, leading to several interesting and useful results. The spatial power spectrum of interplanetary inhomogeneities is found to follow a power-law variation; the mean and standard deviation of the power-law exponent are estimated to be  $3.5 \pm 0.13$  and 0.3, respectively. This result agrees with in situ spacecraft measurements near 1 A.U. In addition, the magnitude of the temporal spectrum of electron-density fluctuations deduced from our scintillation data is also consistent with in situ measurements. Based upon the forms of the observed scintillation spectra, the existence of a gaussian micro-structure in the interplanetary medium, as suggested by many other authors, is precluded. Occasionally the Fresnel structures in the scintillation

spectra are observed. Eight solar wind velocities inferred from eight such structures lie between 400 and 500 km/sec.

The radial dependence of the correlation length of intensity fluctuations is shown to be compatible with the power law model of exponent 3.5. The radial dependence of the scintillation index indicates that the root-mean-square electron-density fluctuation in the solar wind is inversely proportional to the square of the heliocentric distance from the sun. The wavelength dependence of the correlation length and that of the scintillation index, nevertheless, remain unexplained.

The study of the cross-correlation between the integrated electron content and the scintillation index reveals that not only these two parameters but also their deviations from means are approximately linearly related. This suggests that scintillation observations may be employed as an efficient means for monitoring both the density and density enhancements in the regions too near the sun to be accessible to direct measurements.

In cases of very strong scintillations, the form of the observed scintillation spectra becomes exponential, and the occurrence of these exponential spectra may be caused by the very strong wave scattering phenomenon rather than genuine changes of the turbulence spectrum forms.

## ACKNOWLEDGMENT

I am most grateful to Professor Thomas A. Croft, my principal advisor, for suggesting the topic of the dissertation and providing me with the observational data; without his continual guidance and encouragement this work would not have been possible. I am also deeply indebted to Professors G. Leonard Tyler and Von R. Eshleman, whose comments and advice contributed invaluable to this research.

Special thanks are due to Lon W. Raley for operating the ground transmitters; to H. Taylor Howard for help in solving various problems; to Roy A. Long and Boyd C. Fair of Stanford Research Institute (SRI) for numerous useful discussions regarding the Stanford/SRI receiver on board the Pioneer 9 spacecraft; to Sue Johnson, Barbara A. Warsavage, and Diana J. Robinson for assistance with computer programming; to Miki Goldman, William Crosby, and Barbara Shao for aids in data reduction; and to Mary Anne Larimore for her excellent typing of the manuscript.

In addition, I would like to express my appreciation to the individuals at SRI, JPL, DSN (Deep Space Network), and NASA-Ames Research Center, who helped in obtaining the interplanetary scintillation data and electron-content measurements presented in this report.

Financial support for this work was provided jointly by the National Science Foundation under grant DES 75-00493 and by the National Aeronautics and Space Administration under grant NGR 05-020-407. This support is gratefully acknowledged.

# CONTENTS

	<u>Page</u>
I. INTRODUCTION . . . . .	1
A. Background and Previous Research . . . . .	1
B. Advantages of Present Experiment . . . . .	8
C. Organization . . . . .	9
D. Contributions to Knowledge . . . . .	10
II. THEORY . . . . .	13
A. Thin Phase-Diffraction Screen Model . . . . .	13
B. Temporal Spectrum of Intensity Fluctuations . . . . .	19
C. Gaussian Spectrum of Electron Density Fluctuations . . . . .	21
D. Power-Law Electron Density Spectrum . . . . .	25
E. Exponential Spectrum of Electron Density Fluctuations . . . . .	28
F. Logic of Irregularity-Form Tests . . . . .	29
G. Correlation Length of Intensity Fluctuations . . . . .	30
H. Scintillation Index . . . . .	32
I. Effects of Finite Angular Size of Source . . . . .	33
III. EXPERIMENT DESCRIPTION . . . . .	35
A. Trajectory of Pioneer 9 . . . . .	36
B. Transmission System . . . . .	39
C. Receiving Antennas . . . . .	41
D. Phase-Locked Receiver . . . . .	44
E. Spacecraft Telemetry and Transmission Subsystems . . . . .	49
F. Format D Data Calibration . . . . .	53
G. Total Received Noise Temperature . . . . .	56
H. Interplanetary Electron Content Measurement . . . . .	58
IV. DATA REDUCTION . . . . .	65
A. Data Clean-Up . . . . .	67
B. Autocorrelation Function of Intensity Fluctuation . . . . .	80
C. Power Spectrum of Intensity Fluctuation . . . . .	82
D. Linear and Quadratic Regressions of the Estimated Power Spectra on Three Distinct Scales . . . . .	88
1. Determination of the Fitting Regions . . . . .	88

# CONTENTS (Cont)

	<u>Page</u>
2. Testing the Power-Spectrum Forms via Linear and Quadratic Regressions . . . . .	91
3. Spectrum Signal-to-Noise Ratio $\Lambda$ . . . . .	100
E. Scintillation Index . . . . .	102
V. RESULTS AND INTERPRETATIONS . . . . .	107
A. Spatial Power Spectrum $F_n(q)$ of Interplanetary Electron Density Fluctuations . . . . .	108
1. Form of $F_n(q)$ . . . . .	108
2. Power Law Exponent $p$ of $F_n(q)$ . . . . .	112
3. Magnitude of $F_n(v)$ . . . . .	124
B. Fresnel Structure . . . . .	128
C. Correlation Length of Intensity Fluctuations. . . . .	131
D. Scintillation Index . . . . .	141
1. The Radial Variation of Scintillation Index . . . . .	141
2. Scintillation Rate Versus Scintillation Index . . . . .	150
3. Wavelength Dependence of Scintillation Index . . . . .	153
E. Correlation with Integrated Electron Content along the Ray Path . . . . .	160
VI. CONCLUSIONS AND RECOMMENDATIONS . . . . .	165
Appendix A. SIMPLIFICATION OF THE INTEGRAL $Q$ . . . . .	169
Appendix B. PROCEDURE OF DERIVING RECEIVING ANTENNA PATTERNS . . . . .	173
Appendix C. DIGITAL ERRORS OF A/D CONVERSION DUE TO THE SUN PULSE . . . . .	179
Appendix D. RECEIVED COSMIC NOISE TEMPERATURE $T_c$ . . . . .	187
Appendix E. RECEIVED SOLAR NOISE TEMPERATURE $T_s$ . . . . .	191
Appendix F. COMPUTATION OF THE AUTOCORRELATION FUNCTION OF INTENSITY FLUCTUATIONS . . . . .	195
Appendix G. COMPUTATION OF THE POWER SPECTRUM OF INTENSITY FLUCTUATIONS . . . . .	203
REFERENCES . . . . .	213



# TABLES

<u>Number</u>		<u>Page</u>
1.1	Summary of power-law exponents $p$ derived by different investigators . . . . .	6
3.1	Transmission system parameters . . . . .	39
5.1	Percentage results of regression tests on the forms of observed scintillation spectra . . . . .	109
5.2	Means and standard deviations of power-law exponent $F_n(q)$ before $(p')$ and after $(p)$ correcting for the effect of $\Lambda$ . . . . .	113
5.3	Some values of $\rho$ along with the corresponding values of $z^{0.375}$ . . . . .	148
B.1	49.8 MHz receiving antenna pattern $A^{\ell}(\psi, \theta=0^\circ)$ in dB, for $\psi = 1^\circ$ to $360^\circ$ in steps on one degree . . . . .	177
B.2	423.3 MHz receiving antenna pattern $A^{\ell}(\psi, \theta=0^\circ)$ in dB, for $\psi = 0^\circ$ to $359^\circ$ in steps of one degree . . . . .	178
C.1	The values of $b_m$ for $k = 6$ and $x = 23.5$ . . . . .	182
C.2	The values of $b_m$ for $T_2 < \tau_t < T_3$ , with $x$ given by Eq. (C.6) . . . . .	183
C.3	Effects of the tail edge of the sun pulse on Format D data . . . . .	185
G.1	80% confidence limits for $N = 1024$ . . . . .	210
G.2	90% confidence limits for $N = 1024$ . . . . .	211
G.3	$B_e$ and $\epsilon_0$ for $N = 1024$ . . . . .	212

# ILLUSTRATIONS

<u>Figure</u>		<u>Page</u>
2.1	Simplified geometry of IPS . . . . .	14
3.1	Pioneer 9 heliocentric orbit . . . . .	37
3.2	Definition of the proximate distance $\rho$ . . . . .	38
3.3	Spacecraft in-flight configuration . . . . .	42
3.4	Power patterns of receiving antennas in the ecliptic plane. . . . .	43
3.5	Simplified block diagram of the Stanford receiver. . . . .	45
3.6	Spacecraft telemetry and transmission subsystems . . . . .	50
3.7	Format D data calibration. . . . .	55
4.1	Flow chart of data reduction . . . . .	66
4.2	Spin period $\tau_0$ in seconds vs time in years. . . . .	70
4.3	Scintillation records on 9 Feb 1969 when the proximate distance $\rho$ of the radio path is 0.85 A.U. from the sun. . . . .	72
4.4	Scintillation record on 10 April 1969 when $\rho = 0.41$ A.U. . . . .	74
4.5	Scintillation record on 11 Nov 1970 when $\rho = 0.15$ A.U. . . . .	76
4.6	Scintillation record on 20 Sep 1972 when $\rho = 0.88$ A.U. and spacecraft was back near the earth . . . . .	78
4.7	Examples of power spectrum (vs three different scales) and autocorrelation function of intensity fluctuations . . . . .	83
4.8	An example illustrating the procedure of determining the fitting regions . . . . .	92
4.9	Another example illustrating the procedure of determining the fitting regions . . . . .	93
4.10	An example showing the linear regression lines and quadratic regression curves over the three fitting regions . . . . .	98
4.11	Another example showing the linear regression lines and quadratic regression curves over the three fitting regions . . . . .	99

# ILLUSTRATIONS (Cont)

<u>Figure</u>		<u>Page</u>
4.12	Correction factor of $m^2$ for the 49.8 MHz channel. . . .	105
4.13	Correction factor of $m^2$ for the 423.3 MHz channel . . .	106
5.1	Probability distribution of $p'$ for Cases 1-5. . . . .	114
5.2	Observed power-law exponent $p'$ of $F_n(q)$ before correcting for the effect of $\Lambda$ . . . . .	115
5.3	The effect of the noise spectrum on the apparent slope of the observed scintillation spectrum for $p = 3.5$ and $\Lambda = 10, 20, \text{ and } 30 \text{ dB}$ . . . . .	118
5.4	The theoretically predicted dependence of $p'$ upon $\Lambda$ for $p = 3.2, 3.3, \dots, 3.8$ . . . . .	123
5.5	Temporal spectrum of electron density fluctuations deduced from IPS data at 423 MHz. . . . .	127
5.6	Observed Fresnel oscillations in the scintillation spectrum. . . . .	129
5.7	Correlation length vs proximate distance. . . . .	132
5.8	Correlation length vs $\sqrt{\lambda z/2\pi}^2$ . . . . .	139
5.9	Lower limit of scintillation index $m$ at 49.8 MHz vs proximate distance $\rho$ . . . . .	142
5.10	Upper limit of scintillation index $m$ at 49.8 MHz vs proximate distance $\rho$ . . . . .	143
5.11	Lower limit of scintillation index $m$ at 423.3 MHz vs proximate distance $\rho$ . . . . .	144
5.12a	Upper limit of scintillation index $m$ at 423.3 MHz vs proximate distance $\rho$ . . . . .	145
5.12b	Corrected scintillation index $m_p$ of pulsar CP0950 derived by Zeissig and Lovelace <sup>P</sup> (1972) . . . . .	146
5.13	Scintillation rate vs scintillation index at 49.8 MHz . .	151
5.14	Scintillation rate vs scintillation index at 423.3 MHz. .	152
5.15	$x_L$ vs proximate distance $\rho$ . . . . .	158
5.16	$x_U$ vs proximate distance $\rho$ . . . . .	159
5.17	Interplanetary electron content vs scintillation index. .	161

# ILLUSTRATIONS (Cont)

<u>Figure</u>		<u>Page</u>
5.18	Normalized electron content vs normalized scintillation index . . . . .	163
A.1	Regions of integration before and after the coordinate transformation . . . . .	171
B.1	Procedure of deriving receiving antenna patterns . . . . .	173
C.1	Relationship between word and bit rate pulses. . . . .	179
C.2	Values of $v_m$ under normal operating condition for $x = 23.5$ . . . . .	181
C.3	Values of $v_m$ when $T_2 < \tau_t < T_3$ and $x = 23.5$ . . . . .	184
D.1	Ecliptic coordinates and definition of $\psi$ . . . . .	187
F.1	Two portions of a circular autocorrelation function $R_x^C(n\tau)$ . . . . .	198
F.2	Spread of $R_x^C(n\tau)$ when $N$ zeros are appended to $x(n\tau)$ . . . . .	198

## Chapter I

### INTRODUCTION

#### A. Background and Previous Research

The rapid fluctuations in received signal strength caused by the interplanetary plasma inhomogeneities along the propagation path are termed interplanetary scintillations or IPS. IPS was first discovered by Hewish, Scott, and Wills (1964) during a series of observations of radio stars, which exhibit random fluctuations of intensity at 178 MHz, with a time scale of 1-2 seconds. Because observations of IPS provide a valuable and relatively inexpensive means for studying the interplanetary medium (especially those regions of the medium at heliocentric distances not yet accessible to direct measurement), they have since been intensively extended to both lower and higher frequencies over a wide range of solar elongation [see, for example, Cohen et al. (1967), Antonova and Vitkevich (1967), Little and Hewish (1968), Cohen and Gundermann (1969), Hewish and Symonds (1969), Lovelace et al. (1970), Little (1971), Vitkevich and Vlasov (1972), Zeissig and Lovelace (1972), Houminer and Hewish (1972), Watanabe and Kakinuma (1972), Hewish (1972), Rickett (1973), Coles et al. (1974), Rao et al. (1974), and Mariani (1975)].

Like all other inversion problems, in which the characteristics of the medium are extracted from the characteristics of the received signal after its transit through the medium, the interpretation of these IPS data relies completely upon the establishment of an adequate wave-propagation model. Because electron-density fluctuations, and therefore refractive-index fluctuations, of the interplanetary plasma decrease sharply with the radial distance from the sun, most theoret-

ical models adopt for analytical convenience the so-called thin phase-changing screen approximation [e.g., Little and Hewish (1966), Salpeter (1967), Bramley and Young (1967), Jokipii (1970), Lovelace et al. (1970), Cronyn (1970), Jokipii and Hollweg (1970), Cronyn (1972 a, b, c), Matheson and Little (1971), Bourgois (1972), Rumsey (1975), and Mariani (1975)]. In this approximation, the interplanetary irregularities responsible for IPS are assumed to be confined to a thin layer (situated at the point of closest approach of the ray path to the sun) which imposes irregular phase changes on the incident wave. The randomly phase-modulated wavefront emerging from the thin layer can be decomposed into a number of plane waves travelling in different directions. As the wavefront passes beyond the thin layer, these plane-wave components begin to interfere with each other, forming a diffraction pattern (i.e., a two-dimensional pattern of intensity fluctuations) in the plane of observation. Because the irregularities and hence the resultant diffraction pattern are conveyed away from the sun by the solar wind, the record of intensity fluctuations obtained at a fixed site may then be visualized as a line scan of the diffraction pattern along the direction of the solar-wind velocity.

One important theoretical result is worth mentioning here. Due to the Fresnel filtering effect (Sec. II.A), it is well known that density fluctuations on the scale much greater than the radius of the first Fresnel zone ( $\sim$  a few hundred km at VHF/UHF) will not contribute IPS. Stated in another way, IPS can be used to probe only small-scale inhomogeneities in the solar wind.

Almost all interpretations of IPS data published before 1970 were founded on the assumption that the spatial spectrum of electron-density fluctuations in the solar wind followed a gaussian form. Early IPS observations, appearing to be consistent with such an assumption, led to the following major conclusions:

1. The observed temporal spectra of intensity fluctuations in the weak scintillation regime were often fairly close to gaussian [Cohen et al. (1967)].
2. There existed a micro-structure of electron-density fluctuations in the solar wind, whose power spectrum was probably best described by a gaussian function [Hewish (1971), Buckley (1971), Little (1971), Hewish (1972)]. The scale size of this micro-structure, which might be deduced from the width of the observed diffraction pattern, was on the order of a few hundred km near 1 A.U. and decreased approximately linearly with decreasing radial distance from the sun [Little (1971), Readhead (1971), Hewish (1972)].

The validity of the gaussian-density-spectrum assumption began to be suspected in 1970 by Lovelace et al. (1970), Jokipii and Hollweg (1970), Hollweg (1970), Cronyn (1970), and Jokipii (1970). Lovelace et al. (1970) presented eight observed spectra of intensity fluctuations and demonstrated that a number of these spectra over the frequency range 1-10 Hz could be interpreted in terms of a power-law density spectrum. Based upon the fact that the power spectra of interplanetary magnetic-field and plasma-velocity fluctuations near 1 A.U. exhibited a power-law dependence over the frequency range  $10^{-5}$  -  $10^{-2}$  Hz. Coleman (1968), Jokipii and Hollweg (1970), and Hollweg (1970) suggested that the density spectrum would also be of the same

power-law form if the magnetic field was frozen (or locked) into the turbulent plasma. Buckley (1971) agreed that on scales much greater than the proton gyro-radius<sup>†</sup>, variations of proton density (and therefore electron density<sup>‡</sup>) and magnetic field would tend to follow one another; however, he argued that for length scales less than a few hundred km, the "frozen field line" concept might start to break down such that the magnetic-field and plasma-density spectra could uncouple. The first in situ measurement of proton density spectrum near 1 A.U. over the frequency range  $10^{-4}$  to  $10^{-3}$  Hz [Intriligator and Wolfe (1970)] confirmed that the density spectrum in this frequency range did have a similar power-law behavior as that of magnetic-field and velocity spectra; nevertheless, it did not have high enough frequency resolution\* to preclude the existence of the gaussian micro-structure ( $\sim 100$  km) proposed by Hewish (1971), Buckley (1971), and Hewish (1972). Fortunately, the second and also the last (to date) in situ measurement of proton density spectrum near 1 A.U. [Unti et al. (1973)] spanned the frequency range from  $4.8 \times 10^{-3}$  to 13.3 Hz (corresponding to wave-numbers from  $\sim 5 \times 10^{-5}$  to  $\sim 0.1 \text{ km}^{-1}$ ) and thus had enough frequency resolution to yield information about the small-scale inhomogeneities

---

<sup>†</sup> According to Little (1971), the proton gyro-radius increases from  $\sim 1$  km at 0.1 A.U. to  $\sim 100$  km at 1 A.U.

<sup>‡</sup> Because the Debye length is only a few meters, the electron density spectra should follow proton density spectra out to wave numbers near 1 meter<sup>-1</sup> [Coles et al. (1974)].

\* Temporal frequency  $\nu$  in Hz is related to spatial wavenumber  $q$  in  $\text{km}^{-1}$  by

$$\nu = \frac{Uq}{2\pi}$$

where  $U$  is the solar wind velocity in km/sec. For  $U = 500$  km/sec near 1 A.U.,  $\nu = 10^{-4} - 10^{-3}$  Hz corresponds to  $q \approx 10^{-6} - 10^{-5} \text{ km}^{-1}$ .



responsible for IPS. Twenty-five out of 32 (~ 80%) observed spectra were found to be interpretable by a single, continuous, three-dimensional, power-law irregularity spectrum, with the exponent of the power law, denoted by  $p$ , equal to an average value of 3.55.

The controversy between gaussian and power-law models seemed to be temporarily settled after Unti's direct evidence supporting forcibly the power-law model had been put forward. Many questions, however, have remained as yet unresolved. For example, both Intriligator and Wolfe's and Unti's in situ measurements of proton-density spectra covered only regions in the IPM (interplanetary medium) of heliocentric distances ~ 1 A.U. from the sun; is the plasma-density spectrum in regions closer than 1 A.U. from the sun also describable by a power-law function? If so, what is the value of the power-law exponent  $p$  in these regions? Does it vary systematically with the radial distance from the sun?

The answers to the above questions are certainly important because they would help not only in understanding the turbulence structure of the interplanetary plasma but also in determining what energy transport processes cause the turbulence. As most regions of the IPM will remain inaccessible to direct spacecraft measurements in the foreseeable future and since IPS will continue to be one of the major methods to probe the IPM for some time to come, it has become desirable to check if one can reconcile IPS observations with in situ measurements (so that the merits of the IPS method may be reevaluated). For this purpose, Table 1.1 summarizes all six published values of the power-law exponent  $p^+$  obtained

---

<sup>+</sup> In deriving these values of  $p$ , Cronyn's (1970) theoretical results had been invoked. Briefly speaking, his results state that if the three-dimensional, spatial power spectrum of density fluctuations is power law with index  $p$ , then the temporal power spectra of (1) density fluctuations seen by a space probe and (2) intensity scintillations observed at a single site will also be power law with exponent  $p - 2$  and  $p - 1$ , respectively.

Investigators	Power-Law Exponent, p	Temporal Frequency Range	Covered IPM Region	Method
Coleman (1968)	3.2	$10^{-5}$ - $10^{-2}$ Hz	0.9-1 A.U.	In situ measurements of magnetic-field and plasma-velocity spectra <sup>†</sup>
Intrilligator and Wolfe (1970)	3.3	$10^{-4}$ - $10^{-3}$ Hz	~1 A.U.	In situ measurements of proton-density spectra
Unti et al. (1973)	3.55	$5 \times 10^{-3}$ -13 Hz	~1 A.U.	In situ measurements of proton-density spectra
Lovelace et al. (1970)	4-5	1-10 Hz	0.2-0.6 A.U.	IPS observations of quasar CTA 21 before removing source-diameter effect
Houminer (1973)	2.4	0.5-1 Hz	0.5-0.9 A.U.	IPS observations of quasar 3C 28T after removing source-diameter effect
Coles et al. (1974)	2.6	0.5-10 Hz (approximate)	0.6-1 A.U.	IPS observations of quasars 3C 144 and 3C 48 after removing source-diameter effect

Table 1.1. SUMMARY OF POWER-LAW EXPONENTS p DERIVED BY DIFFERENT INVESTIGATORS.

<sup>†</sup> The magnetic field lines are assumed to be frozen into the IPM over  $10^{-5}$ - $10^{-2}$  Hz so that the plasma-density spectra have the same form as the magnetic-field spectra.

by these two different methods. Note that quasars<sup>4</sup>, which are extended, noisy radio stars at an essentially infinite distance (say  $\sim 10^9$  light years) from the earth, were invariably used as sources in all three listed IPS observations. While the three values of  $p$  (3.2, 3.3, 3.55) deduced from in situ measurements are in good accord with one another, the other three values of  $p$  (4-5, 2.4, 2.6) acquired from IPS observations appear to be either too large (4-5) or too small (2.4, 2.6). Although the rather large value of  $p$  (4-5) found by Lovelace et al. (1970) may be attributed to the finite source-diameter effect<sup>†</sup> (Sec. II. I), it is not immediately clear why the two values of  $p$  (2.4 and 2.6) secured by Houminer (1973) and Coles et al. (1974), corrected for the source-diameter effect, are significantly smaller than those resulting from in situ measurements. Coles et al. (1974), during an attempt to compare their spectra with other published IPS spectra, have admitted that the source structures (of quasars) at low radio frequencies are so uncertain that corrections of source-diameter effects cannot be confidently applied to other published IPS spectra. If this is true, then the accuracy and reliability of many published IPS data (including spectral forms, spectral exponents, spectral widths, and temporal widths of the diffraction pattern) are limited to this uncertainty factor, and the use of man-made point source for IPS observations will be preferable to that of quasars or pulsars<sup>‡</sup>.

---

<sup>†</sup> Radio sources having a finite angular size  $\theta_0$  ( $\leq 1$  arc sec for quasars) may blur (or smooth out) the fine structures [namely, structures of sizes smaller than  $\sim z\theta_0$ ,  $z$  ( $\sim 1$  A.U.) being the distance from the earth to the thin screen] of the diffraction pattern, thereby attenuating the high-frequency components of the scintillation spectra and giving rise to a much steeper power law.

<sup>‡</sup> Although pulsars have very small intrinsic size ( $\leq 10^{-6}$  arc sec) and may be regarded as point sources, the pulsed and erratic nature of the radiation (Zeissig and Lovelace, 1972) and the uncertainty of the effects of interstellar scattering are the difficulties associated with using pulsars as sources of IPS observations.

## B. Advantages of Present Experiment

During superior conjunction (March 27 - April 7, 1966) of the Mariner 4 spacecraft to the sun, the bandwidth broadening of the 2295 MHz CW transmissions from Mariner 4 to earth was observed [Goldstein et al (1967)]. Yakovlev and Yefimov (1971) obtained the distance dependence of radio wave fluctuations at 1000 MHz as the Venera 7 spacecraft was flying along the line Earth-Venus. Except for these two cases, all published IPS data so far have been based almost entirely on observations of either quasars or pulsars, whose disadvantages were just pointed out in the last paragraph of the previous section. By sending 49.8 and 423.3 MHz signals simultaneously from Stanford to the sun-orbiting Pioneer 9 spacecraft, digitizing the received signal strength, and then telemetering back to the earth via the spacecraft S-band telemetry system, we have obtained, from 1968 to 1973, 77 usable sets of IPS data over a wide range of solar elongations: 0.1-1 A.U.

A typical set of IPS data for each frequency contains a total of ~1,000 digital samples over a duration of ~30 seconds. The sampling rate 36.6 samples/sec, which corresponds to the Nyquist frequency 18.3 Hz, appears to be sufficient in comparison with the 10 Hz bandwidth of the pre-sampling low-pass filter. The quantization noise introduced during encoding each spacecraft-received signal strength into a 6-bit code word (i.e., into one of the  $2^6 = 64$  discrete levels) for telemetry is a nonlinear function of the received signal strength and is more severe when the received signal strength is weaker.

The greatest advantage of the present experiment over the previous ones is, of course, the use of a man-made, constant-amplitude, monochromatic, point source at a known distance within the IPM; consequently, our scintillation data are sure to be free from such uncertain factors

as source-diameter effects, interstellar scattering, or erratic radiation from natural sources. In addition, the integrated electron content along the propagation path has, for the first time, been simultaneously measured. Comparing these electron-content data with the simultaneously acquired IPS data, therefore, provides a unique opportunity to study the correlation between the electron content and the IPS phenomenon.

### C. Organization

Chapter II reviews IPS theories and other theoretical results relevant to our experiment. The concept of the "thin phase-diffraction screen" approximation is introduced, and different (mainly gaussian and power-law) models for the spatial power spectrum of electron-density fluctuations are considered, leading to different explicit formulae for scintillation parameters, including (1) scintillation spectrum, (2) width of the scintillation pattern, and (3) scintillation index. Finally, possible effects of the finite source-diameter on both the slope of the scintillation spectrum and the magnitude of the scintillation index are discussed.

Chapter III is primarily a description of the geometry and apparatus of the IPS experiment. Instrumental parameters and limitations pertinent to the experiment are included. Because the Stanford PLL (phase-locked loop) receiver on board the spacecraft actually measures SNR (signal-to-noise power ratio) instead of signal power, the calculation of the total received noise temperature, which is essential to the extraction of the signal power from the SNR, is included. Also touched upon is the basic operational principle of the electron content measurement. This whole chapter except Sec. A may be skipped by readers who are not interested in the details of the experiment.

The procedures of data reduction are detailed in Chapter IV. The first step is to clean up the received IPS data, which is contaminated with receiving antenna and received noise patterns. After data clean-up, scintillation parameters (such as the autocorrelation function and power spectrum of intensity fluctuations and the scintillation index) are then computed. During the calculation of the autocorrelation function and power spectrum, the FFT (fast Fourier transform) algorithm is employed to save the computational time. For obtaining a physically meaningful estimate of the power spectrum, the procedures of the so-called Blackman and Tukey method (1958) are followed. Finally, the logic of an important computer program, devised to determine which of the three models (namely, power-law, gaussian, and exponential) fits best our observed power spectra, is thoroughly described.

Chapter V is devoted to results and interpretations. Detailed comparisons between existing theories and measured data are made. The last chapter, Chapter VI, presents conclusions together with recommendations for future research. Several topics of secondary importance are treated in appendices.

#### D. Contributions to Knowledge

Processing and analysis of these unique, dual-frequency, IPS data acquired from a man-made point source at VHF/UHF have yielded many valuable contributions to knowledge:

- (1) The spatial power spectrum of small-scale (~50 to 500 km) interplanetary electron-density fluctuations, over the range 0.1-1 A.U. from the sun, is found to follow a power-law variation; the mean and standard deviation of the power-law exponent are estimated to be  $3.5 \pm 0.13$  and 0.3, respectively. This result is in agreement with in situ measurements, near 1 A.U.

(cf. Table 1.1); it further implies that the micro-structures of the solar wind turbulence within 0.1-1 A.U. from the sun could be generated by the same plasma process, a process that is capable of producing power-law turbulence.

- (2) In cases of very strong scintillations, the form of the observed scintillation spectra becomes exponential rather than power-law; the very strong wave scattering phenomenon may be responsible for the occurrence of these exponential spectra.
- (3) Based upon the forms of the observed scintillation spectra, the existence of a gaussian micro-structure in the IPM, as suggested by Hewish (1971), Buckley (1971), Hewish (1972), and Rao et al. (1974), is shown to be precluded.
- (4) In addition to the power-law exponent  $p$ , the magnitude of the temporal spectrum of electron-density fluctuations inferred from our scintillation data is also found to agree with that measured by the OGO-5 satellite [Unti et al. (1973)], proving further the usefulness of the IPS technique in yielding definite information on the interplanetary turbulence spectrum.
- (5) For the first time the turnover behavior of  $r_w$  vs  $\rho$  is being experimentally reported, where  $r_w$  is the correlation length of intensity fluctuations and  $\rho$  is the proximate distance<sup>†</sup> of the radio path to the sun. The increase of  $r_w$  with  $\rho$  ( $r_w \propto \rho^{2.2}$ ) in the strong scintillation regime [which had been misinterpreted as the manifestation of the increase of the interplanetary irregularity sizes by Cohen and Gundermann (1969), Hewish and Symonds (1969), Little (1971), Readhead (1971), Lotova and Chashey (1972),

<sup>†</sup> The proximate distance of the radio path can be briefly defined as the closest distance from the radio path to the sun. Further discussions of this definition may be found in Sec. III.A.

and Hewish (1972)] is found to be ascribable to the effects of strong scattering from power-law irregularities, whereas the decrease of  $r_w$  with  $\rho$  in the weak scintillation regime is interpreted as caused by the decrease of the radius of the first Fresnel zone.

- (6) In contrast to most results of the scintillation index  $m$  obtained by using quasars as sources [see, for example, Cohen et al. (1967), Cohen and Gundermann (1969), Hewish and Burnell (1970), Rickett (1973), and Marians (1975)], no systematic turnover of  $m$  with decreasing  $\rho$  is observed for our point-source IPS data. This confirms, at least partly, the conjecture that the turnover of  $m$  is due to the finite source-diameter effect.
- (7) The scintillation index  $m$  in the weak scintillation regime varies with the proximate distance  $\rho$  as  $m \propto \rho^{-1.5}$ , implying that the radial dependence of the rms (root-mean-square) electron density fluctuation in the IPM follows approximately an inverse-square law.
- (8) The integrated electron content  $I$  along the propagation path is found to be directly proportional to the scintillation index  $m$  in the weak scintillation regime; furthermore, the deviations of  $I$  and  $m$  from their means are seen to be strongly correlated, suggesting that IPS observations may be utilized as an efficient means for monitoring both the density and density enhancements in the IPM.



## Chapter II

### THEORY

#### A. Thin Phase-Diffraction Screen Model

Consider a radio ray passing close to the sun. Since the density and the density fluctuations of the interplanetary plasma fall off quite rapidly with radial distance from the sun, most of the scattering takes place within a thin plasma slab near the sun. In cases of practical interest, absorption is negligible. If the plasma slab is sufficiently thin, the wavefront on emergence from the slab is modulated in phase only, and the subsequent propagation in the medium beyond can be treated as a phase-screen diffraction problem in the free space. (If the plasma slab is thick, diffraction inside the slab cannot be neglected and the emerging wavefront will be modulated in both amplitude and phase.)

This has led to the idea of an equivalent thin phase-diffraction screen model [Salpeter (1967)]. In this model, the turbulent interplanetary plasma along the line-of-sight is first replaced by a thin plasma slab of thickness  $L$  with its center located at the point of closest approach to the sun. Fig. 2.1 illustrates the simplified geometry, where  $U$  is the solar wind velocity assumed to be in the  $x$ -direction,  $\rho$  is the proximate distance to the sun of the source-observer trajectory, and  $z$  is the distance from the exit plane of the plasma slab to the observer's plane. Consider a monochromatic plane wave propagating in the  $z$ -direction. Diffraction and refraction within the plasma slab may be neglected if  $L$  is small enough such that the total linear deviation of a ray at the exit plane of the slab is much less than the transverse correlation length of the

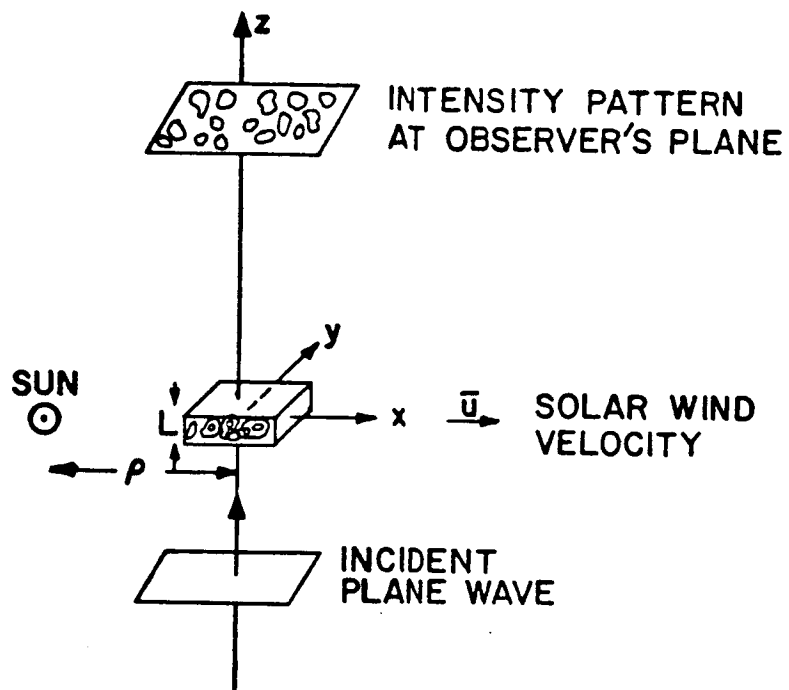


Fig. 2.1. SIMPLIFIED GEOMETRY OF IPS.

irregularities [Salpeter (1969), Lovelace (1970),<sup>4</sup> Cronyn (1970)].

Accepting this approximation, the emergent ray (after traversing through the slab) has suffered no variation but a phase retardation given by

$$\phi(x,y) = \frac{2\pi}{\lambda} \int_{-L/2}^{L/2} \mu(x,y,z) dz \quad (2.1)$$

where  $\mu$  = index of refraction =  $1 - \frac{r_e}{2\pi} \lambda^2 N(x,y,z)$

for the high-frequency approximation and

$r_e$  = classical electron radius

$\lambda$  = radio wavelength

$N$  = electron density

Let 
$$\Delta\phi(x,y) = \phi(x,y) - \langle\phi(x,y)\rangle \quad (2.2)$$

where  $\langle \rangle$  denotes spatial average. Then according to (2.1) and (2.2),

$$\Delta\phi(x,y) = -r_e \lambda \int_{-L/2}^{L/2} \Delta N(x,y,z) dz$$

$$\Delta N(x,y,z) = N(x,y,z) - \langle N(x,y,z) \rangle \quad (2.3)$$

Assuming that  $\Delta N$  (and hence  $\Delta\phi$ ) is a spatially stationary random process, we get

$$\begin{aligned} \phi_0^2 A_\phi(x,y) &= \langle \Delta\phi(x',y') \Delta\phi(x' + x, y' + y) \rangle \\ &= (r_e \lambda N_0)^2 \iint_{-L/2}^{L/2} A_n(x,y,z - z') dz dz' \end{aligned} \quad (2.4)$$

where  $\phi_0$  = r.m.s. phase deviation

$A$  = normalized autocorrelation function of phase fluctuations;  
 $A(0,0) = 1$

$N_0$  = r.m.s. electron density deviation

$A_n$  = normalized autocorrelation function of electron density  
 fluctuations;  $A_n(0,0,0) = 1$

If  $L$  is much greater than the correlation length of  $A_n$  in the  $z$ -direction, we see from Appendix A that

$$\phi_0^2 A_\phi(x,y) \approx L(r_e \lambda N_0)^2 \int_{-\infty}^{\infty} A_n(x,y,z) dz \quad (2.5)$$

Define the two-dimensional spatial spectrum of phase fluctuations as

$$F_\phi(q_x, q_y) = \frac{1}{(2\pi)^2} \iint_{-\infty}^{\infty} e^{i(q_x x + q_y y)} \phi_0^2 A_\phi(x,y) dx dy \quad (2.6)$$

and the three-dimensional spatial spectrum of electron density fluctuations as

$$F_n(q_x, q_y, q_z) = \frac{1}{(2\pi)^3} \iiint_{-\infty}^{\infty} e^{i(q_x x + q_y y + q_z z)} N_0^2 A_n(x,y,z) dx dy dz \quad (2.7)$$

where  $q_x$ ,  $q_y$ , and  $q_z$  are spatial frequencies in  $x$ ,  $y$ , and  $z$  directions respectively. Fourier-transforming both sides of Eq. (2.5) gives [cf. Tatarski (1961), Eq. (6.34)]

$$F_\phi(q_x, q_y) = 2\pi L(r_e \lambda N_0)^2 F_n(q_x, q_y, q_z = 0) \quad (2.8)$$

This implies that the thin plasma slab can further be replaced by a random phase screen at the exit plane of the slab and that the spatial spectrum of the phase screen is proportional to  $F_n(q_x, q_y, 0)$ . Notice that  $q_z = 0$  corresponds to the integration of the irregularities along the  $z$ -direction as seen from (2.5). For conceptional convenience, the randomly corrugated wavefront can be thought of as composed of a number of plane waves propagating in various directions. As the wave travels away from the screen, amplitude (and hence its square, intensity) fluctuations are then built up by the interference of these plane-wave components.

Let  $I(x, y)$  be the received intensity (or power) in the observer's plane, which is parallel to the screen but at a distance  $z$  from it. The normalized spatial autocorrelation function of  $I(x, y)$  is defined by

$$A_I(x, y) = \frac{\langle I(x', y') I(x' + x, y' + y) \rangle - \langle I(x', y') \rangle^2}{\langle I(x', y') \rangle^2} \quad (2.9)$$

and its Fourier transform

$$F_I(q_x, q_y) = \frac{1}{(2\pi)^2} \iint_{-\infty}^{\infty} A_I(x, y) e^{i(q_x x + q_y y)} dx dy \quad (2.10)$$

is termed the "spatial spectrum of intensity fluctuations." If  $z \gg$  outer scale of  $A_\phi \gg$  inner scale of  $A_\phi \gg \lambda$ , then the wave field may be deemed a scalar and the Fresnel approximations to the Huygen-Fresnel principle applies. Furthermore, if the scattering is weak, there is a simple relation between  $F_I(q_x, q_y)$  and  $F_\phi(q_x, q_y)$  [Bowhill (1961), Budden (1965), Salpeter (1967), Lovelace (1970), Cronyn (1972b, c)]:

$$F_I(q_x, q_y) = 4 \sin^2 \left[ \frac{\lambda z}{4\pi} (q_x^2 + q_y^2) \right] F_\phi(q_x, q_y) \quad (2.11)$$

A sufficient condition for the validity of weak-scattering limit is that  $\phi_0^2 \ll 1$ . For  $\phi_0^2 \gg 1$ , Jokipii (1970) has shown that (2.11) may still hold provided that (1) the contribution to  $\phi_0$  from irregularities of size  $\sqrt{\lambda z}$  and smaller is much less than unity and (2)  $F_\phi(q_x, q_y)$  is negligible for  $\sqrt{q_x^2 + q_y^2} > \frac{L\phi_0}{\lambda z}$ . Combination of (2.8) and (2.11) leads to

$$F_I(q_x, q_y) = 8\pi L(\lambda r_e)^2 \sin^2 \left[ \frac{\lambda z}{4\pi} (q_x^2 + q_y^2) \right] F_r(q_x, q_y, 0) \quad (2.12)$$

which has been much used in discussing interplanetary scintillations [Lovelace et al. (1970), Cronyn (1970, 1972b), Matheson and Little (1971)] and ionospheric scintillations [Rufenach (1972), Singleton (1974)].

It is well known that the propagation phenomenon between parallel planes acts as a linear dispersive spatial filter [Goodman (1968)]. Therefore, the  $4 \sin^2 \left[ \frac{\lambda z}{4\pi} (q_x^2 + q_y^2) \right]$  factor in (2.11) and (2.12), which accounts for the propagation effects in the Fresnel diffraction region, is often referred to as the Fresnel filtering function and designated by

$$\mathcal{F} = 4 \sin^2 \left[ \frac{\lambda z}{4\pi} (q_x^2 + q_y^2) \right] \quad (2.13)$$

Defining

$$q = \sqrt{q_x^2 + q_y^2} \quad (2.14)$$

$$q_f = \text{Fresnel spatial frequency} = \sqrt{\frac{4\pi}{\lambda z}} \quad (2.15)$$

Eq. (2.13) can be rewritten as

$$\mathcal{F} = 4 \sin (q/q_f)^2 \approx \begin{cases} 4(q/q_f)^4, & q < q_f \\ 2, & q > q_f \end{cases} \quad (2.16)$$

Inserting (2.16) in (2.12),

$$F_I(q_x, q_y) = 2\pi L(\lambda r_e)^2 \mathcal{F} F_n(q_x, q_y, 0) \quad (2.17)$$

$$= \begin{cases} 8\pi L(\lambda r_e)^2 (q/q_f)^4 F_n(q_x, q_y, 0), & q < q_f \\ 4\pi L(\lambda r_e)^2 F_n(q_x, q_y, 0), & q > q_f \end{cases} \quad (2.18)$$

For  $q > q_f$ ,  $F_I(q_x, q_y)$  has the same form as  $F_n(q_x, q_y, 0)$ . For  $q < q_f \approx \frac{2\pi}{\sqrt{\lambda z}}$ ,  $\mathcal{F}$  imposes fourth-power filtering on  $F_n(q_x, q_y, 0)$ . Therefore, one would not expect to see significant intensity fluctuations caused by irregularities larger than  $\sqrt{\lambda z}$  (i.e., spatial frequency smaller than  $q_f$ ).

In all the previous derivations it has been assumed that the source is a point source at infinity; i.e., the incident wave is a uniform plane wave. It can be easily shown [e.g., Bowhill (1961)], however, that all the above results can be extended to apply to a point source at a finite distance by redefining  $z$  as

$$\frac{1}{z} = \frac{1}{z_s} + \frac{1}{z_0} \quad (2.19)$$

where  $z_s$  and  $z_0$  are the source-to-screen distance and the observer-to-screen distance, respectively. For this statement to hold, the cone angle of diffraction must be small so that paraxial approximation [Goodman (1968)] can be used. This condition is usually well satisfied in IPS studies.

#### B. Temporal Spectrum of Intensity Fluctuations

In principle,  $A_I(x, y)$  (the two-dimensional spatial autocorrelation function of intensity fluctuations) and hence its Fourier transform  $F_I(q_x, q_y)$  can be determined directly by a suitable antenna array. How-

ever, with a single antenna at  $x = y = 0$ , only the temporal autocorrelation function of the intensity fluctuations is measured:

$$A_I(\tau) = \overline{I(t)I(t+\tau)} - \overline{I(t)}^2 \quad (2.20)$$

where  $\tau$  is the time lag. For  $\tau \lesssim 2$  sec [Coles et al. (1974)] and reasonably small elongation of source, it is a fairly good approximation to assume that the solar wind is frozen and moving along the x-direction with speed  $U$ . In this case, a single antenna scans a narrow line across the two-dimensional diffraction pattern, and  $A_I(\tau)$  is readily related to  $A_I(x, y)$  by

$$A_I(\tau) = A_I(x = U\tau, y = 0) \quad (2.21)$$

$$\text{Thus putting } x = U\tau \quad (2.22)$$

$$\text{and } q_x = 2\pi\nu/U \quad (2.23)$$

we have

$$\begin{aligned} F_I(\nu) &= \frac{1}{2\pi} \int_{-\infty}^{\infty} A_I(\tau) e^{i2\pi\nu\tau} d\tau \\ &= \frac{1}{2\pi U} \int_{-\infty}^{\infty} A_I(x, y = 0) e^{iq_x x} dx \\ &= \frac{1}{U} \int_{-\infty}^{\infty} F_I(q_x, q_y) dq_y \end{aligned} \quad (2.24)$$

Substituting (2.12) into (2.24) results in

$$F_I(\nu) = \frac{8\pi L(\lambda r_e)^2}{U} \int_{-\infty}^{\infty} \sin^2 \left[ \frac{\lambda z}{4\pi} (q_x^2 + q_y^2) \right] F_n(q_x, q_y, 0) dq_y \quad (2.25)$$



which is a general expression applicable to all types of irregularities. However, to proceed further with (2.25), it has now become necessary to specify the form of  $F_n(q_x, q_y, 0)$ .

### C. Gaussian Spectrum of Electron Density Fluctuations

Almost all the IPS studies published before 1970 assume that  $F_n(q_x, q_y, q_z)$  is gaussian [e.g., Cohen et al. (1967)]; namely,

$$F_n(q_x, q_y, q_z) = K_N \exp \left[ - \frac{r_0^2}{4} (q_x^2 + n^2 q_y^2 + \xi^2 q_z^2) \right]$$

$r_0$ ,  $nr_0$ , and  $\xi r_0$  being the characteristic sizes of irregularities in the  $x$ ,  $y$ , and  $z$  directions, respectively. Substitution of the above equation into (2.25) gives

$$F_I(\nu) = K \int_0^\infty \sin^2 \left[ \frac{\lambda z}{4\pi} (q_x^2 + q_y^2) \right] \exp \left[ - \frac{r_0^2}{4} (q_x^2 + n^2 q_y^2) \right] dq_y \quad (2.26)$$

where

$$K \equiv \frac{16\pi L (\lambda r_e)^2}{U} K_N \quad (2.27)$$

If irregularities are highly elongated in the  $y$ -direction,  $n \gg 1$ . The integrand in (2.26) decreases rapidly as  $q_y$  increases beyond  $q_x/n$ . As a result, only the values of  $q_y$  which are small compared with  $q_x$  contribute significantly to the integral, and the  $\sin^2$  term can be approximated by

$$\sin^2 \left[ \frac{\lambda z}{4\pi} (q_x^2 + q_y^2) \right] \approx \sin^2 \left( \frac{\lambda z}{4\pi} q_x^2 \right) ; q_y \ll q_x \quad (2.28)$$

with the aid of (2.28) and (2.23), (2.26) reduces to [see also Singleton (1974)]

$$F_I(v) = \frac{K\sqrt{\pi}}{r_0\eta} \sin^2 \left[ \pi\lambda z \left( \frac{v}{U} \right)^2 \right] \exp \left[ - \left( \frac{\pi r_0 v}{U} \right)^2 \right]; \quad \eta \gg 1 \quad (2.29)$$

Therefore, the intensity spectrum will display a sequence of zeros (also minima) at  $v = 0$ ,  $U/\sqrt{\lambda z}$ ,  $\sqrt{2}U/\sqrt{\lambda z}$ ,  $\sqrt{3}U/\sqrt{\lambda z}$ , caused by the modulation of the  $\sin^2$  term. Since this fine oscillating structure is originated from the Fresnel filtering function in the spatial frequency domain, it is frequently called the "Fresnel structure." If  $z$  [defined by (2.19)] is known, then the solar wind speed  $U$  can be readily deduced from the position of the zeros of  $F_I(v)$ .

At the other extreme, if irregularities are highly elongated in the  $x$ -direction (i.e.,  $\eta \ll 1$ ), then only  $q_y$ 's which are much greater than  $q_x$  contribute significantly to the integral in (2.28). The  $\sin^2$  term in (2.28) is hence dominated by  $q_y$ , and  $F_I(v)$  can be approximated by

$$F_I(v) = K \exp \left[ - \left( \frac{\pi r_0 v}{U} \right)^2 \right] \int_0^\infty \sin^2 \left( \frac{\lambda z}{4\pi} q_y^2 \right) \exp \left( - \frac{r_0^2}{4} \eta^2 q_y^2 \right) dq_y \quad (2.30)$$

$$= \frac{K\sqrt{\pi}}{2r_0\eta} \exp \left[ - \left( \frac{\pi r_0 v}{U} \right)^2 \right]; \quad \eta \ll 1 \quad (2.31)$$

a result which is similar to (2.29) except for the disappearance of the "Fresnel structure."

Up to this point we have been dealing exclusively with the two limiting cases,  $\eta \gg 1$  and  $\eta \ll 1$ . Now we wish to derive a general and explicit expression of  $F_I(v)$  for any value of  $\eta$ . Introducing (2.23) into (2.26) and applying the identity

$$\sin^2 \left( \frac{\lambda z}{4\pi} q_y^2 + \frac{\pi \lambda z v^2}{U^2} \right) = 1/2 - 1/2 \cos \left( \frac{\lambda z}{2\pi} q_y^2 + \frac{2\pi \lambda z v^2}{U^2} \right) \quad (2.32)$$

leads to

$$F_I(v) = \frac{K}{2} \exp \left[ - \left( \frac{\pi r_0 v}{U} \right)^2 \right] \int_0^\infty \left[ 1 - \cos \left( \frac{\lambda z}{2\pi} q_y^2 + \frac{2\pi \lambda z v^2}{U^2} \right) \right] \cdot \exp \left[ - \left( \frac{r_0^2}{4} \eta^2 q_y^2 \right) \right] dq_y \quad (2.33)$$

With the help of a standard table of integration<sup>†</sup>, we obtain

$$\int_0^\infty \exp \left( - \frac{r_0^2}{4} \eta^2 q_y^2 \right) dq_y = \frac{\sqrt{\pi}}{r_0 \eta} \quad (2.34)$$

and

$$\begin{aligned} & \int_0^\infty \cos \left( \frac{\lambda z}{2\pi} q_y^2 + \frac{2\pi \lambda z v^2}{U^2} \right) \exp \left( - \frac{r_0^2}{4} \eta^2 q_y^2 \right) dq_y \\ &= \frac{\sqrt{\pi}/(r_0 \eta)}{\sqrt[4]{1 + 4[\lambda z/(\pi r_0^2 \eta^2)]^2}} \cos \left[ \frac{2\pi \lambda z v^2}{U^2} + 1/2 \tan^{-1} \left( \frac{2\lambda z}{\pi r_0^2 \eta^2} \right) \right] \end{aligned} \quad (2.35^+)$$

Substitution of these two equations into (2.33) brings out the desired explicit formula [see also Bourgois (1972)]:

$$F_I(v) = \frac{K \sqrt{\pi}}{2 r_0 \eta} \exp \left[ - \left( \frac{\pi r_0 v}{U} \right)^2 \right] \left[ 1 - \sqrt{\cos \theta} \cos \left( \frac{2\pi \lambda z v^2}{U^2} + \frac{\theta}{2} \right) \right] \quad (2.36)$$

where  $\theta$  is defined by

$$\theta \equiv \tan^{-1} \left( \frac{2\lambda z}{\pi r_0^2 \eta^2} \right) \quad (2.37)$$

<sup>†</sup> See, for example, p. 485 of Tables of Integrals, Series and Products by Gradshteyn and Ryzhik (1965).

Before examining the implications of (2.36), let us check it by considering the two extreme cases discussed previously. As  $\eta \rightarrow \infty$ ,  $\theta \rightarrow 0$  and  $\cos \theta \rightarrow 1$ . Therefore (2.36) becomes

$$\begin{aligned} F_I(\nu) &= \frac{K\sqrt{\pi}}{2r_0\eta} \exp \left[ - \left( \frac{\pi r_0 \nu}{U} \right)^2 \right] \left[ 1 - \cos \left( \frac{2\pi\lambda z \nu^2}{U^2} \right) \right] \\ &= \frac{K\sqrt{\pi}}{r_0\eta} \sin^2 \left[ \pi\lambda z \left( \frac{\nu}{U} \right)^2 \right] \exp \left[ - \left( \frac{\pi r_0 \nu}{U} \right)^2 \right] ; \quad \eta \rightarrow \infty \end{aligned} \quad (2.38)$$

which is identical with (2.29). On the other hand, if  $\eta \rightarrow 0$ , then  $\theta \rightarrow \frac{\pi}{2}$  and  $\cos \theta \rightarrow 0$ . Hence (2.36) can be simplified to

$$F_I(\nu) = \frac{K\sqrt{\pi}}{2r_0\eta} \exp \left[ - \left( \frac{\pi r_0 \nu}{U} \right)^2 \right] ; \quad \eta \rightarrow 0 \quad (2.39)$$

which is indeed (2.31), as expected.

Inspection of (2.36) leads us to three simple yet important conclusions about  $F_I(\nu)$  under the conditions of gaussian irregularities and weak scattering: [Recall that these two were the conditions invoked during the derivation of (2.36).]

1. For any value of  $\eta$ ,  $F_I(\nu)$  always has an envelope proportional to  $\exp [-(\pi r_0 \nu/U)^2]$  in the frequency range  $\nu > \nu_f$ ,  $\nu_f$  being the Fresnel frequency defined by  $\nu_f = U/\sqrt{\pi\lambda z}$ .
2. A small value of  $\eta$  corresponds to a small contrast in the Fresnel structure, and vice versa.
3. While  $\nu$  decreases, the location of the  $n^{\text{th}}$  minimum of the Fresnel structure shifts from  $\sqrt{n} \nu_f$  ( $\eta \rightarrow \infty$ ) to  $\sqrt{n} - 1/8 \nu_f$  ( $\eta \rightarrow 0$ ), with  $n = 1, 2, 3$ , etc.

A few remarks relating to these conclusions are necessary. In the weak scattering regime, the first conclusion usually serves as a rule

of thumb to determine whether the autocorrelation function of the irregularities is gaussian or not. If the autocorrelation function of the irregularities is gaussian, the observed envelope of  $F_I(\nu)$  must also be gaussian for  $\nu > \nu_f$ . Furthermore, according to the second conclusion, the anisotropy ratio  $\eta$  of irregularities may be inferred from the contrast of the Fresnel structure. Finally, unless the frequency resolution bandwidth<sup>†</sup> of  $F_I(\nu)$  is smaller than about  $0.06 \nu_f$ , the slight shifting of the locations of minima mentioned in the third conclusion is normally undetectable.

#### D. Power-Law Electron Density Spectrum

Instead of adopting the gaussian model just discussed in the last section, a number of papers have recently suggested that  $F_n(q)$ , the spatial spectrum of interplanetary electron density fluctuations, may be characterized better by a power law. Among them are Jokipii and Hollweg (1970), Lovelace et al. (1970), Cronyn (1972c), and Coles et al. (1974). Strong support of this viewpoint comes from in-situ measurements of  $F_p(q)$ , the interplanetary proton density spectrum, near the earth [Intriligator and Wolfe (1970), Unti et al. (1973)]. These measurements indicate that  $F_p(q)$  can be well represented by a power law. Since the Debye length in the solar wind is of the order of only a few meters,  $F_n(q)$  should follow the same power law as  $F_p(q)$  does for  $q \lesssim 10 \text{ km}^{-1}$ . In addition to this evidence, power laws are also the spectral forms generally predicted by inertial-

<sup>†</sup> Exact determination of  $F_I(\nu)$  would require an infinitely long piece of data, which is physically impossible. In practice,  $F_I(\nu)$  can only be approximately estimated from a finite string of data.  $F_I(\nu)$  thus secured has a nonzero frequency resolution bandwidth. The calculation of this resolution bandwidth can be found in Appendix G.

range theories of hydromagnetic turbulence [for example, Kraichnan (1965)].

If the three-dimensional power spectrum  $F_n(q)$  of electron-density fluctuations is a power law spectrum, then it may take the following form:

$$F_n(q) = K_N (q_x^2 + \eta^2 q_y^2 + \xi^2 q_z^2)^{-\frac{p}{2}} ; \quad \frac{2\pi}{L_0} < q < \frac{2\pi}{\ell_0} \quad (2.40)$$

where  $\eta$  and  $\xi$  = ellipticities of irregularities along the y- and z-axis directions with respect to the x-axis direction

$p$  = power-law exponent of  $F_n(q)$

$L_0 \equiv$  outer scale of turbulence (i.e., the size of the largest inhomogeneous eddies in the solar wind)

$\ell_0 \equiv$  inner scale of turbulence (i.e., the size of the smallest inhomogeneous eddies in the solar wind)

Physically,  $L_0$  is the eddy size at which energy enters into the turbulence. As suggested by Coleman (1968), the energy available to feed the solar wind turbulence is probably originated from the differential motion of the interplanetary plasma streams. Such energy is then cascaded through to eddies of smaller size until the smallest size  $\ell_0$  of the eddies is reached, where all the energy is dissipated [possibly by proton cyclotron damping--see, again, Coleman (1968)].

Incorporating (2.40) into (2.25) and using a similar argument to that outlined between Eqs. (2.27) and (2.30) in the previous section, it can be derived that

$$F_I(\nu) \approx K' \sin^2 \left( \frac{\nu}{\nu_f} \right)^2 \nu^{-(p-1)} ; \quad \nu > \nu_f \quad \frac{U}{\sqrt{\pi \lambda z}} \quad (2.41)$$

for y-axis elongated ( $\eta \gg 1$ ) irregularities and

$$F_I(\nu) \approx \frac{K'}{2} \nu^{-(p-1)} ; \quad \nu > \nu_f \quad (2.42)$$

for x-axis elongated ( $\eta \ll 1$ ) irregularities, where

$$K' = K_N U^{p-2} \frac{L(\lambda r_e)^2 8\pi^{\frac{3}{2}} \Gamma(\frac{p-1}{2})}{\eta (2\pi)^{p-1} \Gamma(\frac{p}{2})}$$

and  $\Gamma(\ )$  denotes the gamma function. For the case of isotropic irregularities ( $\eta = 1$ ), results obtained from numerical integration of (2.25) [see Fig. 1 of Lovelace et al. (1970) and also Figs. 5 and 6 of Mariani (1975)] indicate that  $F_I(\nu)$ , in addition to having an envelope proportional to  $\nu^{-(p-1)}$ , also displays a small-contrast Fresnel structure, namely, a sequence of "shallow" minima [in comparison with the deep minima or zeros in (2.41)] at  $\nu \approx \nu_1, \sqrt{2}\nu_1, \sqrt{3}\nu_1, \dots$ , where

$$\nu_1 \equiv \frac{\sqrt{\pi}}{\nu_f} = \frac{U}{\sqrt{\lambda z}} \quad (2.43)$$

In summary, if  $F_n(q)$  is power-law with exponent  $p$ , then no matter what value the ellipticity  $\eta$  takes, the envelope of the temporal spectrum  $F_I(\nu)$  of intensity fluctuations in the weak scattering regime is also power-law, but with exponent  $(p-1)$ . (i.e., the spectral index of  $F_I(\nu)$  is lower than that of  $F_n(q)$  by 1). Rumsey (1975) and Mariani (1975) have shown that this statement

essentially still holds--at least for the nearly isotropic cases ( $\eta \approx 1$ )--even in the strong scattering regime.

#### E. Exponential Spectrum of Electron Density Fluctuations

If  $F_n(q)$  is exponential rather than gaussian or power-law, then it may be expressed as

$$F_n(q) = K_N \exp \left[ -r_0(|q_x| + \eta|q_y| + \xi|q_z|) \right] \quad (2.44)$$

Substituting (2.44) into (2.25) and making use of (2.23) results in

$$F_I(\nu) = K \exp \left( -\frac{2\pi r_0 \nu}{U} \right) \int_0^\infty \exp(-\eta q_y) \sin^2 \left[ \frac{\lambda z}{4\pi} (q_x^2 + q_y^2) \right] dq_y \quad (2.45)$$

where

$$K = \frac{16\pi L(\lambda r_e)^2}{U} K_N \quad (2.46)$$

Following the same argument as that outlined between Eqs. (2.27) and (2.30) in Sec. C, one can derive that for  $\eta \gg 1$ ,

$$F_I(\nu) \approx K \exp \left( -\frac{2\pi r_0 \nu}{U} \right) \cdot \sin^2 \left( \frac{\lambda z}{4\pi} q_x^2 \right) \int_0^\infty \exp(-r_0 \eta q_y) dq_y \quad (2.47)$$

$$\approx \frac{K}{r_0 \eta} \sin^2 \left[ \pi \lambda z \left( \frac{\nu}{U} \right)^2 \right] \exp \left( -\frac{2\pi r_0 \nu}{U} \right) \quad (2.48)$$

and for  $\eta \ll 1$ ,

$$F_I(\nu) \approx K \exp \left( -\frac{2\pi r_0 \nu}{U} \right) \cdot \int_0^\infty \sin^2 \left( \frac{\lambda z}{4\pi} q_y^2 \right) \exp(-r_0 \eta q_y) dq_y \quad (2.49)$$

$$\approx \frac{K}{2r_0 \eta} \exp \left( -\frac{2\pi r_0 \nu}{U} \right) \quad (2.50)$$



In general, if  $F_n(q)$  is exponential, then for any value of  $n$  the envelope of  $F_I(v)$  is also exponential.

#### F. Logic of Irregularity-Form Tests

One essential qualitative point emerging from the results of the previous three sections is that if the irregularity spectrum  $F_n(q)$  is gaussian, power-law, or exponential, then  $F_I(v)$ , the temporal spectrum of intensity fluctuations, always possesses the same form as  $F_n(q)$  does. Symbolically,

$$F_I(v) \propto \begin{cases} v^{-(p-1)}, & \text{if } F_n(q) \text{ is power-law with exponent } p \\ \exp(-Av), & \text{if } F_n(q) \text{ is exponential} \\ \exp(-Bv^2), & \text{if } F_n \text{ is gaussian} \end{cases} \quad (2.51)$$

where  $A$  and  $B$  are just two numerical constants. Taking common logarithms of both sides of (2.51) leads to an even more useful expression

$$10 \log [F_I(v)] \propto \begin{cases} -(p-1)\log(v), & \text{if } F_n(q) \text{ is power law with exponent } p \\ -Av & , \text{ if } F_n(q) \text{ is exponential} \\ -Bv^2 & , \text{ if } F_n(a) \text{ is gaussian} \end{cases} \quad (2.52)$$

Therefore, if  $10 \log [F_I(v)]$  [i.e.,  $F_I(v)$  in dB] is plotted versus  $\log(v)$ ,  $v$ , and  $v^2$ , then it will appear as a straight line in one of the three plots provided that the assumed form of  $F_n(q)$  associated with that plot is correct. It should be emphasized that this is also the basic logic that will be used later in Sec. IV.D for devising a computer program to perform irregularity-form tests.

Since the results of these test (which will be presented in Sec. V.A) support the power-law model, except for the case of "very" strong scintillation in which the exponential model appears to be

more appropriate, only the power-law model--especially the isotropic case  $F_n(q) \propto q^{-p}$  for simplicity--will be discussed in the remaining sections of this chapter.

#### G. Correlation Length of Intensity Fluctuations

Consider the case  $F_n(q) \propto q^{-p}$ . As pointed out earlier in Sec. II.B during the discussion of Eq. (2.18), irregularities much larger than  $\sqrt{\lambda z}$  (i.e.,  $q \ll \frac{2\pi}{\sqrt{\lambda z}} = q_f$ ) are strongly suppressed by the  $q^4$  dependence of the Fresnel filtering. Conversely, irregularities much smaller than  $\sqrt{\lambda z}$  ( $\frac{2\pi}{q} \ll \sqrt{\lambda z}$ ) are less important because of the fall-off of  $F_n(q)$  with decreasing irregularity size (increasing  $q$ ). Hence irregularities of size  $\sim \sqrt{\lambda z}$  are expected to contribute most significantly to intensity fluctuations. It follows from (2.17) that the resultant two-dimensional spectrum  $F_I(q_x, q_y)$  of intensity fluctuations will be dominated by wave numbers in the vicinity of  $q \sim \frac{2\pi}{\sqrt{\lambda z}}$ , and the autocorrelation function  $A_I(x, y)$  of intensity fluctuations, which is equal to the inverse Fourier transform of  $F_I(q_x, q_y)$ , will have width on the order of  $\sqrt{\lambda z}$ .

Physically, the above argument can be understood as follows. Consider a plane wave incident on an irregularity of size  $\ell \gg \sqrt{\lambda z}$ ,  $z$  being the distance from the observer's plane to the irregularity. For a given observer in the observer's plane, there are many Fresnel zones across the irregularity of dimension  $\ell$ ; consequently, the contributions of intensity fluctuations from different Fresnel zones of the irregularity, because of destructive phase differences, tend to cancel one another. For this reason, irregularities of size  $\ell \gg \sqrt{\lambda z}$  do not cause significant intensity fluctuations. On the other hand, irregularities of size  $\ll \sqrt{\lambda z}$  impose much smaller amounts of phase

fluctuations upon the incident wave, and hence contribute much less intensity fluctuations in the observer's plane, than irregularities of size  $\sim \sqrt{\lambda z}$ . Qualitatively, insofar as intensity fluctuations are concerned, the random medium can therefore be regarded as consisting of irregularities predominantly of size  $\sim \sqrt{\lambda z}$ . The diffracted wave, which contribute most intensity fluctuations in the observer's plane, is then confined within a conical sector of angle  $\sim \lambda/\sqrt{\lambda z}$ . At a distance  $z$  from irregularities (where the observer's plane is situated), the diffracted wave has a spread of  $\sim \lambda z/\sqrt{\lambda z} = \sqrt{\lambda z}$ . Consequently, the received intensity fluctuations at two points in the observer's plane separated by distance greater than  $\sqrt{\lambda z}$  will not be correlated (because they come from different and hence uncorrelated irregularities); i.e., the correlation length of intensity fluctuations in the observer's plane is on the order of  $\sim \sqrt{\lambda z}$ .

Various definitions are available for the correlation length of intensity fluctuations [Cohen and Gundermann (1969), Lovelace (1970), Lovelace et al. (1970), Matheson and Little (1971), Rufenach (1972), Houminer (1973), Rickett (1973)]--either based on the width of  $F_I(\nu)$  (temporal intensity spectrum) or on that of  $A_I(t)$ , the normalized temporal autocorrelation function of intensity fluctuations. Here, we define the temporal width  $t_w$  of  $A_I(t)$  as the time at which  $A_I(t)$  drops to 1/2 of its maximum value

$$A_I(t=t_w) = \frac{1}{2} \max [A_I(t)] = \frac{1}{2} A_I(0) \quad (2.53)$$

and the correlation length  $r_w$  of intensity fluctuations as

$$r_w = t_w \cdot U \quad (2.54)$$

$U$  being the solar wind velocity. For  $F_n(q) \propto q^{-p}$  and  $\ell_0 < \sqrt{\lambda z/2\pi^2} < L_0$  [ $\ell_0$  and  $L_0$  are inner and outer scales of turbulence defined in (2.40)], Jokipii and Hollweg (1970) have derived the result that  $r_w$  in the weak scintillation regime is of the order of  $\sqrt{\lambda z/2\pi^2}$ :

$$r_w \approx 0 \left( \sqrt{\frac{\lambda z}{2\pi^2}} \right) \quad (2.55)$$

Note that this result is also what one would expect based on the discussions presented earlier in this section.

#### H. Scintillation Index

The scintillation index  $m$ , which is a measure of the degree of scintillations, is defined as the normalized standard deviation of the intensity fluctuations:

$$m \equiv \frac{\sqrt{\langle I^2 \rangle - \langle I \rangle^2}}{\langle I \rangle} \quad (2.56)$$

where  $\langle \rangle$  denotes the time average. Expressed in terms of  $F_I(\nu)$ , we have

$$m^2 = \int_{-\infty}^{\infty} F_I(\nu) d\nu \quad (2.57)$$

Substituting  $F_n(q) = K_N q^{-p}$  into (2.25) and carrying out the integration of (2.57) leads to [Lovelace et al. (1970), Hollweg and Jokipii (1972)]

$$m \propto \sqrt{K_N} z^{\frac{p-2}{4}} \lambda^{\frac{p+2}{4}} \quad (2.58)$$

As mentioned by Cohen et al. (1967),  $m$  is a somewhat erratic quantity. It can change a factor of 2 in one day, although it hardly ever changes more than 20 percent in 2 hours. Based on our dual-frequency scintillation data,  $m$  as a function of the closest distance from the sun to the ray path will be found, and the validity of the wavelength dependence given by (2.58)

$$m \propto \lambda^{\frac{p+2}{4}}$$

will also be tested.

### I. Effects of Finite Angular Size of Source

Radio sources having a finite angular size may blur the fine structure in the diffraction pattern and therefore attenuate high frequencies in  $F_I(\nu)$ . This can explain why  $F_I(\nu)$  derived from radio source observations [Lovelace et al. (1970)] usually has a steeper slope than our point source data (their 3.4 comparing with our 2.5). Mathematically, if the effective thickness of the medium is small compared with  $z$ , then the intensity  $I(r)$ , due to a point source at a small angle  $\theta$  to the  $z$ -direction, is well approximated by  $I(r+z\theta)$  [Hewish and Little (1966)]. Consider a small but finite source with brightness distribution  $b(\theta)$ . The intensity  $g(r)$  for such an extended source is then given by

$$g(r) = \int d\theta b(\theta) I(r + z\theta) \quad (2.59)$$

or by convolution theorem

$$F_g(\nu) = F_I(\nu) F_S(\nu) \quad (2.60)$$

where  $F_s(\nu)$  is an equivalent source spectrum derived from the  $b(\theta)$ . A gaussian form of  $F_s(\nu)$  is often assumed in theoretical discussions of the effects of finite source.

Near the sun  $F_I(\nu)$  extends to higher frequencies than  $F_s(\nu)$  and it is the consequent attenuation of high frequencies in  $F_I(\nu)$  which results in the "turn over" of  $m$  observed by other workers [e.g., Cohen et al. (1967)]. For the point source we use, no "turn over" of  $m$  is expected to happen as the sun is approached. As will be seen later in Sec. V.D, our plot of  $m$  versus solar elongation does appear to be consistent with this argument.

## Chapter III

### EXPERIMENT DESCRIPTION

By transmitting 49.8 and 423.3 MHz signals from Stanford to the Pioneer 9 spacecraft and then telemetering digitally coded measurements back to the earth, 79 usable<sup>†</sup> sets of IPS data (called "Format D data") were obtained over a wide range of solar elongations between November 1968 and July 1973. The Pioneer 9 spacecraft went behind the solar disk during 18-20 December 1970. Intense scattering from the solar corona cut off the tracking of the 2,292 MHz telemetry signal from December 13 until December 22. On 18 January 1971, we were able to acquire Format D data at 49.8 and 423.3 MHz for the first time since 2 December 1970. The smallest proximate distance<sup>‡</sup> at which Format D data was still attainable was 0.08 A.U.\* A complete set of Format D data consists, for each frequency, of 1038 data points (or samples), which at sampling rate 37.57 samples/sec span over a duration of about 30 seconds. Each data point is an integer between 5 and 63, except during the occurrence of the sun pulse (Sec. III.D) when an integer smaller than 5 (usually 1) is possible. The digit can be converted into the received signal-to-noise power ratio by employing a proper calibration curve. The trajectory of the spacecraft, the characteristic of the apparatus, the data format and calibration, the total received noise temperature, and the interplanetary electron content measurement will be briefly described in this chapter.

Readers who are not interested in the details of the experiment may find it adequate to skip to the next chapter after reading Section A.

<sup>†</sup> A usable set of data is defined as the set of data which does not contain gaps longer than 0.1 sec--see Sec. IV.B.

<sup>‡</sup> The proximate distance is defined in Sec. III.A as the closest distance from the earth-to-spacecraft line to the sun.

\* A.U. is the abbreviation of "astronomical unit"; 1 A.U. is the average distance from the sun to the earth ( $\approx 1.496 \times 10^9$  km).

### A. Trajectory of Pioneer 9

Pioneer 9, the fifth spacecraft to carry the Stanford/SRI receiver, was launched into a heliocentric orbit on 8 November 1968.<sup>†</sup> This orbit, which is essentially in the ecliptic plane, is plotted in Fig. 3.1, where the plane of the figure is the ecliptic and the sun-earth line is fixed. Dates in months are marked several places along the trajectory. Note that the spacecraft went behind the sun in late 1970 and emerged in early 1971.

Though all regions along the propagation path contribute IPS observed at the receiver, the region nearest to the sun usually contributes the most (see Sec. II.A for justification). The heliocentric distance of this dominating region, which will be referred to quite often in later discussions, is defined as the proximate distance of the propagation path. According to the trajectory of Pioneer 9,  $\rho$  can be equivalently defined as the closest distance from the earth-to-spacecraft line to the sun. To illustrate this definition, consider a triangle with the earth, the sun, and the Pioneer 9 spacecraft as the three vertices as shown in Fig. 3.2. Let  $P$ ,  $E$ , and  $S$  be the three interior angles of this triangle:

$P$  = earth-Pioneer-sun angle

$E$  = sun-earth-Pioneer angle

$S$  = earth-sun-Pioneer angle

Furthermore, denote

$EP$  = earth-to-Pioneer distance

$PS$  = Pioneer-to-sun distance

$SE$  = sun-to-earth distance

---

<sup>†</sup> SRI (Stanford Research Institute) collaborated with the University, building the receiver, supplying the higher-frequency transmitter and the antenna, and operating them throughout the 8-year experiment.



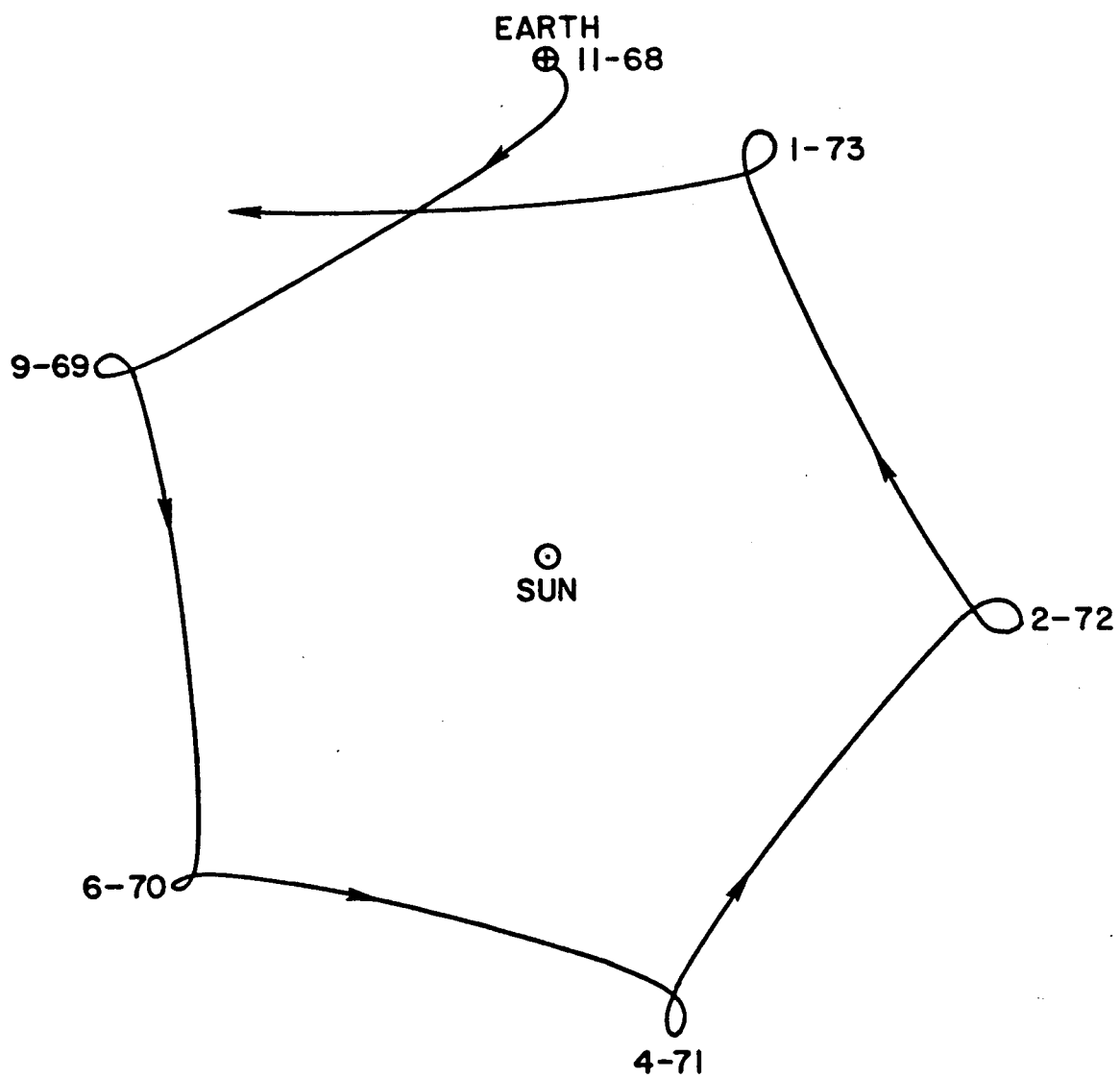
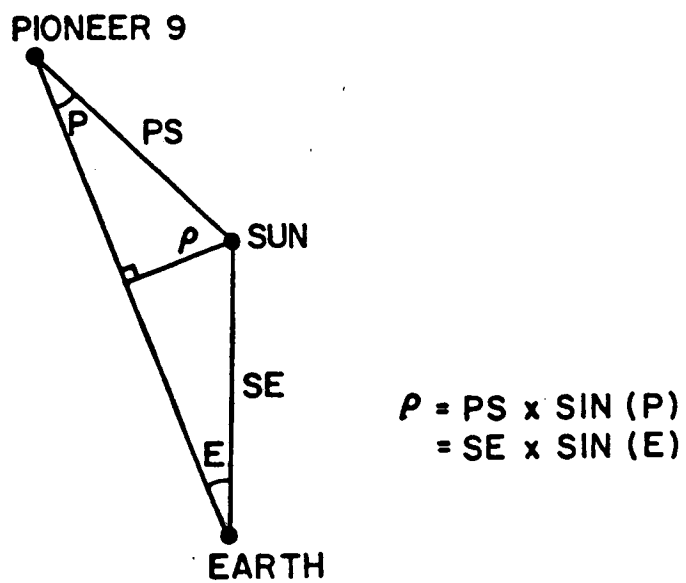
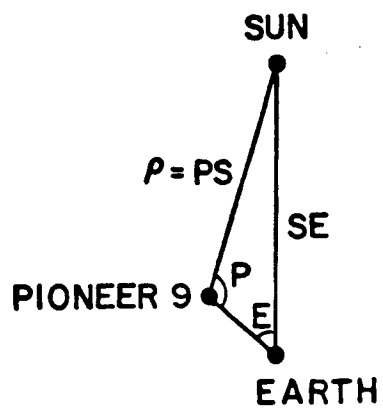


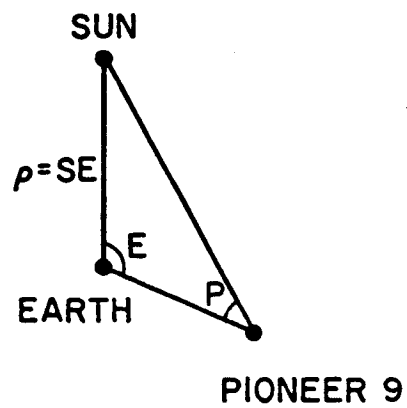
Fig. 3.1. PIONEER 9 HELIOCENTRIC ORBIT.



(a)  $P < 90^\circ$  AND  $E < 90^\circ$



(b)  $P > 90^\circ$



(c)  $E > 90^\circ$

Fig. 3.2. DEFINITION OF THE PROXIMATE DISTANCE  $\rho$ .

Then, for different values of  $P$  and  $E$ ,  $\rho$  can be expressed as

$$\rho = PS \times \sin (P) = SE \times \sin (E) ; P < 90^\circ, E < 90^\circ \quad (3.1)$$

$$\rho = PS ; P > 90^\circ \quad (3.2)$$

and

$$\rho = ES ; E > 90^\circ \quad (3.3)$$

In terms of A.U.,  $\rho$  in (3.1) can be approximated by

$$\rho \approx \sin (E) \text{ A.U. ; } P < 90^\circ, E < 90^\circ$$

This gives a simple relation between  $\rho$  and  $E$  in the case of  $P < 90^\circ$  and  $E < 90^\circ$ , where  $E$  is also conventionally defined as the solar elongation of the spacecraft.

#### B. Transmission System

The ground-based transmission system at Stanford generates phase-modulated signals at 49.8 and 423.3 MHz and then radiates them from the 150-foot parabolic dish to the spacecraft. To control the pointing of the dish to the spacecraft, a PDP 8 computer is employed. Some relevant parameters of the transmission system are summarized in Table 3.1.

Frequency	49.8 MHz	423.3 MHz
Transmitter	Triode linear amplifier	Klystron amplifier
Maximum output power	250 KW	30 KW
Transmitting antenna gain	26.4 dB	45.0 dB
Half power beamwidth	6°	1°
Antenna efficiency	~50%	~50%
Wave polarization	Left-hand elliptical	Right-hand circular

Table 3.1. TRANSMISSION SYSTEM PARAMETERS.

For line-of-sight propagation in the free space, the arriving power at the input terminals of the receiver,  $P_r$ , can be easily calculated by invoking the transmission equation:

$$P_r = \frac{P_t G_t \kappa A_r L_p}{4\pi R^2} \quad (3.4)^\dagger$$

where

$P_t$  = transmitter power in watts

$G_t$  = transmitting antenna gain

$\kappa$  = transmitting antenna efficiency

$A_r$  = receiving antenna aperture

$L_p$  = numerical factor accounting for polarization losses

$R$  = distance between transmitting and receiving antennas in meters

Normally,  $P_t$  is so adjusted that  $P_r \approx 130$ -140 dBm for the 49.8 MHz channel and 135-145 dBm for the 423.3 MHz channel; however for  $\rho \leq 0.08$  A.U., even  $P_t$  is set to its maximum value (see Table 3.1),  $P_r$  is still very small--because of the intense scattering from the outer solar corona. This, coupled with intense signal phase variability, precludes our contact with the Stanford receiver on board the spacecraft during solar occultation.

---

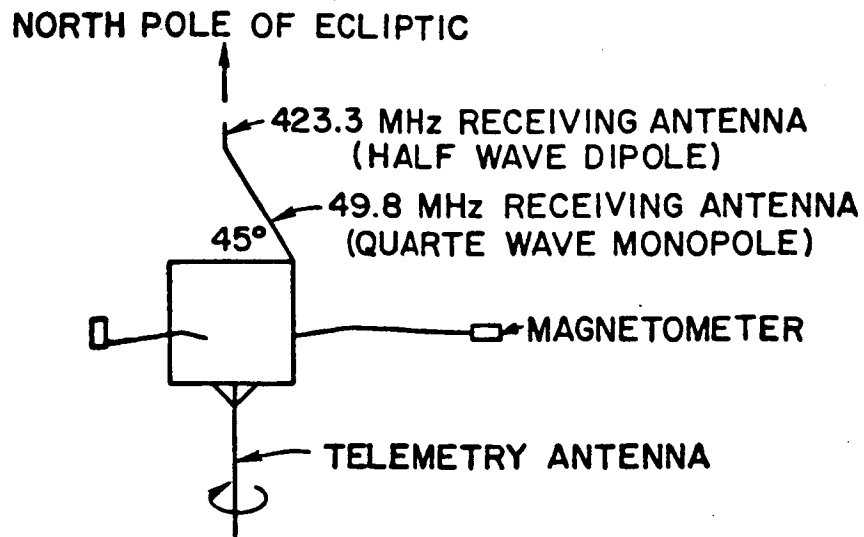
<sup>†</sup> For radio propagation through the turbulent interplanetary plasma, the computation for  $P_r$  becomes much more complicated. The reason is that the wave will, in transit through the solar wind, be scattered by electron-density irregularities in the medium. To account for this scattering effect, the so-called effective scattering cross-section, designated by  $\sigma$ , from a unit volume of the medium has to be introduced; then, integration of  $\sigma$  over the effective scattering volume must be performed. Detailed discussions of these complications may be found in Tatarski's (1971) Chapter 2 and will not be pursued here.

### C. Receiving Antennas

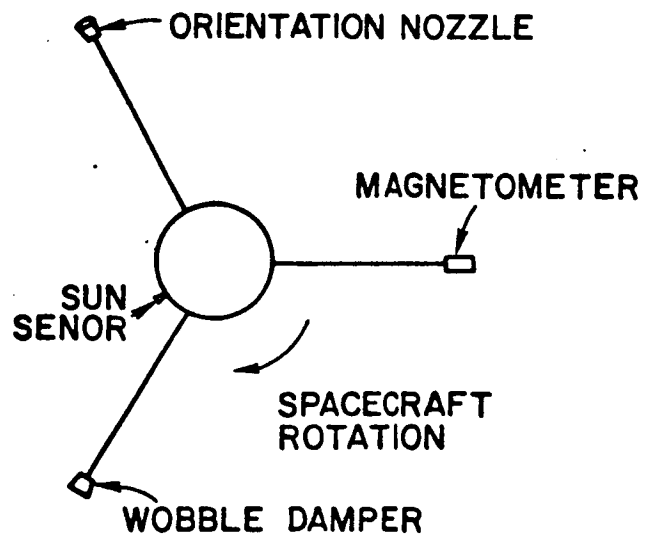
The Stanford receiver on board Pioneer 9 receives 49.8 and 423.3 MHz radiations from the earth by means of two linear antennas mounted on top of the spacecraft (Fig. 3.3). The 49.8 MHz antenna is a quarter wave monopole inclined  $45^\circ$  toward the platform of Pioneer 9. The 423.3 MHz antenna is a half wave dipole centered on the axis of the spacecraft.

In order to stabilize its geometrical configuration, the spacecraft spins about once per second; therefore, the receiving antennas aboard and their power patterns also spin accordingly. The spin is in a retrograde direction (or clockwise when looking from the north ecliptic pole down toward the ecliptic plane) with its axis perpendicular to the ecliptic plane. Variations of the spin rate are explained as follows. When the spacecraft moves close to the sun, it expands--because of the heat absorbed--and hence spins slower so as to conserve its angular momentum; the opposite is true when it moves away from the sun.

Derived from the procedure outlined in Appendix B, the power patterns of the receiving antennas in the ecliptic plane are plotted in Fig. 3.4, where  $\psi$  is the angle measured eastward from the sun-sensor axis (Fig. D.1) and 0 dB corresponds to the isotropic gains. The three main lobes on each pattern evidently result from reflections of the incoming wave by the geometrical structure (especially, the three booms) of the spacecraft.



(a) SIDE VIEW



(b) TOP VIEW

Fig. 3.3. SPACECRAFT IN-FLIGHT CONFIGURATION.

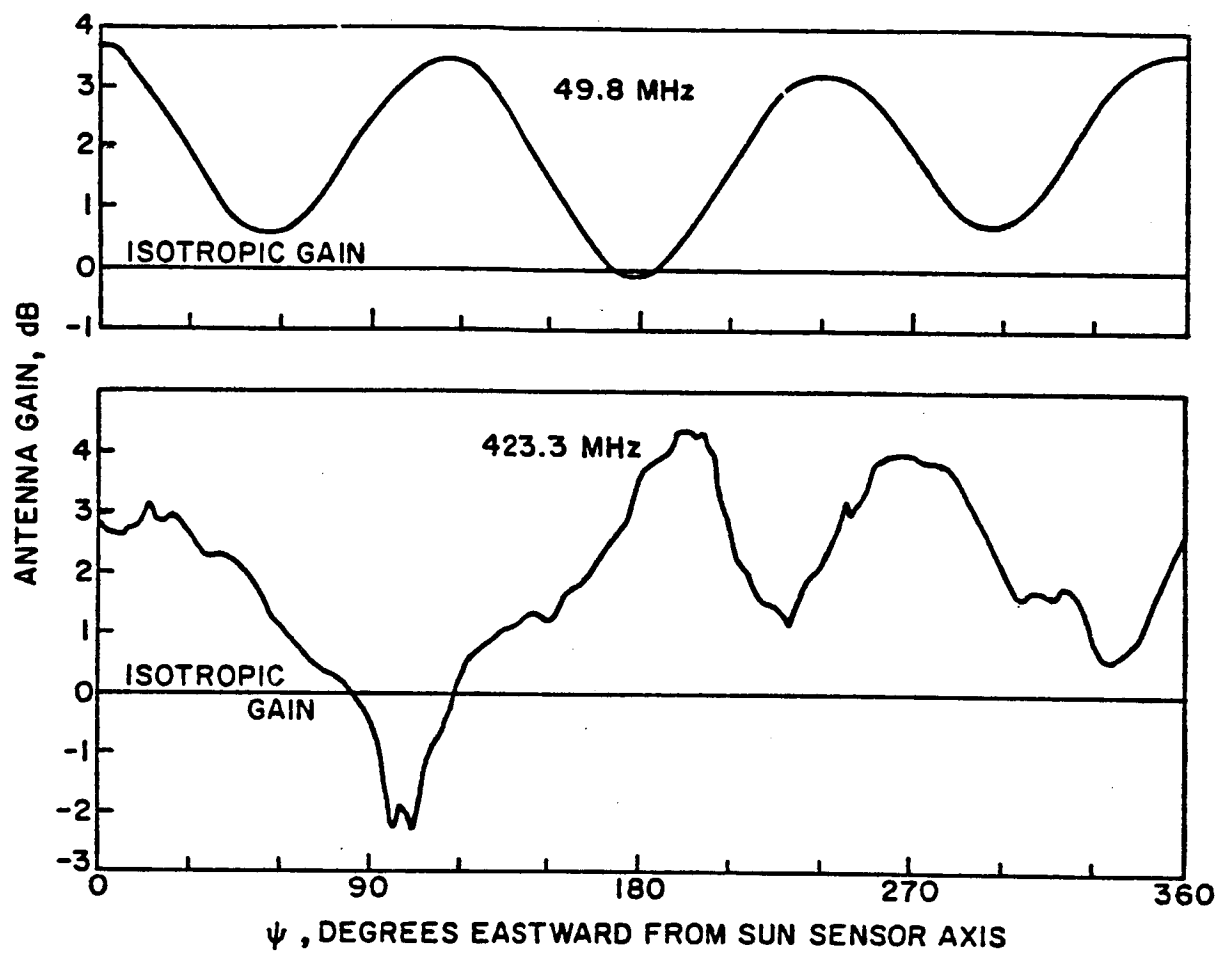


Fig. 3.4. POWER PATTERNS OF RECEIVING ANTENNAS IN THE ECLIPTIC PLANE.

#### D. Phase-Locked Receiver

A simplified block diagram of the Stanford receiver is shown in Fig. 3.5. As we can see, it is basically a dual-frequency phase-locked loop (PLL) system.

Conceptually, the PLL is a feedback demodulator capable of detecting and tracking the carrier and the modulation phases of a narrow-band signal in the presence of wide-band noise. The reason for its being employed in the receiver will not become quite clear until we come to Sec. III.H, where the "interplanetary electron content measurement"--the sole purpose for which the receiver was originally designed--is discussed. Here, we simply remark the following: Had the purpose been the scintillation study, not the content measurement, a demodulator other than the PLL might have been chosen.

As indicated in Fig. 3.5, three outputs finally come out of the receiver: (1) the modulation phase difference output, (2) the carrier phase difference output, and (3) the Format D output.<sup>†</sup> While both (1) and (2) are used for measuring the interplanetary electron content (Sec. III.H), only (3), the Format D output, may be used for studying the interplanetary scintillations (IPS). Because studying the IPS is the main concern here, an attempt will be made to derive an expression for the Format D output. According to the derivations to be followed, the Format D output is essentially proportional to the square root of the input signal-to-noise power ratio.

Referring again to Fig. 3.5, we first observe that each PLL is preceded by an intermediate-frequency (IF) bandpass limiter (BPL)

---

<sup>†</sup> "Format D output" is so named because it is telemetered back to the earth by the spacecraft in a data format called "Format D." Although in addition to Format D, the spacecraft has four other data formats: Format A, B, C, and E, none of these four is used for telemetering IPS data.



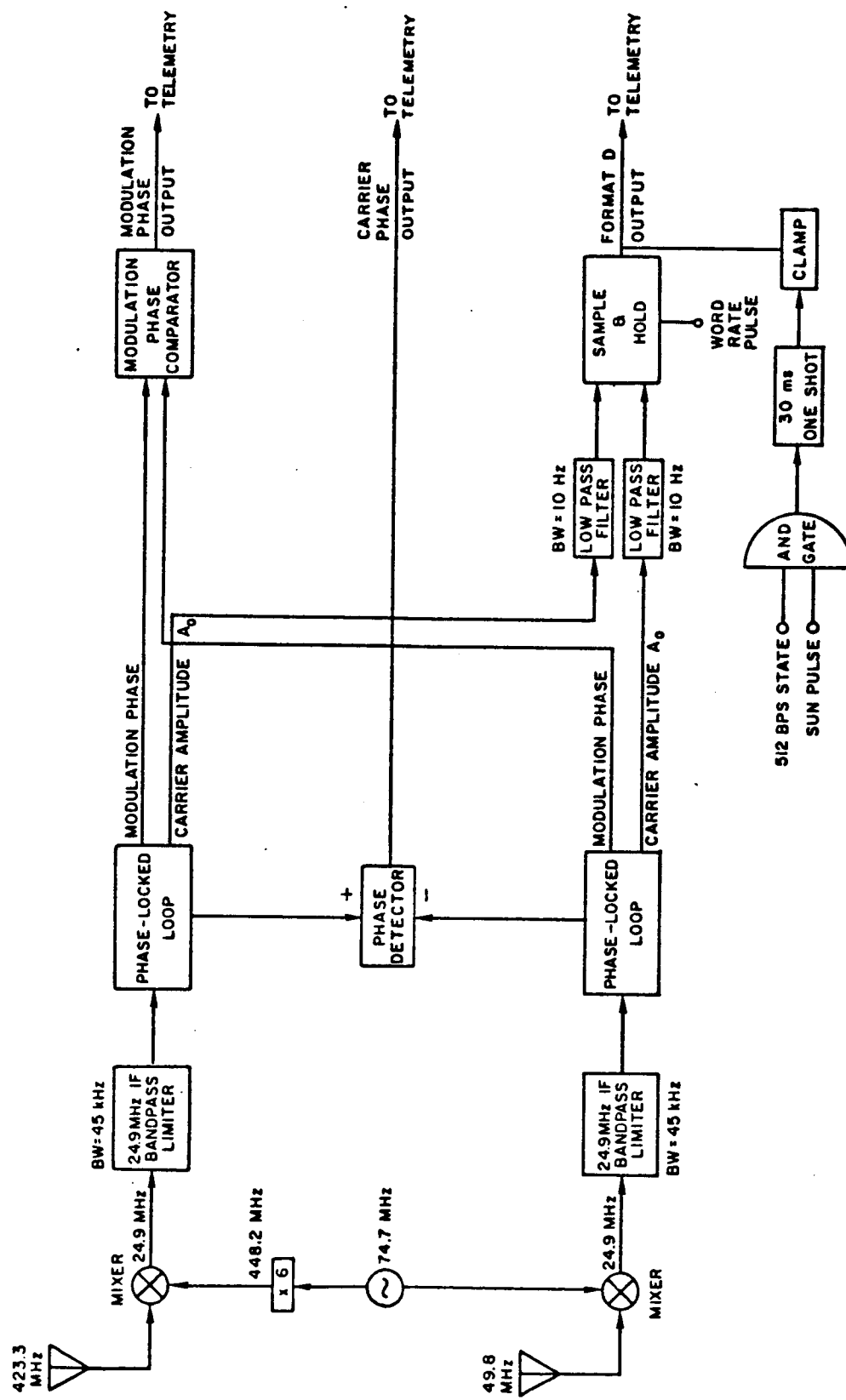


Fig. 3.5. SIMPLIFIED BLOCK DIAGRAM OF THE STANFORD RECEIVER.

having the noise bandwidth of 45 kHz. The reason to insert a BPL in front of the PLL is to yield near-optimum performance for the PLL over a wide range of input signal and noise levels. Davenport (1953) verifies that the output SNR is essentially directly proportional to the input SNR for all values of the latter in the case of an ideal BPL. Furthermore, he demonstrates that

$$\left(\frac{S}{N}\right)_0 \approx \frac{\pi}{4} \left(\frac{S}{N}\right)_i \quad \text{for} \quad \left(\frac{S}{N}\right)_i \lesssim 0.1 \quad (3.5)$$

where  $(S/N)_0$  and  $(S/N)_i$  denote the output SNR and the input SNR, respectively. Jaffe and Rechtin (1955) then point out that the total power output of a limiter in a given zone is constant; i.e.,

$$S_0 + N_0 = L = S' + N' \quad (3.6)$$

where

$S_0$  and  $N_0$  = limiter output signal and noise power

$S'$  and  $N'$  = limiter output signal and noise power for which the loop is designed

$L$  = total power output in a given zone (= constant)

Let  $A_0$  designate the carrier amplitude at the output of the PLL,

then  $A_0$  is related simply to  $S_0$  by

$$A_0 = \sqrt{S_0} \quad (3.7)$$

---

<sup>†</sup> The detailed theory of a PLL when preceded by a BPL may be found in Jaffe and Rechtin (1955) or Lindsey and Simon (1973).

Combining (3.5), (3.6), and (3.7) yields

$$A_0 = \sqrt{\frac{L}{1 + \frac{4}{\pi} \left(\frac{N}{S}\right)_i}} \quad (3.8)$$

Because  $(S/N)_i < 0.1$  during ordinary operation of our receiver, (3.8) can be approximated, within error of 4%, by

$$A_0 \approx \sqrt{\frac{L\pi}{4} \left(\frac{S}{N}\right)_i} \propto \sqrt{\left(\frac{S}{N}\right)_i} \quad (3.9)$$

In words,  $A_0$  is proportional to the square root of the input SNR (over the IF noise bandwidth of 45 kHz).

After being filtered by a 10 Hz low-pass filter,  $A_0$  of each channel is fed into the sample-and-hold circuit to yield the Format D output. If the variation of  $(S/N)_i$  is slower than 10 Hz (which is thought to be true except when the interplanetary scintillations are very strong),  $A_0$  will not be changed appreciably after passage through the low-pass filter. The sample-and-hold circuit samples alternately the two input signals and holds the value until the next sample comes in. The "hold" function is necessary, because it provides the subsequent A/D (analog-to-digital) converter of the spacecraft telemetry subsystem (Sec. III.E) with time to convert every sampled value into a 7-bit telemetry word, the first six bits being the information bits and the last bit being the parity-check bit.

Through a word rate pulse generated by the spacecraft telemetry subsystem, the sampling of the sample-and-hold circuit is synchronized with the subsequent A/D conversion. Although the A/D converter, by

ground command, could operate at any one of the five conversion speeds [8, 16, 64, 256, and 512 bps (bits per second)], the highest speed (512 bps), together with the sampling rate of 512/7 samples/sec, had invariably been selected for operation throughout all of our scintillation observations. Note that 512/7 samples/sec are composed of data coming alternately from 49.8 and 423.3 MHz channels; therefore, the sampling rate for either channel is only one half, or 256/7 ( $\approx 36.57$ ) samples/sec. According to the sampling theorem, sampling at 36.57 samples/sec allows the sampled data to contain components of frequencies as high as  $36.57/2 \approx 18$  Hz. This is more than enough to contain the 10 Hz bandwidth of the pre-sampling low-pass filter (Fig. 3.5).

Insofar as the format D output is concerned, there is one other part of the receiver that remains to be introduced. The sun pulse, energized whenever the sun sensor of the spacecraft (Fig. 3.3) points to the sun, occurs once per spacecraft revolution ( $\approx 1$  rps). With the 512 bps state on, it causes the Format D output to drop to the base line for 30 ms.<sup>†</sup> As the spacecraft spins, this squashing therefore marks on the Format D output all the instants when the sun sensor turns to the sun.

Unlike sampling, the occurrence of the sun pulse is not controlled by any timing signal from the spacecraft telemetry subsystem; it depends only on the orientation of the spinning spacecraft as described in the preceding paragraph. Accordingly, the squashing of the Format D output takes place asynchronously with the subsequent A/D conversion. A discus-

---

<sup>†</sup> At 512/7 samples/sec, 30 ms is slightly longer than the duration of 2 samples.

sion about the digital errors resulted from this asynchronism is given in Appendix C.

#### E. Spacecraft Telemetry and Transmission Subsystems

The generation of timing signals, the A/D conversion, the data storage, and the convolutional encoding are accomplished by the spacecraft telemetry subsystem. As diagramed in Fig. 3.6, it consists mainly of three units: (1) the digital telemetry unit (DTU), (2) the data storage unit (DSU), and (3) the convolutional code unit (CCU).

The DTU A/D converter transforms every Format D output (a sampled analog signal<sup>†</sup>) from the Stanford receiver into a 6-bit binary number (a sampled digital signal). According to binary arithmetic, a 6-bit binary number, say  $b_1b_2b_3b_4b_5b_6$ , represents a decimal number  $N$  given by

$$N = b_1 \times 2^5 + b_2 \times 2^4 + b_3 \times 2^3 + b_4 \times 2^2 + b_5 \times 2^1 + b_6 \times 2^0 \quad (3.10)$$

with each  $b$  having the value 0 or 1; for instance,

BINARY	DECIMAL
000000	0
000001	1
000010	2
000100	4
001000	8
010000	16
100000	32
111111	63

<sup>†</sup> An analog signal (continuous or sampled) is a signal whose amplitude is allowed to have any value in a given range, whereas a digital signal is a signal whose amplitude is restricted to a given set of values.

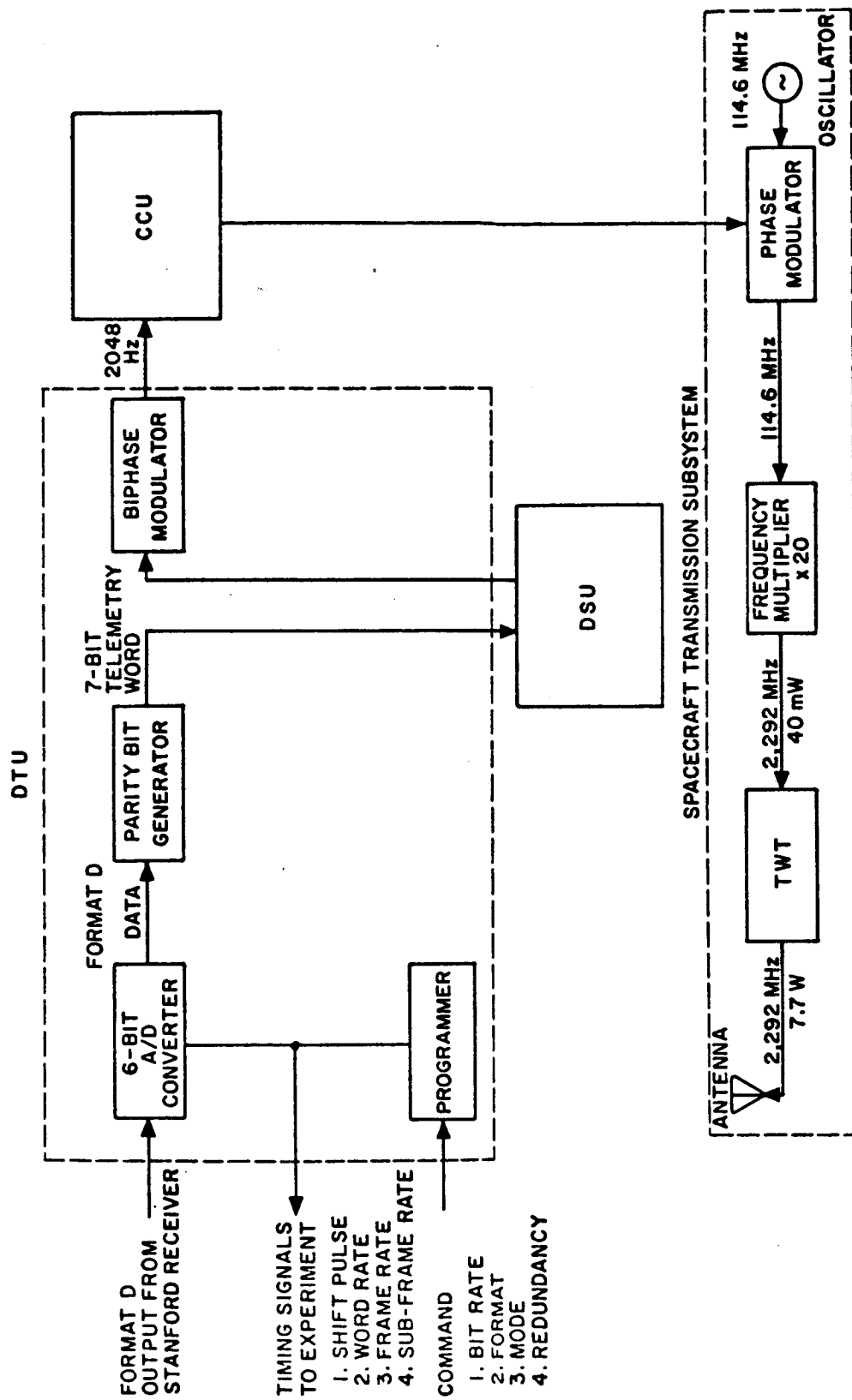


Fig. 3.6. SPACECRAFT TELEMETRY AND TRANSMISSION SUBSYSTEMS.

and so on. Because  $N$  is always an integer from 0 to 63, the amplitude of each format D output is effectively quantized into one of the 64 discrete levels. For convenience, these 6-bit binary numbers or their decimal values are called the digital code of Format D data, which, being nothing but the digital forms of the Format D outputs, are also functions of the input SNR (Sec. III.D). Calibrations for the Format D data will be discussed in the next section.

By calculating the modulo-2<sup>†</sup> sum of the first, the third, and the fifth bits of the inflowing 6-bit binary number, the parity bit generator appends an odd parity-check bit for error detection.<sup>‡</sup> The 7-bit code words thus generated, called telemetry words, are then stored in the DSU until the DSU is full.

The DSU has a capacity of 15,232 bits, which in terms of telemetry words are  $15,232/7 = 2,176$  words. At bit rate of 512 bps, it takes only  $15,232/512 \approx 30$  seconds to fill up this memory unit. Once the unit is full, readout or clearance of all the stored data by ground command is necessary before another storage cycle may begin. Owing to this instrumental limitation, each set of our Format D data (i.e., the data stored

---

<sup>†</sup> In modulo-2 arithmetic,  $0 \oplus 0 = 0$ ,  $0 \oplus 1 = 1 \oplus 0 = 1$ , and  $1 \oplus 1 = 0$ .

<sup>‡</sup> Mathematically,

$$b_1 \oplus b_3 \oplus b_5 \oplus b_7 = 1 \quad (3.11)$$

where

$b_1$ ,  $b_3$ , and  $b_5$  = the first, the third, and the fifth bits of the 6-bit binary number

$b_7$  = the seventh, or the parity-check bit added by the parity bit generator

over one storage cycle) and hence each of our IPS observations cannot span a duration longer than 30 seconds at bit rate 512 bps.

In order to achieve bit error rate<sup>†</sup>  $< 10^{-3}$  (which will be used as the criterion for good data by the ground telemetry-receiving system), a lower bit rate, such as 256, 64, 16, or 8 bps depending on the distance of the spacecraft from the earth, may be selected for memory readout and the subsequent data transmission. Without the interim storage provided by the DSU, the telemetry data would have to be transmitted in real time at 512 bps (the bit rate at which the Format D output is sampled), which, when the spacecraft is far (say 0.5 A.U.) from the earth, can bring about an unbearable bit error rate (i.e., a bit error rate  $\gg 10^{-3}$ ).

After being biphase-modulated by the telemetry words read out of the DSU, a 2048 Hz square wave is convolutionally encoded by the CCU (with a code rate of 1/2 information bit per code symbol) and is then fed to the spacecraft transmission subsystem. The primary functions of the spacecraft transmission subsystem are best understood by examining its simplified block diagram in the lower part of Fig. 3.6:

- (1) The phase modulator accepts the output of the CCU--a convolutionally encoded biphase signal--as the subcarrier to phase-modulate a 114.6 MHz carrier furnished by a crystal-controlled oscillator on board the spacecraft.
- (2) The frequency multiplier increases the frequency of the 114.6 MHz phase-modulated carrier by a factor of 20 so as to produce at its output a 2,292 MHz telemetry signal.
- (3) The TWT (travelling-wave tube) amplifier raises the power of the 2,292 MHz telemetry signal from 40 milliwatts to 7.7 watts.

---

<sup>†</sup> Bit error rate is the average rate or the probability at which bit errors are delivered to the receiver output; for example, bit error rate =  $10^{-3}$  means one bit (on the average) being mistaken in 1000 bits delivered. It is also a common figure of merit for a digital communication system.



- (4) Finally, via the telemetry antenna (which has an axially symmetrical power pattern with respect to the spacecraft spin axis), the amplified telemetry signal at 2,292 MHz ( $\approx 2.3$  GHz) is radiated back to the earth.

On earth, the worldwide Deep Space Network (DSN) managed by the Jet Propulsion Laboratory (JPL) performs the telemetry acquisition, the carrier- and subcarrier-demodulation, and the sequential decoding of the convolutionally encoded data. Recorded on magnetic tapes, the decoded data (which should be a replica of the telemetry words at the output of the spacecraft DTU) are mailed to Ames Research Center (ARC), National Aeronautics and Space Administration, where these data are further processed into digital magnetic tapes, containing the extracted Format D data, to be shipped to Stanford for the IPS studies.

#### F. Format D Data Calibration

As pointed out previously in Sec. III.D, the Stanford receiver was originally designed for interplanetary electron content measurements, not for scintillation studies. Consequently, the Format D data, originally produced just to monitor the performance of the Stanford receiver, were well calibrated (prior to launch) only at high input signal-to-noise ratios, not at low input signal-to-noise ratios.

To attain finer calibration at low input signal-to-noise ratios and to test the aging (if there is any) of the receiver system, the in-flight calibration of the Format D data were carried out during the return of Pioneer 9 to the vicinity of the earth in 1973 (Fig. 3.1). Using pre-launch calibration curve at high input signal-to-noise ratios as the baseline, the procedure consists mainly of (1) varying the input signal-to-noise ratio to the receiver by shifting the ground

transmitter power from one level to another, (2) observing the resultant change in the digital code of Format D data, and (3) adapting the pre-launch calibration curves to the observations. The final calibration curves thus established are shown in Fig. 3.7, where the digital code of Format D data is plotted versus the input signal-to-noise power ratio  $(S/N)_i$  in dB [recall that the Format D data is a function of  $(S/N)_i$  (Sec. III.D)] for each of the two receiver channels.

Obviously, these calibration curves can provide only a mapping from the Format D data to  $(S/N)_i$ ; input signal power  $S_i$ , required for the IPS studies, may further be inferred from  $(S/N)_i$  if and only if the input noise power  $N_i$  is known:

$$S_i = \left(\frac{S}{N}\right)_i \times N_i \quad (3.12)$$

Expressed in terms of the total received noise temperature  $T$  in  $^{\circ}\text{K}$ ,  $N_i$  in watts is

$$N_i = kBT \quad (3.13)$$

where  $k$  = Boltzman's constant =  $1.3805 \times 10^{-23}$  j/ $^{\circ}\text{K}$   
 $B$  = equivalent noise bandwidth as seen by the limiter of the receiver = 45 kHz

Incorporating (3.13) into (3.12) yields

$$S_i = kB \left(\frac{S}{N}\right)_i T = 6.21 \times 10^{-19} \left(\frac{S}{N}\right)_i T \text{ watts} \quad (3.14)$$

Therefore, as evident in this equation, in order to infer  $S_i$  from  $(S/N)_i$ , it has become necessary to compute  $T$ , the total received noise temperature. The calculation of  $T$  is the topic of the next section.

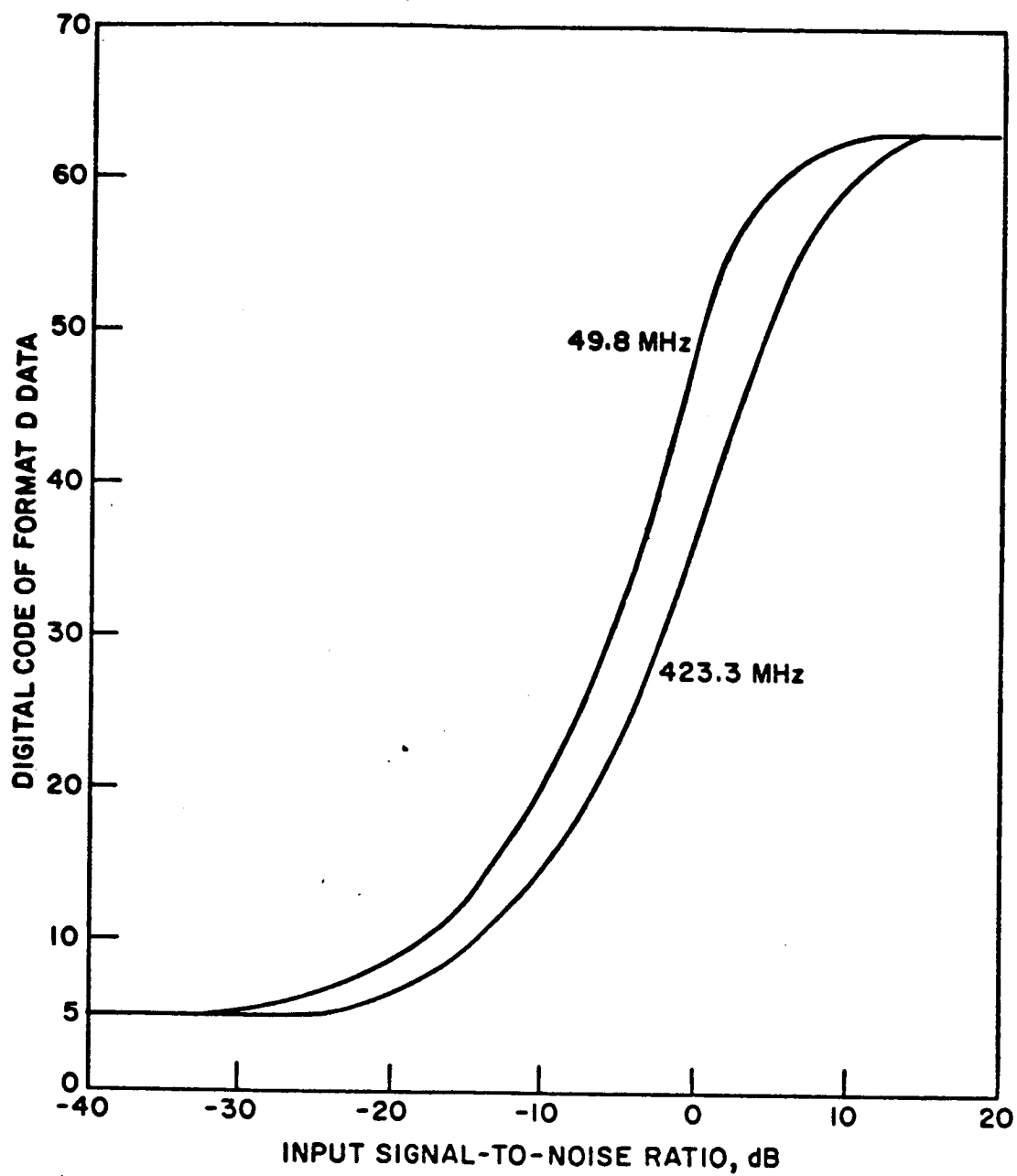


Fig. 3.7. FORMAT D DATA CALIBRATION.

### G. Total Received Noise Temperature

For the receiver and the frequencies (49.8 and 423.3 MHz) of concern, the total received noise temperature  $T$  in  $^{\circ}\text{K}$  is given by

$$T = T_r + \frac{(\mathcal{L} - 1)T_a + T_c + T_s}{\mathcal{L}} \quad (3.15)$$

where

$T_r$  = receiver noise temperature,  $^{\circ}\text{K}$

$\mathcal{L}$  = loss or attenuation of the cable connecting the receiving antenna terminals to the receiver  
[ $\mathcal{L}^{\ell} = 1.047$  and  $\mathcal{L}^{\nearrow} = 1.514$ , where superscripts  $\ell$  and  $\nearrow$  will from now on be used freely along with symbols to indicate low-frequency (49.8 MHz) and high-frequency (423.3 MHz) channels, respectively.]

$T_a$  = cable temperature,  $^{\circ}\text{K}$

$T_c$  = received cosmic noise temperature,  $^{\circ}\text{K}$

$T_s$  = received solar noise temperature,  $^{\circ}\text{K}$

where  $T_c$  and  $T_s$  refer to the receiving antenna terminals. In the following paragraphs, each of these four temperatures is discussed separately. Before getting too involved, it should be remarked that while  $T_r$  and  $T_a$  are essentially constant within a given set of Format D data of  $\sim 30$  seconds,  $T_c$  and  $T_s$  are functions of the spinning (receiving) antenna pattern and hence are functions of the spacecraft spin rate and time.

#### (1) Receiver Noise Temperature $T_r$

According to pre-launch experimental data,  $T_r^{\ell} = 300^{\circ}\text{K}$  and  $T_r^{\nearrow} = 178^{\circ}\text{K}$ , irrespective of surrounding temperature variations over a wide range of interest.

## (2) Cable Noise Temperature $T_a$

All of the 49.8 MHz cable and about half of the 423.3 MHz cable are inside the spacecraft equipment compartment. A thermal control subsystem provides an environment between 30° and 90°F for all scientific instruments mounted within the compartment. Temperatures for cables and antennas external to the spacecraft are also maintained in a similar range via passive thermal coatings having the required absorptivity and emissivity characteristics. Because  $T_a$  is primarily constant within a given set of Format D data, its accuracy has only secondary effects on the final result insofar as normalized intensity fluctuations (i.e., intensity fluctuations divided by the mean intensity) are concerned. Consequently, it is assumed, throughout the analysis, that the cable noise temperatures may be approximated as

$$T_a^{\ell} = T_a^{\nearrow} \approx 300^{\circ}\text{K} \quad (3.16)$$

## (3) Cosmic Noise Temperature $T_c$

Conceptually,  $T_c^{\ell}$  and  $T_c^{\nearrow}$  can be easily obtained by convolving the receiving antenna patterns with the radio sky maps at 49.8 and 423.3 MHz, respectively. Thus, as the spacecraft (hence antenna patterns) spins with period ~1 second,  $T_c^{\ell}$  and  $T_c^{\nearrow}$  will also have the same period. The detailed procedure of the computation of  $T_c^{\ell}$  and  $T_c^{\nearrow}$  is presented in Appendix D and will not be pursued here. According to Eqs. (D.5) and (D.6),

$$5440^{\circ}\text{K} \leq T_c^{\ell} \leq 5920^{\circ}\text{K} \quad (3.17)$$

and

$$37^{\circ}\text{K} \leq T_c^{\nearrow} \leq 43^{\circ}\text{K} \quad (3.18)$$

#### (4) Solar Noise Temperature $T_s$

Briefly speaking, the received solar noise temperature  $T_s$  can be derived by convolving the receiving antenna patterns with the apparent solar disk temperature observed at the spacecraft. Appendix E gives the detailed computational procedure. According to Eqs. (E.4) and (E.5),

$$T_s^{\ell} \approx 20^\circ\text{K} \quad (3.19)$$

and

$$T_s^{\nearrow} \approx 10^\circ\text{K} \quad (3.20)$$

Both are much smaller than other received noise temperatures and hence are less important.

#### H. Interplanetary Electron Content Measurement

The principle of the interplanetary electron content measurement is based upon the effect that electrons have on the phase velocity and the group velocity of a radio wave. Consider a radio wave of frequency  $\nu$  Hz propagating through the interplanetary plasma medium. If the magnetic field and electron collisions of the medium are neglected,<sup>†</sup> the index of refraction is given by

$$\mu = 1 - \frac{40.3 N}{\nu^2} \quad (3.21)$$

where  $N$  = electron density of the medium,  $\text{m}^{-3}$

<sup>†</sup> At frequencies of interest (49.8 and 423.3 MHz), this neglect can be easily justified for regions more than 0.1 A.U. away from the sun, where electron density  $N \leq 7 \times 10^{-7} \text{ el/m}^3$ . Even for the worst case in which  $\nu = 49.8 \text{ MHz}$  and  $N \approx 10^{12} \text{ el/m}^3$  in the ionosphere, Koehler (1967) demonstrates that (3.34) is still a fairly good approximation.

The phase velocity  $V_p$  (i.e., the velocity one must travel to keep the instantaneous phase of the radio wave constant) and the group velocity  $V_g$  [i.e., the velocity of the signal (or the modulation envelope) conveyed by the radio wave if dispersion over the frequency band of the signal is small] of the radio wave are then given by

$$V_p = \frac{\omega}{\mu k} = \frac{c}{\mu} = c \left( 1 + \frac{40.3 N}{v^2} \right) \quad (3.22)$$

$$V_g = \frac{d\omega}{d(\mu k)} = \frac{c}{\mu + \frac{d\mu}{dv}} = c \left( 1 - \frac{40.3 N}{v^2} \right) \quad (3.23)$$

where  $\omega = 2\pi\nu$ ,  $k = 2\pi/\lambda$ ,  $\lambda = c/\nu$ , and  $c$  is the velocity of light in free space. Therefore, compared with  $c$ , the phase velocity is increased by a factor of  $(1 + 40.3 N/v^2)$  whereas the group velocity is decreased by a factor of  $(1 - 40.3 N/v^2)$ . Integrating  $c/V_p$  and  $c/V_g$  from the transmitter at  $z = z_t$  to the receiver at  $z = z_r$  yields the total phase path  $P_p$  and the total group path  $P_g$ , respectively:

$$P_p = (z_r - z_t) - \frac{40.3}{v^2} I \quad \text{m} \quad (3.24)$$

$$P_g = (z_r - z_t) + \frac{40.3}{v^2} I \quad \text{m} \quad (3.25)$$

where

$$I \equiv \int_{z_t}^{z_r} N dz \quad \text{el/m}^2 \quad (3.26)$$

is the integrated electron content between the transmitter and the receiver. In principle, the group path  $P_g$  can be determined from  $T$ , the propagation time of a short pulse at frequency  $\nu$ , via

$$P_g = CT \quad (3.27)$$

whereas the phase path  $P_p$  can be found only within an unknown additive factor of  $n\lambda$ ,  $n$  being an integer. By sending two radio waves at frequencies  $\nu$  and  $\nu + \nu_m$  ( $\nu_m \ll \nu$ ) and with proper choice of  $\nu_m$ , this unknown additive factor  $n\lambda$  may be resolved to bring about a determination of  $P_p$ . At any rate, even though  $P_g$  or  $P_p$  can be measured with great accuracy, it is still difficult to deduce  $I$  accurately from  $P_g$  or  $P_p$  [see (3.24) and (3.25)] in the absence of precise information on the physical path length  $z_r - z_t^+$ .

To circumvent such a difficulty, two coherent carriers of frequencies  $\nu^{\ell} = 49.8$  MHz and  $\nu^{\nearrow} = 423.3$  MHz are phase-modulated at either  $(\nu_m)_1 = 7.692$  kHz or  $(\nu_m)_2 = 8.692$  kHz and transmitted from Stanford to the dual-frequency, phase-locked loop (PLL) receiver (Fig. 3.5) aboard the Pioneer 9 spacecraft. As stated in Sec. III.D, the PLL is basically a feedback demodulator capable of detecting and tracking the carrier phase and the modulation phase of a narrow-band signal in the presence of wide-band noise. Through this capability, the modulation phase comparator in Fig. 3.5 measures  $\Delta\phi_m$ , the relative phase of the two modulation envelopes. Note that  $\Delta\phi_m$  in degrees is related to the group-path difference  $\Delta P_g \equiv P_g^{\ell} - P_g^{\nearrow}$  by

$$\Delta P_g = \frac{\Delta\phi_m}{360^\circ} \lambda_m = \frac{\Delta\phi_m}{360^\circ} \frac{c}{\nu_m} \quad (3.28)$$

Furthermore, from the definition of  $\Delta P_g$  and (3.25),

---

<sup>+</sup> The physical path length  $z_r - z_t$ , which is of order  $10^{11}$  m, is not known to the order of wavelength (few meters).



$$\Delta P_g = 40.3 \left[ \frac{1}{(\nu^{\ell})^2} - \frac{1}{(\nu^{\cancel{\ell}})^2} \right] I \quad (3.29)$$

Incorporating (3.28) into (3.29) and solving for  $I$  produces

$$I = \frac{1}{40.3 \times 360^\circ} \frac{1}{\left[ \frac{1}{(\nu^{\ell})^2} - \frac{1}{(\nu^{\cancel{\ell}})^2} \right]} \frac{c}{\nu_m} \Delta \phi_m = \frac{5.20 \times 10^{19}}{\nu_m} \Delta \phi_m \quad (3.30)$$

a relation which can be used to convert the  $\Delta \phi_m$  measurement to the integrated electron content  $I$ . The use of the modulation frequency  $\nu_m = (\nu_m)_1 = 7.692$  kHz at one time and  $\nu_m = (\nu_m)_2 = 8.692$  kHz at another allows cyclic uncertainties of  $\Delta \phi_m$  measurements up to 8 cycles of 8.692 to be resolved, yielding

$$I \approx 1.70 \times 10^{19} \text{ el/m}^2 \quad (3.31)$$

as the maximum unambiguous measurement of  $I$ . Before being telemetered back to earth, each  $\Delta \phi_m$  measurement--like Format D output--is converted into 6 information bits. This encoding process gives rise to quantization steps of about  $3^\circ$  (i.e., approximately 64 quantization levels over  $180^\circ$ ), thus resulting in an accuracy of about  $\pm 2 \times 10^{16} \text{ el/m}^2$  for the measurement of  $I$ .

The PLL design provides great sensitivity for the receiver and hence makes the measurement of the phase-path difference  $\Delta P_p$ , in addition to  $\Delta P_g$  (or  $\Delta \phi_m$ ), possible at very low signal levels. According to (3.24),

$$\Delta P_p \equiv P_p^{\ell} - P_p = -40.3 \left[ \frac{1}{(\nu^{\ell})^2} - \frac{1}{(\nu^{\cancel{\ell}})^2} \right] I \quad (3.32)$$

Solving for  $I$  and inserting  $\nu^{\ell} = 49.8$  MHz and  $\nu^{\cancel{\ell}} = 423.3$  MHz leads to

$$I = 6.24 \times 10^{13} (-\Delta P_p) \quad (3.33)$$

which, in terms of the number  $n$  of  $\lambda^{\ell}$ , becomes

$$I = -6.24 \times 10^3 (\lambda^{\ell} n) = -3.76 \times 10^{14} n \quad (3.34)$$

In actual operation,  $\Delta P_p$  is not directly measured; instead, the accumulated value of  $2n$  from a certain starting time up to each sampling instance is counted, thereby producing a measure of the rate of change of  $I$ .

The count of the accumulated value of  $2n$  is accomplished by (1) generating in the receiver a sinusoidal signal of frequency  $\Delta v$

$$\Delta v = |v_r^{\ell} - \frac{2}{17} v_r^{\ell}| \quad (3.35)^{\dagger}$$

where  $v_r^{\ell}$  and  $v_r^{\ell}$  are the frequencies of the received carriers, and (2) measuring the zero crossings of this signal in a 10 bit binary counter. This count is always modulo  $2^{10} = 1024$  because of the 10-bit length of the counter. Without being reset to "all zeros," the contents of the counter (10 bits) are sampled, divided into two telemetry words<sup>‡</sup>, and telemetered back to earth.

The rate of change of  $I$  thus obtained is then integrated to yield a plot of  $I$ , within an unknown additive constant, versus time. The unknown additive constant can be determined by comparing this plot with the electron content curve derived from the  $\Delta P_g$  measurement.

<sup>†</sup> In words,  $\Delta v$  is the normalized (with respect to 49.8 MHz) frequency difference between the two received carriers, or between the two arriving carriers at the spacecraft when both PLLs are locked.

<sup>‡</sup> Recall that each telemetry word may contain only 6 information bits (Sec. III.E).

Because the minimum measurable increment of the phase-path is one wavelength of 49.8 MHz, the  $\Delta P_p$  measurement provides a resolution of about  $3.76 \times 10^{14}$  el/m<sup>2</sup> for I, which is about 50 times finer than that provided by the  $\Delta P_g$  measurement.

When the propagation path from Stanford to the spacecraft is far away from the sun, the intermediate ionosphere and magnetosphere contribute a considerable percentage of the measured total content. To obtain the interplanetary content, the sum of the ionospheric and magnetospheric contents, acquired by monitoring at Stanford the Faraday rotation of signals from the geostationary Applied Technology Satellite (ATS), is subtracted from the total content. Imperfect subtraction, however, is always inevitable because (1) the ionospheric and magnetospheric contents thus acquired are along the line-of-sight from Stanford to the ATS, (2) the actual ionospheric and magnetospheric contents contributing to the total content are along the line-of-sight from Stanford to the Pioneer 9 spacecraft, and (3) these two lines-of-sight may not always be in the same direction. To reduce errors introduced by this imperfect subtraction, two computer algorithms have been developed for predicting, from the measured contents between Stanford and the ATS, the contents along the desired line-of-sight. For a full discussion of these two algorithms, see Croft (1971).

When the received signal strength at the spacecraft is weak, the  $\Delta v$  cycle counter may become unlocked, and the operation of the  $\Delta \phi_m$  phase meter may be degraded, thereby necessitating great prudence and special procedures in processing the  $\Delta P_p$  and  $\Delta P_g$  measurements. Further details on this and other topics in connection with the interplanetary electron content measurement can be found in Landt and Croft (1970), Croft (1971, 1973), Eshleman et al. (1960), and Koehler (1967, 1968).

## Chapter IV

### DATA REDUCTION

The primary objectives of the data reduction that will be described are (1) to extract the "clean IPS data" from the received Format D data and then (2) to compute, based on the clean IPS data, statistical parameters--such as the autocorrelation function, the power spectrum, and the scintillation index--for comparison with the theory discussed in Chapter II. Here, the "clean IPS data" is referred to as the power (or intensity<sup>†</sup>) of the signal arriving at the spacecraft after its transit through the turbulent interplanetary medium.

To give an overall view of what is ahead in this chapter, the flow chart of Fig. 4.1 depicts the basic procedure of the data reduction. The first step, the wild-point editing, can be regarded as a preprocessing step, in which errors of Format D data, ensuing from asynchronism of the sun pulse with the A/D conversion (see Sec. III.D and Appendix C), are eliminated by checking the two neighboring samples of each sun pulse and deleting (1) the sample before the sun pulse if its value is even and (2) the sample after the sun pulse if its value is 3, 7, 15, or 31. The second step, the data clean-up, which will be discussed in Sec. IV.A, fulfils the extraction of the clean IPS data from the received Format D data. To reduce the computational time required, the so-called fast Fourier transform (FFT) algorithm is applied in Sec. IV.B to obtain autocorrelation functions. For the same reason, FFT is again employed in Sec. IV.C, in which power spectra are estimated according to procedures given by Blackman and Tukey (1958). Sec. IV.D outlines the logic

---

<sup>†</sup> Recall that the terms "power" and "intensity" are used interchangeably--see p. 17 in Chapter II.

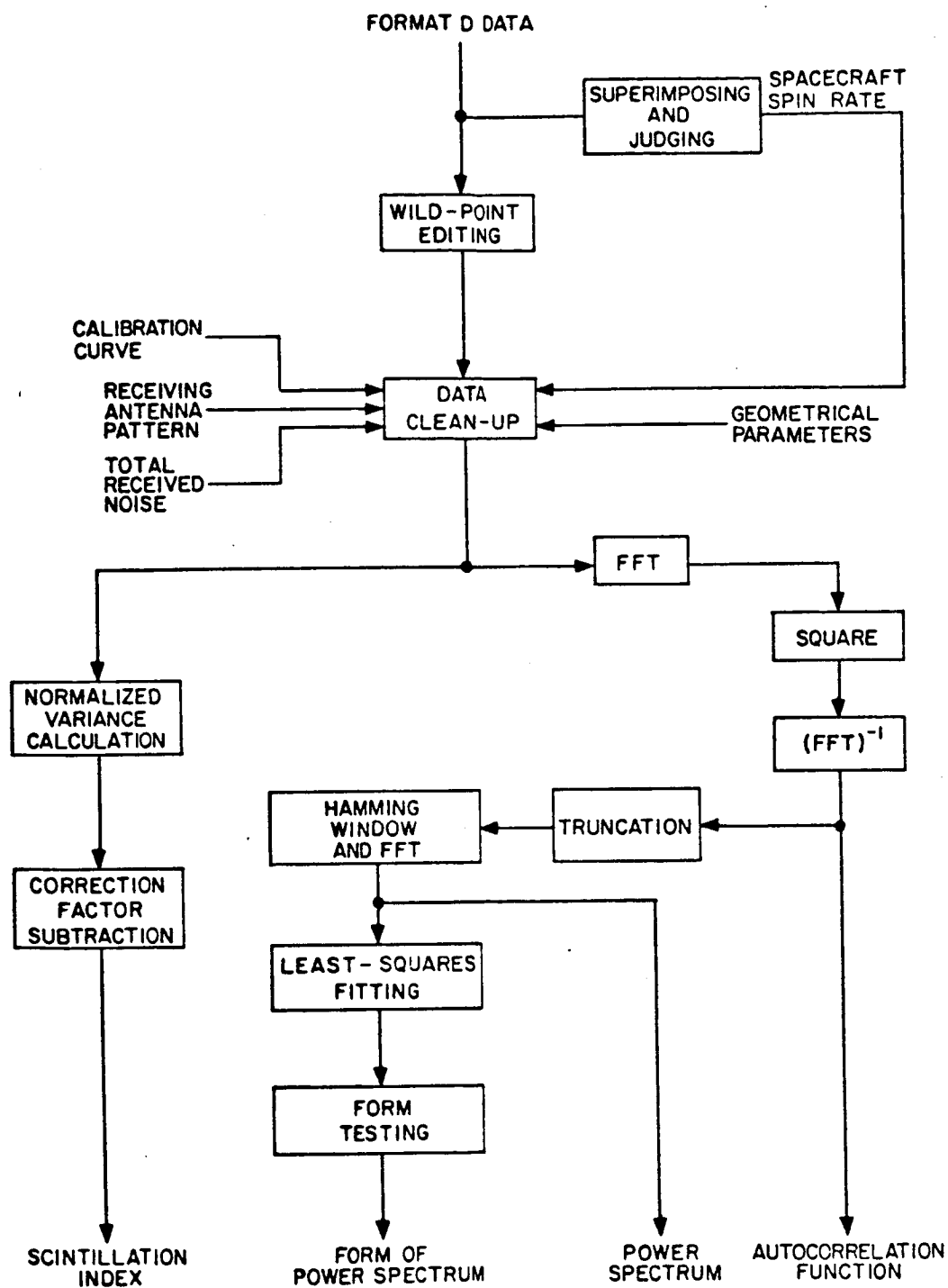


Fig. 4.1. FLOW CHART OF DATA REDUCTION.

of a computer program devised for (1) fitting three proposed forms<sup>†</sup> to the estimated power spectra in least-square sense and then (2) determining which form fits best by comparing the fitting parameters. Finally, in Sec. IV.E, the calculation procedure and the correction factors of scintillation indices--founded on a simplified noise model which can be justified by in-flight calibration data--are presented.

#### A. Data Clean-Up

From the descriptions in the previous chapter, a typical set of Format D data consists of a total of 2,176 digital samples (which span a duration of about 30 seconds) coming alternatively from 49.8 and 423.3 MHz channels at a rate of  $512/7 \approx 73.14$  samples/sec. Represented as functions of sampling instants, these samples appear like the following:

$$D^{\swarrow}(0), D^{\ell}(\tau), D^{\swarrow}(2\tau), D^{\ell}(3\tau), \dots, D^{\swarrow}(2174\tau), D^{\ell}(2175\tau) \quad (4.1)$$

$$\text{where} \quad \tau = \frac{7}{512} \approx 0.0137 \text{ sec} \quad (4.2)$$

is the sampling interval if samples from both channels are counted<sup>‡</sup> and, again, superscripts  $\ell$  and  $\swarrow$  are used to indicate 49.8 and 423.3 MHz channels, respectively. ( $\ell$  and  $\swarrow$  were defined on p. 56.) Except when sun pulses occur, each  $D(k\tau)$  (where  $k = 0, 1, 2, \dots, 2175$ ) has a value between 5 and 63, which can be converted to  $S_i(k\tau)/N_i(k\tau)$ , the input signal-to-noise power ratio at  $k\tau$ , by

<sup>†</sup> The three proposed forms of power spectra of intensity fluctuations are gaussian, exponential, and power-law.

<sup>‡</sup> If only samples from either channel are counted, the sampling interval is  $2\tau \approx 0.0273$  sec, which corresponds to a sampling rate of  $256/7 \approx 36.57$  samples/sec.

employing the calibration curve in Fig. 3.6. Because  $I(k\tau)$ , the clean IPS data (or the arriving signal intensity at the spacecraft) at  $k\tau$ , is related to  $S_i(k\tau)$  via

$$S_i(k\tau) = A(k\tau) \times I(k\tau) \quad (4.3)$$

where  $A(k\tau)$  is the receiving antenna power pattern in the direction of the earth at  $k\tau$ ,  $S_i(k\tau)/N_i(k\tau)$  can further be used to extract  $I(k\tau)$  if both  $A(k\tau)$  and  $N_i(k\tau)$  are known:

$$I(k\tau) = \left[ \frac{S_i(k\tau)}{N_i(k\tau)} \right] \times \frac{N_i(k\tau)}{A(k\tau)} \quad (4.4)$$

In order to infer  $A(k\tau)$  and  $N_i(k\tau)$  from  $A(\psi_E)$  (Fig. 3.4) and  $N_i(\psi_Y, \psi_S)^+$ , it is necessary--as will become clearer later--to first find the spacecraft spin period, say  $\tau_0$ , and the instants, say  $m\tau$ ,  $m\tau + \tau_0$ ,  $m\tau + 2\tau_0$ , . . . , at which the sun sensor of the spacecraft turns to the sun. A clue to the determination of  $\tau_0$  and  $m\tau$  may be obtained by recalling from Sec. III.D that sun pulses [each appearing as two successive 1's in (4.1)]

---

<sup>+</sup> According to (3.13) and (3.15),  $N_i$  is made up of four noise temperatures

$$N_i = 6.21 \times 10^{-19} \left[ T_r + \frac{(\mathcal{L}-1) T_a + T_c + T_s}{\mathcal{L}} \right]$$

While  $T_r$  and  $T_a$  are essentially constant within a given set of Format D data,  $\psi_Y$  and  $\psi_S$  and hence  $T_c = T_c(\psi_Y)$  and  $T_s = T_s(\psi_S)$  [see Eqs. (D.3), (D.4), (E.1), and (E.2)] are, as mentioned in Sec. III.G, periodic functions of time with period equal to that of spacecraft rotation ( $\approx 1$  sec). Therefore,  $N_i$  may in turn be regarded as a function of  $\psi_Y$  and  $\psi_S$ , or, symbolically,

$$N_i = N_i(\psi_Y, \psi_S)$$

mark on the Format D data all the times when the sun sensor points to the sun. Intuitively, one could adopt sun pulses along the data directly as divisions of spacecraft rotations and then count (1) the separation between sun pulses and (2) the position of the first sun pulse to yield (1)  $\tau_0$  and (2)  $m\tau$ , respectively; however, due to the discrete nature of the data,  $\tau_0$  and  $m\tau$  thus determined will be of uncertainty  $\pm\tau$ . To improve the accuracy, the following procedure is utilized in actual data reduction to determine  $\tau_0$  and  $m\tau$  for each set (or pass) of Format D data:

1. Count the separations between sun pulses throughout a given set of Format D data and refer to other available information<sup>†</sup> to give a rough estimate of  $\tau_0$ , say  $\hat{\tau}_0$ .
2. Superimpose the whole given set of data (which usually contains data of about 30 spacecraft rotations) at a period equal to  $\hat{\tau}_0$ .
3. Check and see if every sun pulse is within a narrow opening of width  $\approx 2\tau$ . If not, change the period of superimposition  $\hat{\tau}_0$  until they are.
4. Record the final period of superimposition and the corresponding position at which the narrow opening starts to be  $\tau_0$  and  $m\tau$ , respectively.

Fig. 4.2 illustrates the values of spin period  $\tau_0$  in seconds thus derived versus the dates of taking Format D data from late 1968 to 1972; the sinusoidal variations of  $\tau_0$  can be attributed, as mentioned in Sec. III.C, to the heating and cooling of the spacecraft--when the spacecraft moves closer to or farther from the sun (Fig. 3.1).

<sup>†</sup> For example,  $\tau_0$ 's which had already been found for previous Format D passes are useful pieces of information, for, as will be seen later, the values of  $\tau_0$  have a certain trend (Fig. 4.2).



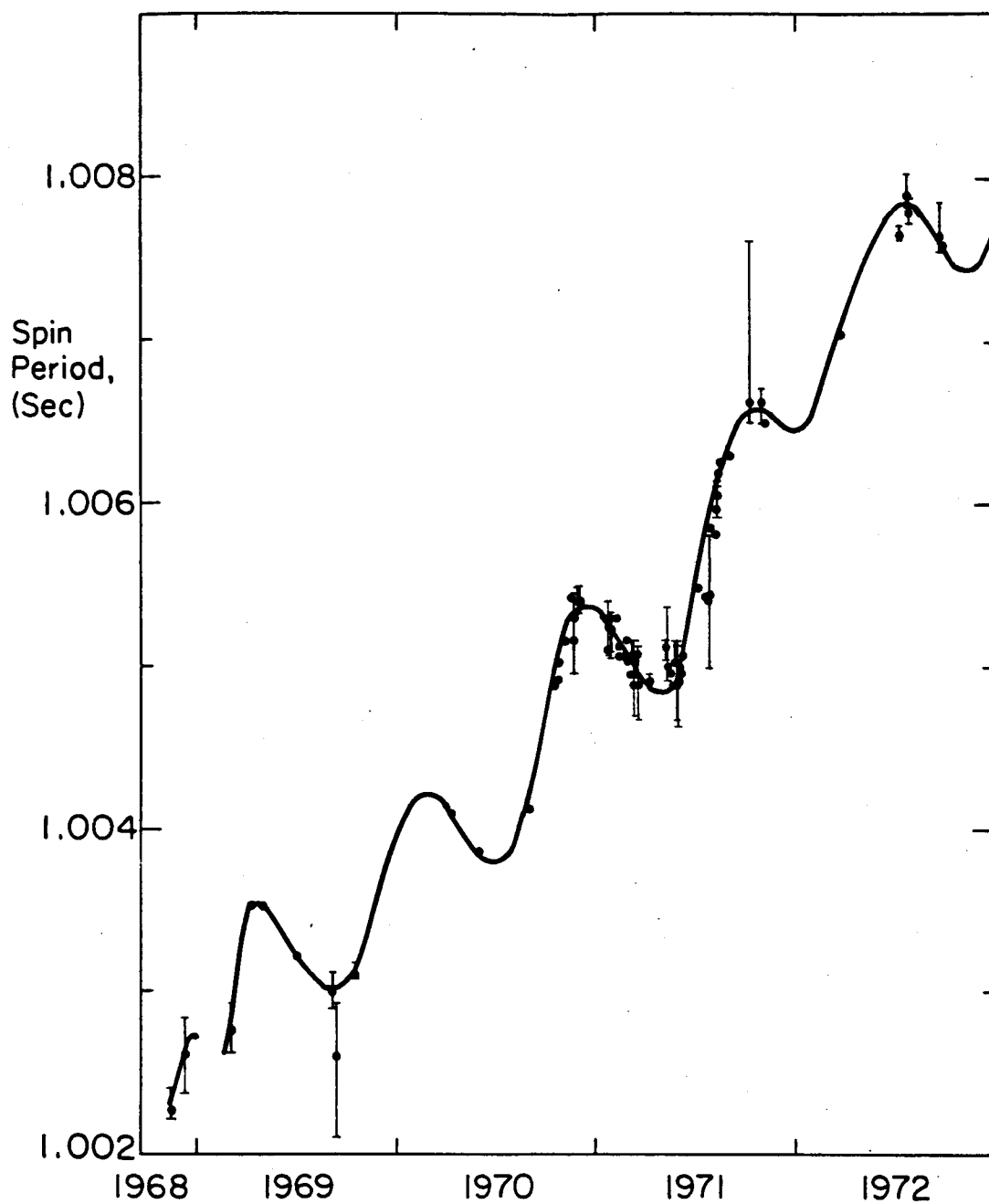


Fig. 4.2. SPIN PERIOD  $\tau_0$  IN SECONDS VS TIME IN YEARS.

Once  $\tau_0$  and  $m\tau$  are known for a given set of Format D data, one can write  $\psi_S$ ,  $\psi_Y$ , and  $\psi_E$  at  $k\tau$  as functions of  $k\tau$  by referring to Figs. 3.2 and D.1:

$$\psi_S(k\tau) = \frac{(k-m)\tau}{\tau_0} \times 360^\circ \quad (4.5)$$

$$\psi_Y(k\tau) = \psi_S(k\tau) + 360^\circ - G - S \quad (4.6)$$

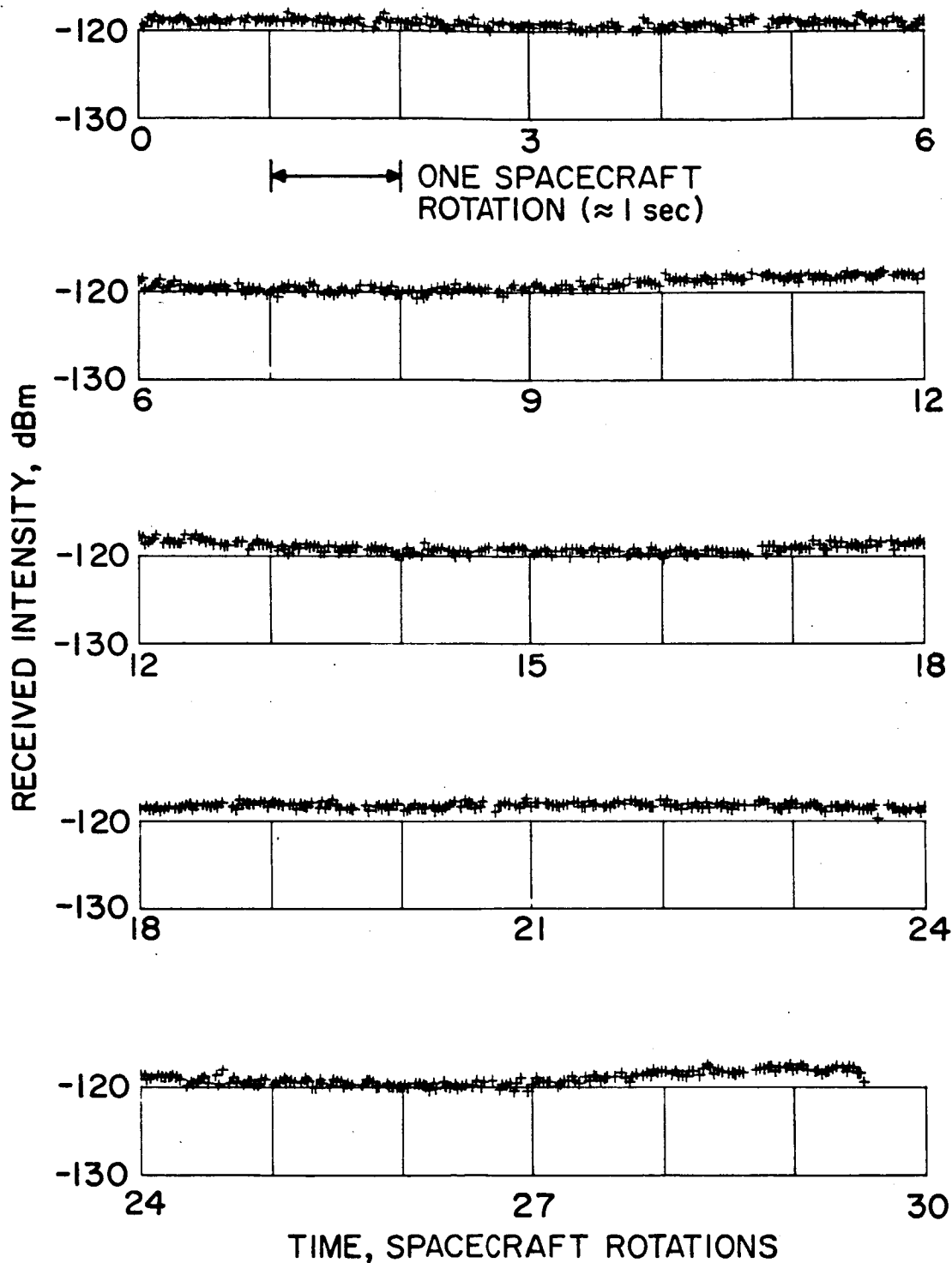
$$\psi_E(k\tau) = \psi_S(k\tau) + 360^\circ - P \quad (4.7)$$

where (1)  $\psi_S$ ,  $\psi_Y$ , and  $\psi_E$  are the  $\psi$  angles of the sun, the vernal equinox, and the earth, respectively, and (2)  $G$  is the celestial longitude of the sun observed from the earth, whose daily values are tabulated in The American Ephemeris and Nautical Almanac.

With the aid of the above three equations,  $A(\psi_E)$  and  $N_i(\psi_Y, \psi_S)$  can be converted to  $A(k\tau)$  and  $N_i(k\tau)$  which can further be incorporated into (4.4) to yield the clean IPS data  $I(k\tau)$ .

All received Format D data are processed by a computer program that fulfills the data clean-up by virtue of the procedure just described, and all  $I(k\tau)$  thus acquired are available in the forms of listing, plots, and cards such that they can be visually inspected or further processed by computers. Several examples of  $I(k\tau)$  plotted in dBm versus time are shown in Figs. 4.3 through 4.6. A complete set of figures and listings of  $I(k\tau)$  versus time for all of our scintillation data may be found in Croft et al. (1975a) and Croft et al. (1975b). Figs. 4.3 (a) and (b) illustrate  $I(k\tau)$  at 49.8 and 423.3 MHz taken simultaneously on 9 February 1969, ninety days after launch, when the spacecraft was still near the earth and IPS was slight. The slow variation of  $I(k\tau)$  in Fig. 4.3(a), which has period  $\approx 10$  seconds, is believed to be due to ionospheric scintillations.

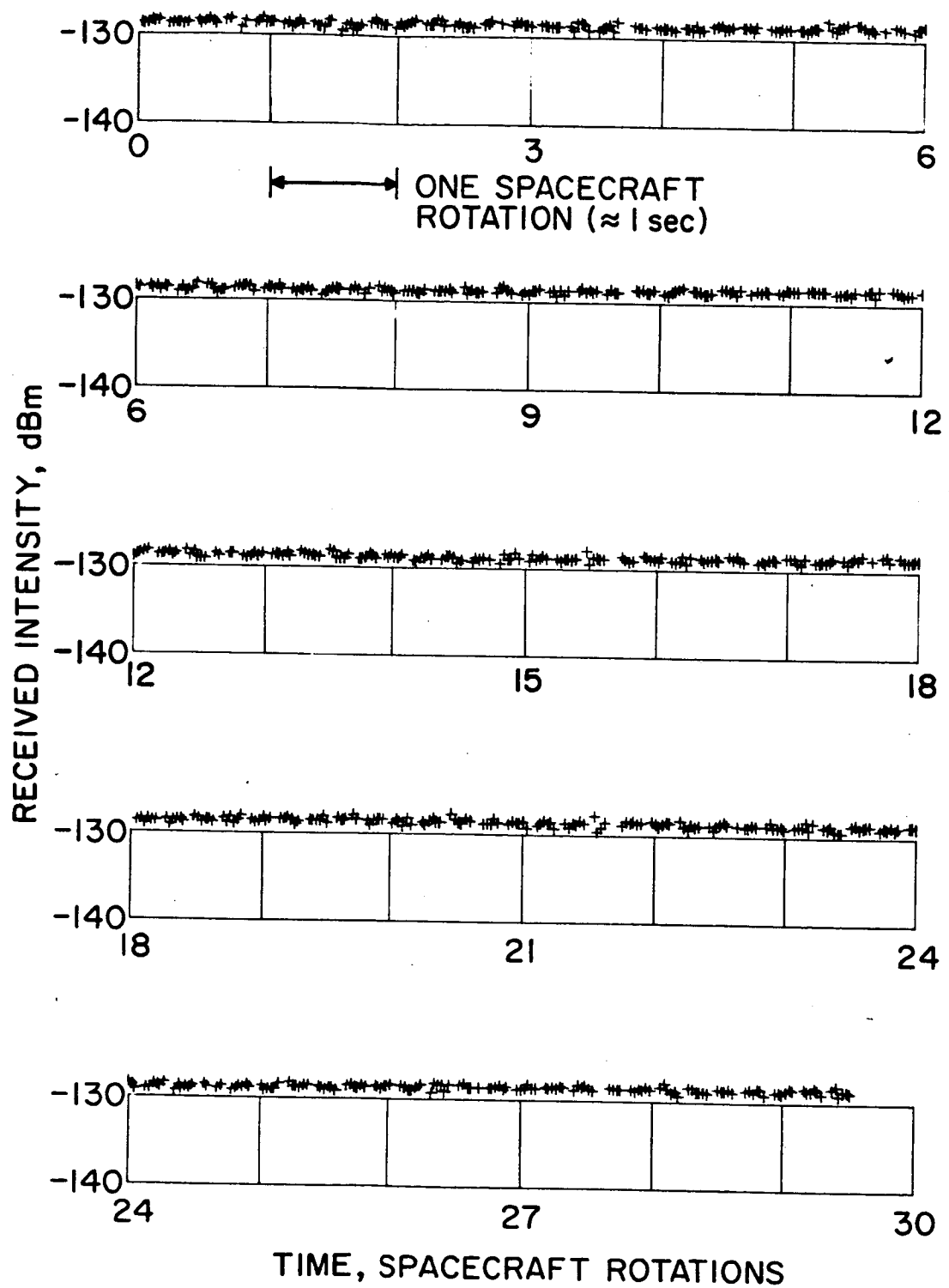
9 FEB 1969, 0.85 A.U.  
49.8 MHz



- a. Almost no IPS at 49.8 MHz. The slow quasi-periodic fluctuations of period  $\sim 10$  seconds are believed to be due to ionospheric scintillations.

Fig. 4.3. SCINTILLATION RECORDS ON 9 FEB 1969 WHEN THE PROXIMATE DISTANCE  $\rho$  OF THE RADIO PATH WAS 0.85 A.U. FROM THE SUN AND THE SPACECRAFT WAS NEAR THE EARTH.

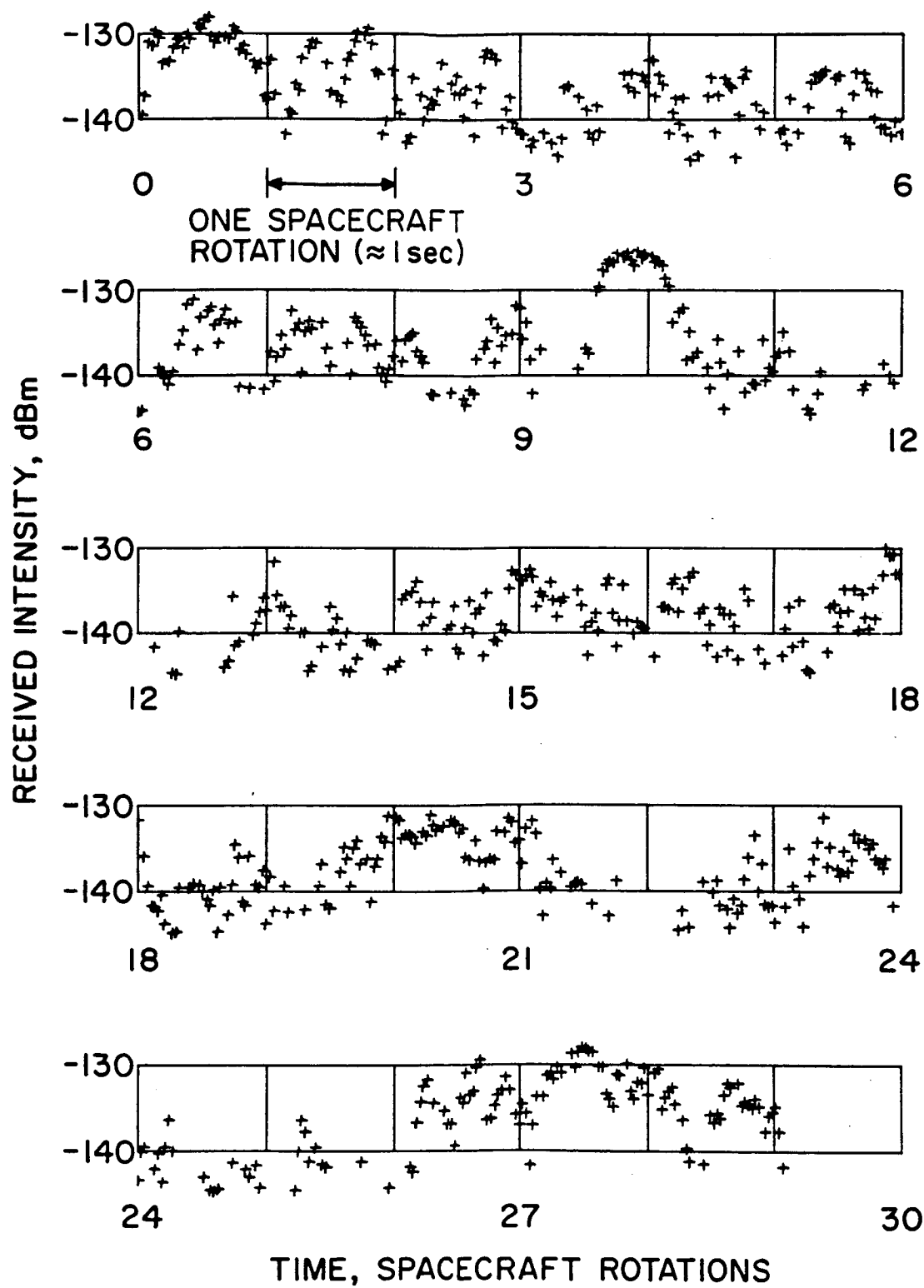
9 FEB 1969, 0.85 A.U.  
423.3 MHz



b. Almost no IPS at 423.3 MHz.

Fig. 4.3. CONTINUED.

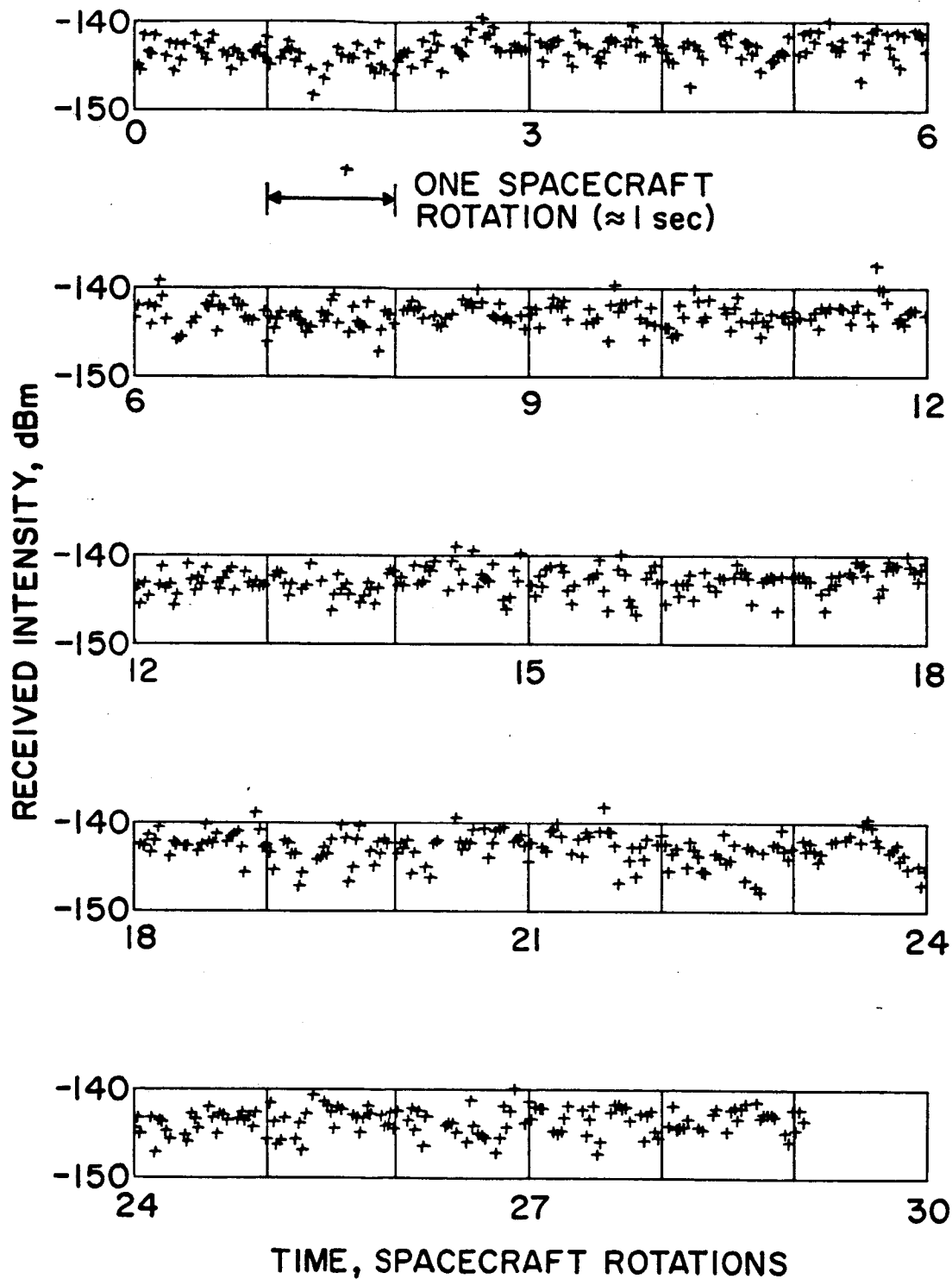
10 APR 1970, 0.41 A.U.  
49.8 MHz



a. Strong IPS at 49.8 MHz.

Fig. 4.4. SCINTILLATION RECORD ON 10 APRIL 1969 WHEN  $\rho = 0.41$  A.U.

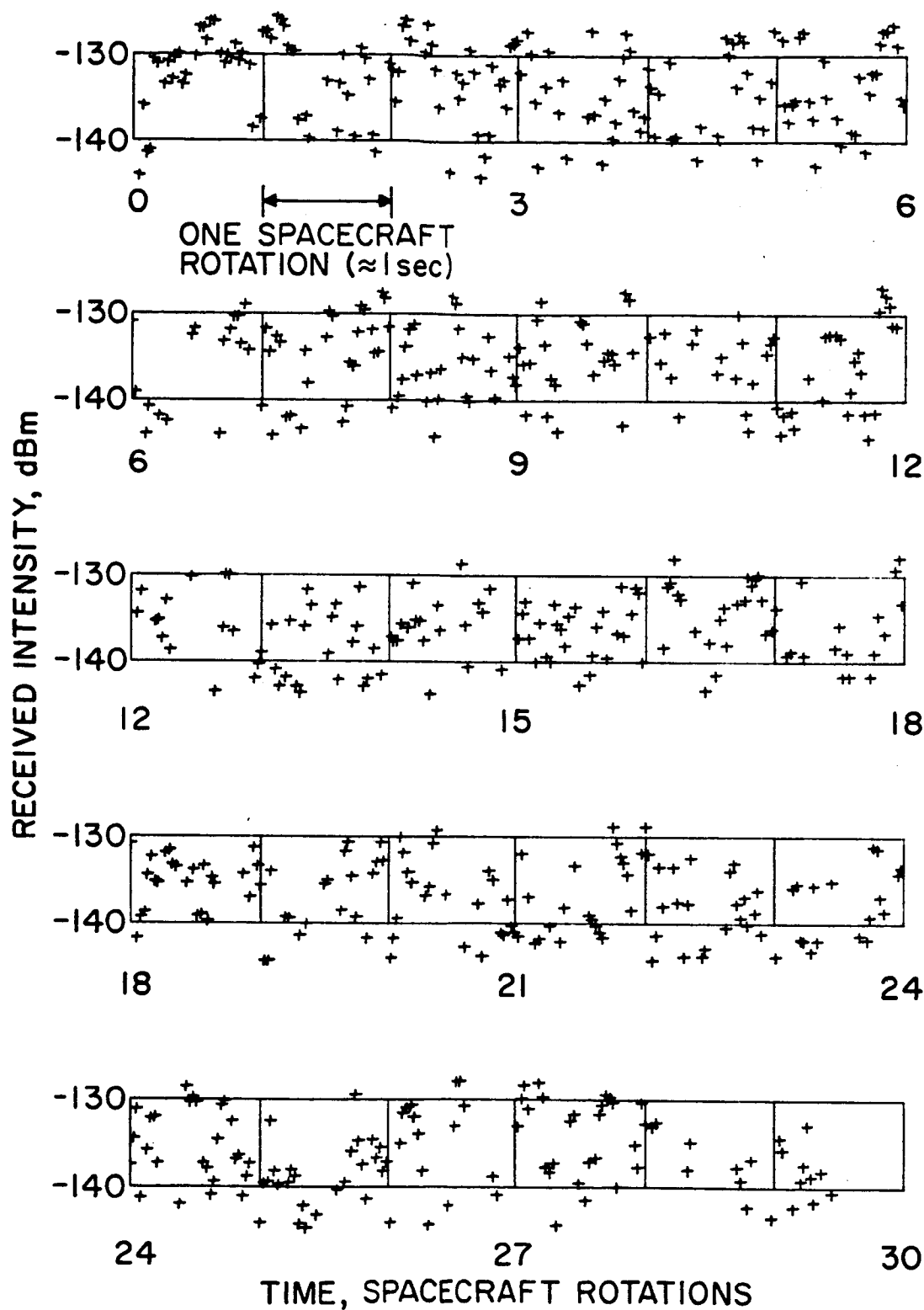
10 APR 1970, 0.41 A.U.  
423.3 MHz



b. Moderate IPS at 423.3 MHz.

Fig. 4.4. CONTINUED.

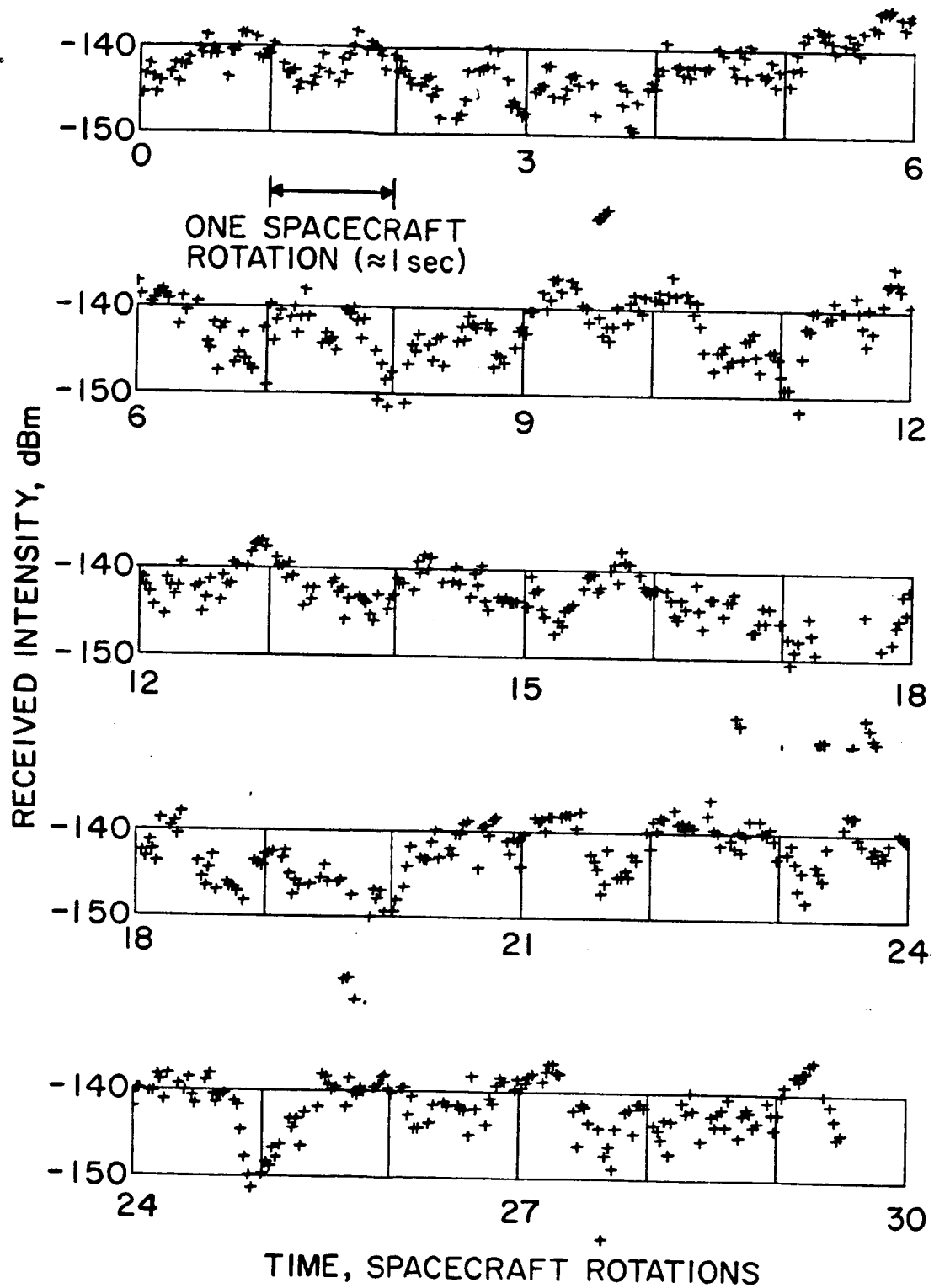
11 NOV 1970, 0.15 A.U.  
49.8 MHz



a. Very strong IPS at 49.8 MHz.

Fig. 4.5. SCINTILLATION RECORD ON 11 NOV 1970 WHEN  $\rho = 0.15$  A.U.

11 NOV 1970, 0.15 A.U.  
423.3 MHz

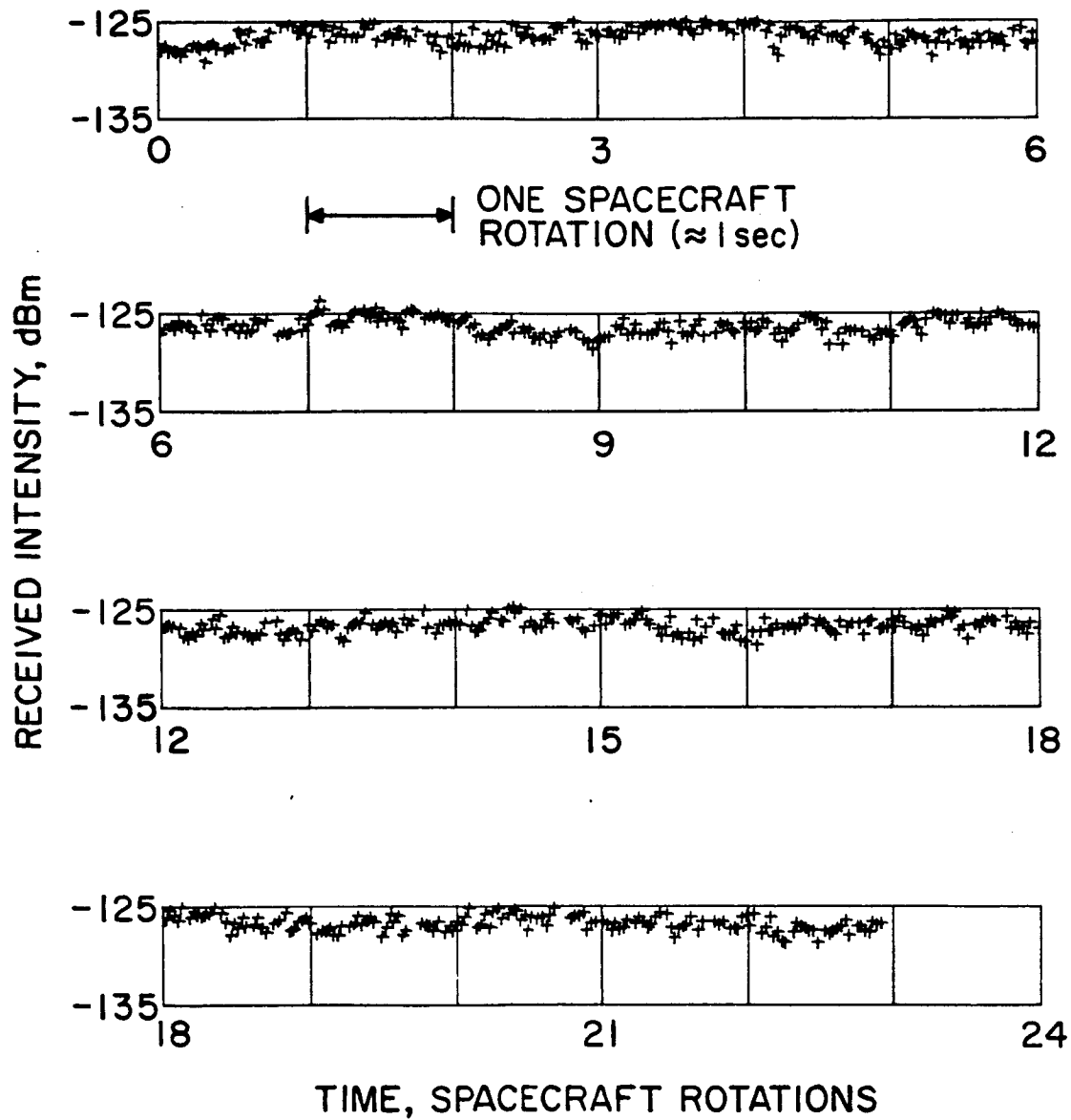


b. Strong IPS at 423.3 MHz.

Fig. 4.5. CONTINUED.



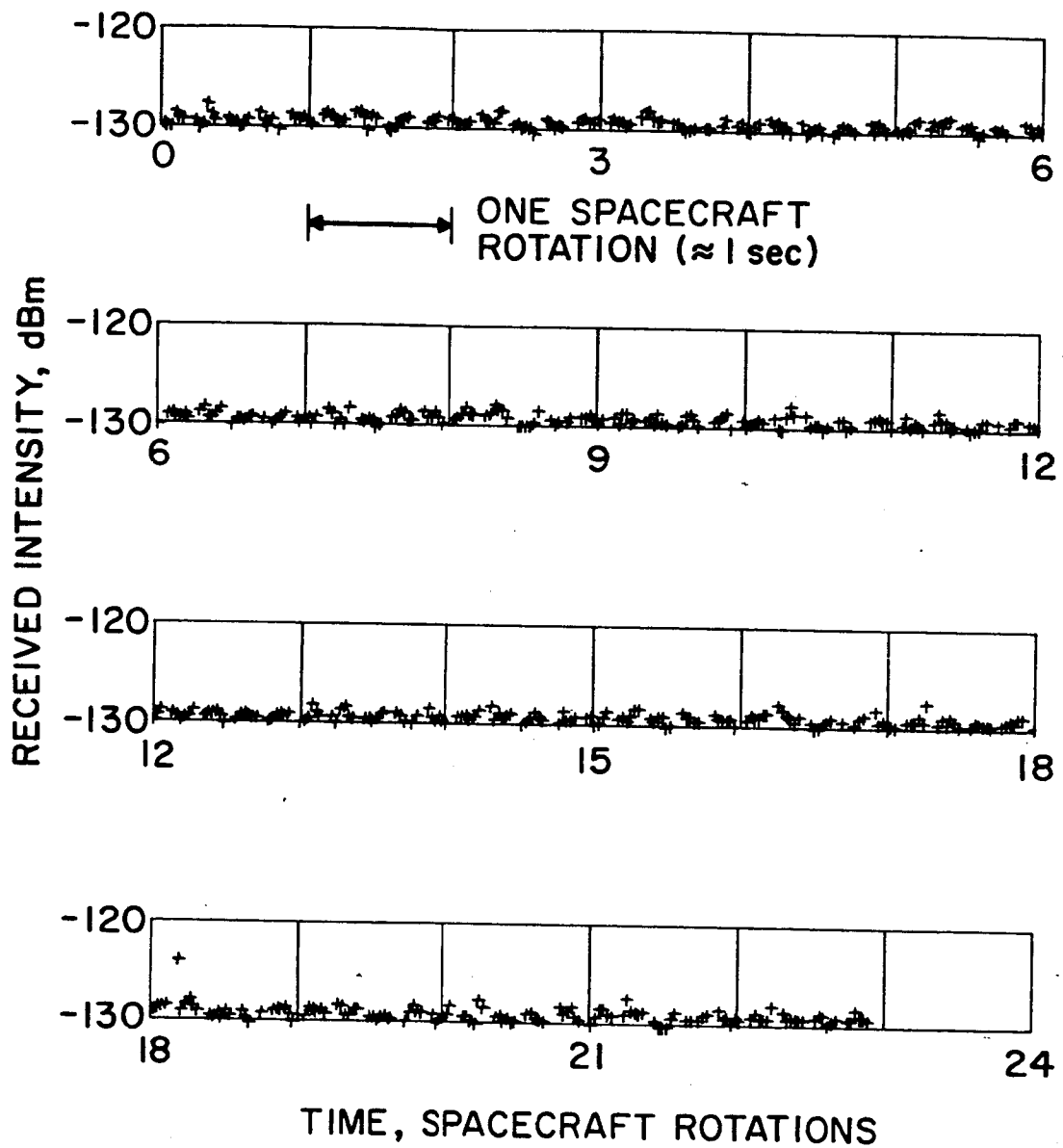
20 SEP 1972, 0.88 A.U.  
49.8 MHz



a. Weak IPS at 49.8 MHz.

Fig. 4.6. SCINTILLATION RECORD ON 20 SEP 1972 WHEN  $\rho = 0.88$  A.U. AND SPACECRAFT WAS BACK NEAR THE EARTH.

20 SEP 1972, 0.88 A.U.  
423.3 MHz



b. Weak IPS at 423.3 MHz.

Fig. 4.6. CONTINUED.

The reason for this belief can be understood as follows. According to the thin-screen diffraction model [as was adopted by Rufenach (1971, 1972, 1973, 1975) and Singleton (1974) to interpret ionospheric scintillations], the dominant component of intensity fluctuations is at the Fresnel frequency  $\nu_f = U/\sqrt{\pi\lambda z}$ . Since the height  $z$  of ionospheric irregularities occurs in a narrow range 300-400 km [Rufenach (1971)] and the velocity  $U$  of ionospheric irregularities is on the order 70-160 m/sec [Singleton (1974)], the dominant period ( $= 1/\nu_f$ ) of ionospheric scintillations at 49.8 MHz is of the order 10-50 sec. [See also Briggs (1966)], who has pointed out that ionospheric scintillations are in the range 10 to 60 sec.] Fig. 4.4 displays  $I(k\tau)$  taken on 16 October 1969 when the proximate distance  $\rho$  of the propagation path was 0.82 A.U. from the sun. The quasi-periodic fluctuations of  $I(k\tau)$  of period  $\approx 2$  seconds, at 49.8 MHz indicate clearly the effect of IPS, because  $\sqrt{\lambda z} \sim 500$  km and  $U \sim 500$  km/sec such that  $\nu_f(\text{IPS}) \sim 0.5$  Hz. Note that at the same time  $I(k\tau)$  at 423.3 MHz is still relatively steady. Fig. 4.5 presents  $I(k\tau)$  taken on 11 November 1970, about one month before solar occultation, when  $\rho = 0.15$  A.U. from the sun. The fluctuations at both frequencies are stronger and faster than those shown in Fig. 4.4. Long after solar occultation (20 September 1972) as the spacecraft returns to the vicinity of the earth,  $I(k\tau)$  becomes steady again as illustrated in Fig. 4.6.

#### B. Autocorrelation Function of Intensity Fluctuation

Consider a finite string of clean IPS data containing  $N$  samples at either 49.8 or 423.3 MHz and appearing as follows:

$$I(0), I(\tau'), I(2\tau'), \dots, I[(N-1)\tau'] \quad (4.8)$$

where  $\tau' = 2\tau \approx 0.0273 \text{ sec} \quad (4.9)$

is the sampling interval if only samples from either channel are counted. The autocorrelation function of intensity fluctuation,  $R_{\Delta I}(m\tau')$ , or equivalently the autocovariance function of the intensity,  $A_I(m\tau')$  is defined by

$$\begin{aligned} R_{\Delta I}(m\tau') &= A_I(m\tau') = \frac{1}{N-m} \sum_{k=0}^{N-m-1} \Delta I(k\tau') \Delta I(k\tau' + m\tau') \\ &= \frac{1}{N-m} \sum_{k=0}^{N-m-1} [I(k\tau') - \bar{I}] [I(k\tau' + m\tau') - \bar{I}] \quad (4.10) \end{aligned}$$

where

$$\Delta I(k\tau') = I(k\tau') - \bar{I} \quad (4.11)$$

is the intensity fluctuation and

$$\bar{I} = \frac{1}{N} \sum_{k=0}^{N-1} I(k\tau') \quad (4.12)$$

is the temporal average of  $I(k\tau')$ .

As suggested by Stockham (1966), an autocorrelation function can be computed via the indirect route of using FFTs. The method is based upon the fact that the product of the discrete Fourier transform<sup>†</sup> (DFT) of any periodic sequence and its complex conjugate is equal to the DFT of the circular autocorrelation function of the sequence. Appendix F details the computational procedure. Examples of the autocorrelation function of intensity fluctuations thus derived will be illustrated in the next section along with the power spectrum of intensity fluctuations.

<sup>†</sup> See, for example, Brigham (1974) for a comprehensive discussion on DFTs.

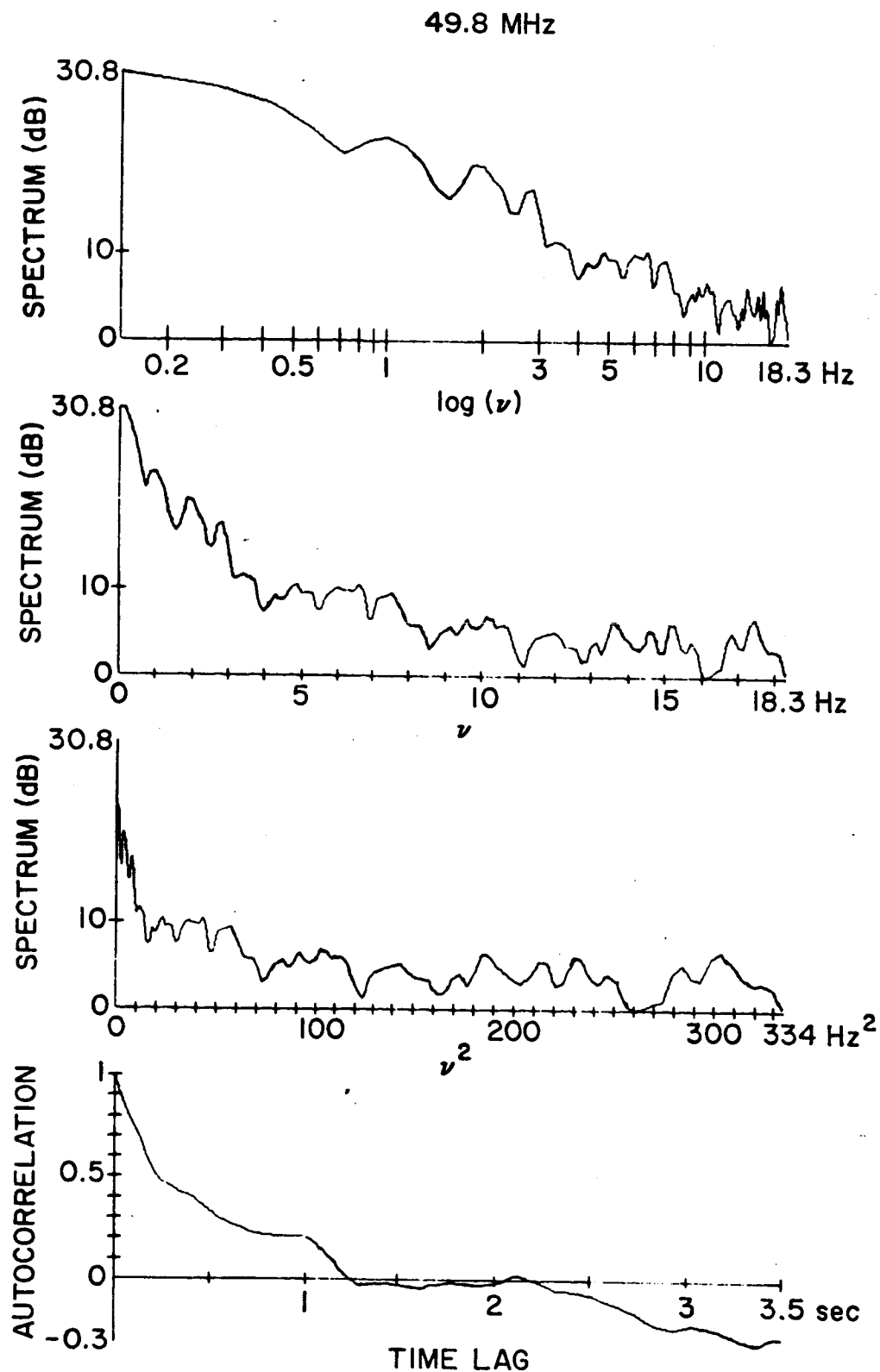
### C. Power Spectrum of Intensity Fluctuations

The power spectrum  $F_I(\nu)$  of intensity fluctuations is defined as the Fourier transform of the autocorrelation function  $R_{\Delta I}(t)$  of intensity fluctuations:

$$F_I(\nu) = \int_{-\infty}^{\infty} R_{\Delta I}(t) e^{-j2\pi\nu t} dt \quad (4.13)$$

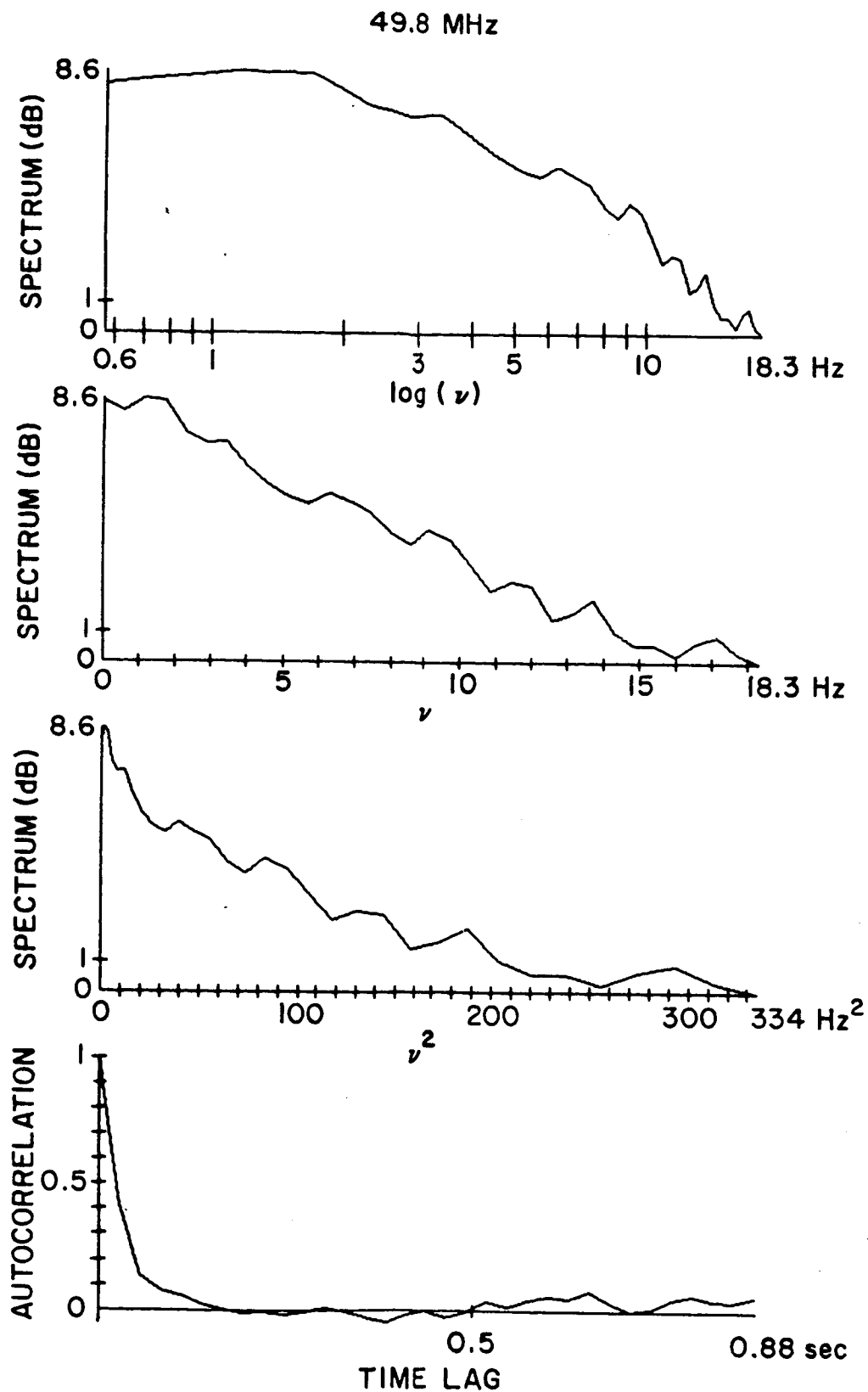
Let  $\hat{F}_I(\nu)$  denote the estimate of  $F_I(\nu)$  using the Blackman-Tukey method. Appendix G describes the computational procedure of  $\hat{F}_I(\nu)$  in detail. Also included in Appendix G are (1) some general considerations of estimating  $F_I(\nu)$  in practical situations and (2) discussions on the stability and confidence limits of power-spectrum estimates.

Figures 4.7a through e illustrate several estimated power spectra  $\hat{F}_I(\nu)$  of intensity fluctuations along with their inverse Fourier transforms: the autocorrelation functions  $R_{\Delta I}(t)$  of intensity fluctuations. A complete set of such plots for all of our IPS data may be found in Chang et al. (1975). Each spectrum in dB is plotted versus three distinct scales:  $\log \nu$ ,  $\nu$ , and  $\nu^2$ , thereby facilitating one to visually differentiate among the three distinct models: power law, exponential, and Gaussian, respectively [see (2.52)]. If the spectrum follows the power law (exponential, or Gaussian) model, then it should appear as a straight line when plotted in dB versus  $\log \nu$  ( $\nu$ , or  $\nu^2$ ). From a visual inspection of all the spectra, it is the authors' impression that most of the spectra fall into two categories: 1) power law, when scintillations are weak, moderate, or strong, and 2) exponential, when scintillations are "very strong."



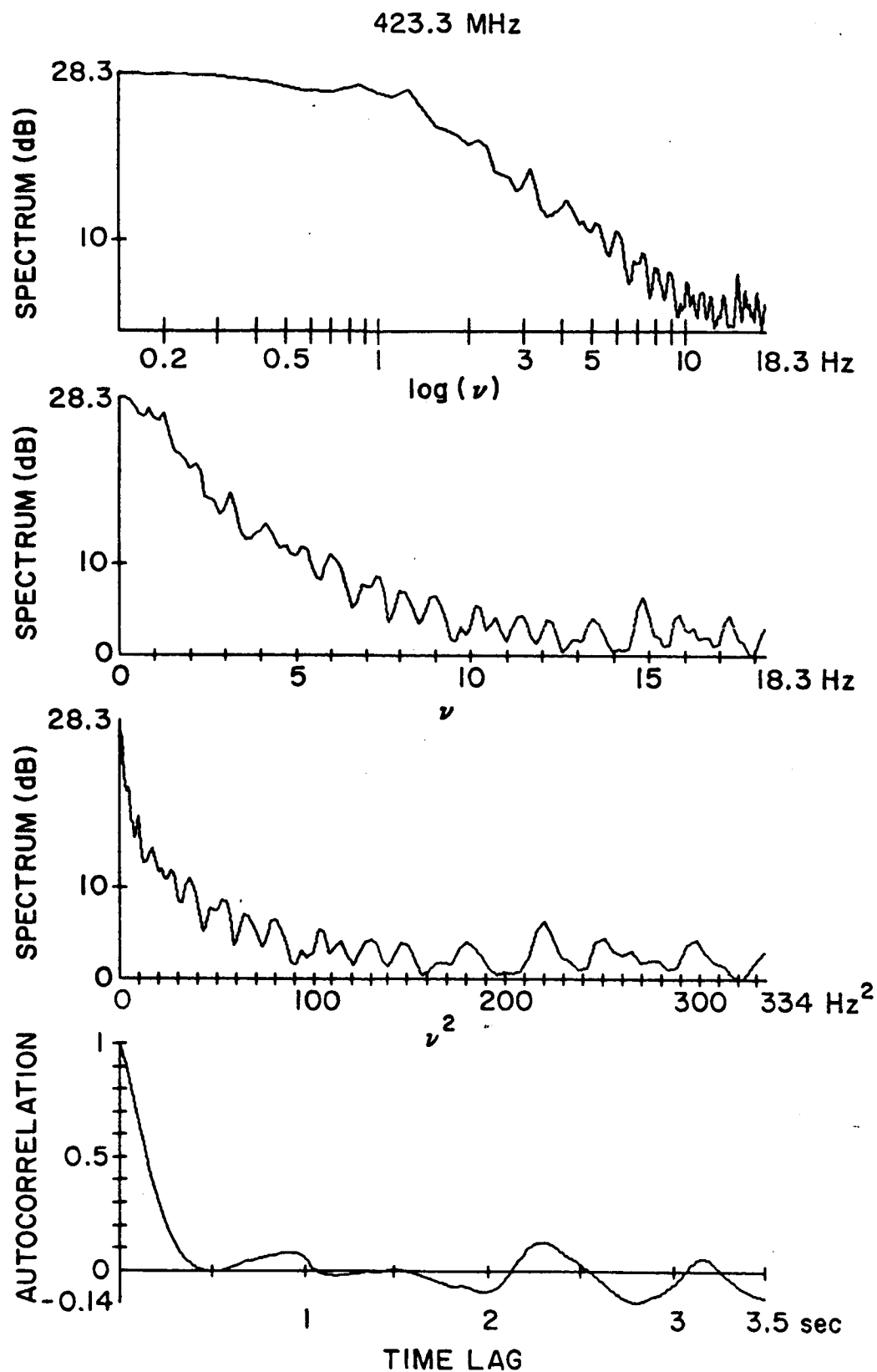
a. 29 Aug 1970,  $\rho = 0.38$  A.U.

Fig. 4.7. EXAMPLES OF POWER SPECTRUM (VS THREE DIFFERENT SCALES) AND AUTOCORRELATION FUNCTION OF INTENSITY FLUCTUATIONS.



b. 8 Feb 1971,  $\rho = 0.13$  A.U.

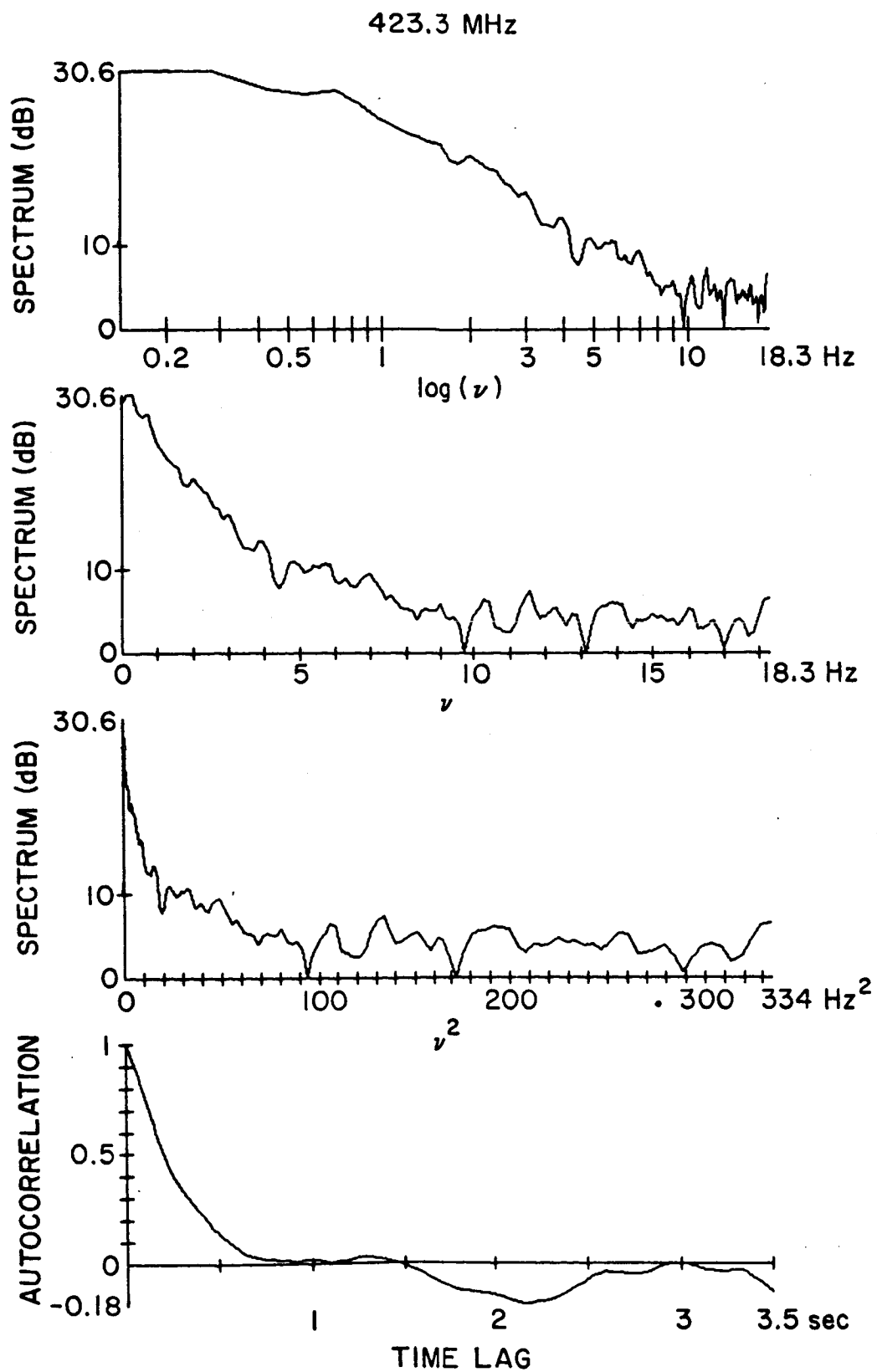
Fig. 4.7. CONTINUED.



c. 13 May 1971,  $\rho = 0.14$  A.U.

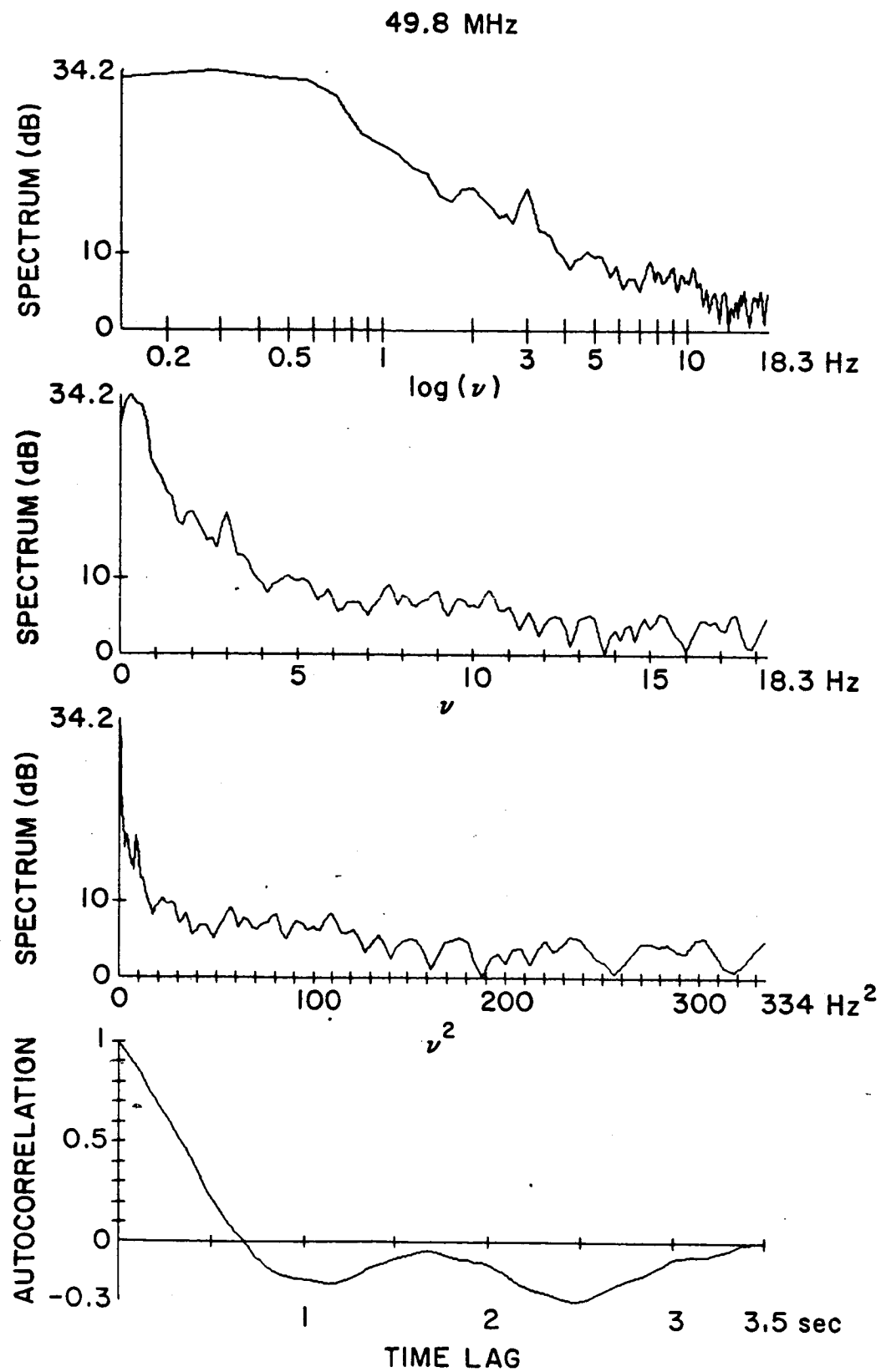
Fig. 4.7. CONTINUED.





d. 7 July 1971,  $\rho = 0.17$  A.U.

Fig. 4.7. CONTINUED.



e. 23 May 1972,  $\rho = 0.65$  A.U.

Fig. 4.7. CONTINUED.

On the basis of least-square fitting, a quantitative approach (which is more objective than the visual inspection) to the differentiation among the three models will be presented in the next section. It is interesting to note first that the result concluded from such an approach essentially corroborates the impression acquired by the visual inspection.

#### D. Linear and Quadratic Regressions of the Estimated Power Spectra on Three Distinct Scales

##### 1. Determination of the Fitting Regions

As just briefly mentioned, the principal purpose of this section is to develop a quantitative approach to testing which one of the three proposed power-spectrum models describes best our estimated scintillation spectra. The basic idea is fairly simple: Perform regressions on least-squares fits of each estimated spectrum on three different scales (namely,  $\log v$ ,  $v$ , and  $v^2$ ) and then decide which fit (and hence which model) is the best by comparing the fitting parameters. Since each estimated spectrum  $\hat{F}_I(v)$  is always available for  $v = 0$  to  $18.3 \text{ Hz}^+$ , one of the major practical problems in applying this idea is to determine over what frequency region the regression should be fulfilled. In other words, what is the "fitting region?" Furthermore, for a given  $\hat{F}_I(v)$ , should this region be different for regressions on different scales?

---

<sup>+</sup> Recall that 18.3 Hz is the fold-over frequency or the highest resolvable frequency at the sampling rate 36.6 samples/sec.

According to the theoretical derivations in Chapter II, the fitting region should start from the Fresnel frequency

$$v_f = U/\sqrt{\pi\lambda z} \quad (4.14)$$

where  $U$  = solar wind velocity (4.15)

and  $\sqrt{\lambda z}$  = radius of the first Fresnel zone (4.16)

Even though under the thin-screen approximation,  $\sqrt{\lambda z}$  is fixed and can be calculated from the geometry of the experiment,  $v_f$  is still unknown for lack of knowledge of  $U$ . A lower bound on  $v_f$  and hence on the fitting region,  $v_m$ , however, may be established by adopting 300 km/sec [which seems to be a reasonable choice in view of the data presented by Armstrong and Coles (1972) and Neugebauer (1974)] as the lowest possible value of  $U$ :

$$v_m = \frac{300}{\sqrt{\pi\lambda z}} \quad (4.17)$$

For most Format D data,  $\sqrt{\lambda z} \approx 650$  km at 49.8 MHz and 200 km at 423.3 MHz, giving rise to the lower bounds on the fitting regions

$$v_m^{\ell} \approx 0.26 \text{ Hz} \quad (4.18)$$

and

$$v_m^h \approx 0.78 \text{ Hz} \quad (4.19)$$

respectively.

Turning now to the high-frequency end of the estimated power spectrum, an examination of all the available power-spectrum plots reveals that after a certain frequency, say  $\gamma$ , up to 18.3 Hz,  $\hat{F}_I(v)$  usually fluctuates around a constant level with a spread approximately equal to the 90% confidence limits given in Table G.2. The general trend of  $\gamma$

looks to be very interesting: The faster or, almost equivalently, the stronger the scintillations, the larger the value of  $\gamma$  (which varies from about 5 Hz for weak scintillations to about 15 Hz for very strong scintillations). Therefore,  $\gamma$  may be thought of as the frequency after which the "signal" (i.e., the intensity fluctuation due purely to IPS) is of comparable magnitude with the background noise,<sup>†</sup> and the region  $[\gamma, 18.3 \text{ Hz}]$  (defined as from  $\gamma$  to 18.3 Hz) may be regarded as the "noise region."

Although for a given  $\hat{F}_I(\nu)$ , the beginning frequency  $\gamma$  of the noise region is often discernible, it cannot be utilized directly as the end frequency of the fitting region because there sometimes exists a small, noise-like region  $[\beta, \gamma]$ , called the transition region, immediately before the noise region such that it would be more appropriate to choose  $\beta$  rather than  $\gamma$  as the end frequency of the fitting region (see, e.g., the bottom figure of Fig. 4.8). The difficulty is that for a given  $\hat{F}_I(\nu)$  plotted in dB versus  $\nu$ ,  $\nu^2$ , and  $\log \nu$ , the transition region and hence the value of  $\beta$  in Hz appears to be different from one plot to another (see, e.g., Figs. 4.8 and 4.9). In order to give each plot and hence each model a fair regression test, it is therefore concluded that the fitting regions should be picked out separately for regressions on different scales.

For simplicity of notation, define

$$Y = 10 \log_{10} \hat{F}_I(\nu) \quad (4.20)$$

$$X_1 = \log_{10} \nu \quad (4.21)$$

<sup>†</sup> Possible sources of this background noise include: 1) the instability of the phase-locked loop receiver when the input signal strength is very weak, 2) the quantization effect resulting from the A/D conversion in the spacecraft telemetry system, 3) the residual noise arising from imperfect data clean-up, 4) the aliasing effect, 4) the leakage error, and 6) the intrinsic variability of the power-spectrum estimate.

$$x_2 = v \quad (4.22)$$

$$x_3 = v^2 \quad (4.23)$$

$$\begin{aligned} \bar{N}_b &= \text{averaged background noise level} \\ &= \text{average of } \hat{F}_I(v) \text{ over the noise region} \\ &\quad [Y, 18.3 \text{ Hz}] \end{aligned} \quad (4.24)$$

and let  $[\alpha_1, \beta_1]$ ,  $[\alpha_2, \beta_2]$ , and  $[\alpha_3, \beta_3]$  denote the three fitting regions to be found for a given  $Y$ . Then, any one of these three regions, say  $[\alpha_i, \beta_i]$  ( $i = 1, 2$ , or  $3$ ), may be determined in accordance with the following steps. To help the reader understand these steps, two practical examples are shown in Figs. 4.8 and 4.9.

1. Examine the plot of  $Y(X_i)$ , i.e.,  $Y$  as a function of  $X_i$ . Estimate  $[\hat{\alpha}_i, \hat{\beta}_i]$ .
2. Fit, in the least-squares sense, a linear function  $\hat{Y}(X_i)$  to  $Y(X_i)$  over the estimated region  $[\hat{\alpha}_i, \hat{\beta}_i]$ . This linear function appears as a straight line in Figures 4.8 and 4.9.
3. The end of the fitting region,  $\beta_i$ , is the frequency at which the height of this straight regression line dips below  $\bar{N}_b$ .
4. The beginning of the fitting region,  $\alpha_i$ , is the lowest frequency satisfying both of the following requirements:
  - a)  $\alpha_i \geq v_m$  (Recall that  $v_m$  is the theoretical lower bound on the fitting region.)
  - b) All  $Y(X_i)$ 's between  $\alpha_i$  and  $\hat{\alpha}_i$  lie within a belt of width  $2\hat{S}$  above and below the regression line,  $\hat{S}$  being the "standard error of the predicted  $Y$ " [Snedecor and Cochran (1967)]

## 2. Testing the Power-Spectrum Forms via Linear and Quadratic Regressions

Once the three fitting regions  $[\alpha_1, \beta_1]$ ,  $[\alpha_2, \beta_2]$ , and  $[\alpha_3, \beta_3]$  of a given  $Y$  are determined, the next question is to decide how many

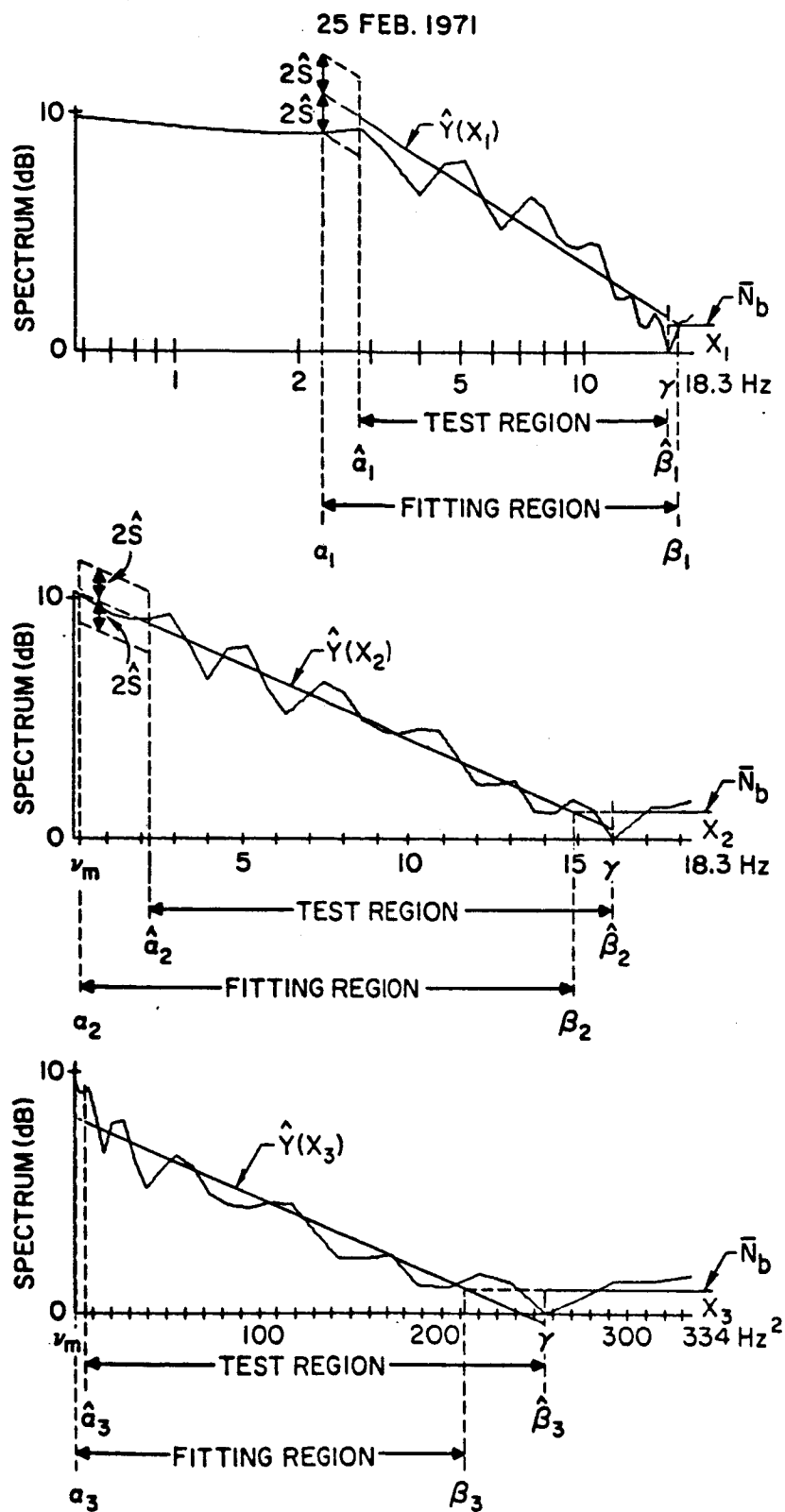


Fig. 4.8. ANOTHER EXAMPLE ILLUSTRATING THE PROCEDURE OF DETERMINING THE FITTING REGIONS.

18 FEB. 1971

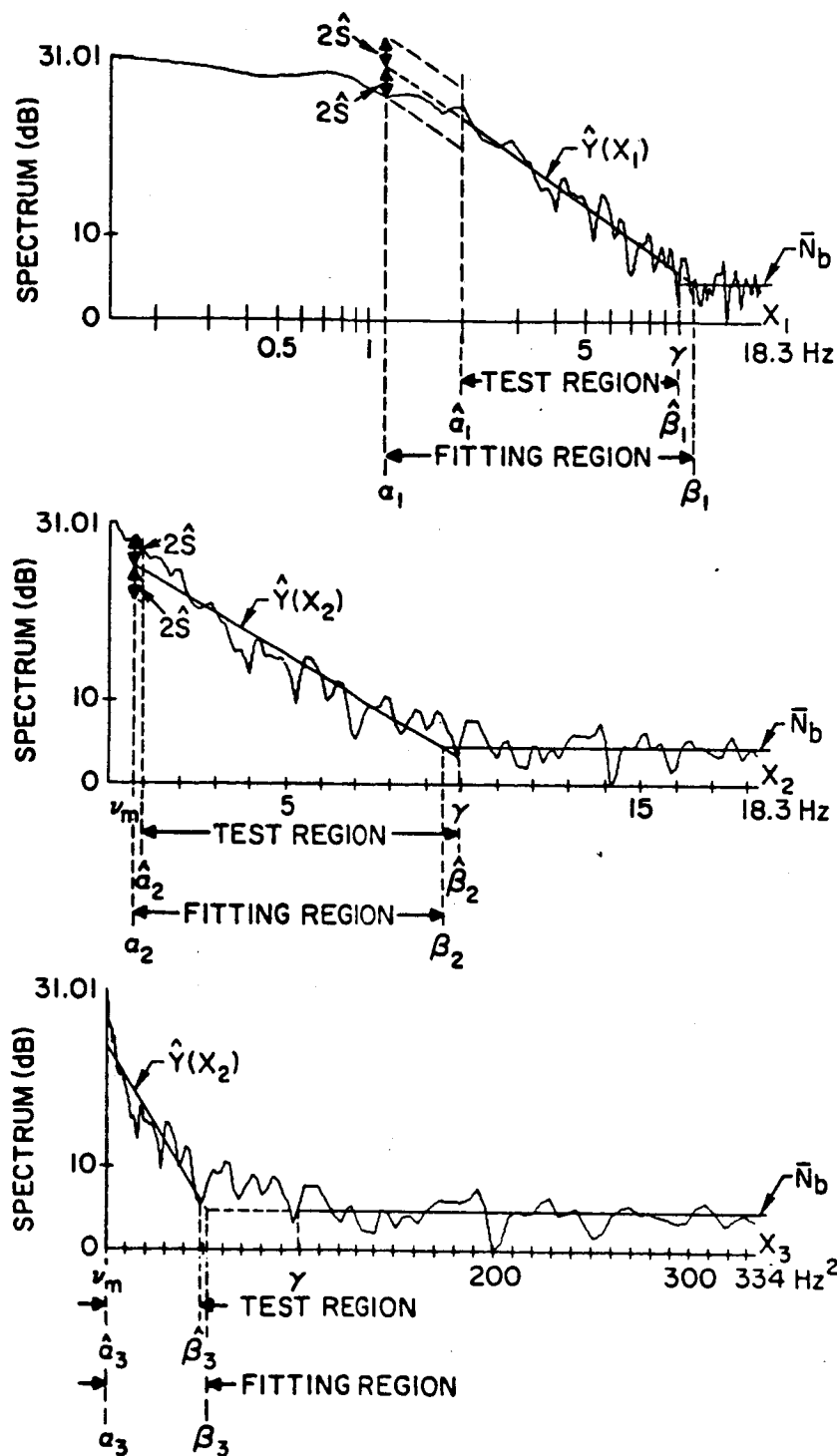


Fig. 4.9. AN EXAMPLE ILLUSTRATING THE PROCEDURE OF DETERMINING THE FITTING REGIONS.



regressions (e.g., linear regression, quadratic regression, etc.)<sup>†</sup> are needed for each plot of  $Y$  versus  $X_i$  such that the resultant regression parameters can be compared to deduce which of the three models fits the given  $Y$  best.

To find a reasonable answer for the above question, consider the case when the  $i^{\text{th}}$  model (let  $i = 1, 2$ , and  $3$  correspond to the power-law, the exponential, and the gaussian models, respectively) describes the given  $Y$  best. Then  $Y$  against  $X_i$  would appear as the most linear and the least curved among the three plots (see Sec. II.F). In addition, it would tend to have the smallest standard (or root-mean-square) deviation from linear regression when compared with the other two. Therefore, the test of power-spectrum forms may be regarded as a procedure consisting mainly of evaluations and comparisons of three types of measurements: 1) standard deviation from linear regression, 2) linearity of  $Y(X_i)$ , and 3) curvature of  $Y(X_i)$ . In what follows, each of these three types of measurements will be discussed separately. Also, for simplicity of notation,  $X$  will from now on be used to represent  $X_i$  (where  $i = 1, 2$ , or  $3$ ) so long as it does not create confusion.

First of all, let  $\hat{Y}(X)$  designate the straight line that fits  $Y(X)$  in least-squares sense over the fitting region bounded by  $X = X_\alpha$ , and  $X = X_\beta$ , where  $X_\alpha$  and  $X_\beta$  are defined as the values of  $X$  [see (4.21)-(4.23)] for frequency  $\nu = \alpha$  and  $\beta$  respectively. Then, like Eq. (4.28), the standard deviation  $\sigma$  from linear regression is given by

$$\sigma = \sqrt{\frac{\sum (Y - \hat{Y})^2}{n-2}} \quad (4.25)$$

<sup>†</sup> Theoretically, for a set of  $N$  arbitrary points, it is possible to fit a polynomial of degree  $N-1$  through all these points exactly; however, for the purpose of distinguishing among the three different models, the coefficients of high-order terms (presumably,  $N \gg 1$ ) would have doubtful significance.

where  $n$  is the total number of the  $(X,Y)$  points in the fitting region, and  $\Sigma$  denotes the summation over the fitting region. Because  $\sigma$  is an estimate of the overall error in fitting a straight line, smaller values of  $\sigma$  correspond to better fits of  $Y(X)$  by a straight line.

Secondly, the linearity of  $Y(X)$  (or of the relationship between  $Y$  and  $X$ ) is conventionally measured via the linear correlation coefficient  $\rho$  defined as

$$\rho = \frac{\Sigma xy}{\sqrt{\Sigma x^2 \Sigma y^2}} \quad (4.26)$$

where  $x = X - \bar{X}$ ,  $y = Y - \bar{Y}$ , and  $\bar{X}$  and  $\bar{Y}$

are the mean values of  $X$  and  $Y$ . The absolute magnitude of  $\rho$  ranges from 0, when there is no correlation, to 1, when there is complete correlation [or equivalently, when  $Y(X)$  is a straight line]. The closer the value of  $|\rho|$  to 1, the more linear the relationship between  $Y$  and  $X$ .

The third type of measurement has to do with measuring the curvature of  $Y(X)$ . Since we are interested only in the general trend, not in the detailed structure, of  $Y(X)$ , such a trend can be reasonably sensed by fitting a quadratic function  $\tilde{Y}$  of  $X$  to  $Y(X)$  in least-squares sense over the fitting region  $[X_\alpha, X_\beta]$ :

$$\tilde{Y} = aX^2 + bX + c \quad (4.27)$$

Then, the normalized curvature of  $\tilde{Y}(X)$  defined by

$$F = \frac{(X_\beta - X_\alpha)^2}{\tilde{Y}(X_\beta) - \tilde{Y}(X_\alpha)} \cdot \frac{d^2 \tilde{Y}}{dX^2} = \frac{2a(X_\beta - X_\alpha)^2}{\tilde{Y}(X_\beta) - \tilde{Y}(X_\alpha)} \quad (4.28)$$

may be considered as a measure of the curvature of  $Y(X)$ . Note that the  $(X_\beta - X_\alpha)^2 / [\tilde{Y}(X_\beta) - \tilde{Y}(X_\alpha)]$  factor in Eq. (4.28) is just a normalization factor to correct the difference of the value of  $F$  caused by differences of the fitting regions.

Founded on the above discussions, the procedure of the regression test on the power-spectrum forms for a given  $Y$  is as follows:

1. Fit, in least squares sense,  $\hat{Y}(X_i)$  (a linear function of  $X_i$ ) and  $\tilde{Y}(X_i)$  (a quadratic function of  $X_i$ ) to  $Y(X_i)$  over the fitting region  $[\alpha_i, \beta_i]$  for  $i = 1, 2$ , and  $3$ .
2. Compute, for each  $i$ , 1) the standard deviation from linear regression,  $\sigma_i$ , 2) the linear correlation coefficient,  $\rho_i$ , and 3) the normalized curvature of  $\tilde{Y}(X_i)$ ,  $F_i$ .

3. Perform three tests:

Test No. 1: the  $i^{\text{th}}$  ( $i = 1, 2$ , or  $3$ ) model wins this test if  $\sigma_i$  is the smallest among  $\sigma_1, \sigma_2$ , and  $\sigma_3$ .

Test No. 2: the  $i^{\text{th}}$  model wins this test if  $|\rho_i|$  is the largest (or the closest to 1) among  $|\rho_1|, |\rho_2|$ , and  $|\rho_3|$ .

Test No. 3: the  $i^{\text{th}}$  model wins this test if  $|F_i|$  is the smallest among  $|F_1|, |F_2|$ , and  $|F_3|$ .

The  $i^{\text{th}}$  model is claimed to fit a given spectrum best if it wins two or all of the three tests. Applying these three tests to a total of 149 spectra, the results indicate that for a given spectrum if one model is the winner of one test, then usually this model is also

(1) the winner of the two other tests

or

(2) the winner of one of the two other tests

Case (1) above (viz., one model wins unanimously all three tests for a given spectrum) happens to 119 ( $\approx 80\%$ ) of 149 spectra tested, implying that the three tests, although different, are consistent for most spectra. Case (2) above happens to 29 ( $\approx 19\%$ ) of 149 spectra tested. There are only 2 spectra out of 149 tested that could not be described by either Cases (1) or

(2) (viz., three tests are won by three different models), and the spectral forms of these two spectra are regarded as indeterminate.

4. For each best fit determined from Step 3 above, record the height difference  $\Lambda$  of the linear regression line  $\hat{Y}$  over the fitting region  $[X_\alpha, X_\beta]$ :

$$\Lambda = \hat{Y}(X_\alpha) - \hat{Y}(X_\beta) \text{ dB} \quad (4.29)$$

The physical meaning of  $\Lambda$ , called the spectrum signal-to-noise ratio or the maximum ratio of the signal spectrum to to the noise spectrum, will be discussed in Sec. D.3.

5. Record the slope  $\mathcal{P}'$  of the linear regression line for cases when the power-law model is the best fit. Note that  $\mathcal{P}'$  is related to  $p'$ , the estimated value of the true power-law exponent  $p$ , via (Sec. II.D)

$$p' = \mathcal{P}' + 1 \quad (4.30)$$

To illustrate, Figs. 4.10 and 4.11 show the linear regression lines and the quadratic regression curves derived from the above procedure over the fitting regions. Also shown are the values of  $\sigma_i$ ,  $\rho_i$ , and  $F_i$  for  $i = 1, 2$ , and  $3$ . Finally, as a supplementary point it was observed that throughout the course of relatively weak interplanetary scintillations, residual antenna and noise (including solar and cosmic noise) patterns arising from imperfect data clean-up may occasionally become visible in the estimated spectra as a prominent peak around 3 Hz. A good example of these 3-Hz peaks is the one manifested in Fig. 4.7e. In order to avoid errors in regression tests which might be introduced by such a spurious peak, a special feature has been added to the computer program that implements all the regression-test procedures described in the previous and the present subsections such that this peak, once identified, can be ignored during both the determination of the fitting regions and the testing of the power-spectrum forms.

18 FEB. 1971

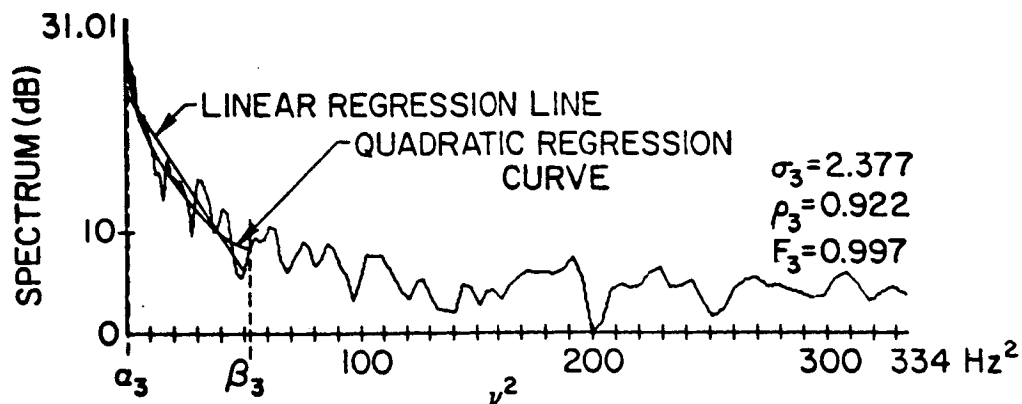
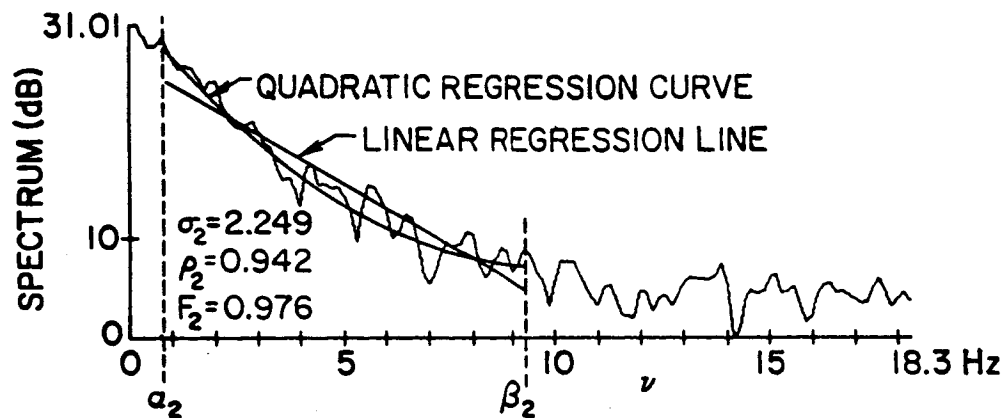
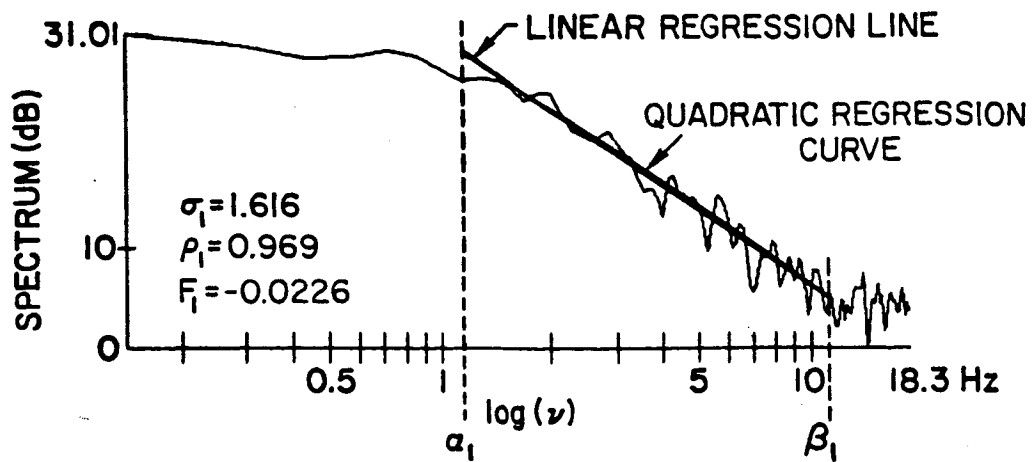


Fig. 4.10. AN EXAMPLE SHOWING THE LINEAR REGRESSION LINES AND QUADRATIC REGRESSION CURVES OVER THE THREE FITTING REGIONS.

25 FEB. 1971

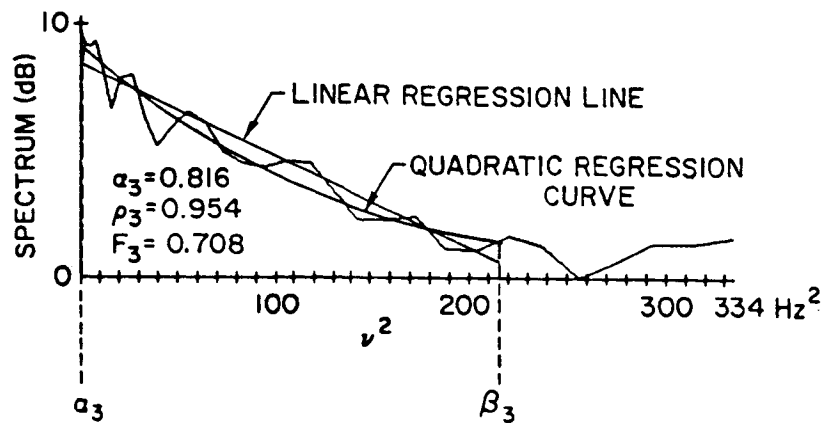
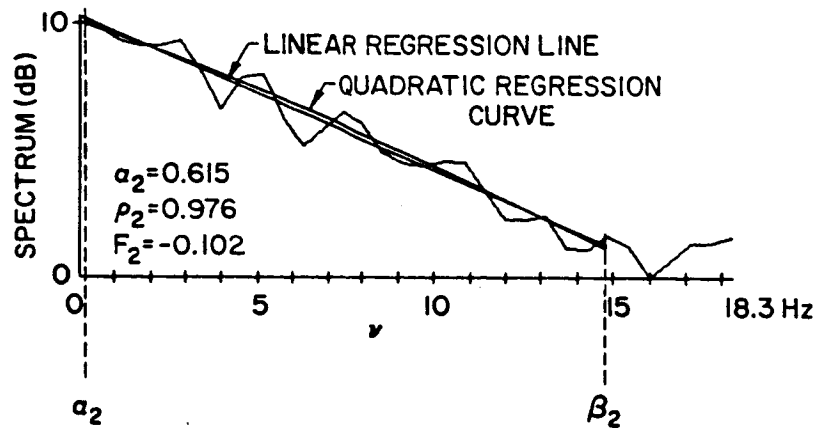
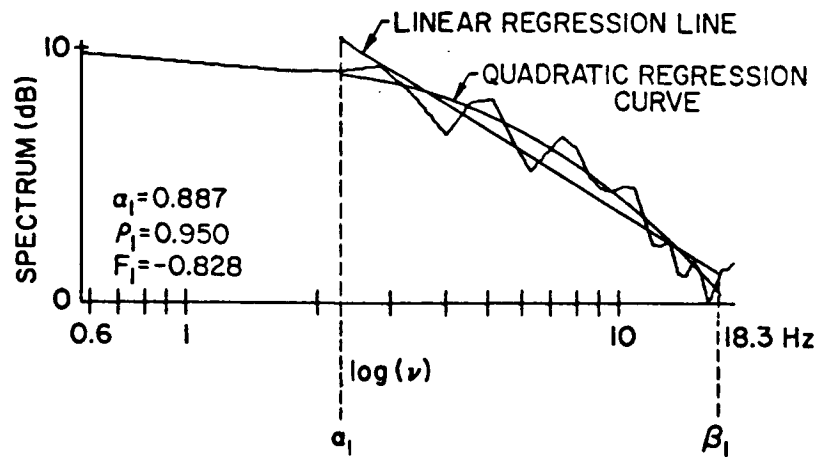


Fig. 4.11. ANOTHER EXAMPLE SHOWING THE LINEAR REGRESSION LINES AND QUADRATIC REGRESSION CURVES OVER THE THREE FITTING REGIONS.

### 3. Spectrum Signal-to-Noise Ratio $\Lambda$

This subsection is devoted to develop the concept and definition of a quantity that will be utilized frequently in the next chapter. This quantity is called  $\Lambda$ , the spectrum signal-to-noise ratio or the maximum ratio of the signal spectrum to the noise spectrum. As will be seen soon, it is a measure of the reliability of the observed power spectrum. First of all, recall that all observed spectra are contaminated by some unwanted noise as evidenced by the existence of the background noise at their ends (see, for example, Fig. 4.8). Secondly, recall from Secs. III.D and III.F that voltage is being measured and then converted to power by a calibration curve. Define the signal  $\Delta I(t)$  here as the zero-mean intensity fluctuations caused purely by IPS:

$$\Delta I(t) = I(t) - \bar{I} \quad (4.31)$$

If the background noise  $N(t) = \Delta N(t) + \bar{N}$  is additive with mean  $\bar{N}$ , then the observed intensity is the sum of  $I(t)$  and  $N(t)$ :

$$R(t) = I(t) + N(t) = \Delta I(t) + \bar{I} + \Delta N(t) + \bar{N} \quad (4.32)$$

with mean 
$$\bar{R} = \bar{I} + \bar{N} \quad (4.33)$$

Assuming that  $\Delta I(t)$  and  $\Delta N(t)$  are statistically independent, then the autocovariance function  $A_R(\tau)$  of  $R(t)$  is

$$\begin{aligned} A_R(\tau) &= \overline{[R(t) - \bar{R}(t)] [R(t+\tau) - \bar{R}(t+\tau)]} \\ &= \overline{[\Delta I(t) + \Delta N(t)] [\Delta I(t+\tau) + \Delta N(t+\tau)]} \\ &= \overline{\Delta I(t)\Delta I(t+\tau)} + \overline{\Delta I(t)\Delta N(t+\tau)} + \overline{\Delta N(t)\Delta I(t+\tau)} \end{aligned}$$

$$= \overline{\Delta N(t) \Delta N(t+\tau)}$$

$$= A_I(\tau) + A_N(\tau) \quad (4.34)$$

$$\text{because} \quad \overline{\Delta N(t)} = 0 \quad (4.35)$$

$$\text{and} \quad \overline{\Delta I(t) \Delta N(t+\tau)} = \overline{\Delta I(t)} \cdot \overline{\Delta N(t+\tau)} = 0 \quad (4.36)$$

$$\overline{\Delta N(t) \Delta I(t+\tau)} = \overline{\Delta N(t)} \cdot \overline{\Delta I(t+\tau)} = 0 \quad (4.37)$$

Fourier transforming both sides of (4.34) leads to

$$F_R(\nu) = F_I(\nu) + F_N(\nu) \quad (4.38)$$

Therefore, each observed power spectrum  $F_R(\nu)$  is indeed the sum of (1) the desired power spectrum  $F_I(\nu)$  of the signal (or the intensity) fluctuation caused purely by IPS and (2) the power spectrum  $F_N(\nu)$  of the background noise. Clearly, the larger the noise spectrum  $F_N(\nu)$  compared with the signal spectrum  $F_I(\nu)$ , the more distorted the form of the observed spectrum  $F_R(\nu)$  from  $F_I(\nu)$ . To find a reasonable measure of such a distortion, we consider the ideal case when the samples of the noise  $N(t)$  at sampling instants  $t=0, \tau', 2\tau', \dots$  are uncorrelated.<sup>†</sup> Then

$$F_N(\nu) = \bar{N}_b \quad \text{for} \quad |\nu| \leq \frac{1}{2\tau'} = 18.3 \text{ Hz} \quad (4.39)$$

and the maximum ratio  $\Lambda$  of the signal spectrum  $F_I(\nu)$  to the noise spectrum  $N_b$  is approximately equal to the height difference of the linear regression line fitted to  $Y(X) [= F_R(\nu) \text{ in dB}]$  over the fitting region  $[X_\alpha, X_\beta]$ :

<sup>†</sup> This assumption appears to be true at least for the quantization noise introduced during A/D conversion.



$$\Lambda \approx \hat{Y}(X_\alpha) - \hat{Y}(X_\beta) \quad \text{dB} \quad (4.40)$$

as given earlier in (4.29). Larger values of  $\Lambda$  correspond to smaller values of the noise spectrum compared with the signal spectrum, implying that the observed spectrum is more reliable (or closer to the true signal spectrum); consequently,  $\Lambda$  may be thought of as a measure of the reliability of the observed spectrum.

#### E. Scintillation Index

From Sec. II.H, the scintillation index  $m$  is defined as the normalized standard deviation of the signal intensity  $I(t)$ :

$$m = \frac{\sqrt{\overline{I^2} - \bar{I}^2}}{\bar{I}} = \frac{\sqrt{(\Delta I)^2}}{\bar{I}} = \frac{\sigma_I}{\bar{I}} \quad (4.41)$$

where

$$\Delta I(t) = I(t) - \bar{I} \quad (4.42)$$

is the zero-mean, intensity fluctuation caused purely by IPS and

$$\sigma_I = \sqrt{(\Delta I)^2} \quad (4.43)$$

is the standard deviation of  $I(t)$ . Again, since the observed intensity  $R(t)$  is the sum of  $I(t)$  and some unwanted noise  $N(t)$ :

$$R(t) = I(t) + N(t) \quad (4.44)$$

Following the noise model presented in Sec. D.3 and considering

$\tau = 0$  for (4.34) gives rise to

$$\sigma_R^2 = \sigma_I^2 + \sigma_N^2 \quad (4.45)$$

Because of the two following reasons:

- (1) Both the quantization error and the system instability increase sharply as  $I(t)/T$  decreases. Here,  $T$  is the total received noise temperature given by (3.15) and is relatively constant in comparison with the systematic decrease of  $\bar{I}$  when the Pioneer 9 spacecraft moves away from the earth.
- (2) For most of our Format D data, the above two effects are dominant sources of the additive noise  $N(t)$ .

it is supposed (and later verified by experimental data) that  $\sigma_N^2$  is a function of  $\bar{I}$ ,

$$\sigma_N^2 = \sigma_N^2(\bar{I}) \quad (4.46)$$

Dividing (4.45) by  $\bar{I}^2$  and making use of (4.41) yields

$$\frac{\sigma_R^2}{\bar{I}^2} = \frac{\sigma_I^2}{\bar{I}^2} + \frac{\sigma_N^2(\bar{I})}{\bar{I}^2} \quad (4.47)$$

and

$$m^2 = m_R^2 - C(\bar{I}) \quad (4.48)$$

where  $m_R$  = scintillation index of the observed intensity  $R(t)$

$$C(\bar{I}) = \frac{\sigma_N^2(\bar{I})}{\bar{I}^2} = \text{correction factor for } m^2 = \text{a function of } \bar{I} \text{ only}$$

Based upon a large body of Format D data collected during the calibration experiment, the validity of (4.48) was checked to be quite satisfactory

especially for the 423.3 MHz channel. The correction factors thus acquired for the 49.8 and the 423.3 MHz channels are plotted versus  $\bar{I}$  in Figs. 4.12 and 4.13, respectively.

Observing the calibration curves given in Fig. 3.7 reveals that Format D data equal to 5 correspond to the lowest detectable  $(S/N)_i$ 's (input signal-to-noise ratios) for both channels. Stated another way, when a Format D datum 5 is received, it means that the  $(S/N)_i$  could be any value lower than about -30 dB for the 49.8 MHz channel or could be any value lower than about -26 dB for the 423.3 MHz channel (Fig. 3.7). Because of this uncertainty, only the upper limit  $m_{RU}$  and the lower limit  $m_{RL}$  on  $m_R$  are obtainable. The upper and lower limits can be derived by setting the input signal-to-noise power ratio  $(S/N)_i$  associated with Format D datum 5 equal to its minimum possible value ( $-\infty$  dB for both channels) and its maximum possible value (-30 dB for the 49.8 MHz channel or -26 dB for the 423.3 MHz channel), respectively. Substituting  $m_{RU}$  and  $m_{RL}$  into (4.48) gives rise to the upper limit  $m_U$  and the lower limit  $m_L$  on scintillation index  $m$ :

$$m_U^2 = m_{RU}^2 - C(\bar{I}) \quad (4.49)$$

$$m_L^2 = m_{RL}^2 - C(\bar{I}) \quad (4.50)$$

With the aid of (4.49), (4.50), and Figs. 4.12 and 4.13, lower and upper limits on scintillation index have been computed for all available data and plotted against various physical parameters of interest.

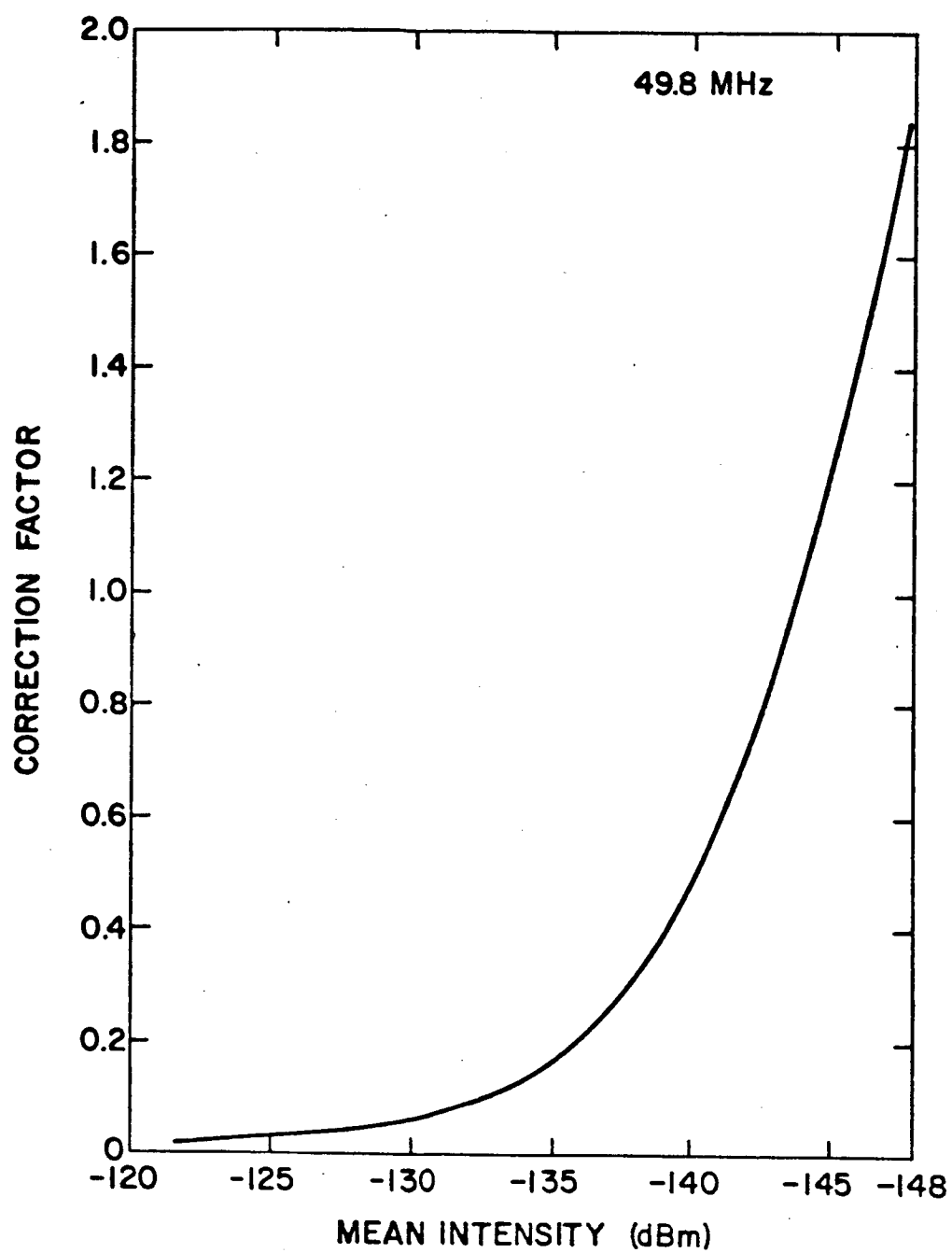


Fig. 4.12. CORRECTION FACTOR OF  $m^2$  FOR THE 49.8 MHz CHANNEL.

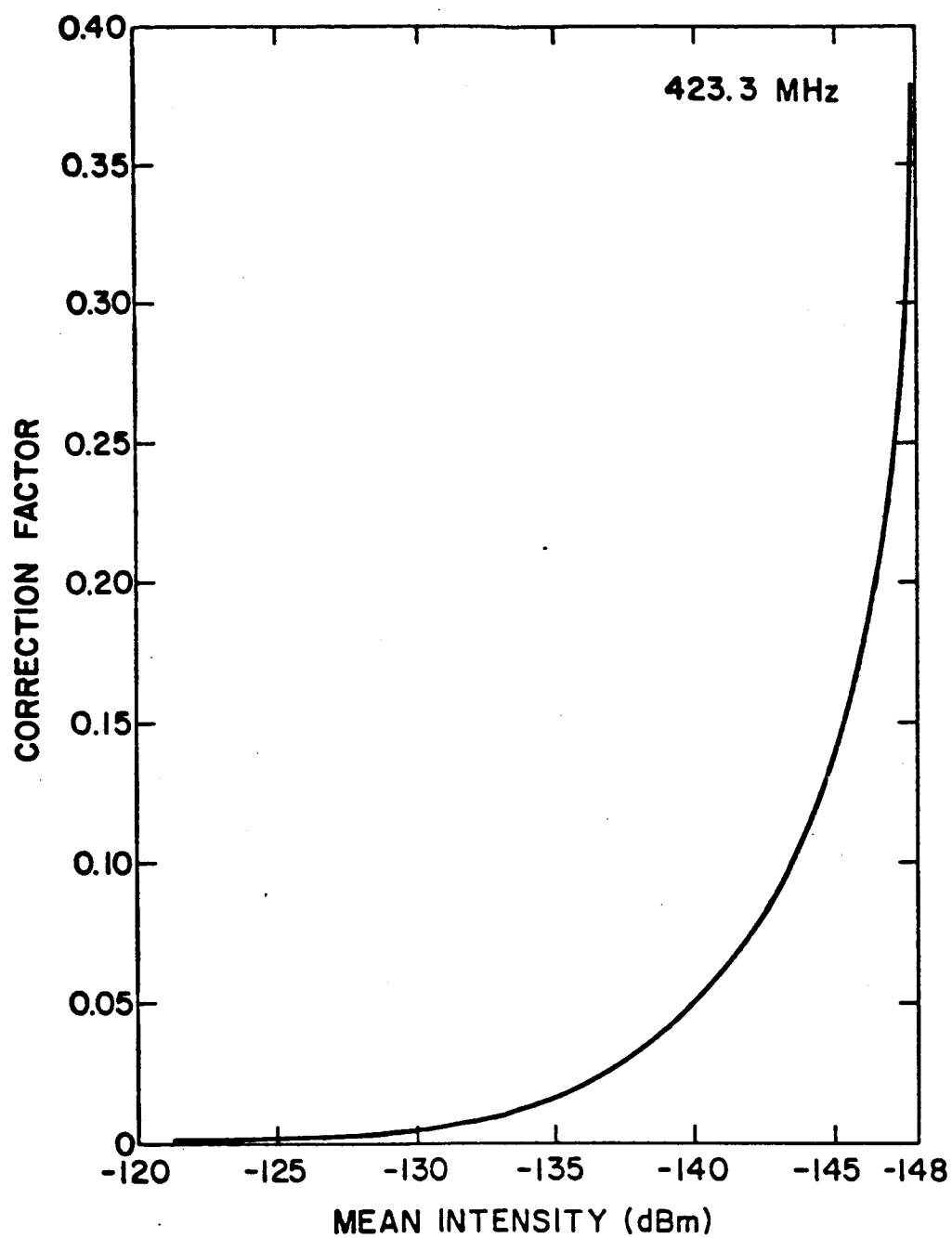


Fig. 4.13. CORRECTION FACTOR OF  $m^2$  FOR THE 423.3 MHz CHANNEL.

## Chapter V

### RESULTS AND INTERPRETATIONS

The results of our interplanetary scintillation experiment derived from the procedure of data reduction given in Chapter IV will be presented and interpreted in this chapter. It will be shown that the observed temporal spectra of intensity fluctuations (and hence the spatial power spectrum  $F_n(q)$  of interplanetary electron-density fluctuations) cannot be of a gaussian form. In addition to the well-known weak and strong scattering regimes, our data appear to suggest that there exists a third scattering regime, called the very strong scattering regime. While more than 80% of the observed scintillation spectra in the weak and strong scattering regimes follow a power-law variation with mean exponent  $\bar{p} \approx 3.5 \pm 0.13$  and standard deviation  $\sigma_p \approx 0.3$ , the shape of the observed scintillation spectra becomes exponential in the very strong scattering regime. Details of these results will be contained in Section A. Several scintillation spectra on which the Fresnel structure is observable are discussed in Section B. Section C shows that the apparent scale size of the diffraction pattern deduced from the width  $t_w$  of  $A_I(t)$  (the autocorrelation function of intensity fluctuations) is compatible with a power-law spatial spectrum  $F_n(q)$  of electron-density fluctuations. In Section D, the scintillation index is found to be  $\propto \rho^{-1.5}$  in the weak scattering regime, and the interplanetary electron-density fluctuation is shown to be  $\propto \rho^{-2}$ , where  $\rho$  is the proximate distance of the propagation path as defined in Sec. III.A. Section E demonstrates that the scintillation index is directly proportional to the integrated electron content along the propagation path. Further, the deviations

of the scintillation index and the electron content from their means are seen to be strongly correlated.

#### A. Spatial Power Spectrum $F_n(q)$

##### 1. Form of $F_n(q)$

The form of the spatial power spectrum  $F_n(q)$  of interplanetary electron-density fluctuations has been a long-standing, controversial, and vital question in interplanetary scintillation theory: Is it gaussian, exponential, or power-law? [See, for instance, Hewish (1971), Cronyn (1972c), and Matheson and Little (1971) for summaries of the argument.] It is a vital question because both the prediction and the interpretation of the interplanetary scintillation phenomenon depend completely on the form of  $F_n(q)$ .<sup>†</sup> To find out which of the three forms describes our observed spectra best, a regression test on the basis of least-squares fitting was described in Sec. IV.D. The results of this regression test are summarized in Table 5.1. Recall from Sec. IV.D.2 that of 149 spectra tested, only 2 ( $\approx 1\%$ ) are not determinable. All 147 determinable spectra have  $\Lambda \geq 0$  dB and are included in Case 1 in this table. Cases 2, 3, 4, and 5 include only determinable spectra that have  $\Lambda \geq 5, 10, 15$  and  $20$  dB, and the total number of spectra included are 138, 96, 76, and 47, respectively.

As mentioned in Sec. IV.D.3,  $\Lambda$  of a given observed spectrum is a measure of its reliability; therefore, one would expect that individ-

---

<sup>†</sup> For example, according to the gaussian model in the weak scattering regime, the width  $r_w$  of the autocorrelation function of intensity fluctuations is equal to the "intrinsic scale size" of interplanetary electron density fluctuations, whereas according to the power-law model,  $r_w$  is merely a parameter related to the first Fresnel zone of the diffraction geometry and does not reflect a genuine scale in the IPM. [See Hewish (1972) and Sec. II.G.]

Case	$\Lambda$	Total Number of Spectra Included	Models	Percentage		
				50 MHz $\rho < 0.35$ A.U. (Very Strong Scattering Regime)	50 MHz $\rho > 0.35$ A.U. (Weak and Strong Scattering Regimes)	423.3 MHz All $\rho$ (Weak and Strong Scattering Regimes)
1	$\geq 0$ dB	147	Power-Law Exponential Gaussian	15% (= 8/54) 67% (= 36/54) 19% (= 10/54)	84% (= 16/19) 11% (= 2/19) 5% (= 1/19)	88% (= 65/74) 11% (= 8/74) 1% (= 1/74)
2	$\geq 5$ dB	138	Power-Law Exponential Gaussian	13% (= 6/47) 77% (= 36/47) 11% (= 5/47)	84% (= 16/19) 11% (= 2/19) 5% (= 1/19)	89% (= 64/72) 11% (= 8/72) 0%
3	$\geq 10$ dB	96	Power-Law Exponential Gaussian	18% (= 4/22) 77% (= 17/22) 5% (= 1/22)	82% (= 14/17) 12% (= 2/17) 6% (= 1/17)	93% (= 53/57) 7% (= 4/57) 0%
4	$\geq 15$ dB	76	Power-Law Exponential Gaussian	17% (= 2/12) 83% (= 10/12) 0%	88% (= 14/16) 6% (= 1/16) 6% (= 1/16)	96% (= 46/48) 4% (= 2/48) 0%
5	$\geq 20$ dB	47	Power-Law Exponential Gaussian	25% (= 1/4) 75% (= 3/4) 0%	85% (= 11/13) 8% (= 1/13) 8% (= 1/13)	100% (= 30/30) 0% 0%

Table 5.1. PERCENTAGE RESULTS OF REGRESSION TESTS ON THE FORMS OF OBSERVED SCINTILLATION SPECTRA.



ual results in Case 5 are more reliable than those in any other four cases. The three columns under the title "percentage" give the percentage at which each of the three models best fits the observed spectra; for instance, in Case 1, 15% (8 out of 54) of the observed spectra at 50 MHz over  $\rho < 0.35$  A.U. can be fitted best by a power-law model.

It can be seen from these three columns that the power-law model best describes from 88 up to 100% of all the observed spectra at 423 MHz, and more than 82% of all the observed spectra at 50 MHz over  $\rho > 0.35$  A.U. If considering only all spectra that have  $\Delta \geq 20$  dB (Case 5), then 12 out of 17 spectra ( $\approx 71\%$ ) observed at 50 MHz and all 30 (100%) spectra observed at 423 MHz can be explained by a power-law  $F_n(q)$ .

The gaussian model is rejected based upon the percentage results shown in this table. In cases of very strong scintillations the exponential model appears to fit best our observed spectra. During an effort to account for the occurrence of these exponential spectra, three suggestions have emerged:

1. Due to the instrumental noise effects in the very strong scattering regime (50 MHz,  $\rho < 0.35$  A.U.), the received signal strength is normally so weak and fluctuates so rapidly that the 50 MHz receiver is pushed to or beyond its accuracy limit. Insufficient sampling rate, heavy quantization noise, severe instability of the receiver, and the resultant aliasing errors may distort greatly the observed scintillation spectra.
2. Due to the genuine change of the turbulence spectrum form from power-law to exponential around  $\rho = 0.35$  A.U.
3. Owing to the very strong wave scattering phenomenon itself, the form of the spectrum of the radio signal

may be affected in a manner (not presently understood) which is not necessarily an indication that the form of the turbulence spectrum underwent a similar change.

If suggestion (1) were correct, then one would expect the scintillation spectra to be distorted systematically into an exponential form as the spectrum signal-to-noise ratio  $\Lambda$  decreases. As a consequence, one would expect the percentage of the exponential spectrum to decrease monotonically from Case 1 to Case 5 because the instrumental noise effects become less important for spectra having larger values of  $\Lambda$ . The percentage results in Table 5.1 indicate almost the opposite: Case 1 has the lowest percentage (67%) of exponential spectrum. Moreover in the region  $0 < \Lambda < 5$  dB in which the instrumental noise effects are most serious, none of the 7 observed scintillation spectra is exponential. Five of them are gaussian and two are power-law.

Based upon the above reasoning together with the fact that exponential spectra had also been observed previously in the very strong scattering regime by Cohen et al. (1967), Cohen and Gundermann (1969), and Rao et al. (1974), it is therefore concluded that the instrumental noise alone cannot account for the occurrence of these exponential spectra.

At the first glance, suggestion (2) appears to be quite plausible. However, this suggestion can also be ruled out by the following arguments. If the shape of the turbulence spectrum  $F_n(q)$  indeed changed from power-law to exponential around  $\rho = 0.35$  A.U., then not only the 50 MHz spectra but also the simultaneously observed 423 MHz spectra should change from power law to exponential in the region  $\rho < 0.35$  A.U. Regression results indicate that among 56 423-MHz spectra observed over

$\rho < 0.35$  A.U., 53 (= 95%) of them are still power-law. Further evidence contradicting suggestion (2) comes from the multiple-frequency measurements by Cohen and Gundermann (1969), who observed that at higher frequencies the transition into the exponential form occurs at smaller elongations.

It appears therefore that the exponential spectra result from the very strong wave scattering phenomenon itself. No interplanetary wave propagation theory has yet predicted the occurrence of exponential spectra in the very strong scattering regime.

## 2. Power-Law Exponent $p$ of $F_n(q)$

Recall from Sec. IV.D.2 that during those linear regression tests in which observed scintillation spectra were best fitted by the power-law model, the slope  $\varphi'$  of the linear regression line was determined. It was shown in Eq. (4.30) that  $p' = \varphi' + 1$ , where  $p'$  is the estimate of the desired parameter  $p$ , the power-law exponent of  $F_n(q)$ . The means and standard deviations of  $p'$  for all cases are listed in Table 5.2. For instance, in Case 1, there are a total of 89 spectra that can be best fitted by the power-law model; among these, the mean value of  $p'$  is 2.91 and the standard deviation is 0.55. In case 2 there are 86 spectra since we have excluded the three spectra possessing  $\Lambda < 5$  dB. The other three cases are similarly derived subsets of the original 89 spectra.

After comparing the means of  $p'$  for Cases 1-5, it becomes clear that scintillation spectra possessing smaller values of  $\Lambda$  usually exhibit smaller values of  $p'$ . To illustrate this point, the probability distributions, the means (shown by vertical arrows), and the standard deviations  $\sigma_p$ 's of  $p'$  for Cases 1 through 5 are displayed

Case	$\Lambda$	Total No. of Power-Law Spectra Included	$p'$ Power-Law Exponent before Correcting for the Effect of $\Lambda$		$p$ Power-Law Exponent after Correcting for the Effect of $\Lambda$	
			Mean	S.D.	Mean	S.D.
1	$\geq 0$ dB	89	2.91	0.55	3.52	0.46
2	$\geq 5$ dB	86	2.92	0.55	3.49	0.44
3	$\geq 10$ dB	71	3.05	0.47	3.47	0.40
4	$\geq 15$ dB	62	3.13	0.37	3.50	0.35
5	$\geq 20$ dB	42	3.21	0.29	3.52	0.29

Table 5.2. MEANS AND STANDARD DEVIATIONS OF POWER-LAW EXPONENT  $F_n(q)$  BEFORE ( $p'$ ) AND AFTER ( $p$ ) CORRECTING FOR THE EFFECT OF  $\Lambda$ .

in Fig. 5.1. As the criterion for the minimum value of  $\Lambda$  increases successively from one case to another, the population of smaller  $p'$  ( $\leq 2.5$ ) decreases sharply, whereas the population of larger  $p$  ( $\geq 2.5$ ) remains relatively unchanged. As a result, the mean value of  $p'$  increases--while the standard deviation decreases--gradually from Case 2 to Case 5.

An even better way to illustrate the observed decrease of  $p'$  with  $\Lambda$  is to plot all 89 values of  $p'$  versus  $\Lambda$  as presented in Fig. 5.2a. Apparently, there is considerable scatter in  $p'$  from day to day. In Fig. 5.2b the same data are shown averaged over 2.5 dB ranges of  $\Lambda$  in order to reduce the scatter. Also shown under each point is the number of original data from which each of these eleven points is derived. For instance, the point at  $\Lambda = 3.75$  dB represents the average of 3 values of  $p'$  in Fig. 5.2a over the range  $2.5 < \Lambda < 5$  dB. It should be emphasized that because the eleven different points in this figure stand

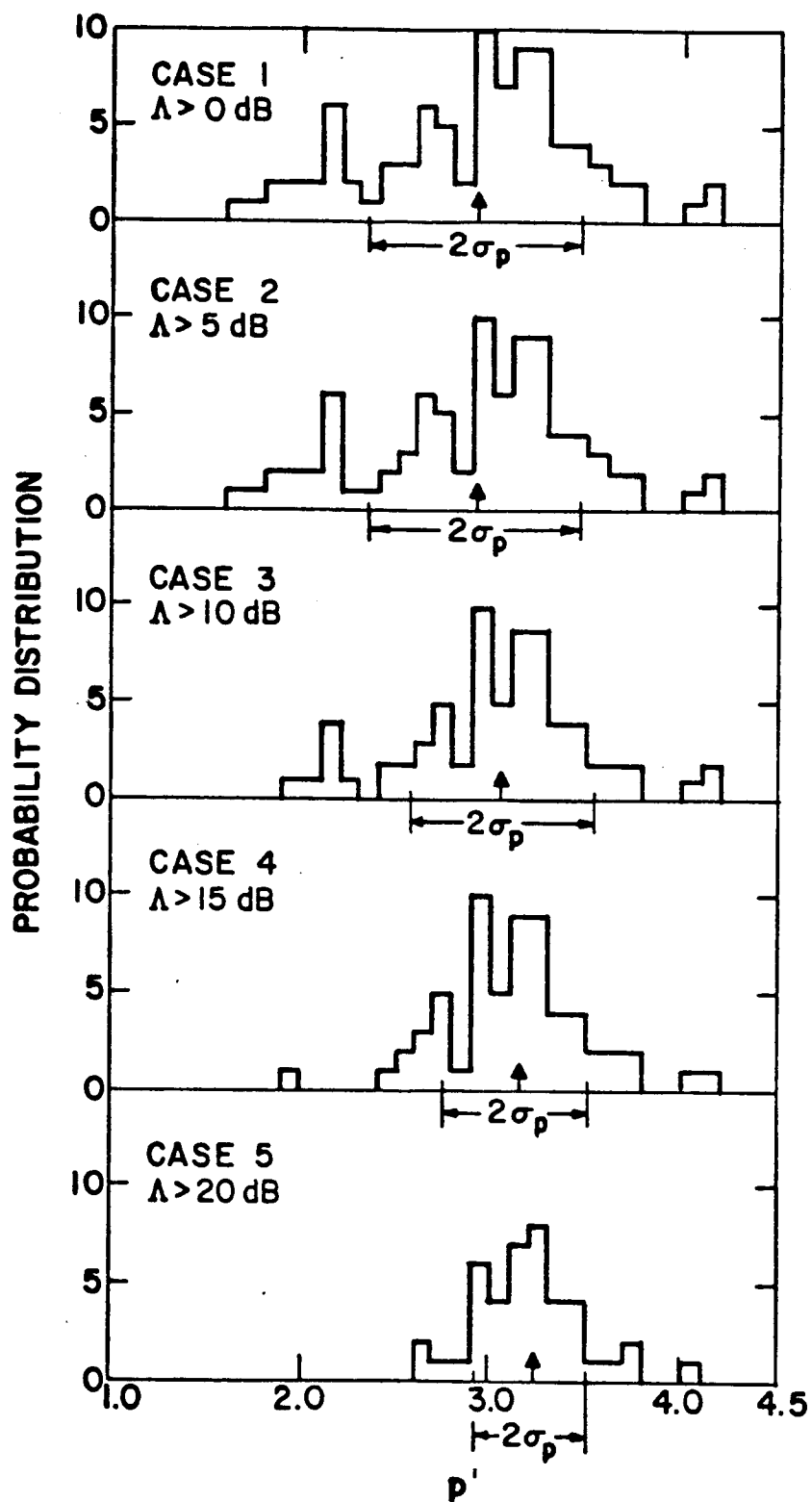
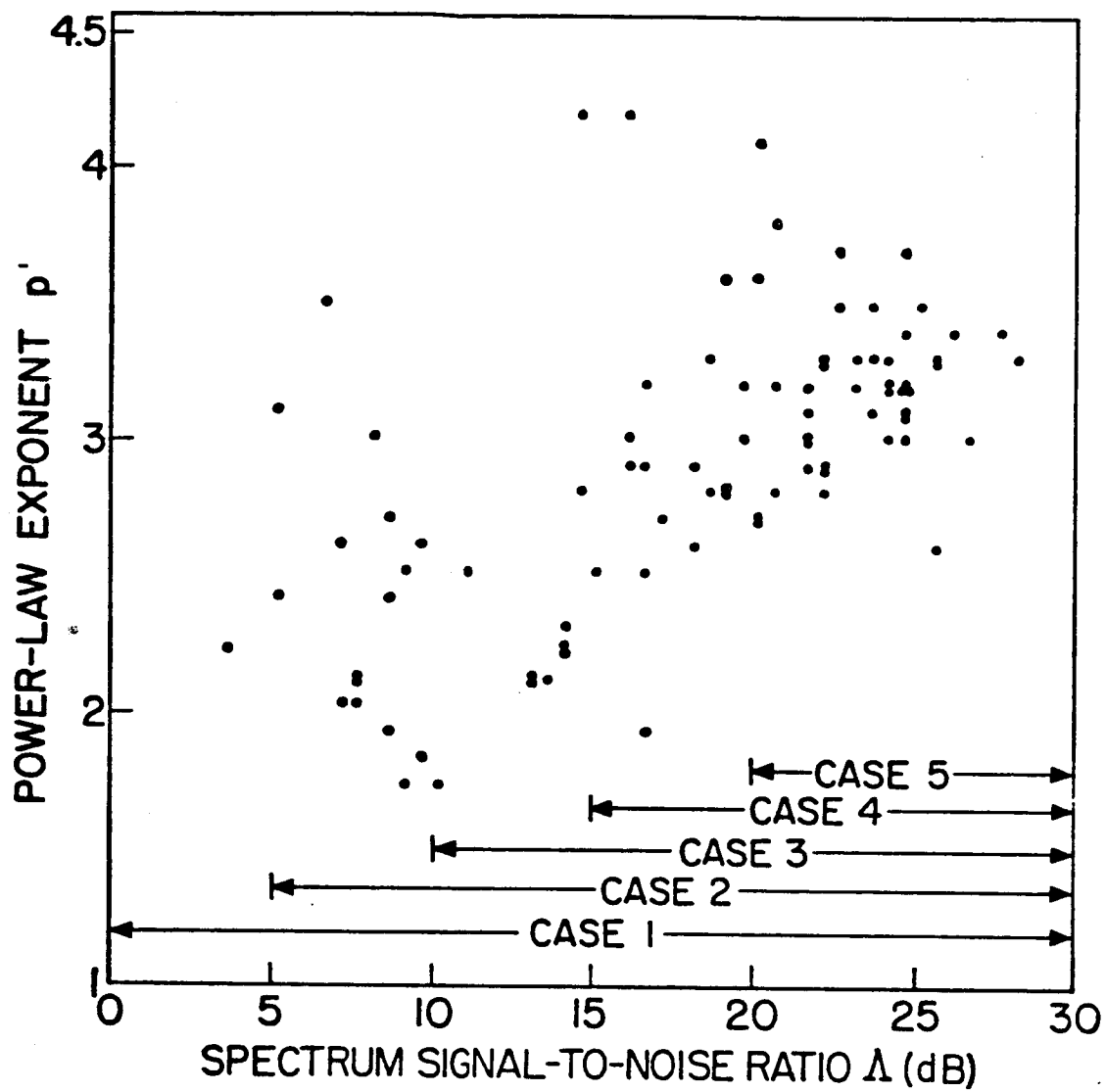
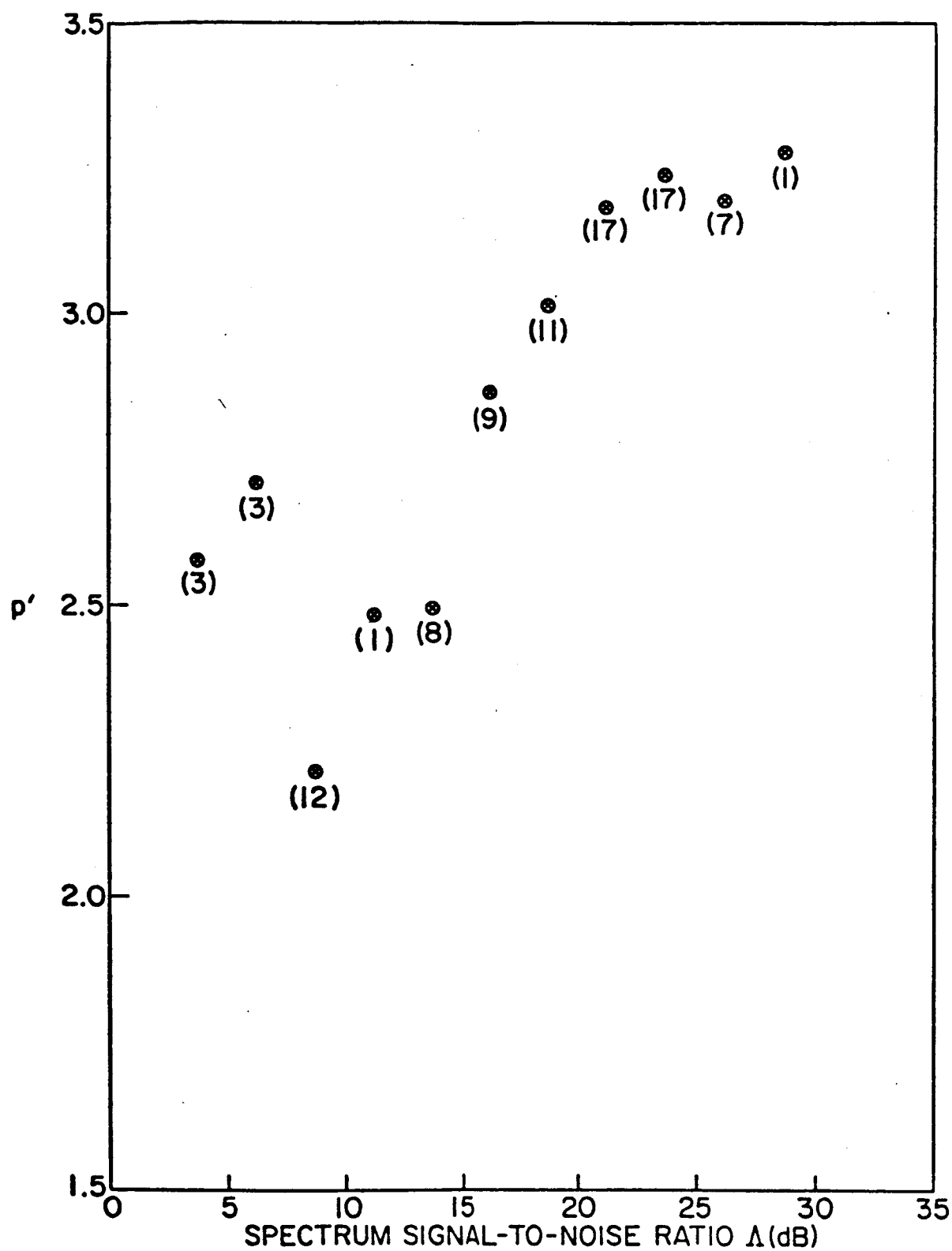


Fig. 5.1. PROBABILITY DISTRIBUTION OF  $p'$  FOR CASES 1-5. Also shown are means (arrows) and two standard deviations ( $2\sigma_p$ ).



a. Plotted as a function of  $\Lambda$ .

Fig. 5.2. OBSERVED POWER-LAW EXPONENT  $p'$  OF  $F_n(q)$  BEFORE CORRECTING FOR THE EFFECT OF  $\Lambda$ .



b. Averaged over 2.5 dB ranges of  $\Delta$  in order to reduce the scatter. The number shown under each point is the number of original data from which each of these eleven points is derived.

Fig. 5.2. CONTINUED.

for the average of  $p'$  over mutually disjoint regions of  $\Lambda$ , these points are independent of one another. Note also that this is different from the situation encountered earlier in Fig. 5.1 in which one case (e.g., Case 1) contains data points of another (e.g., Case 5) such that the resultant means of  $p'$  for distinct cases are not independent. Turning back to Fig. 5.2b, we see that except for the first two points, which were derived from low- $\Lambda$  observations ( $\Lambda < 7.5$  dB), all other nine points of average  $p'$  appear to increase almost monotonically with  $\Lambda$ .

Qualitatively, the decrease of  $p'$  with decreasing  $\Lambda$  may be interpreted as follows. In practice, the observed scintillation spectrum  $F_p(\nu)$  is always the sum of the true scintillation spectrum  $F_I(\nu)$  and the noise spectrum  $F_N(\nu)$ :<sup>†</sup>

$$F_p(\nu) = F_I(\nu) + F_N(\nu)$$

Consequently, the apparent slope  $(p'-1)$  of  $F_p(\nu)$ --when plotted in dB versus  $\log(\nu)$ --is always smaller than the true slope  $(p-1)$  of  $F_I(\nu)$ ; and the smaller the value of spectrum signal-to-noise ratio  $\Lambda$ , the smaller  $p'$  compared with  $p$ .

To determine quantitatively the effect of  $\Lambda$  on  $p'$  (so that later the true power-law exponent  $p$  may be extrapolated from  $p'$ ), consider a simplified model in which the noise spectrum  $F_N(\nu)$  is assumed to be white over the frequency band of interest and the true scintillation spectrum  $F_I(\nu)$  is assumed to be power-law for  $\nu \geq 1$  Hz:

<sup>†</sup> Possible noise sources include (1) inherent instrumental noise, (2) quantization noise resulting from A/D conversion, and (3) noise introduced during digital signal processing (such as aliasing errors).

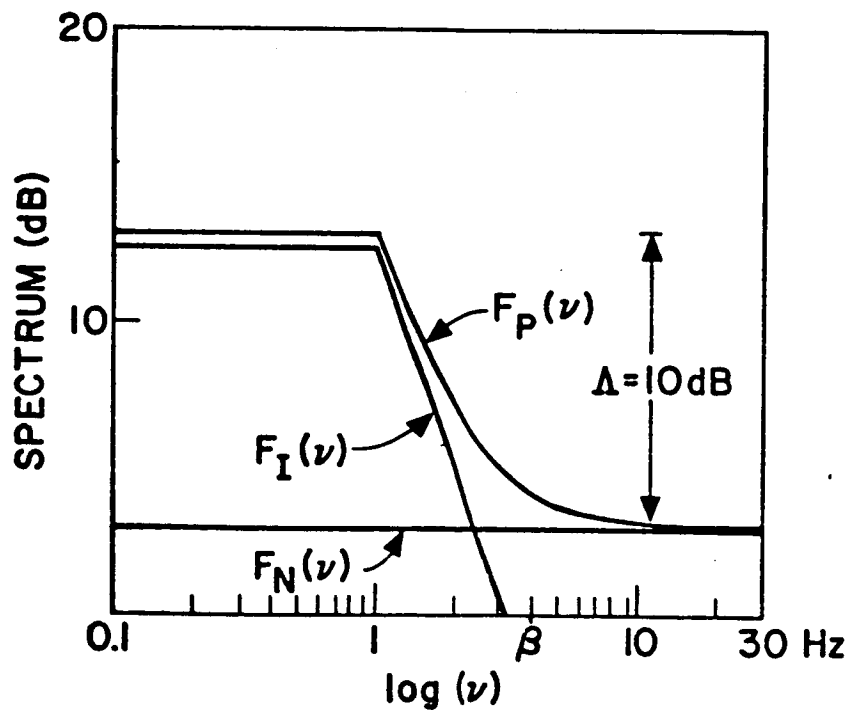


$$F_I(\nu) \propto \nu^{-(p-1)} \quad \text{for } \nu \geq 1 \text{ Hz}$$

Several resultant observed spectra  $F_p(\nu)$  for  $p = 3.5$  and  $\Lambda = 10, 20, \text{ and } 30 \text{ dB}$  are shown in Fig. 5.3. In general,  $F_p(\nu)$  is still roughly power-law over a certain fitting region  $1 \leq \nu \leq \beta \text{ Hz}$ , but with an apparent slope  $(p'-1)$  smaller than  $(p-1)$ . That is,  $F_p(\nu)$  may be approximated as

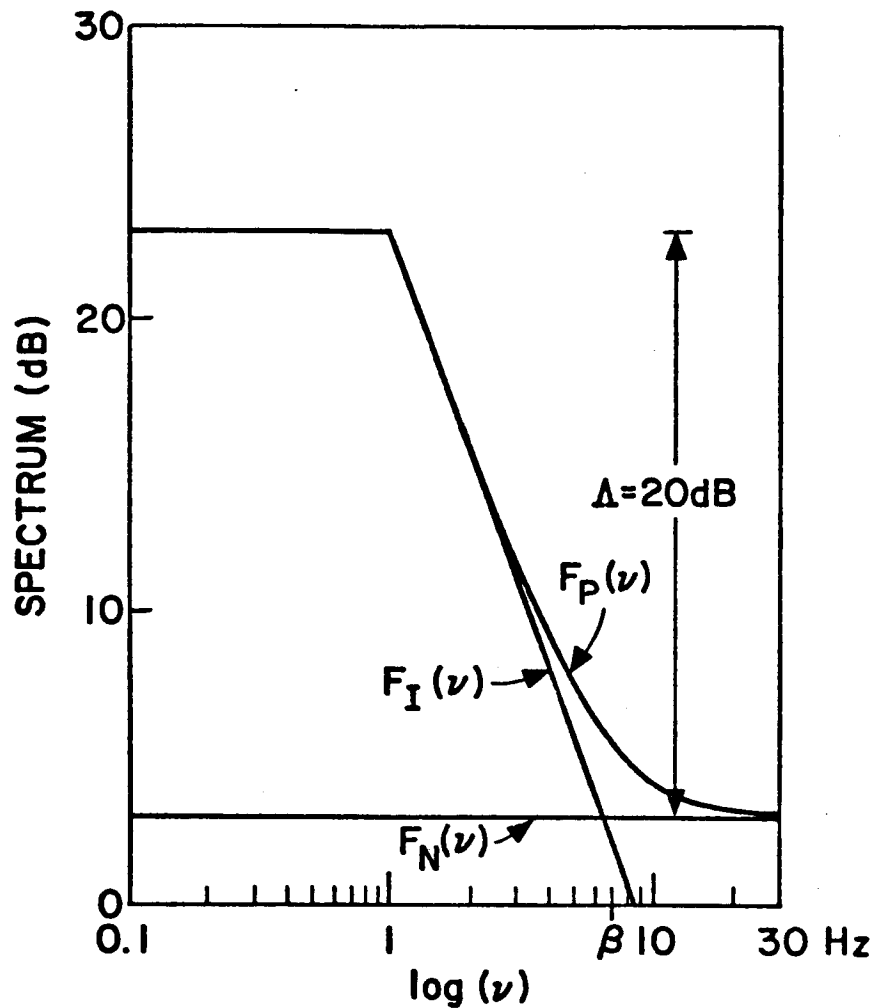
$$F_p(\nu) \propto \nu^{-(p'-1)} \quad \text{for } 1 \leq \nu \leq \beta \text{ Hz}$$

According to this model,  $p'$  is less than  $p$  by an amount that depends not only on  $\Lambda$  but also on the end frequency  $\beta$  of the fitting region,



a.  $\Lambda = 10 \text{ dB}$

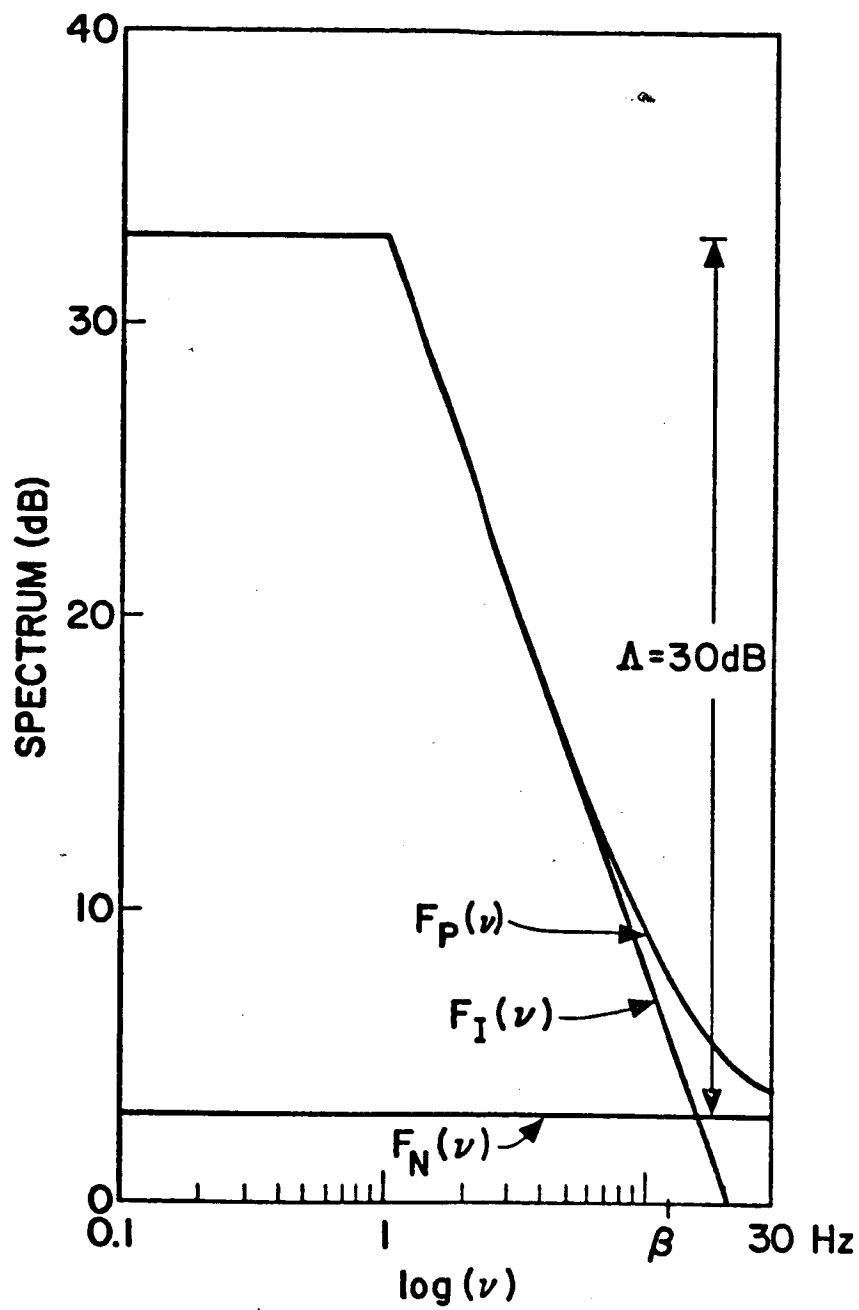
Fig. 5.3. THE EFFECT OF THE NOISE SPECTRUM ON THE APPARENT SLOPE OF THE OBSERVED SCINTILLATION SPECTRUM FOR  $p = 3.5$  AND  $\Lambda = 10, 20, \text{ AND } 30 \text{ dB}$ . Also shown for each case is the estimated end frequency  $\beta$  of the fitting region.



b.  $\Delta = 20 \text{ dB}$

Fig. 5.3. CONTINUED.

although the former usually has the far more predominant effect. Because  $F_p(\nu)$  is inherently curved as can be seen from Fig. 5.3, the value of  $\beta$  is rather difficult to define analytically. Recall that a similar difficulty arose earlier with experimental data in Sec. IV.D.1 in which the fitting region for the regression test had to be selected. The approach of visual estimate with some appropriate guidelines was used there to choose the fitting region and is used here again to estimate  $\beta$ . Such guidelines for estimating  $\beta$  include the following:



c.  $\Lambda = 30 \text{ dB}$

Fig. 5.3. CONTINUED.

- (1) The value of  $\beta$  should be chosen such that  $F_p(\nu)$  appears to be linear or only slightly curved to the eyes; after  $\nu > \beta$ ,  $F_p(\nu)$  becomes curved much more rapidly than before  $\nu < \beta$  and eventually approaches the noise spectrum near  $\nu \approx \gamma$ . Recall that  $[\beta, \gamma]$  was called the "transition region" in Sec. IV.D.
- (2) In any case  $\beta$  should always be smaller than 18.3 Hz, because that is the highest frequency of our observed scintillation spectra (see, for example, Fig. 4.7).
- (3) Spectra possessing larger  $\Lambda$  should generally have wider fitting regions or larger values of  $\beta$ .

Three estimated end frequencies  $\beta$  thus obtained are shown in Fig. 5.3.

Once  $\beta$  was determined, a linear least-squares fit was then applied to each plot of  $F_p(\nu)$  over the fitting region  $1 \leq \nu \leq \beta$  Hz. The theoretically predicted value of  $p'$  was obtained by adding 1 to the slope of the linear regression line. For instance, if models are constructed with  $p = 3.5$ , then the predicted values of  $p'$  are 1.9, 2.4, 2.8, 3.1, 3.2, and 3.3 for  $\Lambda = 5, 10, 15, 20, 25$ , and 30 dB, respectively. These six values of  $p'$  had been used as a basis for deriving the curve labelled " $p = 3.5$ " in Fig. 5.4. Repeating the same procedure for other values of  $p$  from 3.2 to 3.8 led to the other curves. The effect of noise on the measured slopes is thus determined; each curve represents (for one value of  $p$ ) the expected dependence of  $p'$  upon  $\Lambda$ . For comparison, the mean values of the measured  $p'$  as shown in Figure 5.2b are superimposed upon these curves. It is clear that  $p = 3.5$  gives the best fit to the observations over the region  $\Lambda \geq 15$  dB. Because (1) most of our observed spectra lie in this region, (2) the observed spectra in this region are more reliable than those having lower  $\Lambda$ , and (3) the slopes of the regression lines

(and consequently the resulting values of  $p'$ ) in this region are less subject to variations of  $\beta$ , it is concluded that

$$\bar{p} \approx 3.5 \pm \delta \quad (5.1a)$$

is the average value of the power-law exponent  $p$  for our observed scintillation spectra, where  $\delta$  --to be estimated shortly--is the uncertainty associated with the determination of the mean exponent  $\bar{p}$ .

As a check on the conclusion  $\bar{p} \approx 3.5$ , the effect of noise was deleted from each of the 89 spectra using the  $p = 3.5$  curve from Fig. 5.4. This curve can be interpreted as a correction curve, since it provides predicted exponent  $p'$  versus  $\Lambda$  based upon the assumption that the true exponent  $p$  is 3.5. One can therefore subtract the predicted  $p'$  from 3.5 to determine the correction versus  $\Lambda$  that must be applied to experimentally derived exponents. This was done to all 89 observations and the statistics were re-derived. The results are summarized in the last column of Table 5.2. It is seen that the correction brings agreement with  $\bar{p} \approx 3.5$  even in cases (such as Cases 1-3) that low- $\Lambda$  observations are included. In the most reliable case (Case 5), the standard deviation  $\sigma_p$  of the power-law exponent  $p$  is given by

$$\sigma_p \approx 0.3 \quad (5.1b)$$

The uncertainty  $\delta$  associated with the determination of the mean is considered to be three times the standard error of the mean:

$$\delta \approx 3\sigma_{\bar{p}} \approx 3 \cdot \frac{\sigma_p}{\sqrt{42}} \approx 0.13 \quad (5.1c)$$

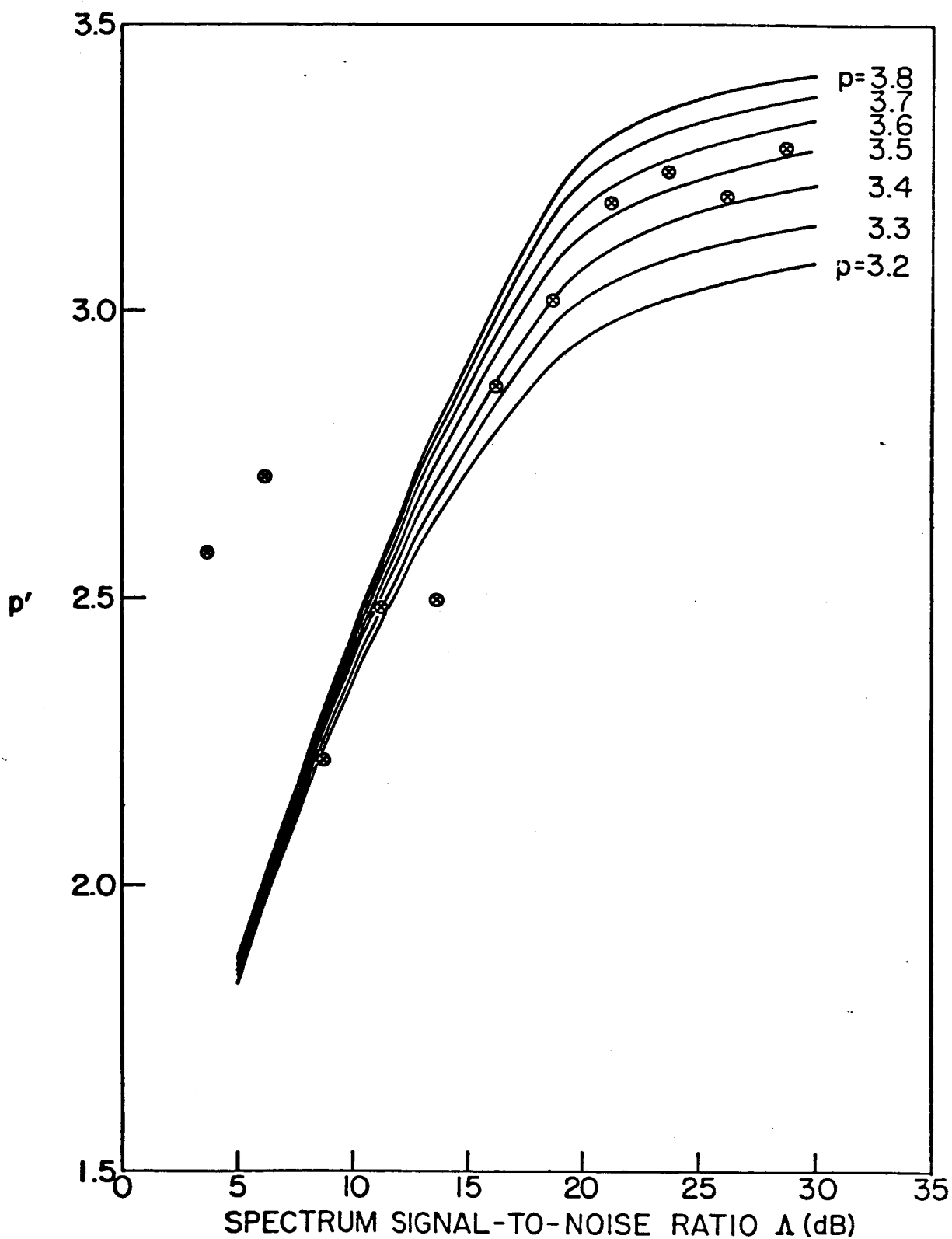


Fig. 5.4. THE THEORETICALLY PREDICTED DEPENDENCE OF  $p'$  UPON  $\Delta$  FOR  $p = 3.2, 3.3, \dots, 3.8$ . For comparison, the mean values of the measured  $p'$  as shown in Fig. 5.2b are superimposed upon these curves.

where  $\sigma_{\bar{p}}$  is the standard deviation of the mean exponent  $\bar{p}$ , and 42 is the total number of spectra included in deriving  $\bar{p}$  and  $\sigma_{\bar{p}}$ .

Incorporating (5.1c) into (5.1a) leads to

$$\bar{p} \approx 3.5 \pm 0.13 \quad (5.1d)$$

Referring to Table 1.1 in Chapter I, it is obvious that among all four scintillation-deduced values of  $p$  (4.5, 2.4, 2.6, and 3.5) ours (3.5) agrees best with the three values of  $p$  (3.2, 3.3, 3.55) inferred from in situ spacecraft measurements. The basis of this agreement is believed to be due to our use of a man-made, point source instead of a radio star as the source of IPS observations.<sup>†</sup>

### 3. Magnitude of $F_I(\nu)$

In addition to comparing the power-law exponent  $p$ , it is of interest to compare the magnitude (or absolute value) of the irregularity spectrum inferred from our IPS data with that derived from in situ measurements. First of all, a typical intensity-fluctuation spectrum  $F_I(\nu)$  estimated from our IPS data at 423 MHz may be approximated by [cf. Cronyn (1972a, b)]

$$F_I(\nu) \approx \begin{cases} c_\phi^2 \lambda^2 \nu^{-(p-1)} & ; \nu_f \leq \nu \leq 10 \text{ Hz} \\ c_\phi^2 \lambda^2 \nu_f^{-(p-1)} & ; \nu < \nu_f \end{cases} \quad (5.2a)$$

<sup>†</sup> As pointed out in Sec. I.B, IPS observations from a man-made, constant-amplitude, monochromatic, point source at a known distance within the IPM are free from such uncertain factors as source-diameter effects, interstellar scattering, and erratic radiation from natural sources.

where  $\nu_f \equiv \frac{U}{\sqrt{\pi \lambda Z}}$  ( $\approx 1$  Hz at 423 MHz) is defined as the Fresnel frequency (Sec. II.C), and  $c_\phi^2$  is a proportionality factor related to the strength of solar-wind turbulence. Notice that the scintillation index  $m$  may be expressed as [see Eq. (2.57)]

$$m^2 = \int_0^\infty F_I(\nu) d\nu$$

Incorporating (5.2a) into this equation, assuming that  $F_I(\nu) \approx 0$  for  $\nu > 10$  Hz, and carrying out the integration leads to

$$c_\phi^2 \approx \frac{p-2}{p-1} \left(\frac{m}{\lambda}\right)^2 \nu_f^{p-2}$$

for  $p > 2$ . With this value of  $c_\phi^2$ ,  $F_I(\nu)$  in (5.2a) may then be restated as

$$F_I(\nu) \approx \frac{p-2}{p-1} m^2 \nu_f^{p-2} \nu^{-(p-1)} \quad (5.2b)$$

for  $\nu_f \leq \nu \leq 10$  Hz. Since our IPS data at 423 MHz ( $\lambda = 0.709$  meter) indicate that  $p = 3.5$ ,  $\nu_f \approx 1$  Hz, and  $m \approx 0.053 \rho^{-1.5}$  [cf. Eq. (5.20)],  $F_I(\nu)$  in (5.2b) can further be reduced to

$$F_I(\nu) \approx 1.53 \times 10^{-3} \rho^{-3.0} \nu^{-2.5}; \quad 1 \text{ Hz} \leq \nu \leq 10 \text{ Hz} \quad (5.2c)$$

According to Cronyn [1972a (loc. cit. Eq. 6b)], the temporal spectrum  $F_n(\nu)$  of electron-density fluctuations obtained by in situ measurements is related to  $F_I(\nu)$  via

$$F_n(\nu) = \frac{0.9 \times 350}{(p-2) U \epsilon} \frac{\Gamma(\frac{p}{2})}{\Gamma(\frac{p-1}{2})} \frac{\nu F_I(\nu)}{\rho \lambda^2} (\text{el/cm}^3) \text{ Hz}^{-1} \quad (5.3a)$$



where  $U$  = solar wind velocity in the x-direction in km/sec

$\xi$  = ellipticity of irregularities along the z (line-of-sight) - direction with respect to the x-direction  
[cf. Eq. (2.40)]

$\rho$  = proximate distance in A.U.

$\lambda$  = wavelength of IPS observations in meter

$\Gamma( )$  = Gamma function

Substituting (5.2c) into (5.3a) and letting  $p = 3.5$ ,  $\lambda = 0.709$  meter,  $\rho = 1$  A.U.,  $U = 500$  km/sec, and  $\xi^{-1} = 1.8$  [Cronyn (1972a)] yields

$$F_n(\nu) \approx 2.15 \times 10^{-3} \rho^{-4.0} \nu^{-1.5} \times \left(\frac{350}{U \xi}\right) \quad (5.3b)$$

$$\approx 2.71 \times 10^{-3} \nu^{-1.5} (e1/cm^3)^2 Hz^{-1}; 1 Hz \leq \nu \leq 10 Hz \quad (5.3c)$$

as shown in Fig. 5.5. Note that the magnitude of  $F_n(\nu)$  thus deduced from our IPS data agrees with Unti's (1973) Fig. 5, which may be expressed explicitly as

$$3.6 \times 10^{-4} \nu^{-1.6} \leq F_n(\nu) \leq 10^{-2} \nu^{-1.5} (e1/cm^3)^2 Hz^{-1} \quad (5.4)$$

for  $\rho = 1$  A.U. and  $1 Hz \leq \nu \leq 13.3 Hz$ . This agreement proves further the usefulness and efficacy of the IPS technique. While Unti's in-situ measurements and hence the validity of Eq. (5.4) are limited to regions of  $\rho \approx 1$  A.U. from the sun, Eq. (5.3b) gives a more general formula of  $F_n(\nu)$ , which is believed to be applicable for  $0.1 A.U. \leq \rho \leq 1 A.U.$  It is interesting to remark that our (5.3b) also agrees (within a factor of  $\sim 2$  at  $\rho = 1$  A.U.) with the following Cronyn's (1972a) result:

$$F_n(\nu) = 1.4 \times 10^{-3} \rho^{-4.2} \nu^{-1.6} (e1/cm^3)^2 Hz^{-1}$$

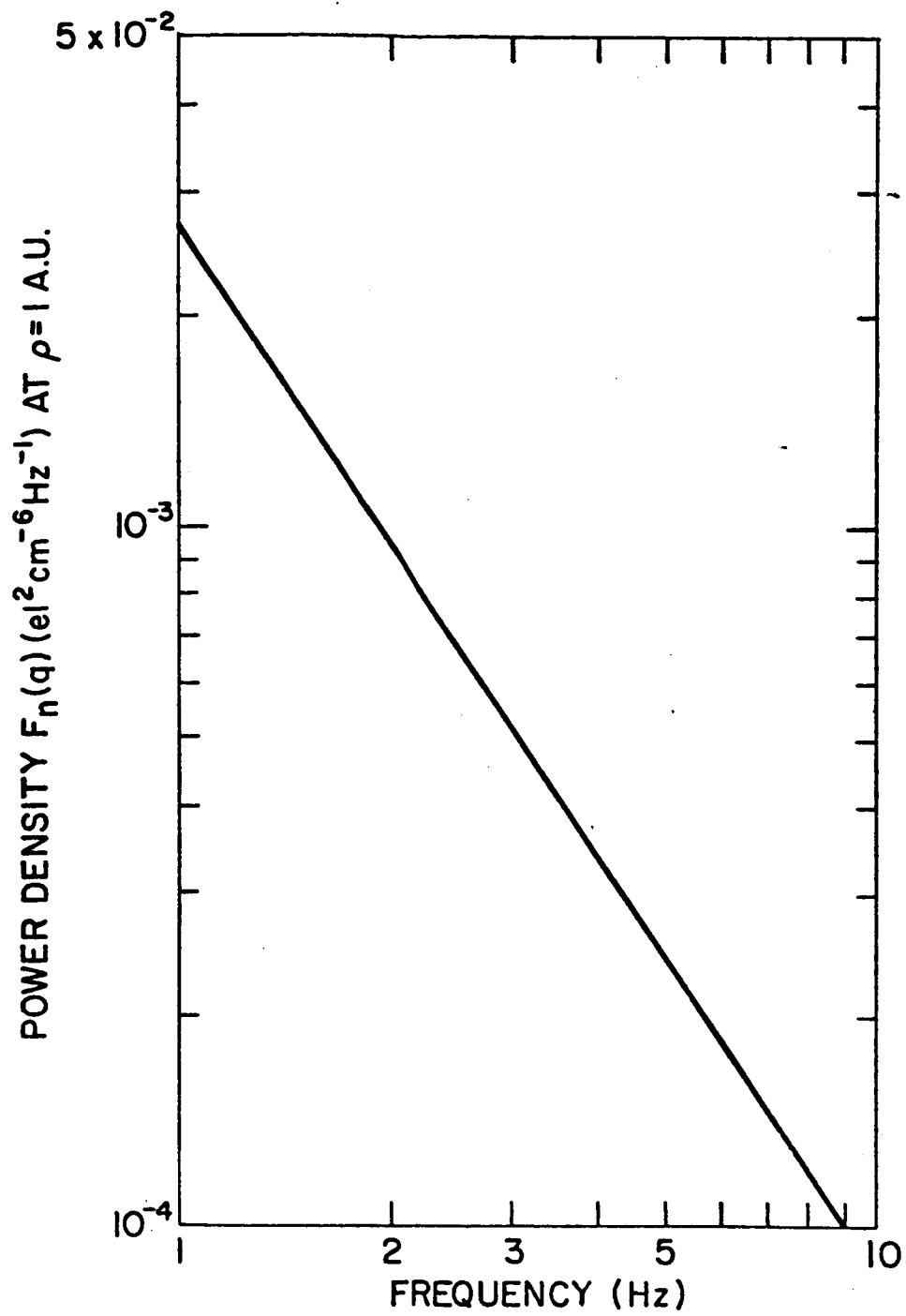


Fig. 5.5. TEMPORAL SPECTRUM OF ELECTRON DENSITY FLUCTUATIONS DEDUCED FROM IPS DATA AT 423 MHz.

## B. Fresnel Structure

It has been shown in Chapter II that under appropriate conditions, the observed temporal spectrum of intensity fluctuations at a single site--as a result of the screen motion and Fresnel diffraction effect--will exhibit a sequence of minima (called the Fresnel structure) at

$$\nu = \nu_1, \sqrt{2}\nu_1, \sqrt{3}\nu_1, \sqrt{4}\nu_1, \dots \quad (5.5a)$$

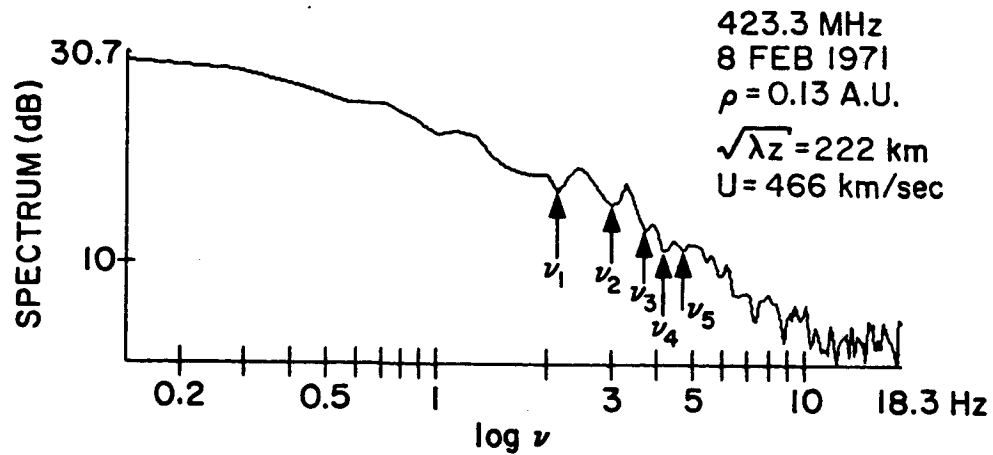
where

$$\nu_1 = U/\sqrt{\lambda z} \quad (5.5b)$$

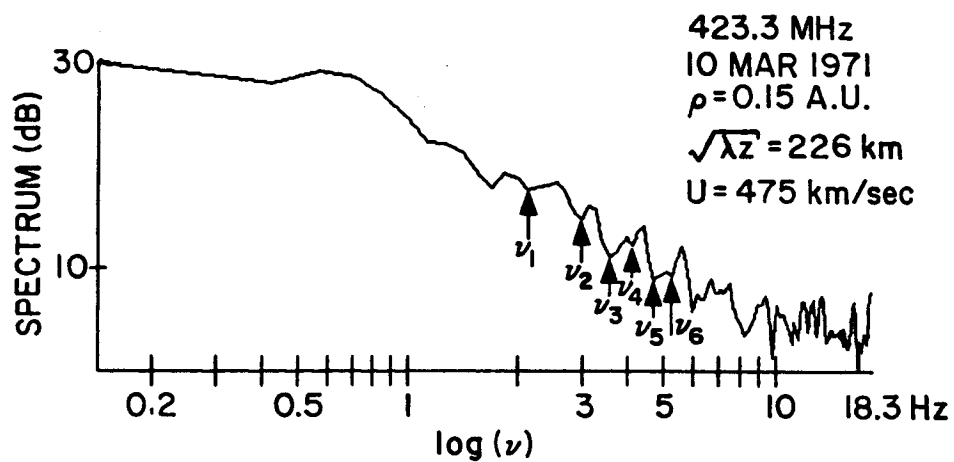
and  $z$  can be uniquely determined from the geometry of the experiment via (2.19), provided that the "thin-screen" approximation is applicable. In an attempt to detect the existence of such a structure in our scintillation spectra, 42 spectra at 423 MHz were examined. All these spectra were obtained at times when the lines-of-sight were less than 0.3 A.U.<sup>†</sup> from the sun. On only eight occasions, the Fresnel structures are convincingly observed. Two such examples are shown in Figs. 5.6a and 5.6b. The arrows indicate the successive positions of theoretical minima with an assumed first minimum at  $\nu_1 = 2.1$  Hz, which, along with  $\sqrt{\lambda z} = 222$  and 226 km, yields the solar wind speed  $U = 466$  and 475 km/sec for Figs. 5.6a and 5.6b, respectively. As evident from these two figures themselves, the positions of the theoretical and the observed minima are in excellent agreement and 466 and 475 km/sec are said to be the solar wind velocities deduced from these two Fresnel structures. Note that for such a value of  $\nu_1 (= 2.1 \text{ Hz})$ , Fresnel

---

<sup>†</sup> The thin-screen model is believed to be a more appropriate model (and hence chances of observing successfully the Fresnel structure are believed to be higher) for  $\rho < 0.3 \text{ A.U.}$  than for  $\rho > 0.3 \text{ A.U.}$



(a)



(b)

Fig. 5.6. OBSERVED FRESNEL OSCILLATIONS IN THE SCINTILLATION SPECTRUM. Arrows indicate the successive theoretical minima of the Fresnel structure with the first minimum chosen to occur at 2.1 Hz for both figures.

oscillations after the 5th or 6th minimum become faster than (or comparable with) the resolution bandwidth ( $= 0.29$  Hz--cf. Table G.3) of the estimated spectra in Figs. 5.6a and 5.6b, and hence are not detectable.

The relatively infrequent observation of the Fresnel structure is not surprising, because normally one expects this structure to be smeared out by integration through the extended medium (i.e., through different parts of the medium along the line-of-sight, which have different values of  $z$  and  $U^+$ ). By the same token, days for which the Fresnel structure is discernible are believed to correspond to days on which IPS are caused predominantly by a thin layer (near the sun) such that  $z$  and  $U$  in (5.5b) [and hence the positions of the minima in (5.5a)] are well defined.

Before leaving this section, it is encouraging to remark that all eight solar wind velocities (inferred from the eight aforementioned Fresnel structures in the range  $\rho = 0.1$ - $0.3$  A.U.) lie between 400 and 500 km/sec, which is of the "correct" order of magnitude as compared with Lovelace's (1970) or Armstrong and Coles' (1972) observations.

---

<sup>+</sup> Even if the solar wind has a constant radial velocity, the projected transverse component of this velocity (i.e., the projected component of this velocity onto the x-direction) is still different at different points along the line-of-sight.

### C. Correlation Length of Intensity Fluctuations

The temporal width  $t_w$  of the autocorrelation function  $A_I(t)$  of intensity fluctuations is defined as the time at which  $A_I(t)$  falls off to one-half of its maximum value:

$$A_I(t=t_w) = \frac{1}{2} \max \{A_I(t)\} = \frac{1}{2} A_I(t=0)$$

For the normalized autocorrelation functions  $\hat{A}_I(t)$  shown in Fig. 4.9,

$$\hat{A}_I(t) = A(t)/A(0)$$

$$\max \{\hat{A}(t)\} = \hat{A}(0) = 1$$

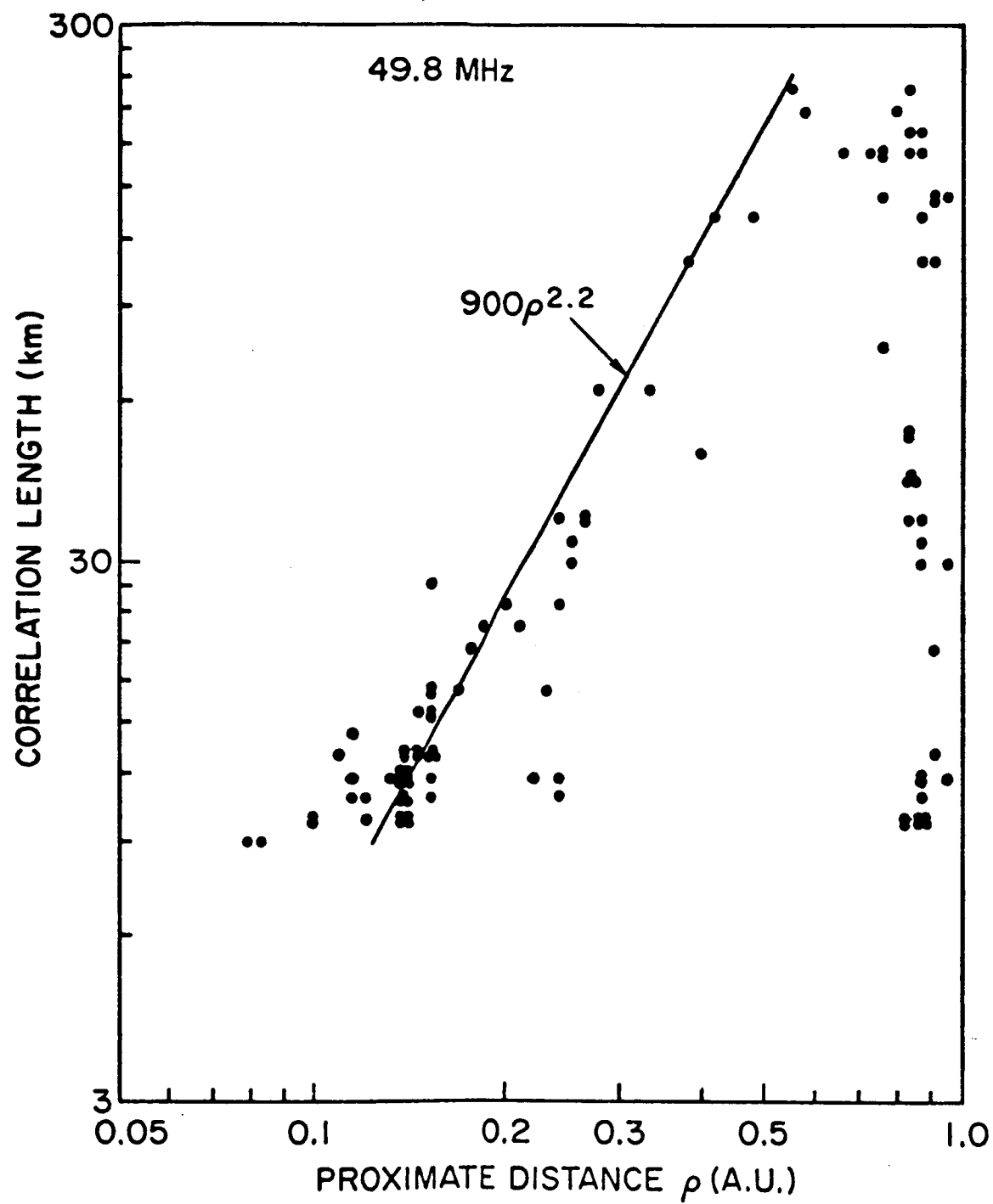
and  $t_w$  is just the time at which  $\hat{A}_I(t)$  drops to 1/2:

$$\hat{A}_I(t=t_w) = \frac{1}{2} \tag{5.6}$$

Multiplying  $t_w$  by the solar wind velocity  $U$  yields the correlation length  $r_w$  (or the apparent scale size) of intensity fluctuations:

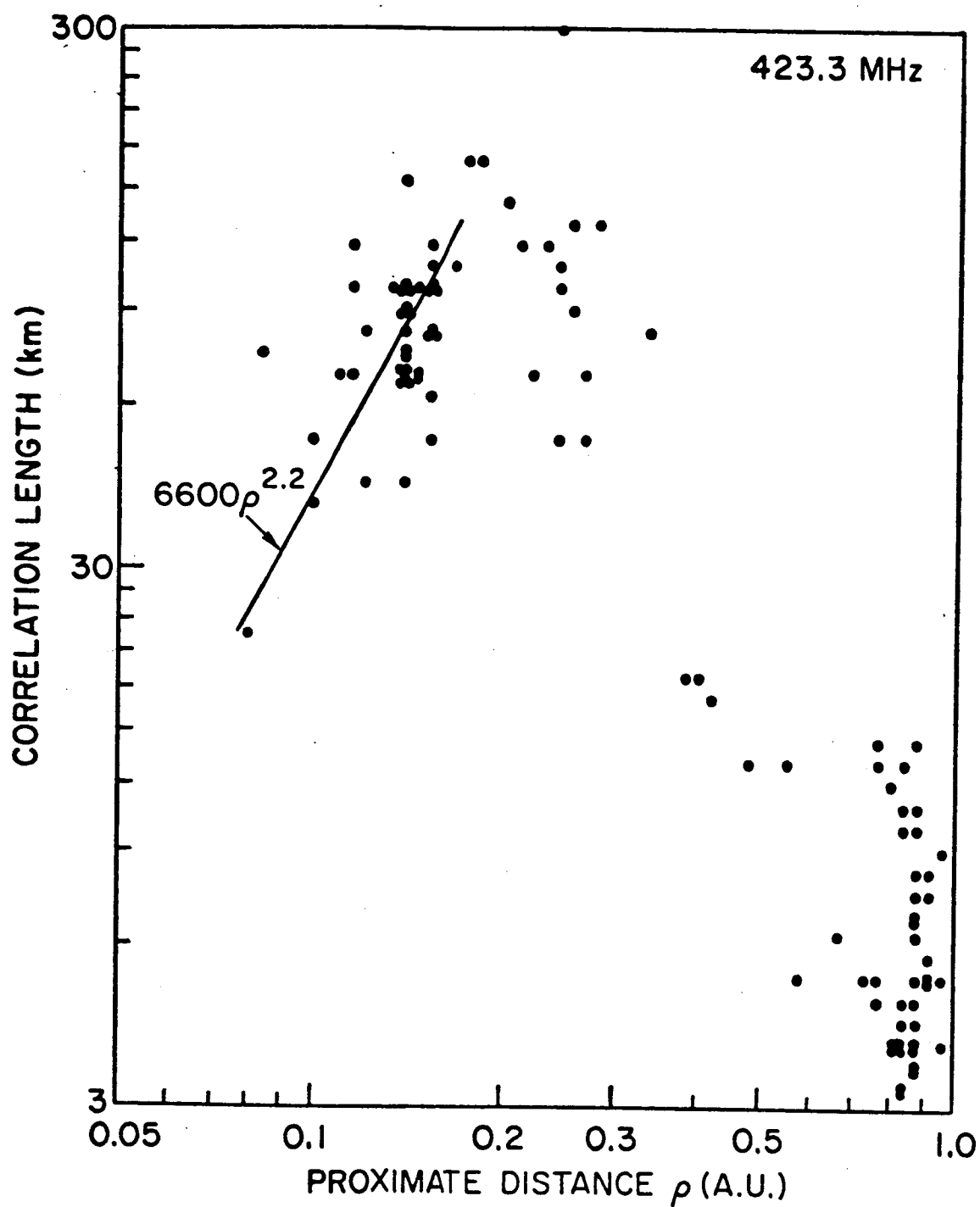
$$r_w = t_w \times U \tag{5.7}$$

For lack of accurate knowledge on the solar wind velocity  $U$ , assume that  $U$  is constant and equal to 500 km/sec. The values of  $r_w$  thus derived are then plotted against the proximate distance  $\rho$ , as shown in Figs. 5.7a (50 MHz) and 5.7b (423 MHz). As evident from these two figures themselves, the values of  $r_w$ , ranging from about



a. 49.8 MHz

Fig. 5.7. CORRELATION LENGTH VS PROXIMATE DISTANCE.



b. 423.3 MHz

Fig. 5.7. CONTINUED.



3 to 300 km, increase with increasing  $\rho$  over the small  $\rho$  region until they reach a certain break point  $\rho_b$  ( $\rho_b^{\ell} \approx 0.55$  A.U. and  $\rho_b^{\nearrow} \approx 0.17$  A.U.) and then turn over with increasing  $\rho$ .

Before proceeding with further analysis of these  $r_w$  data, it is interesting to compare these two figures with Hewish's (1972) Fig. 5. According to the gaussian model as invoked by Hewish to interpret his Fig. 5, the value of  $r_w$  in the weak scattering regime is proportional to the true scale size of the solar wind turbulence and hence is independent of the observing frequency. If this is true, then our  $r_w$  data obtained over  $\rho \gtrsim 0.75$  A.U. by simultaneously transmitting 50 and 423 MHz through the same<sup>†</sup> solar wind region should be the same (or at least very comparable) at both frequencies because the unknown solar wind velocity in (5.7) will be just the same multiplying factor for  $r_w^{\ell}$  and  $r_w^{\nearrow}$ . It can be clearly seen from Figs. 5.7a and 5.7b that our data strongly conflict with this viewpoint. Furthermore, Hewish concludes that the "true" scale size of the solar wind turbulence, or equivalently (in the language of gaussian model)  $r_w$  in the weak scattering regime, increases approximately linearly with  $\rho$ , whereas our data manifest almost the opposite:  $r_w$  decreases sharply with  $\rho$  in the weak scattering regime ( $\rho \gtrsim 0.55$  A.U. at 50 MHz and  $\rho \gtrsim 0.17$  A.U. at 423 MHz).

Because both in situ spacecraft measurements and the results of our regression test (Sec. A) greatly favor the power-law model, in what follows, an attempt will be made to interpret our  $r_w$  data in accordance with the power-law model.

---

† For most of our IPS data, the ray path difference due to regular refraction will be only on the order of a few hundred km or less. Both the characteristic and the velocity of the solar wind are not expected to change appreciably within such a small scale.

Perhaps the most striking feature of Fig. 5.7b is the turn-over of  $r_w$  with  $\rho$  from the weak to strong scattering regime, which, to the author's knowledge, is being experimentally reported for the first time for the IPS. Fortunately, the decrease of  $r_w$  with decreasing  $\rho$  (or increasing turbulence) in the strong scattering regime has been theoretically predicted by Lovelace (1970) [and also by Rumsey (1975)] who demonstrate that the width of the intensity spectrum increases with the strength of the turbulence in the strong scattering regime]. According to Lovelace (1970),

$$r_w \approx \sqrt{\lambda z} \beta^{-\frac{2}{p-2}} \quad (5.8)$$

where  $\beta$  is equal to the scintillation index  $m$  in the weak-scattering limit ( $\beta^2 \ll 1$ )

$$\beta = m \quad (5.9)$$

and  $m$  itself is a function of  $\lambda$  and  $\rho$ :

$$m \propto \lambda^\chi \rho^\psi \quad (5.10)$$

As will be seen in Sec. C, our experimental results indicate that

$$\chi \approx 0.8 \quad (5.11)$$

$$\text{and} \quad \psi \approx -1.5 \quad (5.12)$$

Combining equations (5.8) - (5.12) and, for simplicity, neglecting the radial dependence of  $\sqrt{z}$  over the range of  $\rho$  of interest<sup>†</sup> results

<sup>†</sup> According to the geometry of the experiment,  $\sqrt{z}$  varies less than 20% from  $\rho = 0.08$  A.U. to  $\rho = \rho_b = 0.55$  A.U.

in the theoretical prediction of

$$r_w \propto \left( \lambda^{0.5 - \frac{1.6}{p-2}} \right) \left( \rho^{\frac{3}{p-2}} \right) \quad (5.13)$$

On the other hand, two visual fits to the empirical data--as shown by the two straight lines in Figs. 5.7a and 5.7b--yields

$$r_w^{\ell} = 900 \rho^{2.2} \text{ km}; \quad 0.08 < \rho < 0.55 \text{ A.U.} \quad (5.14a)$$

$$r_w^{\nearrow} = 6600 \rho^{2.2} \text{ km}; \quad 0.08 < \rho < 0.17 \text{ A.U.} \quad (5.14b)$$

which implies an empirical relation of

$$r_w \propto \lambda^{-0.93} \rho^{2.2} \quad (5.15)$$

Comparing the theoretical prediction given by (5.13) with the empirical relation given by (5.15), one may equate

$$\lambda^{0.5 - \frac{1.6}{p-2}} \quad \text{and} \quad \rho^{\frac{3}{p-2}}$$

in (5.13) to

$$\lambda^{-0.93} \quad \text{and} \quad \rho^{2.2}$$

in (5.15), from which it follows that

$$p = 3.12 \quad (5.16a)$$

and

$$p = 3.36 \quad (5.16b)$$

respectively. These two values of  $p$  thus inferred are compatible with  $\bar{p} \approx 3.5 \pm 0.13$  and  $\sigma_p \approx 0.3$  (Sec. A.2) derived directly from least-squares fitting to the scintillation spectra, implying that based on the

power-law model in the strong scintillation regime, the decrease of  $r_w$  with decreasing  $\rho$  (or increasing turbulence) may be attributed purely to the effect of strong scintillation (without the necessity of invoking the change of intrinsic scale size).

Notice that if one sets  $\chi$  in (5.11) to be 1, as was concluded by Hewish (1972) and Rickett (1973) from other empirical data, then the value of  $p$  in (5.16a) will be replaced by

$$p = 3.47 \quad (5.16c)$$

which is in good agreement with (5.1d). Nevertheless, if one substitutes, instead, the theoretical prediction [cf. (2.58) or (5.28)]

$$\chi = \frac{p+2}{4} \quad (5.17)$$

for (5.11), the corresponding value of  $p$  in (5.16a) becomes

$$p = 4.15$$

which then appears to be too large in comparison with the value of  $p$  given by (5.1d). This discrepancy, however, probably results from the failure of (5.17)<sup>†</sup>, the theoretical prediction of the wavelength dependence of  $m$ , rather than from that of (5.9), for (5.9), when combined with the empirical value of  $\chi$  (either 0.8 or 1), provides a satisfactory interpretation of our dual-frequency  $r_w$  data in the strong scattering regime.

There remains to be interpreted the decrease of  $r_w$  with increasing  $\rho$  in the weak scattering regime. Using a semi-quantitative

---

<sup>†</sup> The failure of the power-law model in predicting  $\chi$  will be discussed in detail in the next section.

approach, Jokipii and Hollweg (1970) have derived [see also Matheson and Little (1971)] that  $r_w$  in the weak scattering regime is of the order of  $\sqrt{\lambda z/2\pi^2}$  [see Eq. (2.55)]:

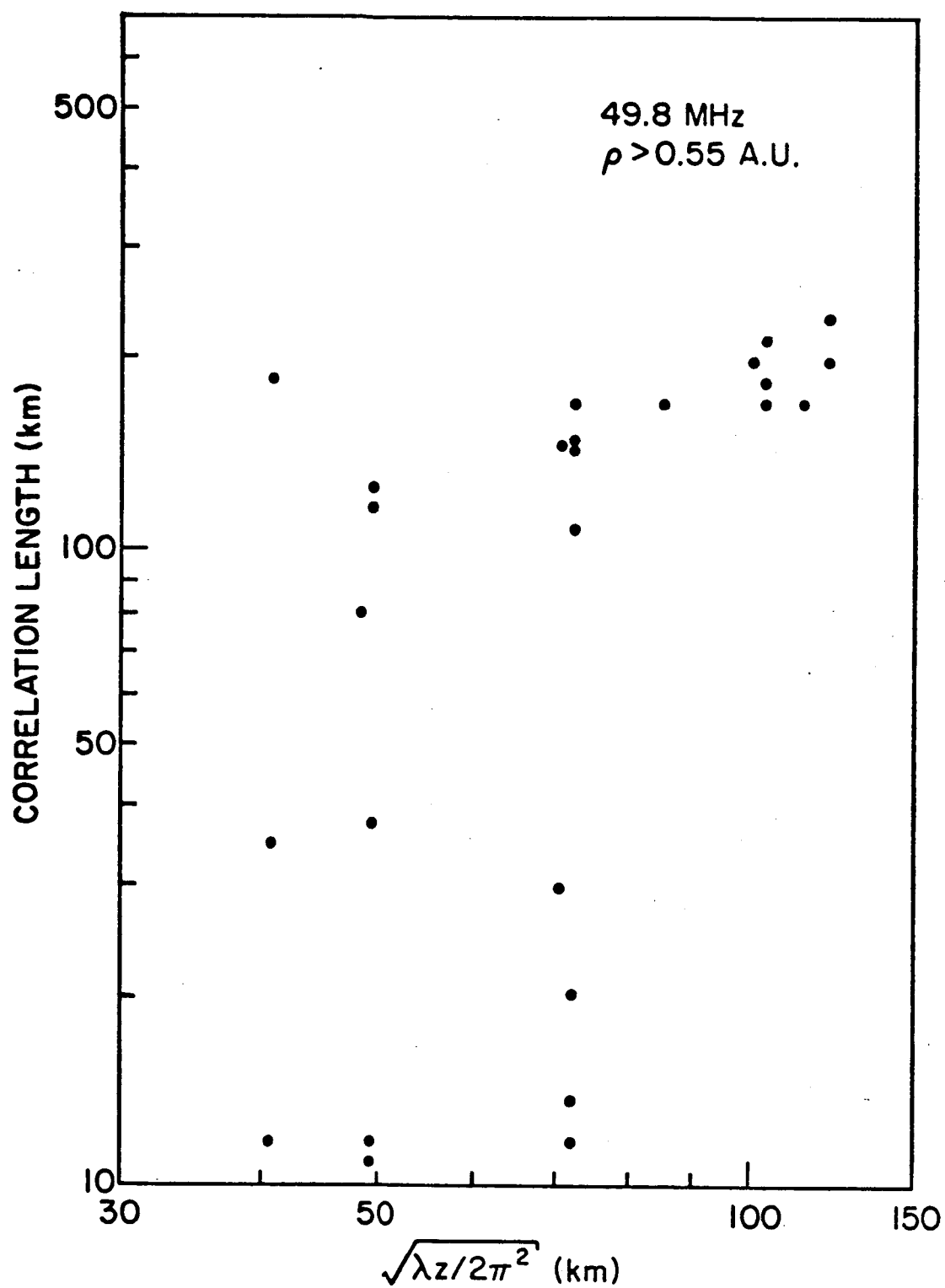
$$r_w \approx 0 \left( \sqrt{\frac{\lambda z}{2\pi^2}} \right) \quad (5.18)$$

provided that

$$\ell_0 < \sqrt{\frac{\lambda z}{2\pi^2}} < L_0$$

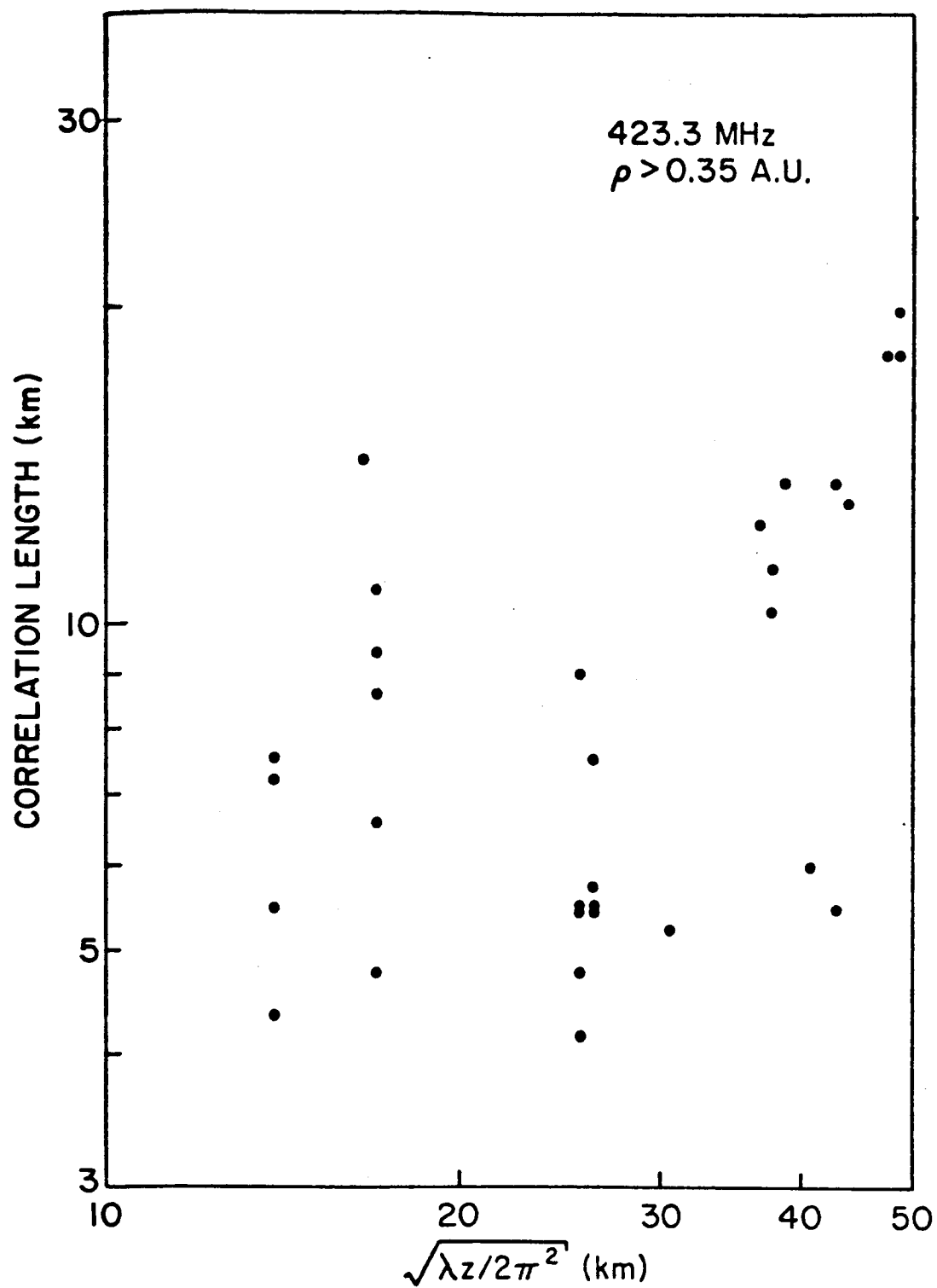
where  $\ell_0$  = inner scale of turbulence  
 $L_0$  = outer scale of turbulence  
 $O(x)$  = the order of magnitude of  $x$

To check the validity of (5.18),  $r_w^{\ell}$  and  $r_w^{\lambda}$  are plotted versus  $\sqrt{\lambda z/2\pi^2}$  in Fig. 5.8a ( $\rho > 0.55$  A.U.) and 5.8b ( $\rho > 0.35$  A.U.), where  $z$  is derived from the geometry of the experiment via (2.19). Before commenting, it should be pointed out that for most cases shown in these two figures, the radio paths are far away from the sun ( $\rho \gtrsim 0.5$  A.U.) and/or the spacecraft is close to the earth such that the thin-screen model may not be a good approximation (i.e., there may not exist a dominant scattering region of thickness  $\ll z$ ). As a result,  $\sqrt{\lambda z/2\pi^2}$  in (5.18) cannot be well defined, and its true value could differ from what is plotted in Figs. 5.8a and 5.8b by a factor of 2-3. Keeping this uncertainty in mind, one may conclude that the theoretical prediction (5.18) based upon the power-law model is compatible, within the same order of magnitude as indicated by (5.18), with our observed  $r_w$  data in the weak scattering regime.



a. 49.8 MHz

Fig. 5.8. CORRELATION LENGTH VS  $\sqrt{\lambda z / 2\pi^2}$ .



b. 423.3 MHz

Fig. 5.8. CONTINUED.

## D. Scintillation Index

### 1. The Radial Variation of Scintillation Index

The upper and the lower limits on the scintillation index  $m$  at 50 and 423 MHz are plotted versus  $\rho$  in Figs. 5.9-5.12a. Because for most indices, the upper limit and the lower limit differ by less than about 20% and do not appear to possess different trends, only the upper limit will be considered in the following discussions.

The radial dependence of  $m$  in the weak scintillation regime ( $m < 1$ ) is of great interest because the radial dependence of the strength  $\sqrt{K_N}$  of solar wind turbulence may be inferred from the radial dependence of  $m$  via Eq. (2.58).

$$m \propto \sqrt{K_N} L \frac{z^{\frac{p-2}{4}}}{\lambda^{\frac{p+2}{4}}} \quad (5.19)$$

where  $L$  is the effective thickness of the medium and  $K_N$  is related to  $F_n(q)$ , the power spectrum of electron density fluctuations by

$$F_n(q) = K_N q^{-P}$$

Because (5.19) is applicable only for weak scintillation, it is advisable to neglect  $m^l$  (Fig. 5.11) in the region  $\rho < 0.55$  A.U. and  $m^h$  (Fig. 5.12a) in the region  $\rho < 0.17$  A.U. As evident from Fig. 5.11,  $m^l$  rises so sharply to  $\approx 1$  over the short region of  $1$  A.U.  $> \rho > 0.75$  A.U. that its variation with  $\rho$  cannot be deduced. Fig. 5.12a, on the other hand, indicates a clear dependence of  $m^h$  on  $\rho$  in the weak scintillation regime ( $\rho \geq 0.17$  A.U.). Suppose for the following two reasons that  $m^h$ 's in the "very" weak scintillation regime



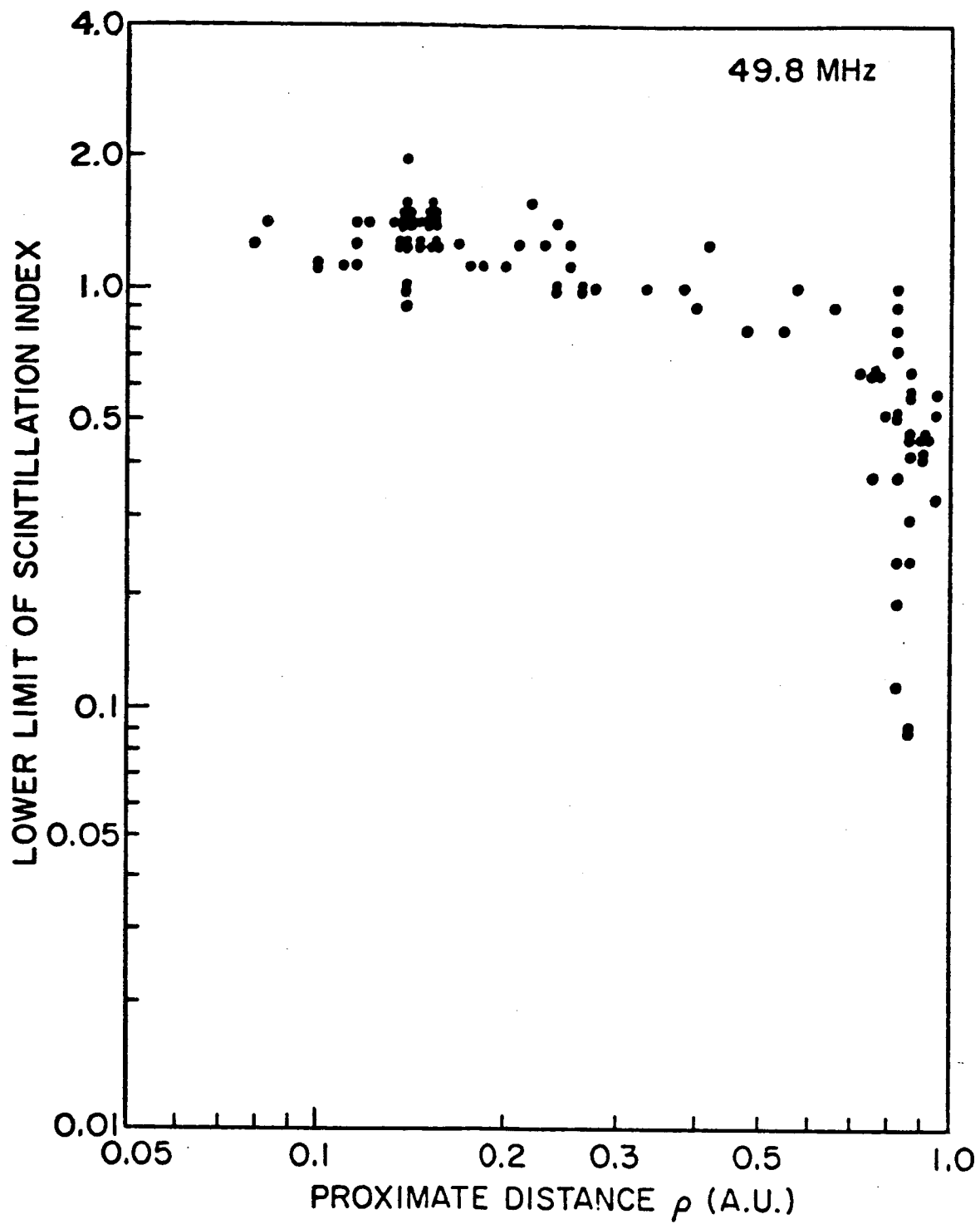


Fig. 5.9. LOWER LIMIT OF SCINTILLATION INDEX  $m$  AT 49.8 MHz VS PROXIMATE DISTANCE  $\rho$ .

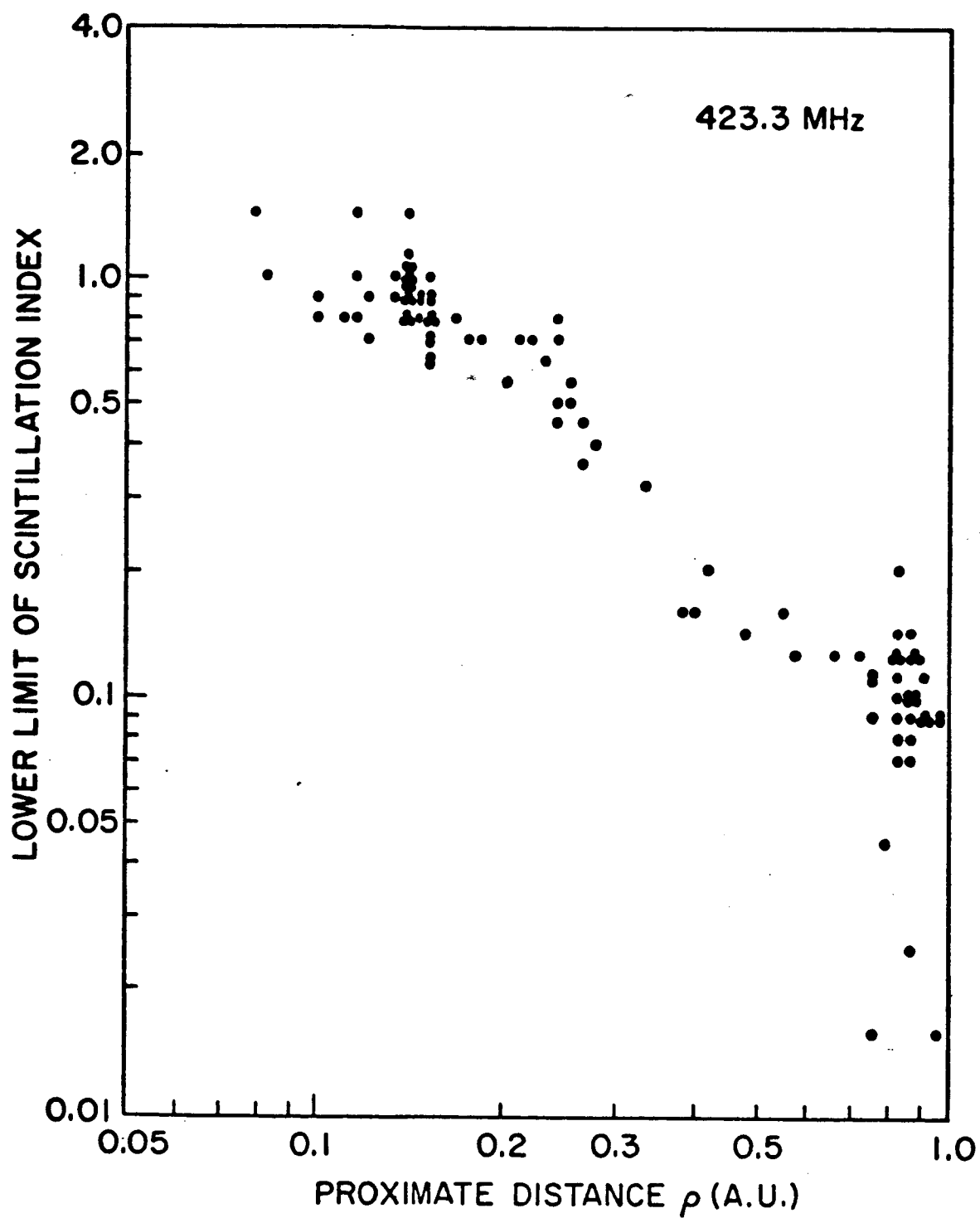


Fig. 5.10. LOWER LIMIT OF SCINTILLATION INDEX  $m$  AT 423.3 MHz VS PROXIMATE DISTANCE  $\rho$ .

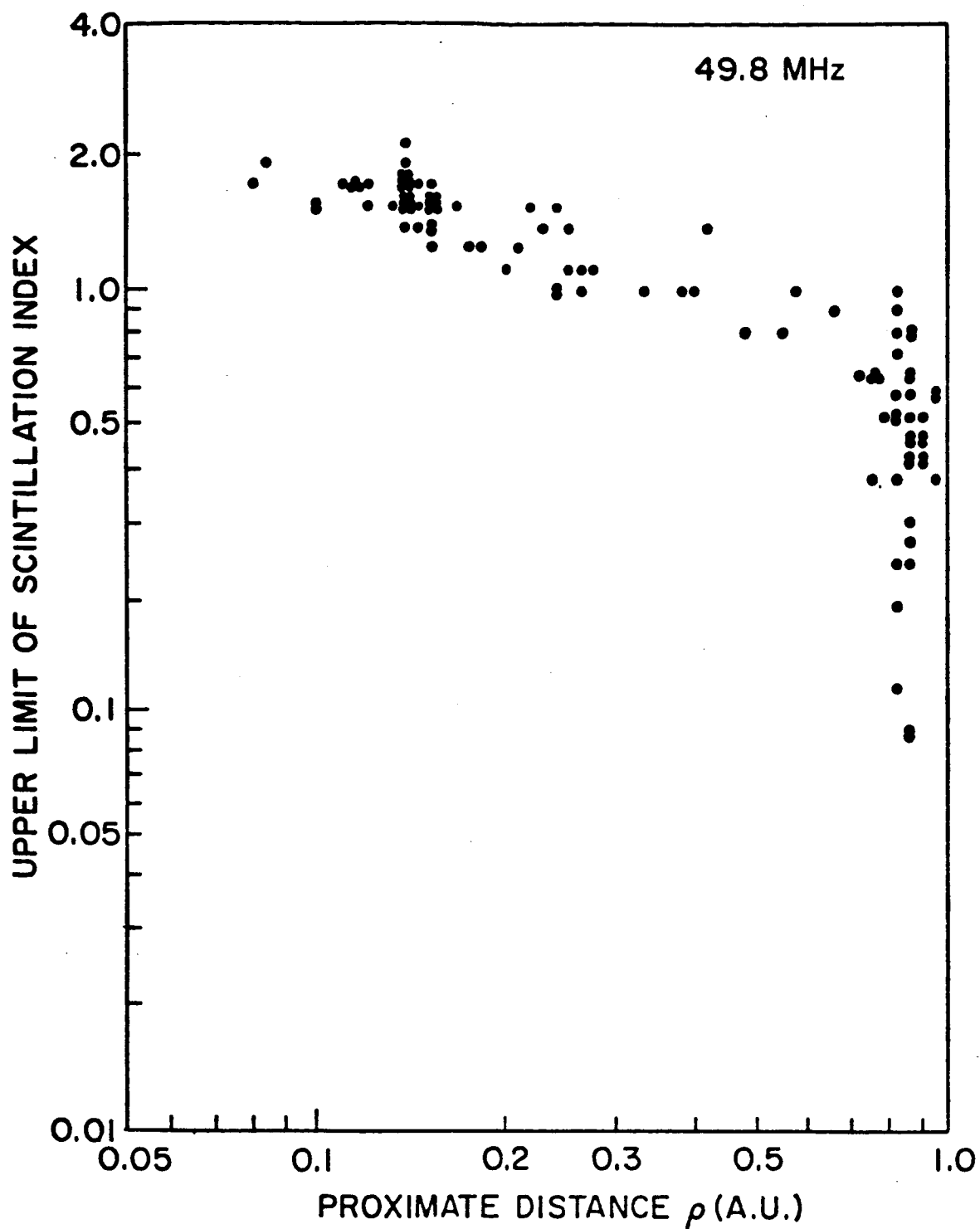


Fig. 5.11. UPPER LIMIT OF SCINTILLATION INDEX  $m$  AT 49.8 MHz VS PROXIMATE DISTANCE  $\rho$ .

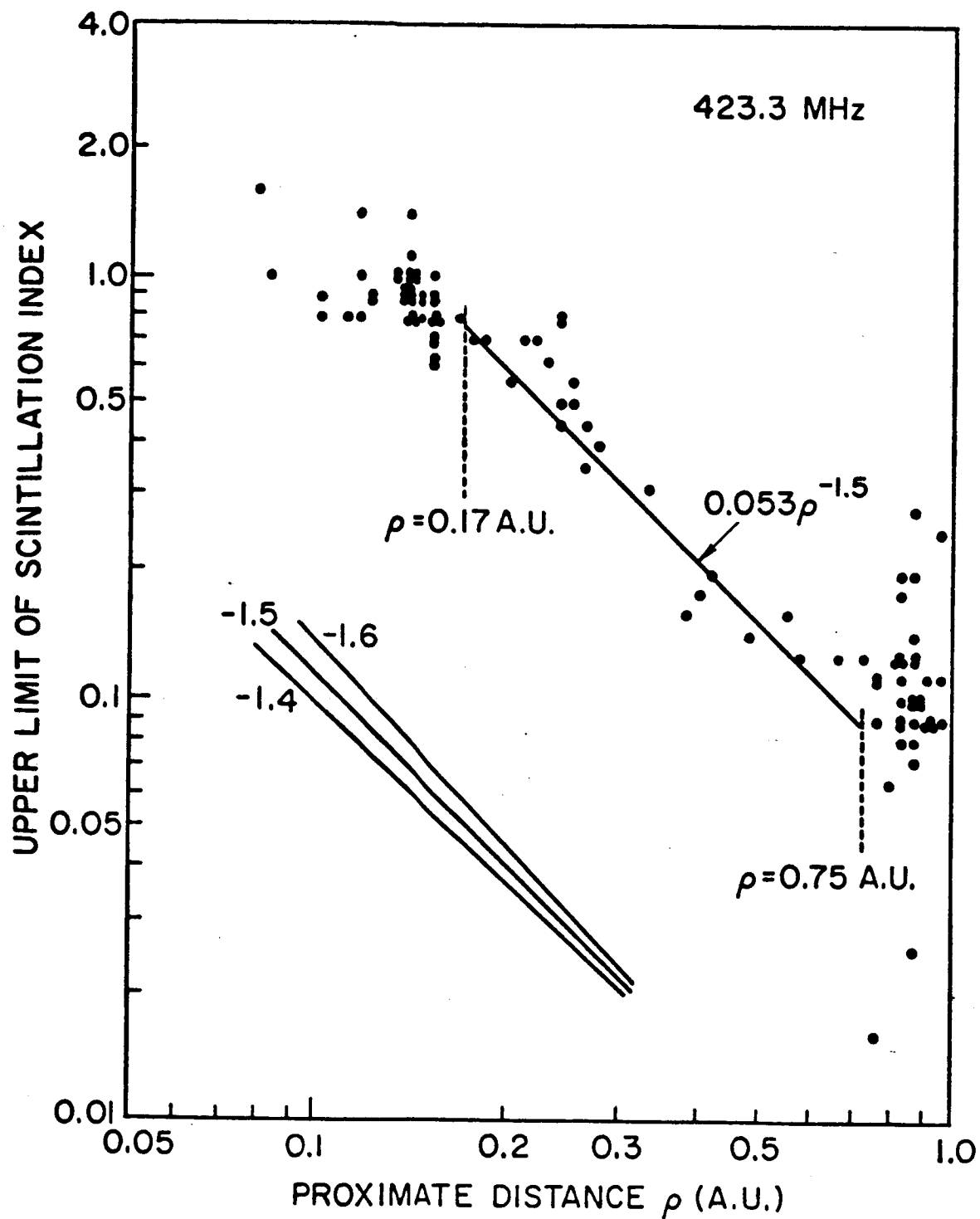


Fig. 5.12a. UPPER LIMIT OF SCINTILLATION INDEX  $m$  AT 423.3 MHz VS PROXIMATE DISTANCE  $\rho$ . The subjective fit ( $0.053\rho^{-1.5}$ ) over  $0.17 < \rho < 0.75 \text{ A.U.}$  and three lines of slopes -1.4, -1.5, and -1.6 are also shown.

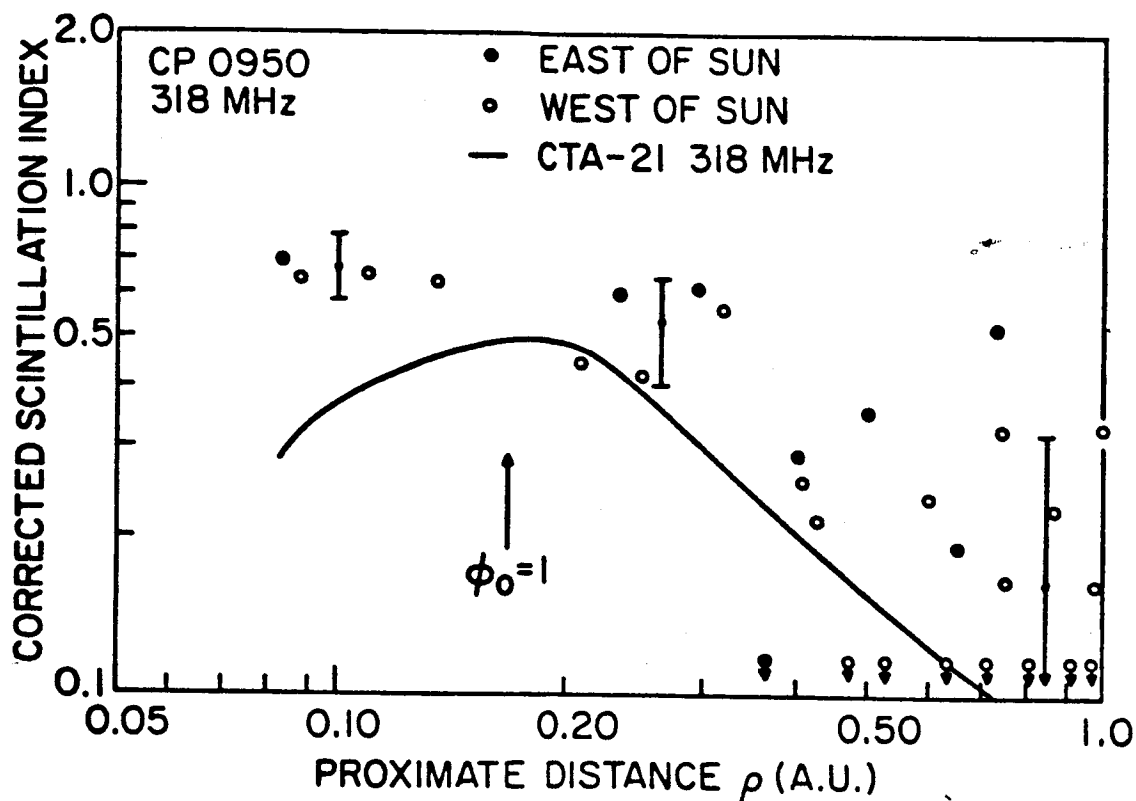


Fig. 5.12b. CORRECTED SCINTILLATION INDEX  $m_p$  OF PULSAR CP0950 DERIVED BY ZEISSIG AND LOVELACE (1972). Intrinsic pulsar noise has been removed. The vertical arrow marked by  $\phi_0 = 1$  divides the weak and strong interplanetary scintillation regimes. The error bars indicate the range of uncertainty for the values of  $m_p$ . The downward pointing arrows indicate that their Eq. (11) gives imaginary values for  $m_p$ . Also shown is the scintillation index of CTA-21 at 318 MHz obtained by Zeissig (1971).

( $\rho > 0.75$  A.U.) are also discarded:

1. In the very weak scintillation regime,  $m$  is normally very small ( $\leq 0.1$ ) and therefore it is difficult to measure accurately.
2. In this regime, there may not exist a dominant scattering region (along the propagation path) of thickness  $L \ll z$  such that the thin-screen model, from which (5.19) is derived, is well-defined.

Then, consider only  $m$  over the region  $0.17 \text{ A.U.} < \rho < 0.75 \text{ A.U.}$  in Fig. 5.12a. Several slopes from  $\rho^{-1.4}$  to  $\rho^{-1.6}$  are shown, and it appears that

$$m \approx 0.053 \rho^{-1.5 \pm 0.1} \quad (5.20)$$

would give a reasonable fit. Substituting (5.20) into (5.19) and neglecting the constant multiplying factor  $\lambda^{\frac{p+2}{4}}$  yields

$$\sqrt{K_N L} z^{\frac{p-2}{4}} \propto \rho^{-1.5 \pm 0.1}$$

Letting, for example,  $p = 3.5$  results in

$$z^{\frac{p-2}{4}} = z^{0.375} \quad (5.21)$$

From the geometry of our experiment, it is learned that for  $0.17 \text{ A.U.} < \rho < 0.75 \text{ A.U.}$ ,  $z^{0.375}$  hardly changes more than about 25% and as a first approximation may be regarded as a constant. To illustrate this point, Table 5.3 tabulates some values of  $\rho$  along with the corresponding values of  $z^{0.375}$ . Thus,

Pass No.	Date	$\rho$ , A.U.	$z^{0.375}$ , km <sup>0.375</sup>
10	10 April 1970	0.41	839
11	30 May 1970	0.41	865
12	29 Aug. 1970	0.38	856
14	21 Oct. 1970	0.24	842
17	27 Oct. 1970	0.22	842
73	13 July 1971	0.18	868
75	25 July 1971	0.20	859
77	9 Aug. 1971	0.24	848
79	13 Aug. 1971	0.25	845
80	14 Aug. 1971	0.26	842
81	15 Aug. 1971	0.27	842
82	16 Aug. 1971	0.27	842
83	3 Sep. 1971	0.34	825
84	9 Oct. 1971	0.48	791
86	2 Nov. 1971	0.56	780
87	5 Nov. 1971	0.57	780
88	23 May 1972	0.65	749
89	7 July 1972	0.72	609

Table 5.3. SOME VALUES OF  $\rho$  ALONG WITH THE CORRESPONDING VALUES OF  $z^{0.375}$ .

$$K_N L \propto \rho^{-3.0 \pm 0.2} \quad (5.22)$$

Assuming the effective thickness  $L$  is proportional to  $\rho$  [Cohen and Gunderman (1969), Cronyn (1972a)] gives rise to

$$K_N \propto \rho^{-4.0 \pm 0.2} \quad (5.23)$$

or

$$\sqrt{K_N} \propto \rho^{-2.0 \pm 0.1} \quad (5.24)$$

which implies that the radial dependence of the root-mean-square electron density fluctuation,  $N_0(\rho)$ , follows approximately an inverse-square law:

$$N_0(\rho) \propto \rho^{-2} \quad (5.25)$$

In contrast to most observations made by using radio stars as sources [see, for example, Cohen et al. (1967), Cohen and Gundermann (1969), and Rickett (1973)], neither Fig. 5.11 (50 MHz) nor Fig. 5.12a (423 MHz) reveals a systematic turnover of the scintillation index with decreasing proximate distance (although there is indication in Fig. 5.11 that the scintillation index increases with decreasing proximate distance at a much slower rate after it exceeds about 1). Moreover, our scintillation index at 423 MHz is about a factor of 6 higher than that at 430 MHz observed by Cohen et al. (Fig. 5, 1967) using 3C 273 as the source. Both discrepancies stated above may be attributed, at least partly, to their use of finite sources (radio stars), instead of a point source, which are subject to angular diameter effects (Sec. II.1).



Another experimental evidence sustaining this point of view comes from IPS observations of the pulsar CP 0950 (which may be regarded as a point source) at 318 MHz by Zeissig and Lovelace (1972). According to Fig. 12b, which is reproduced from Zeissig and Lovelace's Fig. 3, there is again no turnover of  $m$  with decreasing  $\rho$ . Furthermore, a comparison between Figs. 12a and 12b shows that at a fixed  $\rho < 0.75$  A.U., both indices are in rough agreement within a factor of about 2--even though their saturation value ( $\approx 0.7$ ) of the scintillation index is slightly too low in comparison with the theoretically predicted value ( $= 1$ ).

## 2. Scintillation Rate Versus Scintillation Index

Define the scintillation rate  $\nu_s$  as

$$\nu_s = \frac{1}{t_w} \text{ Hz} \quad (5.26)$$

where  $t_w$  in seconds is the width of the autocorrelation function  $A_I(t)$  of intensity fluctuations defined in (2.53). Figs. 5.13 and 5.14 show the relationship between  $m$  and  $\nu_s$  at 50 and 423 MHz, respectively. Similar to Figs. 5.5 and 5.6, there are trends of turnovers. In the small scintillation index ( $m \lesssim 0.8$ ) region, because of the Fresnel filtering and the decrease of the Fresnel frequency, the scintillation rate  $\nu_s$  decreases with the scintillation index  $m$ . For  $m \gtrsim 1$ , strong scattering plays an important role, and the scintillation rate  $\nu_s$  is seen to increase

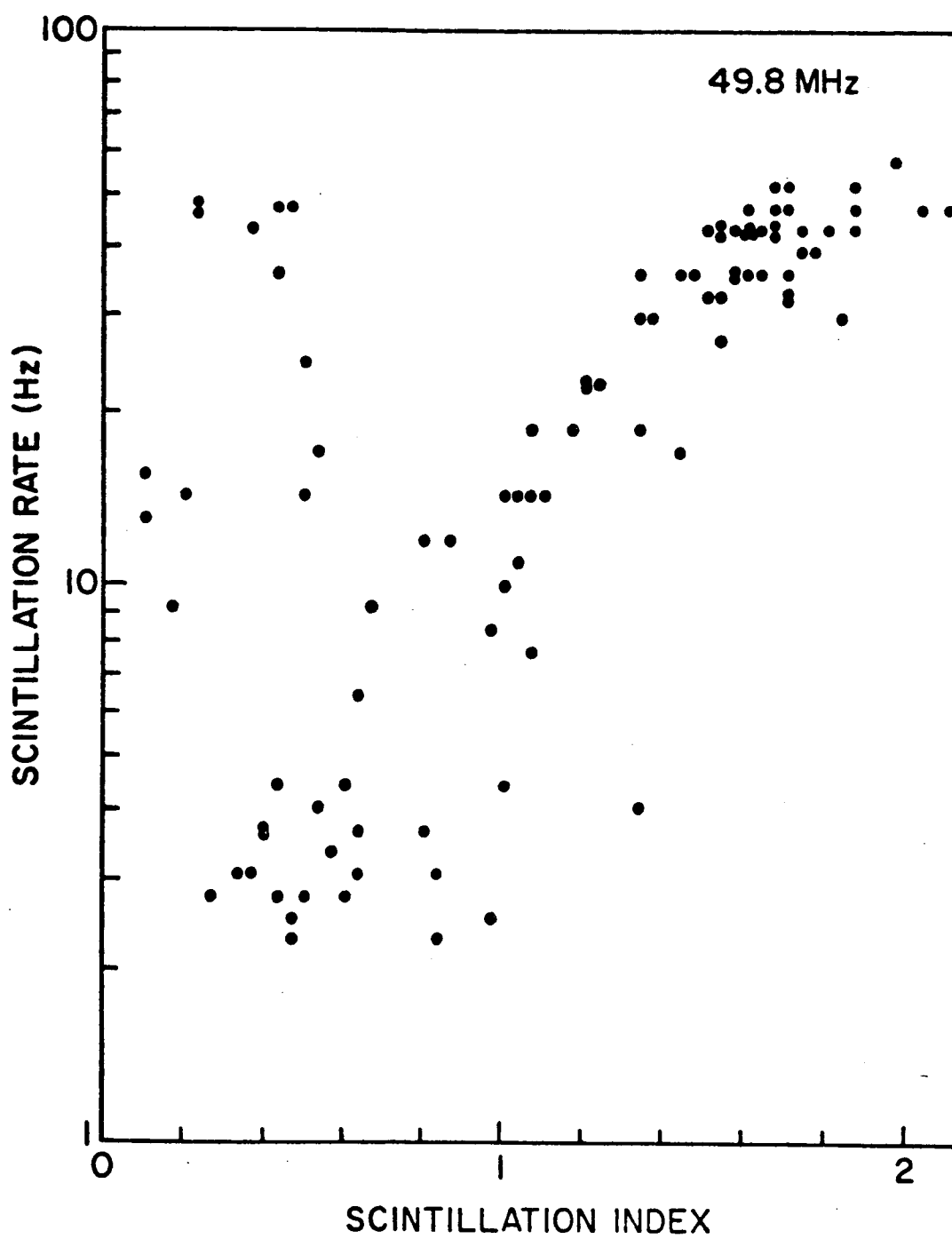


Fig. 5.13. SCINTILLATION RATE VS SCINTILLATION INDEX AT 49.8 MHz.



with the scintillation index.<sup>†</sup> Therefore, one may draw, on the basis of the above results, two interesting conclusions about IPS observed at a fixed frequency:

1. In the weak scintillation regime, stronger scintillations are associated with slower scintillation rates, whereas
2. In the strong scintillation regime, stronger scintillations correspond to faster scintillation rates.

To the author's knowledge, such turnover behavior of  $\nu_s$  (Figs. 5.13 and 5.14), like the turnover behavior of  $r_w$  in Figs. 5.7a and 5.7b is also being experimentally reported here for the first time.

Finally, the wavelength dependence of  $\nu_s$  ( $\propto \frac{1}{r_w}$ ) can be easily inferred from the wavelength dependence of  $r_w$  in (5.18) and (5.15):

$$\nu_s \propto \frac{1}{\sqrt{\lambda}} \quad \text{in the weak scintillation regime}$$

and

$$\nu_s \propto \lambda \quad \text{in the strong scintillation regime}$$

### 3. Wavelength Dependence of Scintillation Index

As mentioned earlier in Sec. C, the wavelength dependence of the scintillation index  $m$  in the weak scintillation regime is still a contested point. The main problem is that simultaneous observations of  $m$  at widely separated frequencies, all in the weak scintillation

---

<sup>†</sup> Recall that the increase of the scintillation rate  $\nu_s$  (or the increase of the spectral width of the scintillation spectra, or the decrease of the scintillation period  $t_s$ ) in the strong scintillation regime had been theoretically<sup>w</sup> predicted by both Lovelace (1970) and Rumsey (1975) using a power-law, thin-screen model.

regime, would unavoidably involve measurements of extremely small  $m$  at higher frequencies; accurate measurements of small  $m$  are often very difficult.

Hewish (1971, 1972) has selected published scintillation indices at four widely different frequencies [81.5, 178, 611, and 2695 MHz, obtained independently by Hewish and Symonds at Cambridge (1969), Harris and Hardebeck at Arecibo (1969), and Bourgois at Nancay (1969)] and derived that

$$m \propto \lambda^{1.0 \pm 0.05} \quad (5.27)$$

over a 30:1 range of wavelength, in the weak scintillation regime. He stressed that (5.27) is not compatible with a power-law spectrum; the reason is that according to power-law model in the weak scintillation regime [see (2.58)]

$$m \propto \lambda^{\frac{p+2}{4}} \quad (5.28)$$

and in order for (5.28) to be consistent with (5.27), the power-law index  $p$  has to be

$$p \approx 2 \quad (5.29)$$

which is too small in comparison with almost all published estimates of  $p$ . Further, using the linear wavelength dependence law (5.27) as the most direct evidence, he [and also Buckley (1971)] proposed a turbulence spectrum containing two distinct components to

reconcile the scintillation data and the in situ spacecraft measurements made by Coleman (1968) and Intriligator and Wolfe (1970): one with large scales of  $\sim 10^6$  km having a power-law form, and the other with small scales of  $\sim 10^2$  km having a gaussian form.

Hollweg and Jokipii (1972) examined the same data utilized by Hewish, plotted  $m\nu^{1.25}$  and  $m\nu$  against the proximate distance, drew individual smooth curves through the data at each frequency, and argued that within the uncertainties<sup>†</sup> of the data

$$m \propto \lambda^{1.25} \quad (5.30)$$

was as good as  $m \propto \lambda$ . Note that (5.30) corresponds to a power-law exponent

$$p = 3.0 \quad (5.31)$$

which is in agreement with Intriligator and Wolfe's (1970) spacecraft-based observations. Rickett (1973), however, pointed out that Hollweg and Jokipii's  $m\nu^{1.25}$  result was not independent of frequency at a fixed proximate distance, and by analyzing mostly the same data he claimed that

$$m \propto \lambda^{1.0 \pm 0.15} \quad (5.32)$$

would be an unbiased fit of these data.

Although Hewish's suggestion that small-scale irregularities (on the order of  $10^2$  km) responsible for IPS possess a gaussian

---

<sup>†</sup> The uncertainties arise mainly from the fact that these indices were measured at different times and at different elongations.

spectrum has been shown to be inadequate on the basis of both Untch's (1973) in situ spacecraft measurements and our scintillation spectra results (Sec. A), the wavelength-dependence law of  $m$  still remains as an unsettled problem. In what follows, an effort to shed light on this problem, using our simultaneously observed scintillation indices at 50 and 423 MHz from a man-made point source, will be presented. First of all, let  $\chi$  denote the exponent of the wavelength-dependence law of  $m$  in the weak scintillation regime:

$$m \propto \lambda^\chi \quad (5.33)$$

Recall that because of the presence of some received intensities below the minimum detectable level, only the lower limit  $m_L$  and the upper limit  $m_U$  of  $m$  at each of our frequencies are known. Therefore, the lower limit  $\chi_L$  of  $\chi$  may be determined from  $m_L^\ell$  (the lower limit of  $m$  at 50 MHz) and  $m_U^\ell$  (the upper limit of  $m$  at 423 MHz) via

$$\frac{m_L^\ell}{m_U^\ell} = \left( \frac{\lambda_L^\ell}{\lambda_U^\ell} \right)^{\chi_L} = 8.5^{\chi_L} \quad (5.34)$$

and, similarly, the upper limit  $\chi_U$  of  $\chi$  may be determined from  $m_U^\ell$  (the upper limit of  $m$  at 50 MHz) and  $m_L^\ell$  (the lower limit of  $m$  at 423 MHz) via

$$\frac{m_U^\ell}{m_L^\ell} = \left( \frac{\lambda_U^\ell}{\lambda_L^\ell} \right)^{\chi_U} = 8.5^{\chi_U} \quad (5.35)$$

The values of  $\chi_L$  and  $\chi_U$  thus obtained are plotted vs the proximate distance  $\rho$  in Figs. 5.15 and 5.16, from which we have excluded those cases when:

- (1)  $m^2 \geq 1$  (corresponding to strong scintillation at 50 MHz)
- (2)  $m^2 < 0.01$  at 50 MHz or 0.001 at 423 MHz (corresponding to less reliable values of  $m$  in view of the minimum resolvable magnitudes of the correction factors in Figs. 4.12 and 4.13.
- (3) the lower and upper limits of  $m$  at either frequency differ by more than a factor of 1.5 (corresponding to  $m$  of great uncertainty)
- (4)  $m$  is derived from data collected during calibration curve experiment in Sec. III.F (corresponding to times when the Stanford receiver is often pushed to its operational limit)

Although instrumental limitations preclude our obtaining accurate values of  $m$  and hence of  $\chi$ , all  $\chi_L$ 's in Fig. 5.15 and most  $\chi_U$ 's in Fig. 5.16 are consistently below 1. A straightforward calculation of the mean and standard deviation over the total of 17 data points yields

$$\chi_L = 0.77 \pm 0.13 \quad (5.36)$$

$$\chi_U = 0.79 \pm 0.15 \quad (5.37)$$

These are even somewhat smaller than Hewish's and Rickett's  $\chi \approx 1$  and are in serious conflict with a thin-screen, power-law model having exponent of turbulence spectrum  $p \approx 3.5$  (Sec. A), which according to (5.28) predicts  $\chi = \frac{p+2}{4} \approx 1.4$ .

The above discrepancy calls for the need to investigate further (both experimentally and theoretically) the scintillation dependence upon wavelength. One theoretical approach which appears to be rewarding



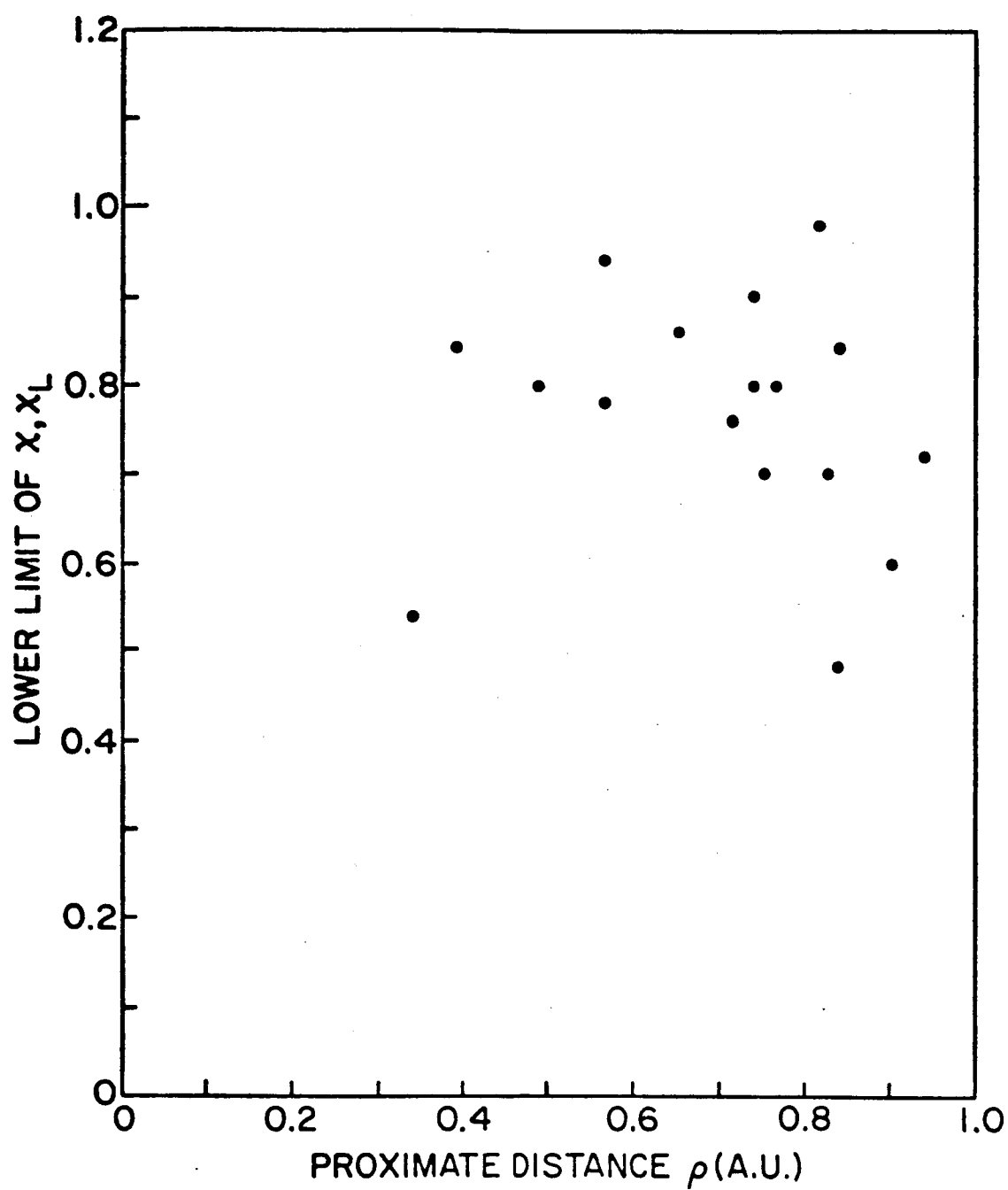


Fig. 5.15. THE LOWER LIMIT OF  $\chi$  VERSUS THE PROXIMATE DISTANCE.

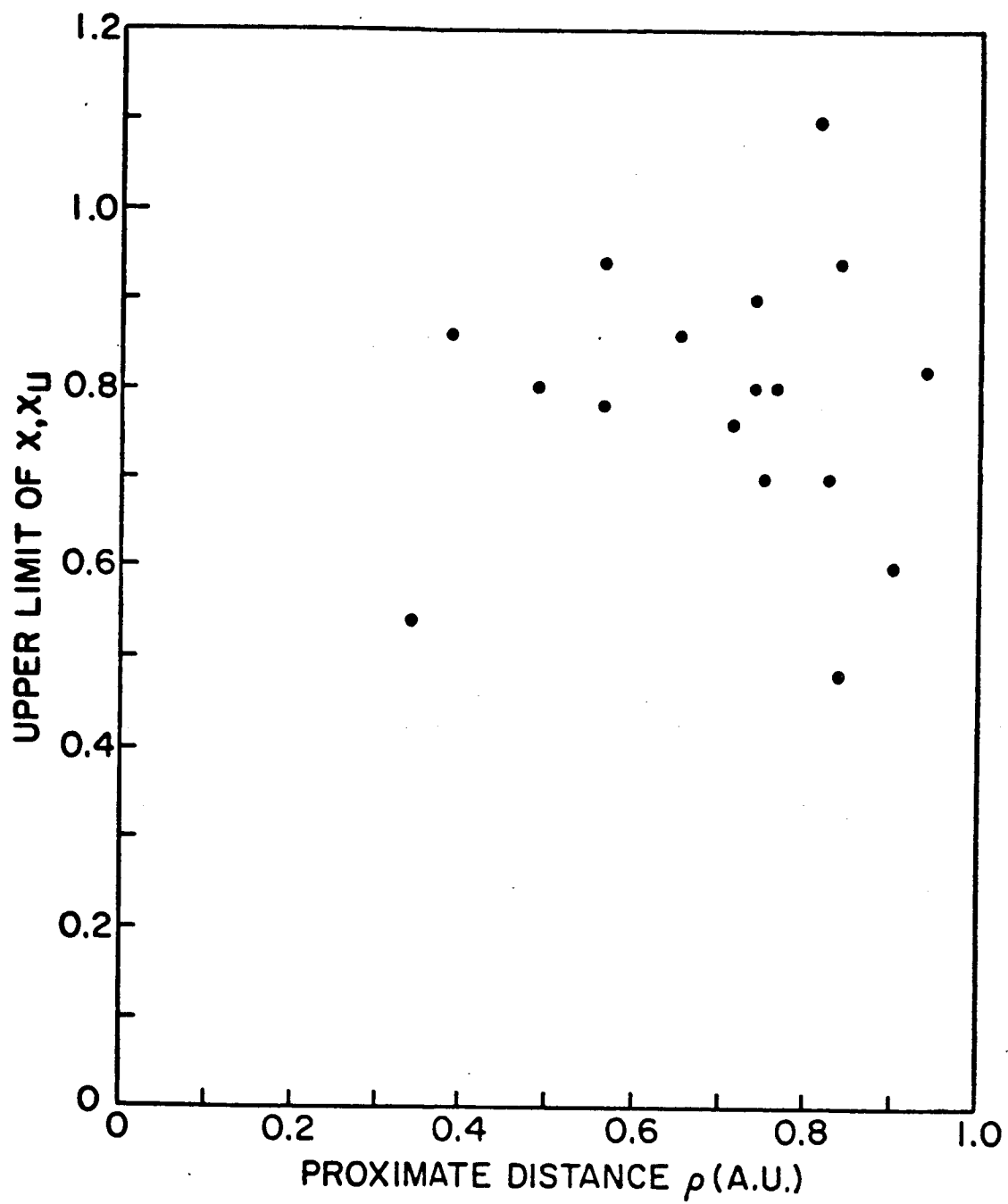


Fig. 5.16. THE UPPER LIMIT OF  $\chi$  VERSUS THE PROXIMATE DISTANCE.

is to include the multiple-scattering effects<sup>†</sup> as proposed by Yeh and Liu (1975), who have found that multiple scattering tends to weaken the frequency dependence of  $m$  so that the exponent  $\chi$  is reduced from  $\frac{p+2}{4}$ .

#### E. Correlation with Integrated Electron Content along the Ray Path

It is generally believed, but not previously measured, that enhanced interplanetary scintillation is associated with enhanced electron content along the ray path, because the energy available to generate instabilities is proportional to the mean plasma density for a given temperature anisotropy [Houminer and Hewish (1972)]. To check if such a belief is indeed true, the integrated electron content  $I$  (Sec. III.H) is plotted vs simultaneous measurement of  $m$  (or  $m_U$  --to be more precise) along the same propagation path in Fig. 5.17. The linear line

$$I \propto m \quad (5.38)$$

seems to give a rather good fit within the scatter of the points, and therefore suggests that IPS observations can be used to monitor the electron content along the propagation path.

To further examine, for a given  $\rho$  of ray path, whether the increases (or decreases) of  $I$  and  $m$  above (or below) their averages are also related, define the averages of  $I$  and  $m$  (at a given  $\rho$ ) as

$$\bar{I} = \frac{1.136 \cdot S}{\rho} \cdot 10^{18} \text{ el/m}^2 \quad (5.39)$$

$$\bar{m} = 0.053 \rho^{-1.5} \quad (5.40)$$

<sup>†</sup> Note that the thin-screen model is effectively a single-scattering model.

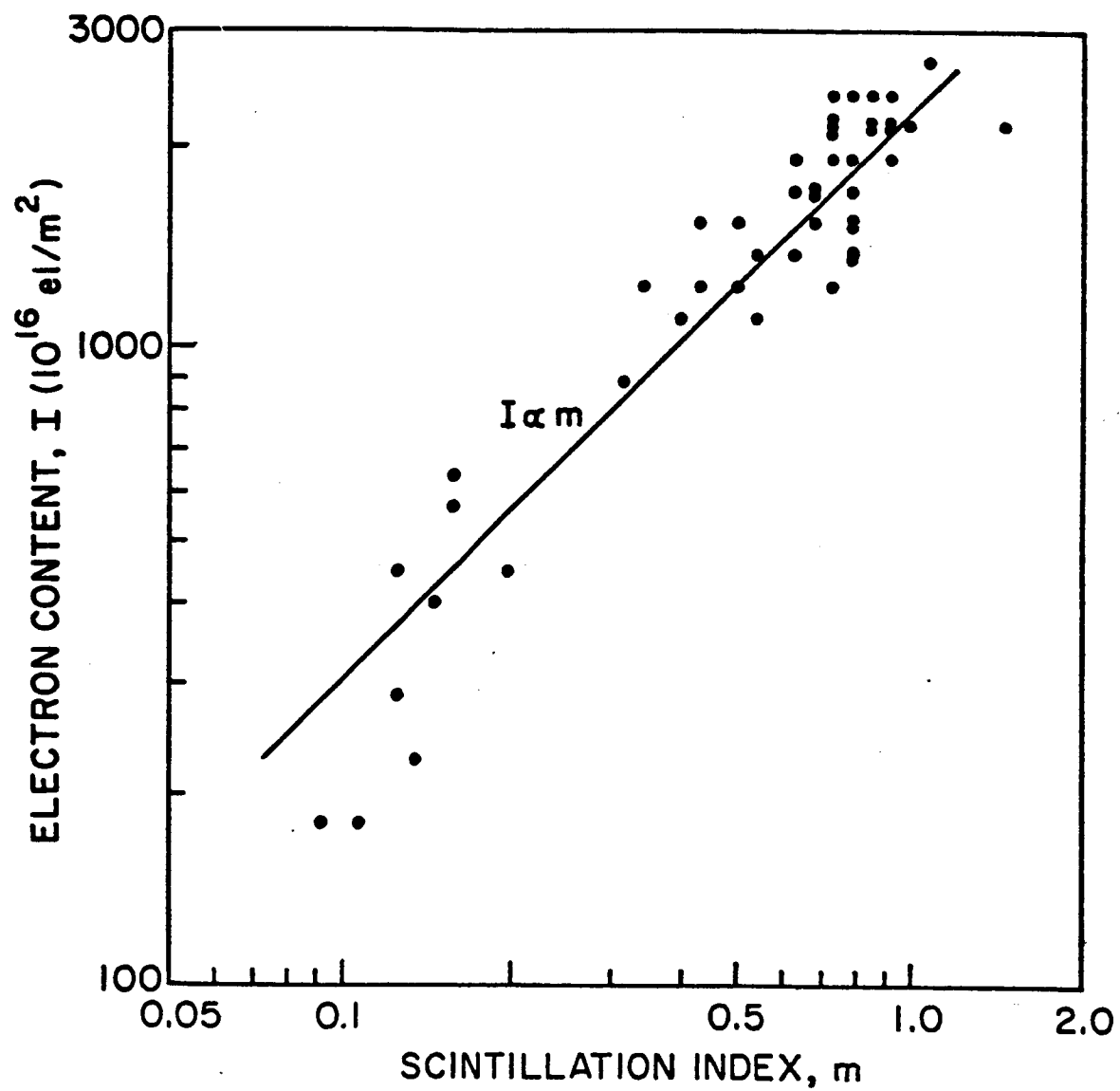


Fig. 5.17. INTERPLANETARY ELECTRON CONTENT VS SCINTILLATION INDEX.

where

$S$  = the earth-sun-Pioneer angle in radian

$\rho$  = the proximate distance of the ray path in A.U.

While (5.40) is simply an empirical equation based upon (5.20), it can be easily shown that (5.39) is in fact derived from

$$\bar{I} = 7.6 \times 10^6 (1.495 \times 10^{11}) \int_{\text{earth}}^{\text{Pioneer}} \rho^{-2} dz \quad (5.41)$$

i.e., from the assumption that the mean electron density of the solar wind, with its value at the earth equal to 7.6 el/cc, are inversely proportional to the square of the radial distance from the sun. Based on these two definitions of  $\bar{I}$  and  $\bar{m}$ , Fig. 5.18 illustrates  $I/\bar{I}$  vs  $m/\bar{m}$ . The strong correlation between  $I/\bar{I}$  and  $m/\bar{m}$  confirms the important conjecture that in the solar wind, enhanced scintillation is closely associated with regions of enhanced electron content (or electron density) along the line of sight. A careful reexamination on this figure appears to suggest that our data points fall into two slightly different groups (one over the upper left half, and the other over the lower right half, of the figure), implying that there may exist two slightly different scattering regimes.

According to Houminer and Hewish (1972, 1974), some of these enhanced density regions may be identified with the compression regions located at the interface between fast and slow solar-wind streams corotating with the sun, and by observing IPS of the regions to the east of the sun, it has already been possible to forecast (up to 6 days in advance) the arrival at the earth of solar wind sectors of enhanced density.

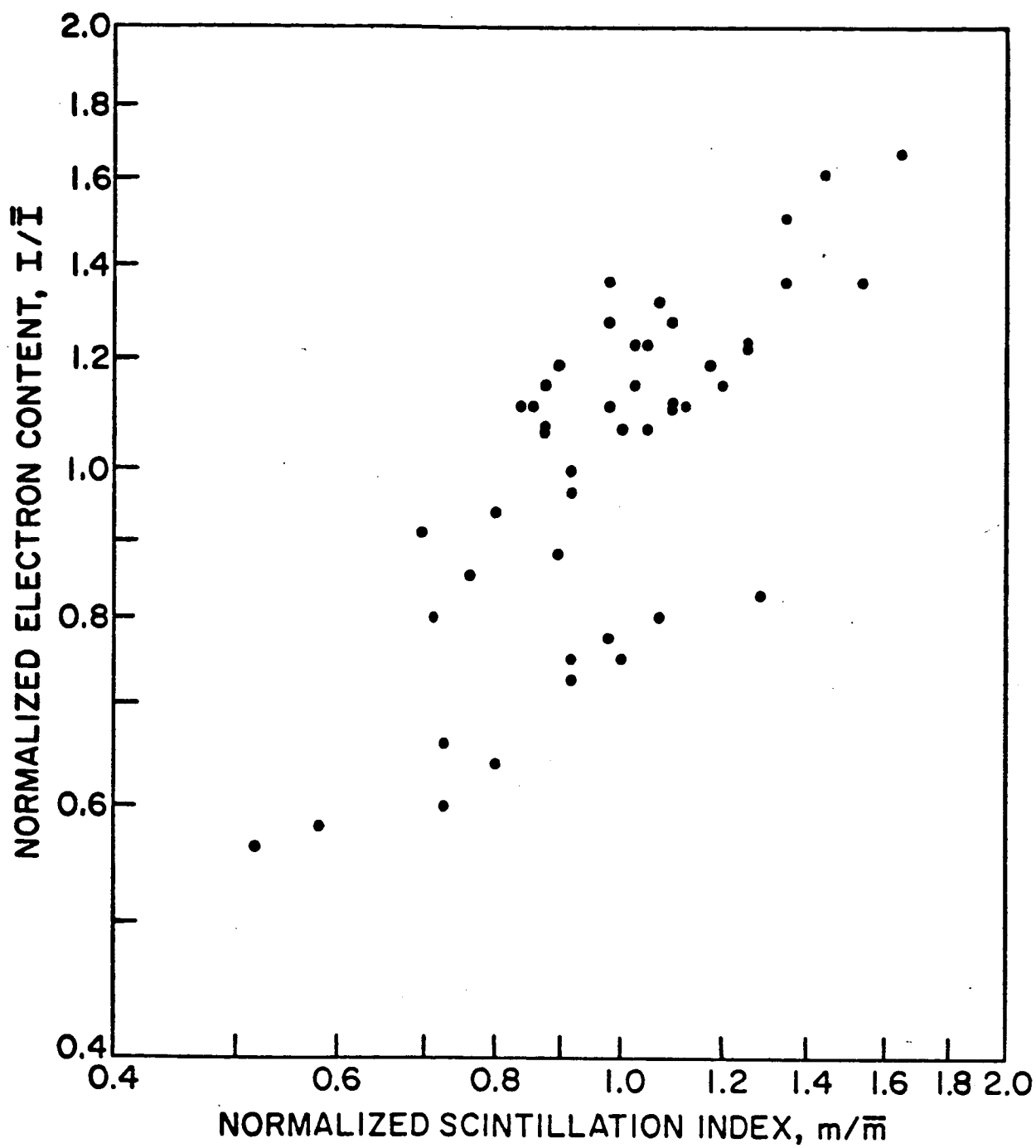


Fig. 5.18. NORMALIZED ELECTRON CONTENT VS NORMALIZED SCINTILLATION INDEX.

## Chapter VI

### CONCLUSIONS AND RECOMMENDATIONS

The existing theory of IPS, based upon the so-called thin-phase-screen approximation, for both weak and strong scintillation regimes has been reviewed and applied to interpret IPS data collected at Stanford during the period 1968-1973. These IPS data were acquired by radiating simultaneously 50- and 423- MHz CW signals from Stanford's 150-ft. parabolic antenna to the sun-orbiting Pioneer 9 spacecraft in the interplanetary space and then telemetering back to the earth. The closest distance of the line-of-sight to the sun ranges from 0.1 to 1 A.U. Experimental apparatus and procedures of data reduction have been described in considerable detail. The inherent ambiguities of the previous IPS data, obtained from observations of quasars or pulsars, were pointed out; and the advantages of the present experiment, stemming mainly from the use of a man-made, point source, were emphasized.

Because the scintillation spectra (i.e., the power spectra of intensity fluctuations) tell directly the structure of small-scale irregularities, they have been carefully estimated and tested for three possible hypothetical forms: power-law, exponential, and gaussian. The logic of a computer program devised to perform such tests was presented, and results of these tests have led to two major conclusions. First, the suggestion of a gaussian micro-structure of interplanetary electron-density fluctuations by Buckley (1971) and Hewish (1971, 1972) is incompatible with the observed spectra. Second, the spatial power spectrum of small-scale electron-density fluctuations at heliocentric distances 0.1-1 A.U. from the sun follows a power law with mean

exponent  $\bar{p} \approx 3.5 \pm 0.13$  and standard deviation  $\sigma_p \approx 0.3$ . This mean value of the power-law exponent  $p$  agrees better with the in situ spacecraft measurements near 1 A.U. than any other scintillation-deduced values of  $p$  (cf. Table 1.1), indicating that IPS observations from a man-made, point source are probably superior to those from radio stars in yielding definite information about the structure of the interplanetary inhomogeneities.

The strong resemblance between the power spectrum of interplanetary magnetic-field fluctuations, reported by Coleman (1968), and that of interplanetary electron-density fluctuations, deduced from our scintillation data and other in situ spacecraft measurements, appears to support plausibly the belief that interplanetary magnetic-field lines are essentially frozen-in to the medium. It is well known that in a perfectly conducting fluid, the magnetic flux lines are frozen into the fluid [see, for example, Cambel (1963) and Sechadri (1973)]. Because the solar wind is highly conducting with a very large magnetic Reynolds number, it is generally believed that magnetic fields present in the interplanetary space are frozen-in to the plasma [Ness (1965), Lüst (1965), Brandt (1970)]. If this is indeed true, then one would expect the power spectra of magnetic-field and electron-density fluctuations to possess the same form such that Kraichnan's (1965) hydromagnetic turbulence theory, which predicts a power-law magnetic-field spectrum of exponent  $p = 3.5$ , may be invoked to account for our scintillation-deduced, electron-density spectra. According to Kraichnan's theory, instabilities first develop at long wavelengths [e.g., as a result of large-scale differential streaming in the solar wind--as suggested by Coleman (1968)] and then cascade down to smaller scale sizes via



nonlinear interactions and equipartition between magnetic and kinetic energy.

We have demonstrated that in cases of very strong scintillations, the observed scintillation spectra tend to be exponential rather than power-law. We have also shown that neither the instrumental effects nor the genuine changes of the turbulence spectrum forms alone can explain the occurrence of these exponential spectra. It appears that these exponential spectra are caused by the very strong wave scattering phenomenon.

Of forty-two 423-MHz scintillation spectra analyzed, all in the range  $\rho = 0.1-0.3$  A.U. and having frequency resolution 0.3 Hz, only eight appeared to have discernible Fresnel structures. The eight solar wind velocities inferred from these structures lie between 400 and 500 km/sec, which are in agreement with the results reported by Lovelace et al. (1970) and Armstrong and Coles (1972). It would certainly be desirable to extend the present single-site experiment to multiple-site observations, so that the solar wind velocities simultaneously determined by the Fresnel-structure method and by the cross-correlation method [e.g., Hewish et al. (1966), Vitkevich and Vlasov (1970), Ekers and Little (1971), Watanabe et al. (1971), Armstrong and Coles (1972)] may be precisely compared. A valuable by-product of multiple-site observations is, of course, to yield information about the ellipticity of the diffraction pattern and therefore that of interplanetary irregularities.

The radial dependence of the correlation length  $r_w$  has been shown to be compatible with the power-law model of exponent 3.5; however, the wavelength dependence of  $r_w$  and that of the scintillation index  $m$  remain unexplained. It is hoped that improved multi-

frequency experiments (e.g., simultaneously at 100, 200, 400, 800, and 1600 MHz) with well-calibrated receivers and further theoretical work (e.g., taking into account the effect of multiple scattering) will help to clarify this question in the near future.

Although the scintillation index  $m$ , calculated from out point-source data and corrected for receiver noise effects, tends to saturate around 1 in the strong scintillation regime, no systematic turnover of  $m$  with  $\rho$  has been observed. This is in contrast to most previously published results using quasars as sources, but agrees well with the theoretical prediction. The radial dependence of  $m$ ,  $m \propto \rho^{-1.5}$ , in the weak scintillation regime was interpreted as a manifestation of  $\Delta N \propto \rho^{-2.0}$ ,  $\Delta N$  being the rms electron density fluctuation.

The cross correlation analysis between the integrated electron content  $I$  and  $m$  has disclosed that not only these two parameters but also their deviations from means are approximately linearly related. This suggests that IPS measurements from an appropriate point source provide an important method for monitoring the density and density fluctuation of the solar wind. A profitable extension of the present experiment would be more frequent observations, so that the relation of IPS to the solar activity [e.g., Vitkevich and Vlasov (1972)] and to the corotating sectors of enhanced density [see, for example, Dennison and Wiseman (1968), Houminer (1971), Watanabe et al. (1972), Houminer and Hewish (1972, 1974)] may be studied on a day-to-day basis.

## Appendix A

### SIMPLIFICATION OF THE INTEGRAL Q

To simplify the following integral:

$$Q = \int_{-L/2}^{L/2} dx \int_{-L/2}^{L/2} dy f(x-y)$$

we transform the variables from  $(x,y)$  to  $(\alpha,\beta)$  by letting

$$\alpha = x - y$$

and

$$\beta = \frac{1}{2} (x+y)$$

In terms of new variable  $\alpha$  and  $\beta$ ,

$$x = \frac{1}{2} \alpha + \beta$$

$$y = -\frac{1}{2} \alpha + \beta$$

$$dx dy = \frac{\partial (x,y)}{\partial (\alpha,\beta)} d\alpha d\beta = \begin{vmatrix} \frac{\partial x}{\partial \alpha} & \frac{\partial x}{\partial \beta} \\ \frac{\partial y}{\partial \alpha} & \frac{\partial y}{\partial \beta} \end{vmatrix} d\alpha d\beta = \begin{vmatrix} \frac{1}{2} & 1 \\ -\frac{1}{2} & 1 \end{vmatrix} d\alpha d\beta = d\alpha d\beta$$

and the integral Q becomes

$$Q = \int_{-L/2}^{L/2} d\beta \int_{\alpha_1}^{\alpha_2} f(\alpha) d\alpha$$

where, as illustrated in Fig. A.1,

$$\alpha_1 = \begin{cases} -L - 2\beta & ; & -L/2 \leq \beta \leq 0 \\ -L + 2\beta & ; & 0 \leq \beta \leq L/2 \end{cases}$$

and

$$\alpha_2 = \begin{cases} L + 2\beta & ; & -L/2 \leq \beta \leq 0 \\ L - 2\beta & ; & 0 \leq \beta \leq L/2 \end{cases}$$

If  $f(\alpha)$  is an autocorrelation function having correlation length  $\ell$  (i.e.,  $|f(\alpha)| \approx 0$  for  $\alpha > \ell$ ) and if  $\ell \ll L$ ,  $Q$  can be approximated by

$$Q \approx \int_{-L/2}^{L/2} d\beta \int_{-\infty}^{\infty} d\alpha f(\alpha) = L \int_{-\infty}^{\infty} d\alpha f(\alpha)$$

which completes the simplification.

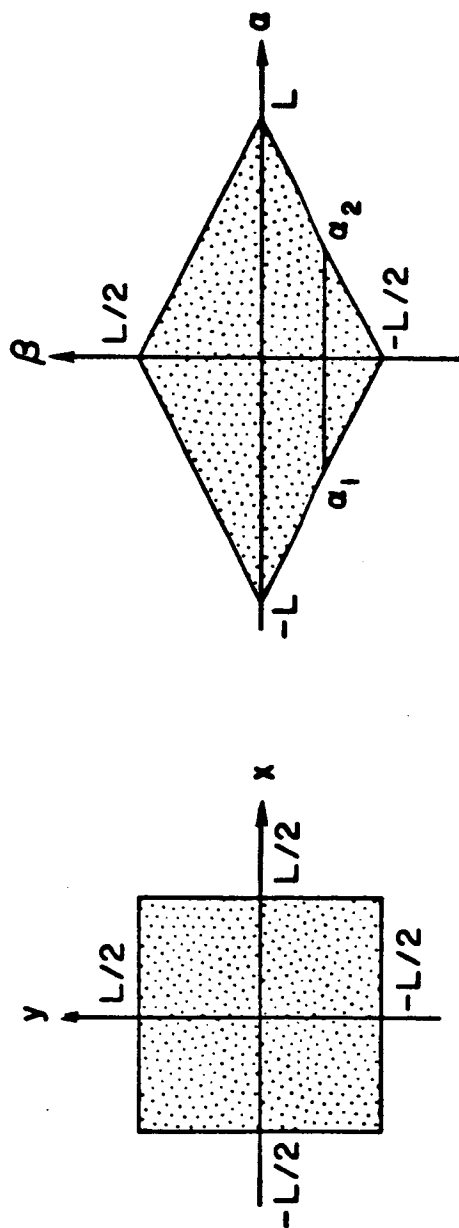


Fig. A.1. REGIONS OF INTEGRATION BEFORE AND AFTER THE COORDINATE TRANSFORMATION.

## Appendix B

### PROCEDURE OF DERIVING RECEIVING ANTENNA PATTERNS

Because the Stanford receiving system on board the Pioneer 9 spacecraft was originally designed for the purpose of interplanetary electron-content measurement, not for IPS study, the receiving antenna patterns at 49.8 and 423.3 MHz were not measured prior to launch (although certain on-ground measurements of small-scale model patterns were made during the design phase of the receiving antennas). As a consequence, the receiving antenna patterns could only be derived from in-flight Format D data (Sec. III.D). In doing so, one of the major difficulties encountered arose from the fact that Format D data is not a measure of input signal power  $S_i$ , but rather is a measure of input signal-to-noise power ratio  $S_i/N_i$ , where both  $S_i$  and  $N_i$  are functions of the receiving antenna pattern  $A(\psi, \theta)^\dagger$ . In particular,  $S_i$  may be expressed as

$$S_i = \left( \frac{S_i}{N_i} \right) \cdot N_i = A(\psi, \theta=0) \cdot I \propto A(\psi, \theta=0) \quad (\text{B.1})$$

where  $I$  (assumed to be constant for days when IPS are negligible) is the arrived signal power (or intensity) at the spacecraft, and  $\theta$  is set to zero because the signal source, earth, is in the plane of ecliptic.

Fortunately, a rough estimation indicates that

$$\frac{(N_i)_{\max}}{(N_i)_{\min}} \approx 0.3 \text{ dB (49.8 MHz) or } 0.2 \text{ dB (423.3 MHz)}$$

---

<sup>†</sup> See Fig. D.1 for definitions of the angles  $\psi$  and  $\theta$ .

which is much smaller than

$$\frac{(S_i)_{\max}}{(S_i)_{\min}} = \frac{[A(\psi, \theta=0)]_{\max}}{[A(\psi, \theta=0)]_{\min}} \approx 4 \text{ dB (49.8 MHz) or } 7 \text{ dB (423.3 MHz)}$$

Therefore,  $N_{i0}$ , the zero-th order approximation of  $N_i$ , may be regarded as a constant

$$N_{i0} = N = \text{constant}$$

to yield  $S_{i0}$  and  $A_0(\psi, \theta=0)$ , the zero-th order approximations of  $S_i$  and  $A(\psi, \theta=0)$ :

$$S_{i0} = \underbrace{\left( \frac{S_i}{N_i} \right)}_{\text{Format D output}} \cdot N_{i0} \propto A_0(\psi, \theta=0) \quad (\text{B.2})$$

Note that (D.4c) may be used to determine the constant of proportionality for  $A_0(\psi, \theta=0)$  in (B.2). Furthermore, the assumption (see the footnote on p. 189)

$$A(\psi, \theta \neq 0) \propto A(\psi, \theta=0) \quad (\text{B.3})$$

along with (D.4b) enables the computation of  $A_0(\psi, \theta \neq 0)$  from  $A_0(\psi, \theta=0)$ .

Once  $A_0(\psi, \theta)$  is known, the first-order approximation  $T_1$  of the total received noise temperature  $T$  can then be calculated via procedures described in Sec. III.G to give rise to  $N_{i1}$ , the first-order approximation of  $N_i$  [see (3.13)]:

$$N_{i1} = kBT_1 \quad (\text{B.4})$$

Replacing  $N_{i0}$  in Eq. (B.2) with  $N_{i1}$  (and later with  $N_{i2}, N_{i3}, \dots$ ) and iterating the process between Eqs. (B.2) and (B.4) results in  $A_1(\psi, 0) [A_2(\psi, \theta), A_3(\psi, 0), \dots]$ . A more detailed description of such a procedure is illustrated by the flow chart in Fig. B.1, where subscript  $n$  ( $= 1, 2, 3, \dots$ ) denotes the  $n$ -th order approximation. Note that Format D data on 9 Feb. 1969 (ninety days after launch) was chosen as the base record for deriving receiving antenna patterns because 9 Feb. 1969 was the date on which Pioneer 9 spacecraft was very close to the earth ( $\approx 0.14$  A.U.), IPS effect appeared to be negligible, and the arrived signal intensity  $I$  was steadier than any other days.

As  $n$  increases,  $A_n(\psi, \theta)$  at either 49.8 or 423.3 MHz converges so rapidly that for all values of  $\psi$  and  $\theta$ ,

$$\underbrace{|10 \log A_7(\psi, \theta) - 10 \log A_6(\psi, \theta)|}_{A_7(\psi, \theta) \text{ in dB} \quad A_6(\psi, \theta) \text{ in dB}} \leq 10^{-4} \text{ dB}$$

or, equivalently,

$$1 - 2 \times 10^{-5} \leq \frac{A_7(\psi, \theta)}{A_6(\psi, \theta)} \leq 1 + 2 \times 10^{-5}$$

Thus, the seventh order patterns  $A_7^{\ell}(\psi, \theta)$  and  $A_7^{\ell}(\psi, \theta)$  at 49.8 and 423.3 MHz respectively were selected to be the final receiving antenna patterns, whose values in dB, in the ecliptic plane (i.e.,  $\theta=0$ ), are shown in Fig. 3.4. A detailed listing of these values is provided in Tables B.1 and B.2, where all numbers are read from left to right and then top to bottom. For example in Table B.1,  $A^{\ell}(\psi=1^{\circ}) = 3.7337$  dB,  $A^{\ell}(\psi=8^{\circ}) = 3.5461$  dB,  $A^{\ell}(\psi=9^{\circ}) = 3.5070$  dB, etc.



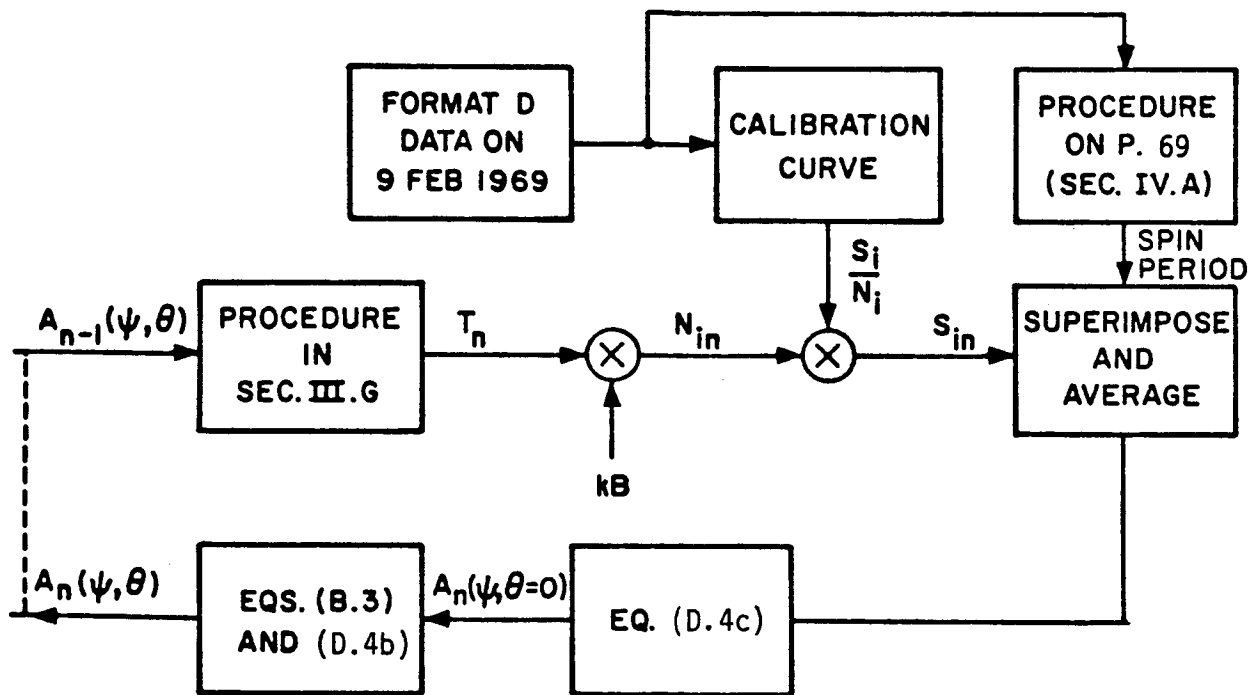


Fig. B.1. PROCEDURE OF DERIVING RECEIVING ANTENNA PATTERNS.

3.7337	3.7167	3.6963	3.6726	3.6456	3.6155	3.5823	3.5461
3.5070	3.4650	3.4198	3.3682	3.3137	3.2566	3.1970	3.1350
3.0700	2.9978	2.9238	2.8478	2.7701	2.6902	2.6078	2.5242
2.4396	2.3546	2.2682	2.1817	2.0950	2.0087	1.9219	1.8358
1.7502	1.6659	1.5826	1.5003	1.4199	1.3414	1.2652	1.1912
1.1199	1.0513	0.9857	0.9229	0.8638	0.8078	0.7557	0.7071
0.6623	0.6218	0.5851	0.5529	0.5244	0.5006	0.4809	0.4661
0.4554	0.4495	0.4480	0.4512	0.4590	0.4712	0.4881	0.5092
0.5351	0.5649	0.5994	0.6377	0.6803	0.7266	0.7770	0.8309
0.8883	0.9493	1.0131	1.0804	1.1502	1.2230	1.2977	1.3751
1.4544	1.5353	1.6178	1.7015	1.7864	1.8713	1.9570	2.0429
2.1290	2.2140	2.2987	2.3825	2.4654	2.5471	2.6269	2.7052
2.7814	2.8558	2.9265	2.9941	3.0590	3.1212	3.1802	3.2357
3.2837	3.3284	3.3699	3.4077	3.4421	3.4728	3.4998	3.5227
3.5409	3.5542	3.5639	3.5698	3.5720	3.5704	3.5650	3.5559
3.5430	3.5265	3.5062	3.4803	3.4503	3.4165	3.3788	3.3376
3.2927	3.2444	3.1929	3.1357	3.0727	3.0065	2.9374	2.8655
2.7906	2.7116	2.6304	2.5473	2.4623	2.3752	2.2867	2.1971
2.1066	2.0149	1.9225	1.8300	1.7377	1.6451	1.5531	1.4618
1.3717	1.2828	1.1956	1.1100	1.0263	0.9446	0.8653	0.7884
0.7140	0.6422	0.5731	0.5070	0.4436	0.3832	0.3257	0.2711
0.2193	0.1703	0.1241	0.0804	0.0391	-0.0000	-0.0370	-0.0733
-0.1082	-0.1419	-0.1746	0.0005	0.0095	0.0210	0.0352	0.0523
0.0727	0.0963	0.1234	0.1541	0.1885	0.2267	0.2686	0.3143
0.3637	0.4167	0.4734	0.5336	0.5973	0.6641	0.7340	0.8070
0.8826	0.9608	1.0413	1.1240	1.2087	1.2949	1.3824	1.4711
1.5607	1.6509	1.7415	1.8320	1.9224	2.0117	2.1002	2.1877
2.2739	2.3579	2.4399	2.5200	2.5978	2.6730	2.7451	2.8144
2.8807	2.9437	3.0025	3.0569	3.1076	3.1547	3.1978	3.2370
3.2721	3.3014	3.3253	3.3453	3.3614	3.3734	3.3815	3.3855
3.3856	3.3817	3.3738	3.3621	3.3465	3.3272	3.3042	3.2777
3.2475	3.2141	3.1771	3.1341	3.0877	3.0383	2.9860	2.9309
2.8731	2.8130	2.7494	2.6833	2.6154	2.5459	2.4749	2.4026
2.3288	2.2543	2.1793	2.1040	2.0285	1.9524	1.8768	1.8020
1.7279	1.6547	1.5824	1.5118	1.4429	1.3759	1.3111	1.2488
1.1889	1.1319	1.0777	1.0266	0.9788	0.9344	0.8936	0.8564
0.8230	0.7934	0.7679	0.7465	0.7291	0.7159	0.7069	0.7024
0.7020	0.7061	0.7142	0.7269	0.7436	0.7649	0.7900	0.8196
0.8528	0.8903	0.9317	0.9765	1.0254	1.0774	1.1331	1.1917
1.2537	1.3183	1.3858	1.4557	1.5282	1.6026	1.6790	1.7572
1.8367	1.9172	1.9985	2.0810	2.1639	2.2466	2.3292	2.4120
2.4941	2.5758	2.6563	2.7357	2.8141	2.8909	2.9648	3.0362
3.1059	3.1732	3.2384	3.2968	3.3516	3.4035	3.4527	3.4991
3.5424	3.5799	3.6130	3.6434	3.6705	3.6944	3.7150	3.7323
3.7462	3.7568	3.7639	3.7674	3.7677	3.7644	3.7576	3.7474

Table B.1. 49.8 MHz RECEIVING ANTENNA PATTERN  $A^{\lambda}(\psi, \theta=0^{\circ})$  IN dB,  
FOR  $\psi = 1^{\circ}$  TO  $360^{\circ}$  IN STEPS OF ONE DEGREE.

2.9346	2.5702	2.7442	2.9210	2.6617	2.6746	2.6884	2.7067
2.5674	2.6931	2.8075	2.3394	2.4511	2.5585	2.7613	3.0015
3.2421	2.7995	2.7946	2.7914	2.7902	2.8557	3.0313	3.2063
2.9416	2.9822	3.0256	2.9178	2.8473	2.8474	2.7070	2.6854
2.6638	2.6416	2.4818	2.3245	2.1691	2.5074	2.5039	2.5027
2.4226	2.4094	2.3969	2.3848	2.3227	2.2570	2.1916	1.9845
2.1426	2.3091	1.9517	1.9084	1.8664	1.8257	1.6802	1.5321
1.3815	1.0937	1.1186	1.1426	0.9864	1.0964	1.2063	1.2300
1.1099	0.9824	0.8412	0.8274	0.8186	0.8096	0.5620	0.6183
0.6739	0.5911	0.4590	0.3262	0.5853	0.3334	0.3325	0.6759
0.3251	0.3240	0.3244	0.6666	0.1497	-0.3648	0.1903	0.0241
-0.1451	-0.3110	-0.4494	-0.5868	-0.7235	-0.4946	-0.9543	-1.4305
-1.5357	-1.8854	-2.2567	-1.8352	-1.8398	-1.8449	-1.8475	-2.2700
-2.1052	-1.9414	-1.6005	-1.4664	-1.3512	-0.9492	-0.8631	-0.7744
-0.7758	-0.6633	-0.5493	-0.4306	-0.1982	0.0366	0.2628	0.1429
0.2575	0.3743	0.5203	0.5624	0.6017	0.8030	0.9703	0.9400
0.9417	0.9149	0.8818	0.8526	0.9357	0.9983	1.0592	1.1193
1.0188	0.9194	1.3144	1.2248	1.1292	1.0390	1.1393	1.2365
1.3326	1.4655	1.4233	1.3864	1.3518	1.2315	1.2319	1.2298
1.5377	1.5831	1.6324	1.6988	1.8241	1.9508	1.6237	1.7393
1.8545	1.9993	2.0565	2.1212	2.1895	2.2582	2.3254	2.3978
2.4734	2.5397	2.6088	2.6872	2.7541	2.8204	2.8903	2.9603
3.0276	3.1010	2.9852	3.3232	3.4472	3.3785	3.3829	3.3896
3.8797	3.8742	3.8677	3.8672	3.8999	3.9338	3.9708	4.4775
4.4266	4.3725	4.3527	4.4113	4.4684	4.2274	4.2308	4.2317
4.2372	4.4616	4.2337	4.0044	4.0513	3.8544	3.6477	3.5440
3.3755	3.2071	2.8571	2.5071	2.2283	2.0912	2.1684	2.0483
1.9292	1.8553	1.7020	1.5478	1.5471	1.4845	1.4204	1.3552
1.5380	1.5021	1.4692	1.4298	1.5307	1.6299	1.2236	1.3491
1.4721	1.5916	1.7449	1.9002	2.0638	1.9849	2.1017	2.2220
2.1392	2.3063	2.4717	2.5567	2.6915	2.8272	2.9582	3.0912
3.2139	3.3348	3.0515	3.1705	3.2779	3.4262	3.3774	3.3289
3.8831	3.8800	3.8772	3.8746	3.9471	3.9628	3.9748	3.8870
3.9852	4.0809	3.8514	3.9659	4.0783	4.1377	4.0771	4.0740
3.8475	3.9746	3.9139	3.8529	3.9287	4.0067	4.0839	4.0096
3.9135	3.8208	3.7230	3.6612	3.6005	3.5408	3.6922	3.4809
3.2562	3.0773	3.1143	3.1504	2.8707	2.7818	2.6893	2.5957
2.4559	2.2876	2.1191	2.5406	2.1058	1.7054	1.8841	1.8188
1.7511	1.6826	1.7254	1.7694	1.8060	2.0149	1.7559	1.5058
1.7326	1.7741	1.8106	1.5845	1.5985	1.6114	1.6252	1.8050
1.8091	1.8126	1.6127	1.6022	1.5927	1.5210	1.3625	1.2059
0.9946	0.8990	0.7981	0.6962	0.5642	0.6502	0.7361	0.5709
0.7409	0.9108	0.4057	0.5807	0.7508	1.0007	0.9232	0.8589
0.7945	0.9312	1.2505	1.5661	1.3457	1.4631	1.5742	1.6738
1.9399	2.2093	1.6695	2.2098	2.1702	2.1342	2.2148	2.5236

Table B.2. 423.3 MHz RECEIVING ANTENNA PATTERN  $A^*(\psi, \theta=0^\circ)$  IN dB,  
FOR  $\psi = 0^\circ$  TO  $359^\circ$  IN STEPS OF ONE DEGREE.

## Appendix C

### DIGITAL ERRORS OF A/D CONVERSION DUE TO THE SUN PULSE

As was pointed out in Sec. III.D, the occurrence of the sun pulse, unlike the sampling of the sampler, is not controlled by any timing signal from the spacecraft telemetry subsystem; the sun pulse is energized (and hence the Format D output is quashed) whenever the sun sensor of the spacecraft points to the sun (approximately once per second). As a result, the quashing of the Format D output takes place asynchronously with the subsequent A/D conversion, thereby creating digital errors at the output of the A/D converter. This appendix is intended to give a brief account of these errors.

Recall from Secs. III.D and E that each Format D output is transformed by the A/D converter into a 6-bit binary number and then appended with a parity-check bit to form a 7-bit telemetry word. The relationship between the word rate pulse and bit rate pulse is shown in Fig. C.1 [see Fig. B.2 of Koehler (1965)], where  $T_m$  ( $m = 1, 2, \dots, 7$ ) denotes the time at which the  $i^{\text{th}}$  bit shifts to the  $(i+1)^{\text{th}}$  bit. The process of A/D conversion is carried out by a 6-bit successive-approximation converter.<sup>†</sup> In general, the operation of a  $k$ -bit successive-approximation converter can be mathematically described as follows. Let  $x$  designate the analog input to the converter and  $b_1 b_2 \dots b_k$  be the binary output,  $b_1$  and  $b_k$  being the most and least significant bits, respectively. During the time interval  $T_{m-1} \leq t < T_m$  of the  $m$ -th bit conversion, the converter supplies--via an appropriate feedback circuit--a reference voltage  $v_m$  for

---

<sup>†</sup> See Cadzow and Martens (1970) and Peatman (1972) for discussions of the so-called successive-approximation method.

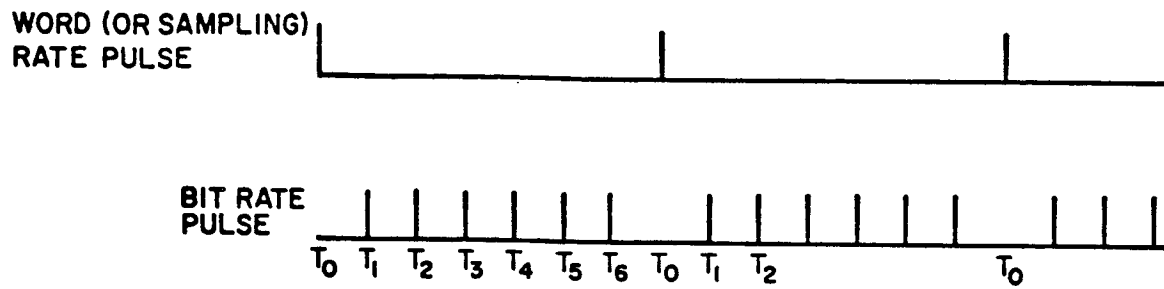


Fig. C.1. RELATIONSHIP BETWEEN WORD AND BIT RATE PULSES.

comparison with  $x$ . The value of the  $m$ -th bit  $b_m$  is then given by

$$b_m = \begin{cases} 1 & \text{if } x \geq v_m \text{ at } t = T_{m-1} \\ 0 & \text{if } x < v_m \text{ at } t = T_{m-1} \end{cases} ; m = 1, 2, \dots, k \quad (C.1)$$

where 
$$v_1 = 2^{k-1} \quad (C.2)$$

and 
$$v_m = v_{m-1} \begin{cases} +2^{k-m} & \text{if } x \geq v_{m-1} \text{ at } t = T_{m-2} \\ -2^{k-m} & \text{if } x < v_{m-1} \text{ at } t = T_{m-2} \end{cases} ; m = 2, 3, \dots, k \quad (C.3)$$

Under normal operating conditions, the sample-and hold circuit holds the values of  $x$  constant over the entire period of each conversion (i.e., over  $T_0 \leq t < T_k$ ) so that the resulting binary output  $b_1 b_2 \dots b_k$  can approximate  $x$  with an accuracy of the value of the least significant bit (LSB). An example for  $k = 6$  and  $x = 23.5$  is illustrated in Fig. C.2, where the values of  $v_m$  are derived from Eqs. (C.2) and (C.3). Based on Eq. (C.1), Table C.1 lists the resultant values of  $b_m$  and the corresponding reasons. Note that  $b_1 b_2 b_3 b_4 b_5 b_6 = 010111$  has a decimal value of 23, which is approximately equal to  $x$  ( $= 23.5$ ).

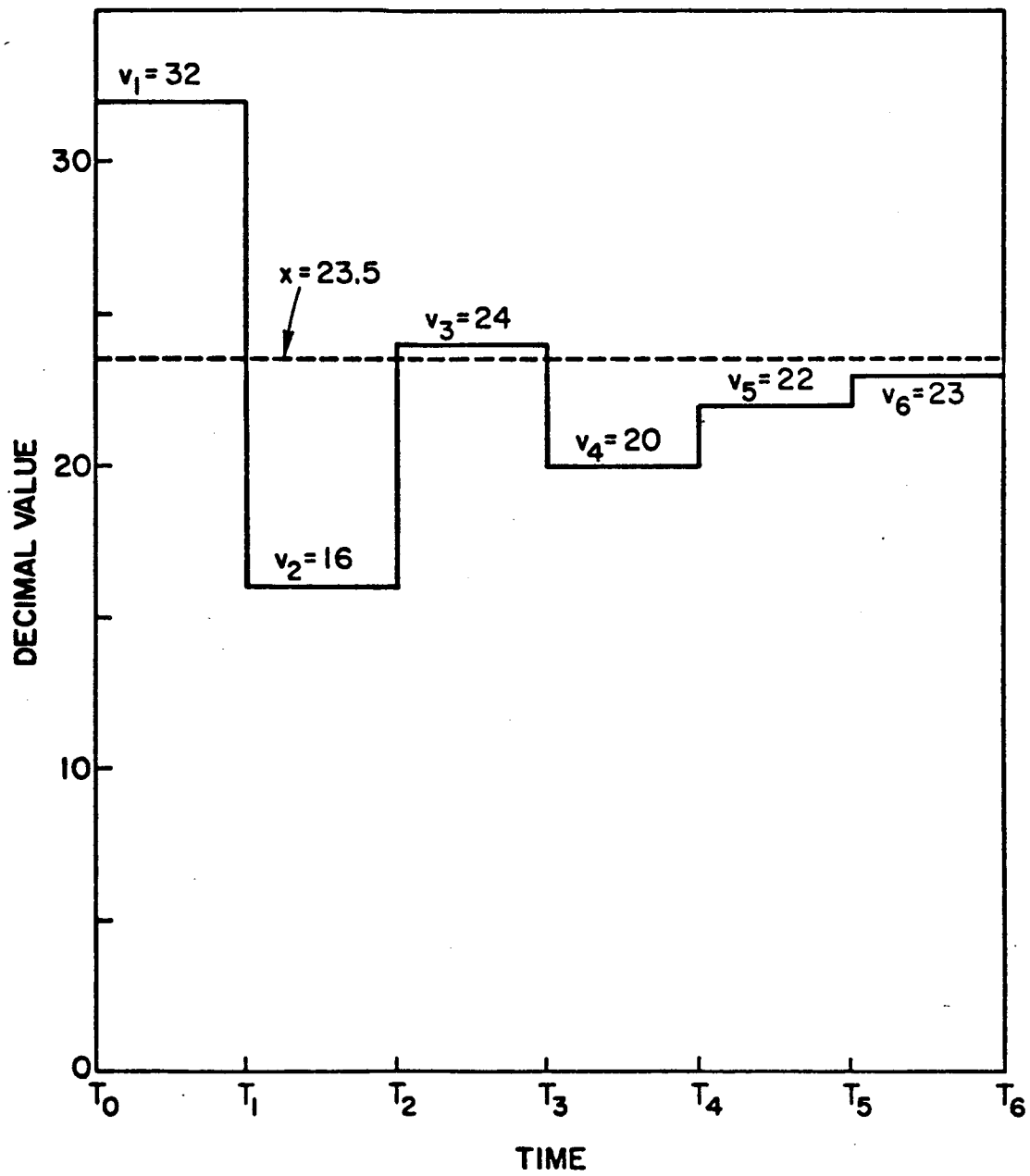


Fig. C.2. VALUES OF  $v_m$  UNDER NORMAL OPERATING CONDITION FOR  $x = 23.5$ .

$b_m$	Reason
$b_1 = 0$	$23.5 < v_1 = 32$
$b_2 = 1$	$23.5 > v_2 = 16$
$b_3 = 0$	$23.5 < v_3 = 24$
$b_4 = 1$	$23.5 > v_4 = 20$
$b_5 = 1$	$23.5 > v_5 = 22$
$b_6 = 1$	$23.5 > v_6 = 23$

Table C.1. THE VALUES OF  $b_m$  FOR  $k = 6$  and  $x = 23.5$ .

During the occurrence of the sun pulse, the Format D output (or the input to the A/D converter) is quashed down to the base line (which has a decimal value of 1) for a duration slightly longer than two telemetry-word time (Sec. III.D). Because the sun pulse is triggered whenever the sun sensor points to the sun, this quashing could take place any time--before (or after) a certain conversion begins (or ends), thereby interrupting the normal operation just described in the above paragraph. Consider first the effect of such interruption near the tail edge of the sun pulse. As an example, suppose the clock time  $\tau_t$  of the tail edge is given by

$$T_2 < \tau_t \leq T_3 \quad (C.4)$$

and, again, the value of the Format D output (before quashing)

$$x = 23.5 \quad ; \quad T_0 \leq t < T_6 \quad (C.5)$$

After quashing, the input to the A/D converter can be expressed as

$$x = \begin{cases} 1 & ; T_0 \leq t < \tau_t \\ 23.5 & ; \tau_t < t < T_6 \end{cases} \quad (C.6)$$

as shown in Fig. C.3, where the values of  $v_m$  are again derived from Eqs. (C.2) and (C.3). Based on Eq. (C.1), Table C.2 lists the resultant values of  $b_m$  and the corresponding reasons. Note that this time the Format D data (i.e., the output of the A/D converter as indicated by Fig. 3.6)  $b_1b_2b_3b_4b_5b_6 = 000111$  has a decimal value of only 7, which no longer approximates the value (23.5) of the Format D output and hence should be regarded as an error caused by the sun pulse. In fact, the above discussion can be easily extended to show that for  $T_2 < \tau_t \leq T_3$  and any  $x$  in (C.5) greater than 7, the Format D data is always 000111 (= 7). Carrying out this argument further for other values of  $\tau_t$  leads to Table C.3, which summarizes all possible errors of Format D data due to the effect of the tail edge of the sun pulse. As evident from Fig. C.3, the tail edge of the sun pulse usually tends to affect bits near (and including) the most significant bit.

$b_m$	Reason
$b_1 = 0$	$x = 1 < v_1 = 32$ at $t = T_0$
$b_2 = 0$	$x = 1 < v_2 = 16$ at $t = T_1$
$b_3 = 0$	$x = 1 < v_3 = 8$ at $t = T_2$
$b_4 = 1$	$x = 23.5 > v_4 = 4$ at $t = T_3$
$b_5 = 1$	$x = 23.5 > v_5 = 6$ at $t = T_4$
$b_6 = 1$	$x = 23.5 > v_6 = 7$ at $t = T_5$

Table C.2. THE VALUES OF  $b_m$  FOR  $T_2 < \tau_t < T_3$ , WITH  $x$  GIVEN BY EQ. (C.6).



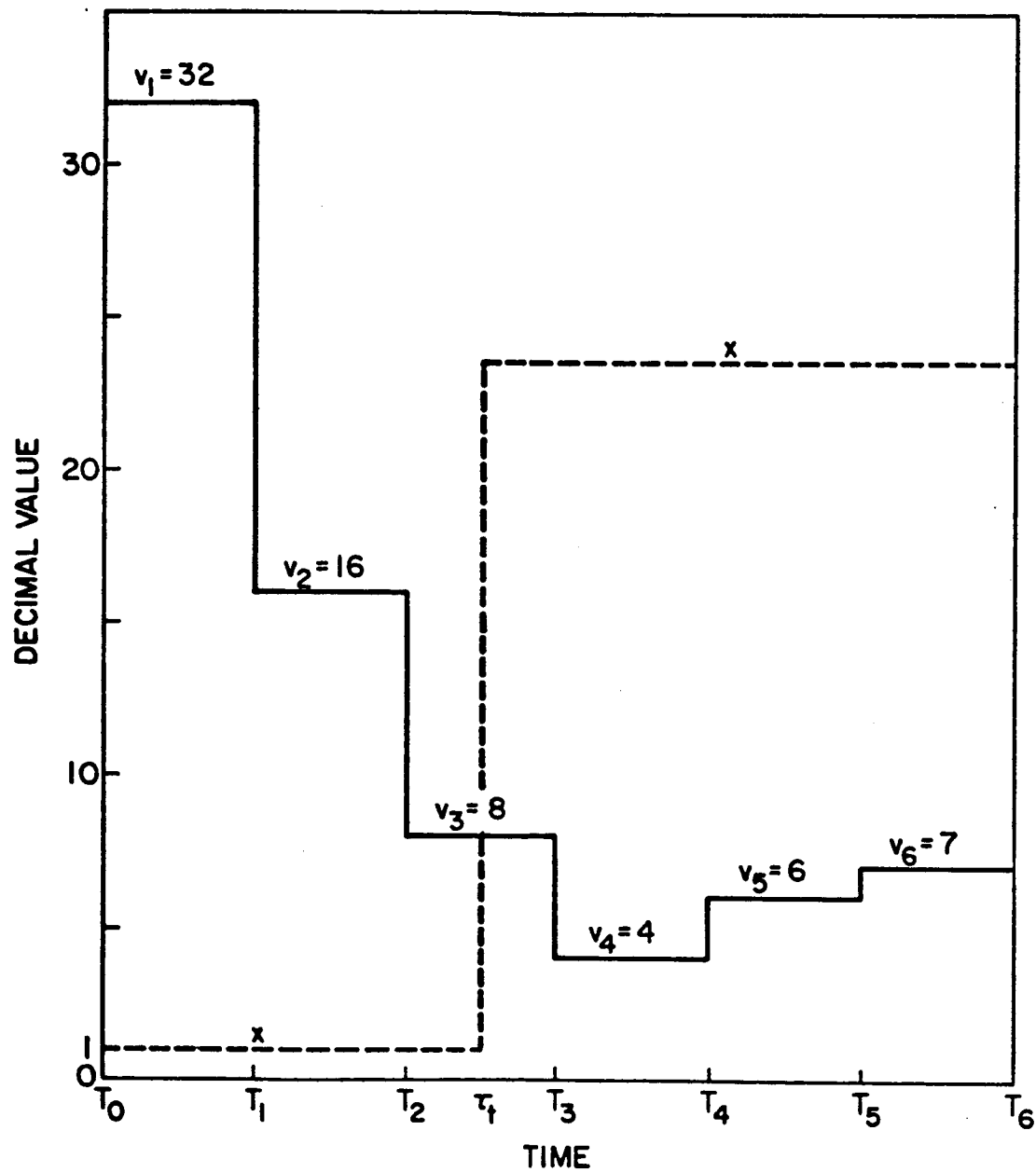


Fig. C.3. VALUES OF  $v_m$  WHEN  $T_2 < \tau_t < T_3$  AND  $x = 23.5$ .

Conditions		Resultant Format D Data That Could Be in Error
$\tau_t$	$x$	$b_1b_2b_3b_4b_5b_6$
$T_0 < \tau_t \leq T_1$	$x \geq 31$	0 1 1 1 1 1 (= 31)
$T_1 < \tau_t \leq T_2$	$x \geq 15$	0 0 1 1 1 1 (= 15)
$T_2 < \tau_t \leq T_3$	$x \geq 7$	0 0 0 1 1 1 (= 7)
$T_3 < \tau_t \leq T_4$	$x \geq 3$	0 0 0 0 1 1 (= 3)
$T_4 < \tau_t \leq T_5$	$x \geq 1$	0 0 0 0 0 1 (= 1)

Table C.3. EFFECTS OF THE TAIL EDGE OF THE SUN PULSE ON FORMAT D DATA.

The effect of the leading edge of the sun pulse on Format D data is in general less severe than that of the tail edge just described, because normally only bits near (and including) the least significant bit will be affected. Consider for example the case when the clock time  $\tau_\ell$  of the leading edge is given by

$$T_2 < \tau_\ell \leq T_3 \quad (C.7)$$

and the Format D output before quashing is again

$$x = 23.5 \quad ; \quad T_0 \leq t < T_6 \quad (C.8)$$

After quashing, the input to the A/D converter becomes

$$x = \begin{cases} 23.5 & ; \quad T_0 \leq t < \tau_\ell \\ 1 & ; \quad \tau_\ell \leq t < T_6 \end{cases} \quad (C.9)$$

Based on Eqs. (C.1)-(C.3), it can be shown easily that  $v_1 = 32$ ,  $v_2 = 16$ ,  $v_3 = 24$ ,  $v_4 = 20$ ,  $v_5 = 18$ ,  $v_6 = 17$ , and  $b_1b_2b_3b_4b_5b_6 = 010000$  (= 16). Let  $D$  denote the decimal value of the Format D data

$b_1b_2b_3b_4b_5b_6$ . Further considerations of other values of  $x$  in (C.8) give rise to

$$D = \begin{cases} 8 & \text{if } 8 \leq x < 16 \\ 16 & \text{if } 16 \leq x < 24 \\ 24 & \text{if } 24 \leq x < 32 \\ 32 & \text{if } 32 \leq x < 40 \\ 40 & \text{if } 40 \leq x < 48 \\ 48 & \text{if } 48 \leq x < 56 \\ 56 & \text{if } 56 \leq x < 63 \end{cases} \quad (\text{C.10})$$

In other words,  $D$  is always a multiple of 8 (or  $b_2b_5b_6 = 000$ ) if  $x \geq 8$  and  $T_2 \leq \tau_\ell < T_3$ . This result can be readily generalized to the following: For  $T_{m-1} \leq \tau_\ell < T_m$ , the Format D data  $D$  is always a multiple of  $2^{6-m}$  if  $x \geq 2^{6-m}$ . Particularly, when  $T_4 \leq \tau_\ell < T_5$ ,  $D$  is always a multiple of 2 (i.e.,  $D$  is even) if  $x \geq 2$ . Because these values of  $D$  for  $m \leq 5$  could differ from the expected values of  $D$  (which always approximate the values of  $x$  to accuracy of 1) under normal operation, they should also be regarded as errors from a conservative point of view. Note that all these possible errors are even.

In summary, if any Format D datum before (or after) the sun pulse has an even value (or one of the following values: 31, 15, 7, 3), then it could be an error ensuing from the asynchronism of the sun pulse with the A/D conversion. During wild-point editing of data reduction (see Fig. 4.1 and p. 65), all these possible errors are discarded.

# Appendix D

## RECEIVED COSMIC NOISE TEMPERATURE $T_c$

As pointed out in Sec. III.G,  $T_c^{\ell}$  and  $T_c^{\nearrow}$  can be obtained by convolving the receiving antenna patterns with the radio sky maps at 49.8 and 423.3 MHz, respectively. Because the spin axes of the receiving antenna patterns are perpendicular to the ecliptic plane (Sec. III.C), it is desired for simplicity of numerical convolution that the radio sky maps are plotted in an ecliptic coordinate system (Fig. D.1), in which the ecliptic is the reference plane and the coordinates are  $\phi$ , the celestial longitude measured eastward in the ecliptic plane from the vernal equinox, and  $\theta$ , the celestial latitude measured northward ( $0 \leq \theta \leq \frac{\pi}{2}$ ) or southward ( $-\frac{\pi}{2} \leq \theta \leq 0$ ) from the ecliptic plane.

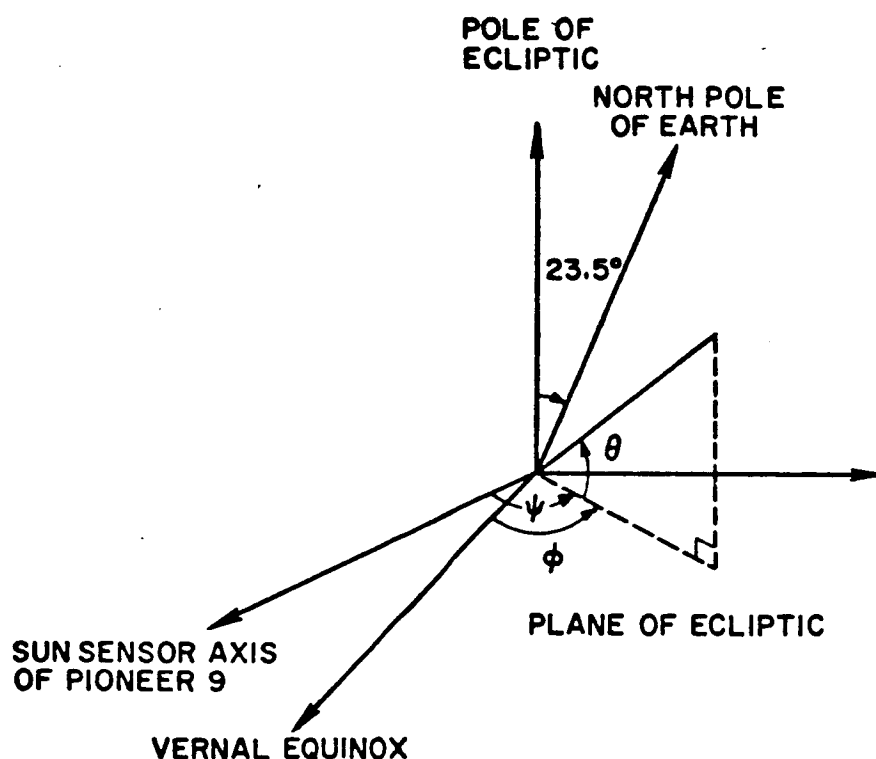


Fig. D.1. ECLIPTIC COORDINATES AND DEFINITION OF  $\psi$ .

Unfortunately, almost all the radio sky maps available are shown only in equatorial or galactic coordinates. As a consequence, conversion of these maps into ecliptic coordinates is necessary before they may be directly utilized.

During actual evaluation of  $T_c^{\ell}$  and  $T_c^{\angle}$ , Kraus' (1966) 250 MHz radio sky map of brightness temperature distribution  $T_b(\alpha, \delta)$  in equatorial coordinates  $(\alpha, \delta)$  was adopted and transformed into ecliptic coordinates  $(\phi, \theta)$ . The formulae relating  $(\alpha, \delta)$  to  $(\phi, \theta)$  are

$$\begin{aligned}\cos \delta \cos \alpha &= \cos \theta \cos \phi \\ \cos \delta \sin \alpha &= \cos \theta \sin \phi \cos \epsilon - \sin \theta \sin \epsilon \\ \sin \delta &= \cos \theta \sin \phi \sin \epsilon + \sin \theta \cos \epsilon\end{aligned}$$

where  $\alpha$  = right ascension  
 $\delta$  = declination  
 $\epsilon$  = the obliquity of the ecliptic with respect to the earth's equator =  $23.5^\circ$

$T_b(\phi, \theta)^{\dagger}$ , the brightness temperature distribution of the radio sky at 250 MHz in ecliptic coordinates, thus attained is then frequency-scaled by using  $T_b \propto \nu^{-2.32}$  as the scaling law [see Fig. 4 in Chap. 27 of Reference Data for Radio Engineers (1968)] to result in

$$T_b^{\ell}(\phi, \theta) = T_b(\phi, \theta) \times \left(\frac{49.8}{250}\right)^{-2.32} \quad (D.1)$$

and

$$T_b^{\angle}(\phi, \tau) = T_b(\phi, \tau) \times \left(\frac{423.3}{250}\right)^{-2.32} \quad (D.2)$$

<sup>†</sup> Because the earth-spacecraft distance is sufficiently small compared with the galactic dimensions,  $T_b(\phi, \theta)$  observed at earth is also applicable to the receiver on board the spacecraft.

Convolving  $T_b^{\ell}(\phi, \theta)$  and  $T_b(\phi, \theta)$  with the receiving antenna patterns  $A^{\ell}(\psi, \theta)$  and  $A^{\nearrow}(\psi, \theta)^{\dagger}$  gives rise to the received cosmic noise temperatures  $T_c^{\ell}$  and  $T_c$  wanted:

$$T_c^{\ell}(\psi_Y) = \frac{1}{4\pi} \int_{\phi=0}^{2\pi} \int_{\theta=-\pi/2}^{\pi/2} T_b^{\ell}(\phi, \theta) A^{\ell}(\psi=\phi+\psi_Y, \theta) \cos \theta \, d\theta \, d\phi \quad (D.3)$$

$$T_c^{\nearrow}(\psi_Y) = \frac{1}{4\pi} \int_{\phi=0}^{2\pi} \int_{\theta=-\pi/2}^{\pi/2} T_b^{\nearrow}(\phi, \theta) A^{\nearrow}(\psi=\phi+\psi_Y, \theta) \cos \theta \, d\theta \, d\phi \quad (D.4a)$$

<sup>†</sup> Recall that  $10 \log_{10} A^{\ell}(\psi, \theta=0)$  and  $10 \log_{10} A^{\nearrow}(\psi, \theta=0)$ , i.e., receiving antenna patterns in dB in the ecliptic plane, were shown in Fig. 3.4. For lack of knowledge,  $A^{\ell}(\psi, \theta \neq 0)$  and  $A^{\nearrow}(\psi, \theta \neq 0)$  are assumed to have the same normalized patterns as  $A^{\ell}(\psi, \theta=0)$  and  $A^{\nearrow}(\psi, \theta=0)$ , respectively, such that

$$\frac{1}{2\pi} \int_{\psi=0}^{2\pi} A^{\ell}(\psi, \theta \neq 0) d\psi = \frac{1}{2\pi} \int_{\psi=0}^{2\pi} A^{\nearrow}(\psi, \theta \neq 0) d\psi = 1.64 \frac{\cos^2(\frac{\pi}{2} \sin \theta)}{\cos^2 \theta} \quad (D.4b)$$

= power pattern of a half-wave dipole

Notice that this equation along with

$$\frac{1}{2\pi} \int_0^{2\pi} A^{\ell}(\psi, \theta=0) d\psi = \frac{1}{2\pi} \int_0^{2\pi} A^{\nearrow}(\psi, \theta=0) d\psi = 1.64 \quad (D.4c)$$

= gain of a half-wave dipole in the  $\theta = 0^\circ$  plane

assures that

$$\frac{1}{4\pi} \int_0^{2\pi} \int_{-\pi/2}^{\pi/2} A^{\ell}(\psi, \theta) \cos \theta \, d\theta \, d\psi = \frac{1}{4\pi} \int_0^{2\pi} \int_{-\pi/2}^{\pi/2} A^{\nearrow}(\psi, \theta) \cos \theta \, d\theta \, d\psi = 1$$

the conservation of total power radiated when the antennas are used for radiation.

where, as defined in Sec. III.C,

$\psi$  = longitude measured, with origin at Pioneer 9, counterclockwise (when looking from the north ecliptic pole) in the ecliptic plane from the axis of the sun sensor

and  $\psi_Y = \psi$  of the vernal equinox (Fig. D.1)

As the receiving antenna patterns spin with period  $\approx 1$  second (Sec. III.C),  $\psi_Y$  and hence  $T_C^{\ell}(\psi_Y)$  and  $T_C^{\nearrow}(\psi_Y)$  change recurrently with the same period. After numerically integrating (D.3) and (D.4), it is found that for  $\psi_Y = 0^\circ$  to  $360^\circ$  (i.e., for one whole period of spacecraft rotation),

$$5440^\circ\text{K} \leq T_C^{\ell}(\psi_Y) \leq 5920^\circ\text{K} \quad (\text{D.5})$$

is of order  $\left(\frac{49.8}{423.3}\right)^{-2.32} \approx 143$  higher than

$$36^\circ\text{K} \leq T_C^{\nearrow}(\psi_Y) \leq 43^\circ\text{K} \quad (\text{D.6})$$

thereby agreeing with the frequency scaling law  $\nu^{-2.32}$  used in (D.1) and (D.2).

## Appendix E

### RECEIVED SOLAR NOISE TEMPERATURE $T_s$

In view of the fact that (a) solar radio emission is a complex, fast fluctuating phenomenon and (b) no measurements of this phenomenon were made at times of taking Format D data in the direction of the spacecraft, it is concluded that only an estimate of  $T_s$  is possible. Luckily, as will be seen soon,  $T_s$  is much smaller than other noise temperatures (except when intense solar radio bursts occur) and therefore plays a relatively unimportant role.

The radio emission from the sun has three distinct components [Kundu (1965)]: (a) the quiet sun component, due to thermal emission in the solar atmosphere; (b) the slowly varying component, due to thermal emission in regions of high electron densities and magnetic fields that exist in the vicinity of sunspots and chromospheric plages; and (c) the rapidly varying component, due to burst-radiation from all levels of the solar atmosphere. The quiet sun component is a background component remaining at a constant level for periods of months or years. The regions generating the slowly varying component (or, for short, the S-component) may persist over several solar rotations; thus, as the sun rotates (in the same direction as the earth's daily rotation and annual revolution) with period 27 days, the S-component observed at the earth is expected to exhibit a 27-day periodicity.

Finally, the rapidly varying component, generally associated with solar flares and characterized by great variability and complexity, may only last over intervals of seconds, minutes, or hours.



The solar radio flux density has been measured daily at a number of frequencies ranging from 100 MHz up to 15.4 GHz by various ground observatories, with its daily mean  $F$  tabulated in IAU (International Astronomical Union) Quarterly Bulletin on Solar Activity. An auto-correlation analysis of  $F$  has revealed that it tends to recur periodically with period  $\approx 27$  days over several solar rotations; moreover, the rotation of the sun along with its active regions (from which the S-component originates) is thought to be responsible for this recurring tendency [El-Raey and Scherrer (1972)].

Adopting the above result (i.e., 27-day periodicity), choosing available data of  $F$  at frequencies closest to 49.8 and 423.3 MHz, and using an appropriate frequency-scaling law [see Kraus' (1965) Fig. 8-21], we have derived  $T_d^{\ell}$  and  $T_d^{\nearrow}$  for each set of our Format D data, where

$T_d^{\ell}$  and  $T_d^{\nearrow}$  = the apparent disk (or brightness) temperatures of the sun observed in the direction of the receiver, on the date of taking Format D data, at frequencies 49.8 and 423.3 MHz, respectively.

Analogous to (3.24) and (3.25), the received solar noise temperatures (referred to the receiving antenna terminals) are

$$\begin{aligned} T_s^{\ell}(\psi_s) &= \frac{1}{4\pi} \int_{\phi=0}^{2\pi} \int_{\theta=-\pi/2}^{\pi/2} T_d^{\ell}(\phi, \theta) A^{\ell}(\psi=\phi+\psi_s, \theta) \cos \theta \, d\theta \, d\phi \\ &= \frac{\Omega_s'}{4\pi} T_d^{\ell} A^{\ell}(\psi_s, \theta=0) \end{aligned} \quad (E.1)$$

and

$$T_s^{\nearrow}(\psi_s) = \frac{\Omega_s'}{4\pi} T_d^{\nearrow} A^{\nearrow}(\psi_s, \theta=0) \quad (E.2)$$

where

$$\Omega_s' = \Omega_s \times \left(\frac{1 \text{ A.U.}}{PS}\right)^2 = 6.8 \times 10^{-5} \times \left(\frac{1 \text{ A.U.}}{PS}\right)^2 \text{ steradian} \quad (E.3)$$

is the solid angle subtended by the radio sun at the receiver aboard the spacecraft,  $\psi_s$  is the  $\psi$  of the sun (Fig. D.1), and PS is the Pioneer-to-sun distance. As evident in (E.1) and (E.2),  $T_s^{\nearrow}(\psi_s)$  and  $T_s^{\nearrow}(\psi_s)$  are, except for constant scaling factors, identical to the receiving antenna patterns in the ecliptic plane  $A^{\nearrow}(\psi_s, \theta=0)$  and  $A^{\nearrow}(\psi_s, \theta=0)$ , respectively. Due to the spin of the spacecraft,  $\psi_s$ ,  $T_s^{\nearrow}(\psi_s)$ , and  $T_s^{\nearrow}(\psi_s)$  [like  $\psi_Y$ ,  $T_c^{\nearrow}(\psi_Y)$ , and  $T_c^{\nearrow}(\psi_Y)$ ] are all periodic functions of time with period equal to that of the spacecraft rotation ( $\approx 1$  sec). Typically,

$$T_s^{\nearrow}(\psi_s) \approx 20 \text{ }^\circ\text{K} \quad (E.4)$$

$$T_s^{\nearrow}(\psi_s) \approx 10 \text{ }^\circ\text{K} \quad (E.5)$$

Both are much smaller than other received noise temperatures and therefore are less important.

## Appendix F

### ON COMPUTATING THE AUTOCORRELATION FUNCTION OF INTENSITY FLUCTUATIONS

In order to save the computational time required, the autocorrelation functions of intensity fluctuations are computed using FFT (fast-Fourier transforms). The basic idea is originated from the fact that the product of the DFT (discrete-Fourier transform) of any periodic sequence and its complex conjugate is equal to the DFT of the circular autocorrelation function of the sequence. To verify this point, consider a real, periodic sequence  $x(n\tau)$  of period  $N$  with its  $N$ -point DFT  $X(k\Omega)$  defined as

$$X(k\Omega) = \text{DFT}\{x(n\tau)\} = \sum_{n=0}^{N-1} x(n\tau) e^{-j\Omega\tau nk} \quad (\text{F.1})$$

where  $\Omega = \frac{2\pi}{N\tau}$ . Then, there exists an inverse DFT (IDFT), a transformation that maps  $X(k\Omega)$  back into  $x(n\tau)$ :

$$x(n\tau) = \text{IDFT}\{X(k\Omega)\} = \frac{1}{N} \sum_{k=0}^{N-1} X(k\Omega) e^{j\Omega\tau kn} \quad (\text{F.2})$$

As evident from (F.1) and (F.2), both the sequences  $X(k\Omega)$  and  $x(n\tau)$  are periodic with period  $N$  samples. It is also evident from (F.1) that  $X(k\Omega)$  may be determined exactly from just one period of  $x(n\tau)$ . Using (F.1) and (F.2) gives rise to

$$\begin{aligned} \text{IDFT}\{X(k\Omega)X^*(k\Omega)\} &= \frac{1}{N} \sum_{k=0}^{N-1} X(k\Omega)X^*(k\Omega) e^{j\Omega\tau kn} \\ &= \frac{1}{N} \sum_{k=0}^{N-1} \left[ \sum_{r=0}^{N-1} x(r\tau) e^{-j\Omega\tau rk} \right] \times \left[ \sum_{s=0}^{N-1} x(s\tau) e^{j\Omega\tau sk} \right] e^{j\Omega\tau kn} \end{aligned}$$

$$= \sum_{r=0}^{N-1} \sum_{s=0}^{N-1} x(r\tau)x(s\tau) \left[ \frac{1}{N} \sum_{k=0}^{N-1} e^{j2\pi k(n+s-r)/N} \right] \quad (F.3)$$

Applying the orthogonality relationship [see, for example, Brigham (1974)]

$$\frac{1}{N} \sum_{k=0}^{N-1} e^{j2\pi k(n+s-r)/N} = \delta(n+s-r) \quad (F.4)$$

to (F.3) yields

$$\text{IDFT}\{X(k\Omega)X^*(k\Omega)\} = R_x^c(n\tau) = \sum_{s=0}^{N-1} x(s\tau)x(s\tau+n\tau)$$

= the circular or periodic autocorrelation  
function of  $x(s\tau)$  obtained by circularly  
correlating  $x(s\tau)$  with itself (F.5)

which is the desired result. The direct evaluation of  $R_x^c(n\tau) = \sum_{s=0}^{N-1} x(s\tau)x(s\tau+n\tau)$  for all  $n = 0, 1, 2, \dots, N-1$  requires  $N^2$  real multiply-add operations, while the indirect evaluation of  $R_x^c(n\tau)$  via calculating  $\text{IDFT}\{X(k\Omega)X^*(k\Omega)\} = \text{IDFT}\{|\text{DFT}[x(s\tau)]|^2\}$  requires only on the order of  $4N\log_2 N$  complex multiply-add operations if  $N$  is a power of 2 and if the FFT algorithm is employed to compute the DFT and the IDFT.<sup>†</sup> Therefore, for moderately large  $N$ , say  $N$  greater than 1,000, the indirect evaluation results in a dramatic saving (greater than 92 percent) in computational time.

<sup>†</sup> The FFT algorithm is a highly efficient method for computing the DFT and the IDFT of a series of discrete data samples. If the series consists of  $N = 2^p$  samples, then only about  $N\log_2 N = N_p$  complex multiply-add operations are needed to compute all  $N$  associated DFT or IDFT coefficients. Many fine texts and papers dealing with FFT have been written. Some of the more recent include Brigham (1974), Rabiner and Gold (1975), and Oppenheim and Schaffer (1975).

Notice that the "noncircular" (or aperiodic) autocorrelation function of the  $x(s\tau)$  sequence is defined by [see also (4.10)]

$$R_x(n\tau) = \frac{1}{N-n} \sum_{s=0}^{N-n-1} x(s\tau) x(s\tau+n\tau) \quad (\text{F.5})$$

which can be easily proved to be related to the circular autocorrelation function  $R_x^c(n\tau)$  defined in (F.5) by

$$R_x^c(n\tau) = (N-n)R_x(n\tau) + nR_x(N\tau-n\tau) \quad (\text{F.6})$$

as illustrated in Fig. F.1. The effect on  $R_x^c(n\tau)$  of adding zeros to  $x(s\tau)$  is to spread apart the two portions of  $R_x^c(n\tau)$ . In particular, suppose  $N$  zeros are appended to form the new periodic sequence

$$x'(s\tau) = \begin{cases} x(s\tau) & 0 \leq s \leq N-1 \\ 0 & N \leq s \leq 2N-1 \end{cases} \quad (\text{F.7})$$

of length  $2N$ ; then, the circular autocorrelation function of the new sequence becomes

$$R_{x'}^c(n\tau) = \begin{cases} (N-n)R_x(n\tau) & 0 \leq n \leq N-1 \\ 0 & n = N \\ (n-N)R_x(2N\tau-n\tau) & N+1 \leq n \leq 2N-1 \end{cases} \quad (\text{F.8a})$$

$$(\text{F.8b})$$

$$(\text{F.8c})$$

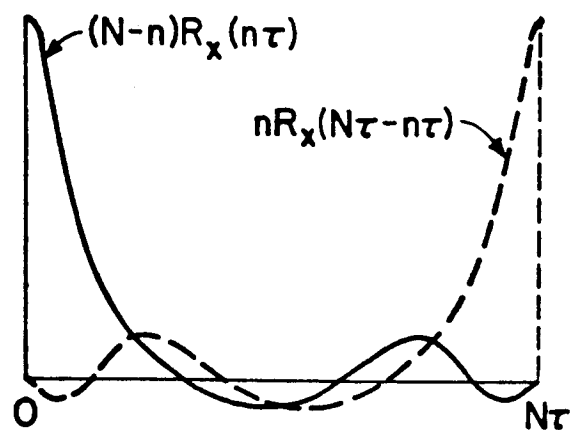


Fig. F.1. TWO PORTIONS OF A CIRCULAR AUTOCORRELATION FUNCTION  $R_x^c(n\tau)$ .

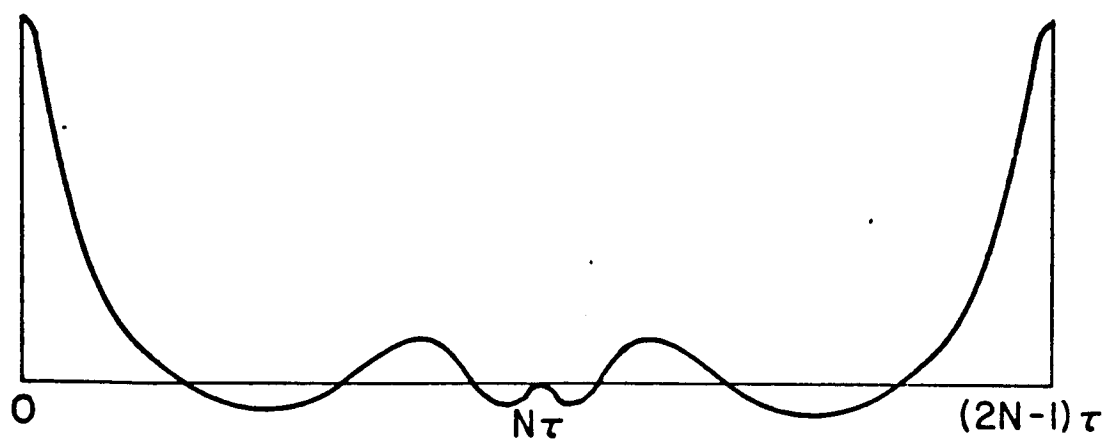


Fig. F.2. SPREAD OF  $R_x^c(n\tau)$  WHEN  $N$  ZEROS ARE APPENDED TO  $x(n\tau)$ .

as depicted in Fig. F.2. If the length of the original sequence  $N$  and hence the length of the new sequence  $2N$  are powers of 2,  $R_{x,c}(n\tau)$  can be computed via FFT, thereby yielding  $R_x(n\tau)$  through (F.8a) at high (FFT) speed. If  $N$  and hence  $2N$  are not powers of 2, then the original sequence  $x(s\tau)$  could be augmented with  $N_z (N < N_z < 2N)$  zeros until  $N + N_z$  reached a power of 2. The new sequence

$$x''(s\tau) = \begin{cases} x(s\tau) & 0 \leq s \leq N-1 \\ 0 & N \leq s \leq N+N_z-1 \end{cases} \quad (F.9)$$

has an autocorrelation function

$$R_{x''}(n\tau) = \begin{cases} (N-n)R_x(n\tau) & 0 \leq s \leq N-1 & (F.10a) \\ 0 & N \leq s \leq N_z & (F.10b) \\ (n-N_z)R_x(N\tau+N_z\tau-n\tau) & N_z+1 \leq s \leq N_z+N-1 & (F.10c) \end{cases}$$

which can, again, be calculated via FFT to yield  $R_x(n\tau)$  through (F.10a) at high speed.

Basically, the preceding computational method can be applied directly to  $\Delta I(k\tau')$  [defined in (4.11)] to efficiently obtain the "non-circular" autocorrelation function of intensity fluctuation  $R_{\Delta I}(n\tau')$  desired. However, because the original IPS data are interspersed (1) regularly with sun pulses and experimental information and (2) occasionally with spurious values (due probably to loss of signal in the transmission link or failure of the equipment), there are gaps in the data, and these gaps have to be replaced by some reasonable

values before the FFT of the data may be taken.<sup>†</sup> A number of replacement schemes had been considered, none of which appears to be fully satisfactory.

Recall from Sec. III.D that the Format D output was fed into a low-pass filter of bandwidth 10 Hz before being sampled; as a result, the frequency spectrum of  $I(k\tau')$  and hence of  $\Delta I(k\tau')$  is expected, and later confirmed by analysis, to have a bandwidth less than about 10 Hz. In the time domain, this implies that  $I(k\tau')$  and  $\Delta I(k\tau')$  are primarily composed of sinusoidal components of periods greater than about 0.1 second ( $\approx 3.7 \tau'$ ). Thus, theoretically speaking, if the data gap is shorter than 0.1 second or so, it may be replaced with samples obtained by linear interpolation between the existing data without introducing serious distortions. [In fact, linear interpolation was also the scheme employed by Cohen et al. (1967) in replacing their missing data of IPS observations.] However, if a data set contains gaps longer than 0.1 second, linear interpolation will be misleading, and the best treatment is simply not to use that data set at all.

In summary, the autocorrelation function of intensity fluctuation  $R_{\Delta I}(n\tau')$  [or, equivalently, the autocovariance function of the intensity  $A_I(n\tau')$ ] is calculated via the following steps:

1. Check the data gaps in a given set of clean IPS data  $I(k\tau')$ .
2. Discard the whole set of data if it contains any gaps longer than about 0.1 second, or if it does not, replace the gaps by linear interpolations between the existing data.
3. Compute the average (of the interpolated data),  $\bar{I}$ , and subtract  $\bar{I}$  from the interpolated data to obtain

---

<sup>†</sup> Setting  $I(k\tau')$ 's in the gaps equal to zeros would generate ungenuine discontinuities in the data, thereby resulting in an erroneous spectrum when the FFT of the data is taken.



the intensity fluctuation  $\Delta I(k\tau') = I(k\tau') - \bar{I}$ ,  $k = 0, 1, 2, \dots, N - 1$ .

4. Append  $N_z^+$  zeros to the sequence  $\Delta I(k\tau')$  such that  $(N + N_z)$  is a power of  $2^\ddagger$  to form a new sequence  $\Delta I'(n\tau')$ .
5. Compute  $S(k\Omega) = \text{FFT} \{\Delta I'(n\tau')\}$ ,  $k = 0, 1, \dots, N + N_z - 1$ .
6. Compute  $R_{\Delta I}^C(n\tau') = \text{IFFT} \{S(k\Omega)\}$ ,  $n = 0, 1, \dots, N + N_z - 1$ .
7. Preserve only the first  $N_m^+$  points of  $R_{\Delta I}^C(n\tau')$  and multiply each point by  $(N + N_z)/(N - n)$  to yield  $R_{\Delta I}(n\tau')$ ,  $n = 0, 1, \dots, N_m - 1$ .

---

<sup>†</sup> In general, if only the first  $N_m (< N)$  values of the noncircular correlation function  $R_{\Delta I}(n\tau')$  [i.e.,  $R_{\Delta I}(0), R_{\Delta I}(\tau'), \dots, R_{\Delta I}(N_m - 1)\tau'$ ] are wanted, then the number of zeros appended  $N_z \geq N_m$  will suffice. The reason is that augmenting  $\Delta I(k\tau')$  with  $N_z$  zeros will cause the second portion of the circular auto-correlation function  $R_{\Delta I}^C(n\tau')$  to be spread apart from the first portion by  $N_z\tau' (\geq N_m\tau')$ , which is enough for obtaining the first  $N_m$  points of  $R_{\Delta I}(n\tau')$  unbiasedly.

<sup>‡</sup> Although some FFT subroutines do not require the length of the input data to be a power of 2 [e.g., Singleton's (1969) FFT subroutine], maximum computational efficiency is always achieved when the length of the data is a power of 2.

## Appendix G

### ON COMPUTING THE POWER SPECTRUM OF INTENSITY FLUCTUATIONS

#### 1. General Considerations

Mathematically, the power spectrum  $F_I(\nu)$  of intensity fluctuation  $\Delta I(t)$  (which is assumed to be stationary) is defined as the Fourier transform of the autocorrelation function  $R_{\Delta I}(t)$  of intensity fluctuation:

$$F_I(\nu) = \int_{-\infty}^{\infty} R_{\Delta I}(t) e^{-j2\pi\nu t} dt \quad (G.1)$$

where  $t$  denotes time. As evident from the above equation, precise determination of  $F_I(\nu)$  would require  $R_{\Delta I}(t)$  and in turn  $\Delta I(t)$  to be available continuously over infinitely long duration (from  $-\infty$  to  $\infty$ ). This requirement is, of course, physically impossible to fulfill. In most practical cases, only a sample function<sup>†</sup> of the random process over a finite duration is observed. Furthermore, in order for the observed function to be processable by a digital computer, it must first be passed through a sampler (or an A/D converter) and transformed into a finite, discrete time series consisting of sampled values of the original function. Any power spectrum estimated from such a finite, discrete time series is inherently contaminated by at least two types of errors: leakage and aliasing.

Leakage arises from the fact that the original function and hence its digital samples are known only for a finite time interval (time truncation). The sharp discontinuity in the time domain due to this

---

<sup>†</sup> A random process is composed of an ensemble of time functions; the individual time functions are called "sample functions" of the random process [see, for example, Wozencraft and Jacobs (1965)].

truncation is expected to produce additional frequency components or sidelobes in the frequency domain. As a consequence, the original concentration of energy at a certain frequency will be smeared or "leaked" into the sidelobes.

Contrary to leakage which is caused by the fact that the observed function is time-limited, aliasing ensues from the fact that the observed function is not band-limited<sup>†</sup>; consequently, sampling must create errors<sup>†</sup>. Generally speaking, if the sampling rate for a continuous waveform is  $2\nu_s$ , then frequency components originally below  $\nu_s$  in the continuous waveform will appear in the spectrum of the sampled waveform as they ought, while all components above  $\nu_s$  will fold over into the frequency band between 0 and  $\nu_s$  and appear as impersonations of aliases. For example, a component at  $n\nu_s + \nu$  ( $\nu < \nu_s$ ) in the original waveform will appear in the spectrum of the sampled waveform as an alias (1) at  $\nu_s - \nu$  if  $n = 1, 3, 5, \dots$ , or (2) at  $\nu$  if  $n = 2, 4, 6, \dots$ . This shifting (or fold-over) of high-frequency information into lower frequencies (arising from sampling at too low a rate) is usually referred to as aliasing.

Because of these two intrinsic errors and, furthermore, because only a sample function  $\Delta I(t)$  of the random process  $\Delta i(t)$  is

---

<sup>†</sup> Because time-limiting and band-limiting are mutually incompatible [see, e.g., pp. 97-98 of Carlson (1968)], the observed function which is time-limited cannot be band-limited.

<sup>†</sup> The well-known sampling theorem (Nyquist criterion) states that when sampling a continuous waveform, the sampling rate must be at least twice the highest frequency present in the continuous waveform for the continuous waveform to be completely characterized by the sampled waveform. Thus, for a continuous waveform which is not bandlimited, the sampling rate would have to be infinitely fast in order to satisfy this criterion, and any finite sampling rate would inevitably result in errors.

observed, the power spectrum  $F_I(\nu)$  can merely be estimated approximately at best. Assuming that  $\Delta I(t)$  is an ergodic process, i.e., a random process for which ensemble (or probability) averages are equal to time averages, then all its statistics can be determined from a single sample function. However, since the sample function  $\Delta I(t)$  is always available only over a finite duration ( $\leq 30$  seconds or so), the following question arises immediately: can 30-second data of  $\Delta I(t)$  provide a statistically meaningful estimate of  $F_I(\nu)$ ?

First, recall from Chapter II that most of the intensity fluctuations are caused by turbulent eddies about the size of the first Fresnel zone  $\sqrt{\lambda z}$  ( $\approx 800$  km at 49.8 MHz or 250 km at 423.3 MHz for most Format D data). As the solar wind moves across the propagation path at a speed  $\approx 350$  km/sec,  $\Delta I(t)$  received at the spacecraft during 30 seconds will contain the effects resulting from about 15 (at 49.8 MHz) or 40 (at 423.3 MHz) Fresnel-zone-sized scatters, which appears to be barely enough for yielding a statistically meaningful estimate of  $F_I(\nu)$ . Although the above discussion has left an impression that the longer the data record, the better the statistical estimation, one must, on the other hand, realize that the nonstationarity of the interplanetary medium would tend to impose an upper limit on the maximum usable length of the data.

Based upon estimation theory, a variety of methods have been proposed for power spectrum estimation. [See, for example, Blackman and Tukey (1958), Welch (1967), and Oppenheim and Schaffer (1975).] But before proceeding with any method, there is one more preliminary question to be considered: How serious is the aliasing error present in the data to be analyzed?

The answer to this question is exceedingly important, for failure to adequately examine this question first can make the entire subsequent computation worthless or frequently, even worse, produce completely misleading results. Clearly, if the aliasing error is too heavy, then the appearance of the power spectrum will be dominated by this error<sup>†</sup> rather than by the physical phenomenon to be investigated; consequently, it will be pointless to go any further.

Insofar as Format D data are concerned, recall again that the signal is fed through a low-pass filter (or "guard filter," or "anti-aliasing filter," in digital-signal-processing terminology) of bandwidth 10 Hz before being digitized. At sampling rate 36.6 sample/sec, any aliasing effects would involve only components of frequencies greater than 18.3 Hz (which is greater than the 10 Hz bandwidth of the pre-sampling low-pass filter) and hence are not expected to be too serious.

## 2. Power Spectrum Estimate by the Blackman-Tukey Method

Of the various techniques for power spectrum estimation, the so-called Blackman-Tukey method (1958) has been most widely adopted in the field of interplanetary scintillation studies. [See, for instance, Cohen et al. (1967), Cohen and Gundermann (1969), Intriligator and Wolfe (1970), and Unti et al. (1973).] When applying this method to our Format D data, the procedures for estimating the power spectrum  $F_I(\nu)$  of intensity fluctuations can be briefly outlined as follows:

---

<sup>†</sup> For example, if the spectrum of a continuous waveform is believed to spread out up to 1 kHz with substantial amplitude and if the sampling rate for this continuous waveform is only 20 Hz, then the spectrum of the sampled waveform (from 0 to 10 Hz) will look nothing like the original spectrum, but the original spectrum (from 0 to 1 kHz) folded one hundred times over into the frequency range  $0 \leq \nu \leq 10$  Hz.

1. Let  $\Delta I(k\tau')$ ,  $k = 0, 1, \dots, N-1$ , be a zero-mean,  $N$ -point sequence of intensity fluctuations, where  $\tau'$  is the time interval between adjacent samples, and let  $R_{\Delta I}(k\tau')$ ,  $k = 0, 1, \dots, m^\dagger$ , be the autocorrelation function of the intensity fluctuations attained from the preceding section. Form the sequence

$$\tilde{R}_{\Delta I}(k\tau') = \begin{cases} R_{\Delta I}(k\tau') & ; 0 \leq k \leq m \\ R_{\Delta I}[(2m-k)\tau']; & m+1 \leq k \leq 2m-1 \end{cases} \quad (G.2)$$

2. Compute the  $2m$ -point FFT of  $\tilde{R}_{\Delta I}(k\tau')$  to yield  $\tilde{F}_I(\nu)$  the raw estimate of  $F_I(\nu)$ :

$$\tilde{F}_I(\nu) = \tilde{F}_I(r\nu_0) = \tau' \cdot \text{FFT} \{ \tilde{R}_{\Delta I}(k\tau') \} \quad (G.3)^\ddagger$$

where  $r = 0, 1, 2, \dots, 2m-1$ ,  $\nu = r\nu_0$ , and

$$\nu_0 = \frac{1}{2m\tau'} \quad (G.4)$$

is the resolution bandwidth of the raw estimate  $\tilde{F}_I(\nu)$ . Since  $\tilde{F}_I(r\nu_0)$  is symmetric in  $\ell$  with respect to every integral multiple of  $m$ , the last  $m$  points of  $\tilde{F}_I(\ell\nu_0)$  may be disregarded.

<sup>†</sup> For efficiency of the succeeding FFT computation, the maximum autocorrelation lag  $m$  is normally chosen to be a power of 2; moreover, as will be discussed shortly,  $m$  has to be smaller than a moderate fraction (say, 15 per cent) of  $N$  in order to secure a reasonable stability for the power-spectrum estimate.

<sup>‡</sup> Invoking the definition of FFT and substituting (G.2) and (G.4) into (G.3) leads to

$$\begin{aligned} \tilde{F}_I(r\nu_0) &= \sum_{k=0}^{2m-1} R_{\Delta I}(k\tau') e^{-j2\pi\nu_0\tau'kr} = \tau' \cdot [\tilde{R}_{\Delta I}(0) + 2 \sum_{k=1}^{m-1} \tilde{R}_{\Delta I}(k\tau') \\ &\quad \times \cos(\frac{\pi kr}{m}) + \tilde{R}_{\Delta I}(m\tau') \cos \pi r] \end{aligned}$$

which is identical to the equation of raw spectral density estimates given by Blackman and Tukey (1958) on p. 121.

3. Compute  $\tilde{F}_I(rv_0)$ , the refined estimate of  $F_I(v)$ , via

$$\hat{F}_I(rv_0) = \begin{cases} 0.54 \tilde{F}_I(0) + 0.46 \tilde{F}_I(v_0) & ; r=0 \\ 0.23 \tilde{F}_I[(r-1)v_0] + 0.54 \tilde{F}_I(rv_0) + 0.23 \tilde{F}_I[(r+1)v_0] & ; r=1, 2, \dots, m-1 \\ 0.54 \tilde{F}_I(mv_0) + 0.46 \tilde{F}_I[(m-1)v_0] & ; r=m \end{cases} \quad (G.5)$$

Step 3 above is equivalent to convolving  $\tilde{F}_I(rv_0)$  with

$$H(v) = 0.54 Q(v) + 0.23 [Q(v + \frac{1}{2m\tau'}) + Q(v - \frac{1}{2m\tau'})] \quad (G.6)$$

where

$$Q(v) = 2m\tau' \cdot \text{sinc}(2m\tau'v) = 2m\tau' \cdot \frac{\sin(2\pi m\tau'v)}{2\pi m\tau'v} \quad (G.7)$$

In the time domain, this corresponds to multiplying  $\tilde{R}_{\Delta I}(k\tau')$  by the Hamming (after R. W. Hamming) window

$$h(t) = \mathcal{F}^{-1}\{Q(v)\} = \begin{cases} 0.54 + 0.46 \cos\left(\frac{\pi t}{m\tau'}\right) & ; |t| \leq m\tau' \\ 0 & ; |t| > m\tau' \end{cases} \quad (G.8)$$

before taking FFT to yield  $\tilde{F}_I(rv_0)$  directly and is commonly referred to as "windowing." As evident from the form of  $h(t)$  in (G.8), the main purpose for windowing is to reduce the discontinuity, and hence the leakage error, introduced by the rectangular truncation of  $R_{\Delta I}(k\tau')$  in the time domain.

The cost for such leakage reduction is that the effective resolution bandwidth  $B_e$  of power-spectrum estimates has been broadened from  $\frac{1}{2m\tau'}$  to [Blackman and Tukey (1958)]

$$B_e \approx 1/m\tau' \quad (G.9)$$

### 3. Stability and Confidence Limits of Power-Spectrum Estimates

If  $\{\Delta I(k\tau')\}$ ,  $k=0,1,2,\dots,N$ , are gaussian and independent, then it can be easily proved [see, for example, Otnes and Enochson (1974)] that so are  $\{\Delta g(r\nu_1)\}$ , where

$$r = 0,1,2,\dots N/2 \quad (G.10)$$

$$\Delta g(r\nu_1) = \text{DFT}\{\Delta I(k\tau')\} \quad (G.11)$$

and

$$\nu_1 = \frac{1}{N\tau'} \quad (G.12)$$

As a consequence,  $\hat{F}_I(r\nu_0)$  derived from the preceding subsection will follow a Chi-square distribution with the number of degrees of freedom [Otnes and Enochson (1974)]

$$n \approx \frac{2N}{m} \quad (G.13)$$

Recall that  $N$  is the total number of  $\Delta I(k\tau')$  originally available, and  $m$  is the maximum lag of  $R_{\Delta I}(k\tau')$  used to attain  $\hat{F}_I(r\nu_0)$ . For most Format D data,

$$N \leq 1088 \quad (G.14)$$

and for reasons stated in the footnote on p.

$$m = 128, 64, \text{ or } 32 \quad (G.15)$$

have been invariably selected. Thus,

$$n \approx 16, 32, \text{ or } 64 \quad (G.16)$$

depending upon which  $m$  is chosen.



The stability of  $\hat{F}_I(rv_0)$  can therefore be expressed in terms of the probability  $P$  that  $F_I(rv_0)$  lies between  $A$  and  $B$ :

$$\text{Prob } [A \leq F_I(rv_0) \leq B] = P \quad (\text{G.17})$$

where

$$A = \frac{n \hat{F}_I(rv_0)}{\chi^2_{n, \frac{1-P}{2}}} = C \cdot \hat{F}_I(rv_0) \quad (\text{G.18})$$

and

$$B = \frac{n \hat{F}_I(rv_0)}{\chi^2_{n, \frac{1+P}{2}}} = D \cdot \hat{F}_I(rv_0) \quad (\text{G.19})$$

Another way to interpret (G.17) is the following: With  $100 \cdot P \%$  confidence, the true value of  $F_I(rv_0)$  lies between  $A$  and  $B$ . For  $N = 1024$ , the values of  $C$  and  $D$  in dB plus some other relevant parameters peculiar to our power-spectrum estimates are listed in Tables G.1 and G.2 for  $P = 0.80$  and  $0.90$ , respectively.

m Maximum Auto- Correlation Lags	n=2N/m Degrees of Freedom	C Lower Limit, dB	D Upper Limit, dB	D-C Spread, dB
128	16	-1.68	2.35	4.03
64	32	-1.24	1.57	2.81
32	64	-0.91	1.07	1.98

Table G.1. 80% CONFIDENCE LIMITS FOR  $N = 1024$ .

m Maximum Auto- Correlation Lags	n=2N/m Degrees of Freedom	C Lower Limit, dB	D Upper Limit, dB	D-C Spread, dB
128	16	-2.16	3.03	5.19
64	32	-1.59	2.03	3.62
32	64	-1.16	1.38	2.54

Table G.2. 90% CONFIDENCE LIMITS FOR  $N = 1024$ .

Although these stability results are exact only when  $\{\Delta I(k\tau')\}$ 's are Gaussian and independent, they usually serve as rather good approximations in practical situations when such assumptions are not closely satisfied [Blackman and Tukey (1958)].

It can be gathered from the confidence limits given in Tables G.1 and G.2 that for a fixed value of  $N$ , the smaller the value of  $m$  selected, the more stable the resultant power-spectrum estimate. On the other hand, for the purpose of fine resolution, the value of  $m$  has to be large [see Eq. (G.9)]. Accordingly, there exists a compromise (or trade-off) between stability and frequency resolution for any specific value of  $N$ ; one can increase stability (or frequency resolution) only by sacrificing frequency resolution (or stability). To further illustrate this point, Table G.3 lists the effective resolution bandwidth  $B_e$  along with  $v_0$ , the ratio of RMS (root-mean-square) deviation of the power-spectrum estimate to its average (or true) value for  $N = 1024$  and  $m = 128, 64$ , and  $32$ , respectively. Note that for a Chi-square distribution with  $n = 2N/m$  degrees of freedom,

$$\epsilon_0 = \sqrt{2/n} = \sqrt{m/N} \quad (G.20)$$

It is clear from this table that one can improve frequency resolution at an expense of variability, and vice versa.

m Maximum Auto- Correlation Lag	Maximum Lag in Sec	$B_e = 1/\pi\tau'$ Effective Resolution Bandwidth	$\epsilon_0 = \sqrt{m/N}$ Normalized RMS Deviation
128	3.5 sec	0.29 Hz	0.35
64	1.75 sec	0.57 Hz	0.25
32	0.88 sec	1.14 Hz	0.18

Table G.3.  $B_e$  AND  $\epsilon_0$  FOR  $N = 1024$ .

In order to find good compromises for individual power spectra, each spectrum is normally calculated using two or all three different values of  $m$  (occasionally a fourth value of  $m$ ,  $m = 256$ , is also tried to see the general trend of this trade-off), and the best compromise is picked out by human judgment. Generally speaking, when the background noise level (including the quantization noise, the noise resulting from instability of phase-locked loop, etc.) is low compared with the signal,  $m/N \approx 1/8$  appears to be a good choice; on the contrary, when the background noise level is high,  $m/n \approx 1/32$  is required to secure a reasonable stability of the estimate.

## BIBLIOGRAPHY

- The American Ephemeris and Nautical Almanac, U.S. Government Printing Office, Washington, D.C., published annually.
- Abramowitz, Milton, and Irene A. Stegun (eds.), Handbook of Mathematical Functions, Dover Publications, Inc., New York, 1968.
- Antonova, T. D., and V. V. Vitkevich, "Results of Radio Observations of Irregularities in the Interplanetary Plasma, 1967-1966," Sov. Astron. - AJ, 12, 5, Mar-Apr, 1967.
- Armstrong, J. W., and W. A. Coles, "Analysis of Three-Station Interplanetary Scintillation," J. of Geophys. Res., 77, 25, pp. 4602-4610, Sep 1, 1972.
- Blackman, R. B., and J. W. Tukey, The Measurement of Power Spectra, Dover Publications, Inc., New York, 1958.
- Blanco, V. M., and S. W. McCuskey, Basic Physics of the Solar System, Addison-Wesley Publishing Company, Inc., Reading, Massachusetts; London, England, 1961.
- Bourgois, G., "Interplanetary Scintillations of Radiosources at 2695 MHz," Astron. & Astrophys., 2, 2, pp. 209-217, 1969.
- Bourgois, G., "Study of the Solar Wind Using the Power Spectrum of Interplanetary Scintillation of Radio Sources," Astron. & Astrophys., 19, 2, pp. 200-206, 1972.
- Bowhill, S. A., "Statistics of a Radio Wave Diffracted by a Random Ionosphere," J. of Res. NBS - D. Radio Propagation, 65D, 3, pp. 275-292, May-June 1961.
- Bramley, E. N., and Margaret Young, "Diffraction by a Deeply Modulated Random-Phase Screen," Proc. IEEE, 114, 5, pp. 553-556, May 1967.
- Brandt, John C., Introduction to the Solar Wind, W. H. Freeman and Company, San Francisco, 1970.
- Briggs, B. H., "Brief Review of Scintillation Studies," Radio Science, 1, 10, pp. 1163-1167, Oct 1966.
- Brigham, E. Oran, The Fast Fourier Transform, Prentice-Hall, Inc., Englewood Cliffs, New Jersey, 1974.
- Buckley, R., "Fluctuations in the Interplanetary Plasma," Planet. Space Sci., 19, pp. 421-436, 1971.
- Budden, K. G., "The Amplitude Fluctuations of the Radio Wave Scattered from a Thick Ionospheric Layer with Weak Irregularities," J. Atmos. Terr. Phys., 27, pp. 155-172, 1965.

- Cadzow, James A., and Hinrich R. Martens, Discrete-Time and Computer Control Systems, Prentice-Hall, Inc., Englewood Cliffs, New Jersey, pp. 355-356, 1970.
- Cambel, Ali Bulent, Plasma Physics and Magnetofluid-Mechanics, McGraw-Hill Book Company, Inc., New York, 1963.
- Carlson, Bruce A., Communication Systems, An Introduction to Signals and Noise in Electrical Communication, McGraw-Hill Book Company, New York, 1968.
- Carlson, Bruce A., Communication Systems, An Introduction to Signals and Noise in Electrical Communication, Second Edition, McGraw-Hill Book Company, New York, 1975.
- Chang, H., T. A. Croft, and M. L. Goldman, "Processed Data Derived from the Pioneer 9 Scintillation Measurements at 50 and 423 MHz near Solar Occultation," SU-SEL-75-027, Center for Radar Astronomy, Stanford University, Stanford, CA, Aug 1975.
- Cohen, M. H., E. J. Gundermann, H. E. Hardebeck, and L. E. Sharp, "Interplanetary Scintillations. II. Observations," Astrophys. J., 147, 2, pp. 449-466, 1967.
- Cohen, M. H., and E. J. Gundermann, "Interplanetary Scintillations IV. Observations Near the Sun," Astrophys. J., 155, 2, pp. 645-663, Feb 1969.
- Coleman, Paul J., Jr., "Turbulence, Viscosity, and Dissipation in the Solar-Wind Plasma," Astrophys. J., 153, Aug 1963.
- Coles, W. A., B. J. Rickett, and V. H. Rumsey, "Interplanetary Scintillations," Solar Wind, NASA Scientific and Technical Information Office, Washington, D.C., 1974.
- Croft, T. A., "Corotating Regions in the Solar Wind, Evident in Number Density Measured by a Radio-Propagation Technique," Radio Science, 6, 1, pp. 55-63, Jan 1971.
- Cronyn, Willard M., "The Analysis of Radio Scattering and Space-Probe Observations of Small-Scale Structure in the Interplanetary Medium," Astrophys. J., 161, 2, pp. 755-763, Aug 1970.
- Cronyn, Willard M., "Density Fluctuations in the Interplanetary Plasma: Agreement between Space-Probe and Radio Scattering Observations," Astrophys. J., 171, 3, pp. L101-L105, Feb 1, 1972a.
- Cronyn, Willard M., "Interferometer Visibility Scintillation," Astrophys. J., 174, 1, pp. 181-200, May 15, 1972b.
- Cronyn, Willard M., "Evidence for a Continuous, Power Law, Electron Density Irregularity Spectrum," Solar Wind, Scientific and Technical Information Office, NASA, NASA SP-308, Washington, D. C., pp. 517-519, 1972c.

- Croft, T. A., private communication, 1973.
- Croft, T. A., M. L. Goldman, and H. Chang, "Scintillations in Amplitude of Simultaneous 50 and 423 MHz Spacecraft Signals at Many Elongations Due to Turbulence in the Solar Wind," SU-SEL-75-025, Center for Radar Astronomy, Stanford University, Stanford, CA, Aug 1975a.
- Croft, T. A., M. L. Goldman, and H. Chang, "Numerical Records of the Amplitude Scintillations Measured by Pioneer 9 at 50 and 423 MHz," SU-SEL-75-026, Center for Radar Astronomy, Stanford University, Stanford, CA, Aug 1975b.
- Davenport, W. B., Jr., "Signal to Noise Ratios in Band-pass Limiters," J. Appl. Phys., 24, 6, pp. 720-727, June 1953.
- Dennison, P. A., and M. Wiseman, "Preliminary Observations of the Effects of a Corotating Stream on Interplanetary Scintillation," Proc. ASA, 1, 4, Dec 1968.
- Ekers, R. D., and L. T. Little, "The Motion of the Solar Wind Close to the Sun," Astron & Astrophys., 10, 2, pp. 310-316, 1971.
- El-Raey, Mohamed, and Philip H. Scherrer, "Differential Rotation in the Solar Atmosphere Inferred from Optical, Radio and Interplanetary Data," Solar Physics, 26, pp. 15-20, 1972.
- Erdélyi, A., (ed.), Tables of Integral Transforms, Volume 1, McGraw-Hill Book Company, Inc., New York, 1954.
- Eshleman, V. R., P. B. Gallagher, and R. C. Barthle, "Radar Methods of Measuring the Cislunar Electron Density," J. Geophys. Res., 65, pp. 3079-3086, 1960.
- Goldstein, R. M., et al., "The superior conjunction of Mariner 4," Jet Propulsion Laboratory Techn. Rept., 32-1092, 1967.
- Goodman, Joseph W., Introduction to Fourier Optics, McGraw-Hill Book Company, Inc., New York, 1968.
- Harris, D. E., and E. G. Hardebeck, Astrophys. J. Suppl., 19, 170, p. 115, 1969.
- Hewish, A., P. F. Scott, and D. Wills, "Interplanetary Scintillation of Small Diameter Radio Sources," Nature, 203, pp. 1214-1217, Sep 19, 1964.
- Hewish, A., P. A. Dennison, and J. D. H. Pilkington, "Measurements of the Size and Motion of the Irregularities in the Interplanetary Medium," Nature, 209, 5029, pp. 118-1189, Mar 19, 1966.
- Hewish, A., and M. D. Symonds, "Radio Investigation of the Solar Plasma," Planet. Space Sci., 17, pp. 313-320, 1969.

- Hewish, A., and S. J. Burnell, "Fine Structure in Radio Sources at Metre Wavelengths--I The Observations," Mon. Not. R. astr. Soc., 150, 2, pp. 141-147, 1970.
- Hewish A., "The Spectrum of Plasma-Density Irregularities in the Solar Wind," Astrophys. J., 163, 3, pp. 645-647, Feb 1, 1971.
- Hewish, A., "Observations of the Solar Plasma Using Radio Scattering and Scintillation Methods," Solar Wind, NASA Scientific and Technical Information Office, NASA SP-308, Washington, D.C., pp. 477-485, 1972.
- Hollweg, Joseph V., "Angular Broadening of Radio Sources by Solar Wind Turbulence," J. Geophys. Res., Space Physics, 75, 19, pp. 3715-3727, July 1, 1970.
- Hollweg, J. V., and J. R. Jokipii, "Wavelength Dependence of the Interplanetary Scintillation Index," Solar Wind, Scientific and Technical Information Office, NASA, NASA SP-308, pp. 494-496, 1972.
- Houminer, Z., "Corotating Plasma Streams revealed by Interplanetary Scintillation," Nature Physical Science, 231, pp. 165-167, June 21, 1971.
- Houminer, Z., and A. Hewish, "Long-Lived Sectors of Enhanced Density Irregularities in the Solar Wind," Planet. Space Sci., 20, pp. 1703-1716, 1972.
- Houminer, Z., "Power Spectrum of Small-Scale Irregularities in the Solar Wind," Planet. Space Sci., 21, pp. 1367-1379, 1973.
- Houminer, Z., and A. Hewish, "Correlation of Interplanetary Scintillation and Spacecraft Plasma Density Measurements," Planet. Space Sci., 22, pp. 1041-1042, 1974.
- Intriligator, D. S., and J. H. Wolfe, "Preliminary Power Spectra of the Interplanetary Plasma," Astrophys. J., 162, pp. L187-L190, Dec 1970.
- Jaffe, R., and E. Rechtin, "Design and Performance of Phase Lock Circuits Capable of Near Optimum Performance Over a Wide Range of Input Signal and Noise Levels," IRE Transactions-Information Theory, pp. 66-76, Mar 1955.
- Jokipii, J. R., and Joseph V. Hollweg, "Interplanetary Scintillations and the Structure of Solar-Wind Fluctuations," Astrophys. J., 160, 2, pp. 745-753, May 1970.
- Jokipii, J. R., "On the 'Thin Screen' Model of Interplanetary Scintillations," Astrophys. J., 161, 3, pp. 1147-1152, Sep 1970.
- Koehler, R. L., "A Phase Locked Dual Channel Spacecraft Receiver for Phase and Group Path Measurements," Scientific Report No. 1, SU-SEL-65-007, Stanford Electronics Laboratories, Stanford University, Stanford, CA, Feb 1965.

- Koehler, Richard L., Interplanetary Electron Content Measured Between Earth and the Pioneer VI and VII Spacecraft Using Radio Propagation Effects, Scientific Report No. SEL-67-051, Stanford Electronics Laboratories, Stanford University, Stanford, CA, 1967.
- Koehler, Richard L., "Radio Propagation Measurements of Pulsed Plasma Streams from the Sun Using Pioneer Spacecraft," J. of Geophys. Res., Space Physics, 73, 15, pp. 4883-4894, Aug 1, 1968.
- Kraichnan, Robert H., "Inertial-Range Spectrum of Hydromagnetic Turbulence," The Physics of Fluids, 8, 7, July 1965.
- Kraus, John D., Radio Astronomy, McGraw-Hill Book Company, New York, 1966.
- Kundu, Mukul R., Solar Radio Astronomy, Interscience Publishers, a Division of John Wiley & Sons, 1965.
- Landt, Jeremy A., and Thomas A. Croft, "Shape of a Solar Wind Disturbance on July 9, 1966, Inferred from Radio Signal Delay to Pioneer 6," J. Geophys. Res., Space Physics, 75, 25, pp. 4623-4630, Sep 1, 1970.
- Lindsey, W. C., and M. K. Simon, Telecommunication Systems Engineering, Prentice-Hall, Inc., Englewood Cliffs, New Jersey, 1973.
- Little, L. T., and A. Hewish, "Interplanetary Scintillation and Its Relation to the Angular Structure of Radio Sources," Mon. Not. astr. Soc., 134, pp. 221-237, 1966.
- Little, L. T., and A. Hewish, "Radio Source Structure Derived from Interplanetary Scintillation," Mon. Not. R. astr. Soc., 138, 4, pp. 393-406, 1968.
- Little, L. T., "Small Scale Plasma Irregularities in the Interplanetary Medium," Astron. & Astrophys., 10, 2, pp. 301-305, 1971.
- Lovelace, R. V. E., E. E. Salpeter, and L. E. Sharp, "Analysis of Observations of Interplanetary Scintillations," Astrophys. J., 159, 3, pp. 1047-1055, Mar 1970.
- Lovelace, Richard V. E., "Theory and Analysis of Interplanetary Scintillations," Ph.D. dissertation, Cornell University, Ithaca, New York, Sep 1970.
- Lotova, N. A., and I. V. Chashey, "Spectrum of Small-Scale Interplanetary Plasma Inhomogeneities," Geomagnetism & Aeronomy, XII, 5, pp. 694-699, 1972.
- Lüst, R., "Interplanetary Plasma," Chapter 13 in Introduction to Solar Terrestrial Relations, (J. Ortner and H. Maseland, eds.), 1965.
- Marians, Marilyn, "Computed Scintillation Spectra for Strong Turbulence," Radio Science, 10, 1, pp. 115-119, Jan 1975.



- Matheson, D. N., and L. T. Little, "Radio Scintillations Due to Plasma Irregularities with Power Law Spectra: The Interplanetary Medium," Planet. Space Sci., 19, pp. 1615-1624, 1971.
- Ness, Norman F., "The Interplanetary Medium," Chapter 8 in Introduction to Space Science, (Wilmot N. Hess, Gilbert D. Mead, eds.), Gordon and Breach, Science Publishers, New York, London, Paris, 1965.
- Neugebauer, Marcia, "Large-Scale and Solar-Cycle Variations of the Solar Wind," a paper presented at the International Symposium on Solar-Terrestrial Physics, São Paulo, Brazil, June 17, 1974.
- Oppenheim, Alan V., and Ronald W. Schaffer, Digital Signal Processing, Prentice-Hall, Inc., Englewood Cliffs, New Jersey, 1975.
- Otnes, Robert K., and Loren Enochson, Digital Time Series Analysis, John Wiley & Sons, New York, 1974.
- Peatman, John B., The Design of Digital Systems, McGraw-Hill Book Company, New York, pp. 305-309, 1972.
- Rabiner, L. R., and Bernard Gold, Theory and Application of Digital Signal Processing, Prentice-Hall, Inc., Englewood Cliffs, New Jersey, 1975.
- Rao, A. Pramesh, S. M. Bhandari, and S. Ananthakrishnan, "Observations of Interplanetary Scintillations at 327 MHz," Aust. J. Physics, 27, pp. 105-120, 1974.
- Readhead, A. C. S., "Interplanetary Scintillation of Radio Sources at Metre Wavelengths-II," Mon. Not. R. astr. Soc., 155, 2, pp. 185-197, 1971.
- Rickett, B. J., "Power Spectrum of Density Irregularities in the Solar Wind Plasma," J. Geophys. Res., 78, 10, pp. 1543-1552, Apr 1, 1973.
- Rufenach, C. L., "A radio scintillation method of estimating the small-scale structure in the ionosphere," J. Atmos. Terr. Phys., 33, pp. 1941-1951, 1971.
- Rufenach, Clifford L., "Power-Law Wavenumber Spectrum Deduced from Ionospheric Scintillation Observations," J. of Geophys. Res., 77, 25, pp. 4761-4772, 1972.
- Rufenach, C. L., "Radio Scintillation on Stellar Signals during Artificial Ionospheric Modification," J. Geophys. Res., 78, 25, pp. 5611-5621, Sep 1, 1973.
- Rufenach, C. L., "Ionospheric scintillation by a random phase screen: Spectral approach," Radio Science, 10, 2, pp. 155-165, Feb 1975.
- Rumsey, V. H., "Scintillations Due to a Concentrated Layer with a Power Law Turbulence Spectrum," Radio Science, 10, 1, pp. 107-114, Jan 1975.

Ryzhik, I. M., and I. S. Gradshteyn, Table of Integrals, Series and Products, Academic Press, New York and London, 1965.

Salpeter, E. E., "Interplanetary Scintillations. I. Theory," Astrophys. J., 147, 2, pp. 433-448, 1967.

Salpeter, E. E., "Pulsar Amplitude Variations," Nature, 221, 5175, pp. 31-33, Jan 4, 1969.

Seshadri, S. R., Fundamentals of Plasma Physics, American Elsevier Publishing Company Inc., New York, London, Amsterdam, 1973.

Singleton, Richard C., "An Algorithm for Computing the Mixed Radix Fast Fourier Transform," IEEE Trans. Audio Electroacoust., AU-17, pp. 93-103, June 1969.

Singleton, D. G., "Saturation and Focusing Effects in Radio-Star and Satellite Scintillations," J. Atmos. Terr. Phys., 32, pp. 187-208, 1970.

Singleton, D. G., "Power Spectra of Ionospheric Scintillations," J. Atmos. Terr. Phys., 36, pp. 113-133, 1974.

Snedecor, George W., and William G. Cochran, Statistical Methods, The Iowa State University Press, Ames, Iowa, pp. 155-156, 1967.

Stockham, Thomas G., Jr., "High-Speed Convolution and Correlation," 1966 Spring Joint Computer Conf., AFIPS Conf. Proc., 28, pp. 229-233, 1966.

Tatarski, V. I., Wave Propagation in a Turbulent Medium, translated from Russian by R. A. Silverman, McGraw-Hill Book Company, Inc., New York, 1961.

Tatarski, V. I., The Effects of the Turbulent Atmosphere on Wave Propagation, translated from Russian, Israel Program for Scientific Translations, Keter Press, Jerusalem, 1971.

Unti, T. W. J., M. Neugebauer, and B. E. Goldstein, "Direct Measurements of Solar-Wind Fluctuations Between 0.0048 and 13.3 Hz," Astrophys. J., 180, 2, pp. 591-598, Mar 1, 1973.

Vitkevich, V. V., and V. I. Vlasov, "Radioastronomical Investigations of the Drift of the Inhomogeneous Interplanetary Plasma," Sov. Astron. - AJ, 13, 4, pp. 669-676, Jan-Feb, 1970.

Vitkevich, V. V., and V. I. Vlasov, "Characteristics of Interplanetary Electron Irregularities According to Observations in 1967-1969," Sov. Astron. - AJ, 16, 3, Nov-Dec, 1972.

Waldmeier, M. (ed.), IAU Quarterly Bulletin on Solar Activity, published by the Eidgenössische Sternwarte Zürich, XV, 1969.

- Watanabe, Takashi, Haruichi Washimi, Takakiyo Kakinuma, Masayoshi Kojima, Kazuo Maruyama, and Yoshio Ishida, "Preliminary Observations of Interplanetary Scintillation at 69.3 MHz," Proceedings of the Research Institute of Atmospherics, Nagoya University, 18, pp. 59-71, 1971.
- Watanabe, Takashi, and Takakiyo Kakinuma, "The Recurrent Solar Wind Streams Observed by Interplanetary Scintillation of 3C 48," Publ. Astron. Soc. Japan, 24, pp. 459-467, 1972.
- Welch, Peter D., "The Use of Fast Fourier Transform for the Estimation of Power Spectra: A Method Based on Time Averaging Over Short, Modified Periodograms," IEEE Trans. Audio Electroacoust., AU-15, pp. 70-73, June 1967.
- Westman, H. P. (ed.), Reference Data for Radio Engineers, Fifth Edition, Howard W. Sams & Co., Inc., a subsidiary of ITT, Indianapolis, Kansas City, New York, 1968.
- Wozencraft, John M., and Irwin Mark Jacobs, Principles of Communication Engineering, John Wiley & Sons, Inc., New York, London, Sydney, 1965.
- Yakovlev and Yefimov, Kosmicheskiye issledovaniya, 9, p. 748, Nov 5, 1971.
- Yeh, K. C., and C. H. Liu, "A Theoretical Study of the Ionospheric Scintillation Behavior Caused by Multiple Scattering," Radio Science, 10, 1, pp. 97-106, Jan 1975.
- Zeissig, G. A., and R. V. E. Lovelace, "Interplanetary Scintillation, Interstellar Scattering of Two Pulsars," Astron. & Astrophys., 16, 2, pp. 190-196, 1972.